A Theoretical Exploration of Emerging Solar Absorber Materials

University College London

Christopher N. Savory

Primary Supervisor: Dr. David O. Scanlon

Secondary Supervisor: Dr. Robert G. Palgrave

A thesis submitted in partial fulfillment of the requirements of the degree of

Doctor of Philosophy

October 30, 2018

Declaration

I, Christopher Niall Savory, confirm that the work presented in this thesis is my own. Where information has been derived from other sources, I confirm that this has been indicated in the thesis.

Abstract

Renewable energy sources are the only sustainable solutions that can address the increasing worldwide demand for energy without significantly furthering anthropogenic climate change and damage to our environment. Photovoltaics are able to harness the massive amount of solar radiation onto the earth each day through direct conversion to electricity, however have historically been expensive to produce and deploy on a large scale.

In this thesis, we examine some of the challenges facing current photovoltaic technologies and how recently-developed materials, such as the inorganic-organic lead halide perovskites, have inspired the search for materials that may be used to provide highly-efficient, yet also cheap, mass-producible and flexible solar cells. Through *ab initio* density functional theory, we examine three families of compounds and, through the calculation of their electronic, optical and defect properties, are able to assess their suitability and potential as absorbers within photovoltaic devices. The caesium silver bismuth halides are lead-free analogues of the lead halide perovskites, however our calculations demonstrate that they are limited in comparison to their lead counterparts due to a mismatch in orbital angular momentum in their electronic structure, weakening their absorption. The silver copper sulfides have also shown recent promise as solar absorber materials, although we show that consideration of the optical properties is essential in successfully predicting the potential of such emergent materials. Finally, our survey of the lead bismuth sulfides predicts a promising compound for solar absorption, including the cell architecture that would be necessary to produce high device efficiencies. Through this study, we can accurately calculate properties of these materials but also hope to provide guidance in the future search for new photovoltaic technologies at the atomic scale.

Impact Statement

The work in this thesis examines a number of compound families that are either at the forefront of current international research into photovoltaics or show promise to become one of these emergent materials. Much of this research is pushing our understanding of the intrinsic properties that materials need to perform well as solar absorbers; indeed with the increased resources and developed theories available to computational chemists of today, accurate theoretical prediction of such properties, and even other properties difficult to examine through experiment, of complex compounds and structures is becoming possible. As such research has the potential to develop cheaper, non-toxic materials with less stringent manufacturing requirements and efficiencies that match or exceed those of current records, new directions in photovoltaic technologies are opening up, including flexible cells based on plastic substrates or roll-to-roll printable solar cells, as well as the improving the marketability and attractiveness of current applications.

Increasing the availability of photovoltaic materials and diversifying potential technologies stands to further boost the potential economic and social impact that photovoltaics promise to have on the energy sector over the next few decades. The reduction of carbon emissions while increasing overall electrical generation capacity is a challenge occurring on many scales – from consumers, to national grid architectures and even international policy makers such as the European Union or United Nations. The potential capacity for photovoltaics is demonstrable through the scale of solar radiation incident on the Earth every day, and far exceeds the capacity of non-renewable resources, however cost, difficulty and scale of manufacture has historically led to them not being considered economically viable for large scale energy generation. Recently, numerous countries, including Germany and the UK, have invested significantly in renewable energy generation and have seen dividends –

whether homeowners benefiting from feed-in tariffs, companies being able to market large-scale solar farms or national services being able to remove coal-based power stations from the electricity grid altogether.

Acknowledgements

Firstly, I would like to thank immensely my supervisor, Dr. David Scanlon, for all his amazing support, advice and encouragement throughout my time studying for this degree. David has always been willing to answer any question, scientific or not, and at every step of the PhD journey, has inspired me to become a better researcher. The unending font of new-materials-to-try-out has helped to keep these years plenty busy too! The members of the Scanlon Materials Theory Group across the years have been of great help and support, but I would like to give especial thanks to Alex Ganose, for his astounding scripting wizardry and being a superb comrade in the search for new photovoltaics, Dr. Ben Williamson, for his defect wisdom and endlessly enjoyable supply of in-jokes, and Dr. Adam Jackson for so many idea-stimulating discussions, both in the office and in the bar. Additional thanks to all the occupants/inmates of our offices KLB 349 and CIB G19, including Catan-masters Dr. Dougal Howard and Dr. Ian Johnson, who have made the research environment such a wonderful place to work.

I would also like to thank all our collaborators at UCL and abroad in both the work included in this thesis and all the other projects over the past few years. Especial thanks to my secondary supervisor Dr. Robert Palgrave, both for his – and his group members, Dr. Will Travis and Ria Atri – work on the silver copper sulfides but also his support throughout this degree. I would also like to thank Dr. Max Birkett and Prof. Tim Veal at University of Liverpool for all their extremely thorough and impressive ellipsometry, XPS and Raman work, along with Dr. Vin Dhanak and Dr. Jon Major and their research groups, also at Liverpool. Across the Atlantic, I would like to thank Prof. Brent Melot as well as his group at the University of South California and Prof. Jamie Neilson at the University of Colorado for their amazing (and entertaining) collaborations too. Finally, I would like to thank Prof. Aron

Walsh, for all his insights into the silver bismuth double perovskites, as well as many clear and educational presentations, and also the members of his research group for their always friendly company at conferences.

The work for this thesis was supported by EPSRC and the Department of Chemistry at UCL by the provision of a Doctoral Training Partnership studentship (1492829). The computational work in this these made use of a number of high-performance computing (HPC) facilities: Archer U.K. National Supercomputing Service, via membership of the U.K.'s HEC Materials Chemistry Consortium, funded by EPSRC (Grant No. EP/L000202); Iridis cluster, provided by the EPSRC funded Centre for Innovation (EP/K000144/1 and EP/K000136/1); and the UCL Legion (Legion@UCL) and Grace (Grace@UCL) HPC facilities.

On a personal note, I would like to thank Sasha for being the best and most understanding housemate I could ask for over the past 3 years, and Elena, Hugh, Gavin, Chris and Alice for the many, many board games at Beresford Road. Finally, my utmost thanks to my parents – Kathren and Nigel – who have supported my life, education and happiness for the past 26 (hopefully not-too-long-seeming!) years with all their love and attention. Thank you so much to all.

Abbreviations

Theory

QM – Quantum Mechanics

TISE – Time-Independent Schrödinger Equation

BO – Born-Oppenheimer (approximation)

HF – Hartree Fock

LCAO – Linear Combination of Atomic Orbitals

UEG – Uniform Electron Gas, or jellium

DFT – Density Functional Theory

DFPT – Density Functional Perturbation Theory

DFT+U – Density Function Theory with the inclusion of Hubbard U

PES – Potential Energy Surface

SCF – Self-Consistent Field

SOC – Spin-Orbit Coupling

Density Functionals

LDA – Local Density Approximation

GGA – Generalized Gradient Approximation

PBE – Perdew, Burke and Ernzerhof functional (1996)

PBEsol – Perdew, Burke and Ernzerhof 1996 functional adapted for solids and surfaces (2008)

PBE0 – Perdew, Burke and Ernzerhof 1996 functional with 25 $\%$ HF exchange (1999)

HSE06 – Heyd, Scuseria and Ernzerhof 2003 functional using $\omega = 0.11\,\text{bohr}^{-1}$ (2006)

Intrinsic properties and qualities

VBM – Valence Band Maximum

CBM – Conduction Band Minimum

IP – Ionisation Potential

EA – Electron Affinity

(P)DOS – (Partial) Density of States

TDM – Transition Dipole Moment

TL – Transition Level

Photovoltaic properties

PV – Photovoltaic

PCE – Power Conversion Efficiency

AM 1.5G – Air Mass 1.5 Global (solar spectrum)

V_{oc} – Open Circuit Voltage

J_{sc} – Short Circuit Current Density

FF – Fill Factor

EQE – External Quantum Efficiency

SQ – Shockley-Queisser (limit)

SRH – Shockley-Read-Hall (recombination)

EM – Electromagnetic (Spectrum)

Methods

VASP – Vienna *Ab initio* Simulation Package

PAW – Projector Augmented Wave

XRD – X-ray diffraction

XPS – X-ray Photoemission Spectroscopy

PL – Photoluminescence

ICSD – Inorganic Crystal Structure Database

SOD – Site Occupancy Disorder

SLME – Spectroscopically Limited Maximum Efficiency

Materials

QD – Quantum Dot

TCO – Transparent Conducting Oxide

CIGS(Se) – $Cu(In, Ga)S(Se)_2$

CZTS – Cu_2ZnSnS_4

MA – Methylammonium ($CH_3NH_3^+$) ion

FA – Formamidinium ($CH(NH_2)_2^+$) ion

BA – Butylammonium ($(CH_3(CH_2)_3NH_3)^+$) ion

PEA – Phenylethylammonium ($(C_6H_5(CH_2)_2NH_3)^+$) ion

MAPI – Methylammonium Lead Iodide, $(CH_3NH_3)PbI_3$

P3HT – poly(3-hexylthiophene)

PEDOT:PSS – poly(3,4-ethylenedioxythiophene) polystyrene sulfonate

PCBM – [6,6]-phenyl-C_61-butyric acid methyl ester

ITO – Tin-doped indium oxide

FTO – Fluorine-doped tin oxide

Publications

1. *The vapour phase detection of explosive markers and derivatives using two fluorescent metal-organic frameworks*, M. Jurcic, W.J. Peveler, **C.N. Savory**, D.O. Scanlon, A.J. Kenyon and I.P. Parkin, *Journal of Materials Chemistry A*, **3**, 6351-6359 (2015)
2. *$(CH_3NH_3)_2Pb(SCN)_2I_2$: A More Stable Structural Motif for Hybrid Halide Photovoltaics?*, A.M. Ganose, **C.N. Savory** and D.O. Scanlon, *Journal of Physical Chemistry Letters*, **6**, 4594-4598 (2015)
3. *Spatial Electron-hole Separation in a One Dimensional Hybrid Organic-Inorganic Lead Iodide*, **C.N. Savory**, R.G. Palgrave, H. Bronstein and D.O. Scanlon, *Scientific Reports*, **6**, 20626 (2016)
4. *An assessment of silver copper sulfides for photovoltaic applications: theoretical and experimental insights*, **C.N. Savory**, A.M. Ganose, W. Travis, R.S. Atri, R.G. Palgrave and D. O. Scanlon, *Journal of Materials Chemistry A*, **4**, 12648-12657 (2016)
5. *Hybrid Organic-Inorganic Coordination Complexes as Tuneable Optical Response Materials*, W. Travis, C.E. Knapp, **C.N. Savory***, A.M. Ganose*, P. Kafourou *et al.*, *Inorganic Chemistry*, **55**, 3393-3400 (2016)
6. *Vibronic Structure in Room Temperature Photoluminescence of the Halide Perovskites $Cs_3Bi_2Br_9$*, K.K. Bass, L. Estergreen, **C.N. Savory**, J. Buckeridge, D.O. Scanlon, P.I. Djurovich, S.E. Bradforth, M.E. Thompson and B.C. Melot, *Inorganic Chemistry*, **56**, 42-45 (2016)
7. *Can Pb-Free Halide Double Perovskites Support High-Efficiency Solar Cells?*, **C.N. Savory**, A. Walsh and D.O. Scanlon, *ACS Energy Letters*, **1**, 949-955 (2016)
8. *Beyond methylammonium lead iodide: prospects for the emergent field of ns^2 containing solar absorbers*, A.M. Ganose*, **C.N. Savory*** and D.O. Scanlon, *Chemical Communications*, **53**, 20-44 (2017)
9. *Electronic and defect properties of $(CH_3NH_3)_2Pb(SCN)_2I_2$ analogues for photovoltaic applications*, A.M. Ganose, **C.N. Savory** and D.O. Scanlon, *Journal of Materials Chemistry A*, **5**, 7485-7853 (2017)

10. *Atypically small temperature-dependence of the direct band gap in the metastable semiconductor copper nitride Cu_3N*, M. Birkett, **C.N. Savory**, A.N. Fioretti, P. Thompson, C. A. Muryn *et al.*, *Physical Review B*, **95**, 115201 (2017)

11. *Exploring the PbS–Bi_2S_3 series for next generation energy conversion materials*, **C.N. Savory**, A.M. Ganose and D.O. Scanlon, *Chemistry of Materials*, **29**, 5156-5167 (2017)

12. *Core Levels, Band Alignments and Valence-Band States in $CuSbS_2$ for Solar Cell Applications*, T.J. Whittles, T.D. Veal, **C.N. Savory**, A.W. Welch, F.W. de Souza Lucas, *et al.*, *ACS Applied Materials & Interfaces*, **9**, 41916-41926 (2017)

13. *Band gap temperature-dependence and exciton-like state in copper antimony sulphide, $CuSbS_2$*, M. Birkett, **C.N. Savory**, M.K. Rajpalke, W.M. Linhart, T.J. Whittles, J.T. Gibbon, A.W. Welch, I.Z. Mitrovic, A. Zakutayev, D.O. Scanlon, and T.D. Veal, *APL Materials*, **6**, 084904 (2018)

14. *A scalable synthesis approach to antimony selenide solar cells*, L.J. Philips, **C.N. Savory**, P.J. Yates, H. Shiel, O.S. Hutter, S. Mariotti, L. Bowen, K. Durose, D.O. Scanlon, and J.D. Major, *in submission* (2018)

15. *Exploiting excited-state aromaticity to design highly stable singlet fission materials* K.J. Fallon, P. Budden, E. Salvadori, A.M. Ganose, **C.N. Savory**, L. Eyre, D.O. Scanlon, C.W.M. Kay, A. Rao, R.H. Friend, A.J. Musser and H. Bronstein, *in submission* (2018)

16. *Band Alignments, Band Gap, Core-levels and Valence-Band States in Cu_3BiS_3 for Photovoltaics* T.J. Whittles, T.D. Veal, **C.N. Savory**, P.J. Yates, P.A.E. Murgatroyd, J.T. Gibbon, M. Birkett, R.J. Potter, J.D. Major, K. Durose, D.O. Scanlon and V.R. Dhanak, *in submission* (2018)

17. *Sensing and discrimination of explosives at variable concentration with a large-pore MOF as part of a fluorescent array* M. Jurcic, W.J. Peveler, **C.N. Savory**, D.-K. Bučar, A.J. Kenyon, D.O. Scanlon and I.P. Parkin, *in submission* (2018)

* Authors provided equal contribution to the work

Contents

List of Figures

List of Tables

Chapter 1

Introduction

1.1 Energy: the case for Renewables and Photovoltaics

The generation of energy in a usable form has driven the technological and societal progress of humanity throughout history – from the humble origins of fire and the water mill to enable us to process food, to the immense, international electricity consumption needed to power the devices and production of the modern era. As global population and development ever increases, so must our capability to meet that population's demand for energy; indeed, as the population is set to increase to over 9 billion by 2050, the energy consumption is projected by the US and EU to at least double from 13.5 TW in 2001 to 27.6 TW in the same amount of time.[1,2] Throughout the latter half of the 20th and current 21st century, however, it has become clear that while this demand could be met through consumption of current natural gas, oil and coal reserves, it must not, at least wholly, in order to avoid increasing the highly detrimental impact of anthropogenic global warming and ocean acidification on coastal and terrestrial ecosystems, food production and numerous other systems, both natural and human.[3] Instead, we must turn from fossil fuels to other energy sources if governmental and international emissions targets are to be met; renewable energy resources such as wind and solar provide low carbon intensity energy generation without the inherent immense upfront cost and dangerous waste products of nuclear fission reactors, thus presenting some of the most promising and fast-growing solutions to humanity's demand for more power.[2]

Solar energy demonstrates, by far, the greatest potential of supply, with the power from the Sun incident onto the Earth far outstripping our need, and even the capabilities of the entire remaining stocks of fossil fuels – harnessing just 0.001 % of it would be sufficient to power the entire planet,[1] and yet renewable sources represent less than 20 % of the total energy generated internationally, dropping to near 5 % when biomass is excluded. Photovoltaic cells (PV) present arguably the most useful route through which incident energy might be harnessed into usable electricity by directly converting absorbed photons into electrical power – the lack of many mechanical parts and long lifetimes of currently used materials allows PV modules (numerous individual solar cells connected in series) to be mounted on individual houses or buildings and directly provide power wherever needed. Historically, the high cost per kWh of PV relative to fossil fuels have disincentivised the widespread

usage of PV. In recent decades, however, improved efficiencies and lower overall costs have been important in driving the substantial market expansion that PV has seen: where the total global renewable power capacity increased 10 times from 2000 to 2015, PV capacity increased 60 times in that same period, now making up nearly one third of that total.[4] As photovoltaics become an increasingly important part of a diversifying and delocalised energy generation economy, much attention has been paid towards photovoltaics as a direct competitor to current energy generation technologies – an electricity cost of \$0.03/kWh would bring parity with fossil fuel generation, allowing the gateway to future expansion, but requires high thermodynamic efficiency and a reduction in module cost, from values around \$4/W in 2010, to approximately \$0.3/W.[5] As such, current solar cell architectures but also promising emergent non-toxic, abundant and potentially highly-efficient photovoltaic materials are an extremely worthwhile target for scientific research in order to reach, or even succeed this target.

1.2 The Photovoltaic effect

In 1839, Edmond Becquerel reported "*sur les effets det la radiation chimique de la lumière solaire, au moyen des courants électriques*", giving the first known description of light-generated electric current as he observed the response of a galvanometer between two platinum electrodes submerged in a solution of chloride salt as light shone on them.[6] The experiments of Adams and Day in 1877 on bars of selenium then confirmed that such a response was solely the effect of 'light', and not thermally induced, through the rapid drop in conductivity seen when covering a match flame illuminating the selenium – they termed this electronic response solely from the action of light 'photoelectric', now referred to as the *photovoltaic effect*.[7]

In current times, we now know the cause of the photovoltaic effect – as light is shone on a material, photons can excite electrons within it to a higher energy state, and leaving behind a positively-charged hole – a space in the electronic structure that the electron used to occupy. If this excitation occurs in a solid semiconductor, like selenium, the electron is excited to the nominally-unoccupied *conduction band* (CB), leaving behind a hole in the fully-occupied *valence band* (VB). If some mechanism exists to separate the electron and hole in space, both can act as free charge carriers,

and thus increase the conductivity through the creation of a photocurrent; equally, given that the two are separated in energy by the *band gap* (a region of energy between the VB and CB in which there are no electronic states), and the difference in charge between them, a potential difference occurs, creating a photovoltage. As with other electronic devices, the presence of both a current and a voltage ensures the generation of electrical power, and thus the photovoltaic effect can be used to convert solar power into electrical power with no consumption of chemical resources – the goal of renewable energy technologies.

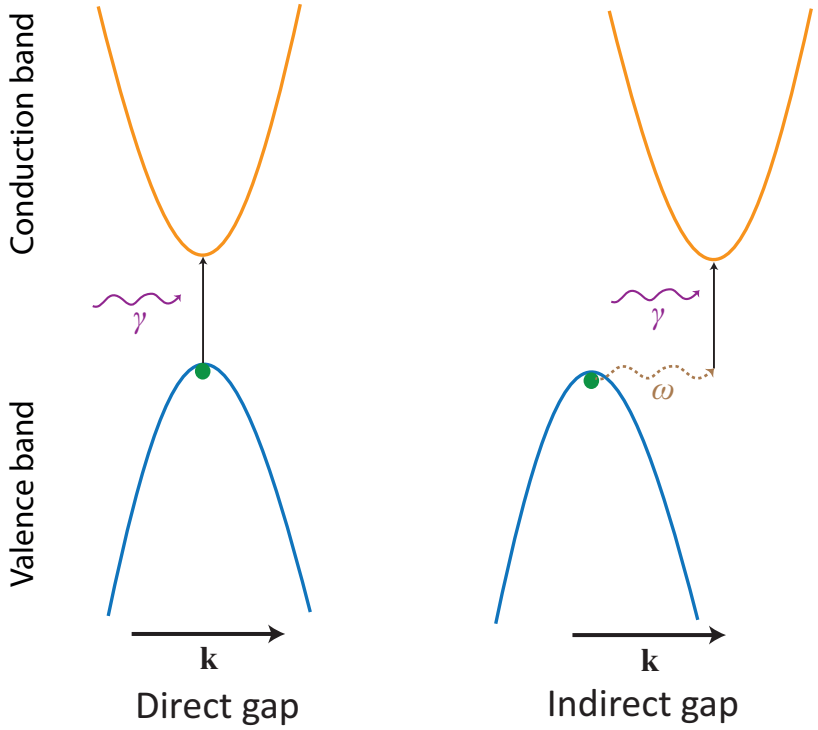

Figure 1.1: Representation of photoexcitation of an electron (green circle) in direct and indirect semiconductors. The electronic transition in each case is represented by the black arrow, while the incident photon is represented by the purple (γ) and a phonon, providing the change in momentum for an indirect transition, by the brown (ω) arrow respectively.

For photoabsorption, the first stage of the photovoltaic effect, in semiconductors, there are two arrangements of valence and conduction band that need to be considered: when the minimum of the conduction band (CBM) and maximum of the valence band (VBM) occur in $\mathbf{k}$-space (a reflection of the momentum and periodicity of the bands themselves, discussed further in Section 3.1.2) at the same point, forming a *direct* fundamental band gap; or when they occur at different points in $\mathbf{k}$-space, where the band gap is termed *indirect*. The excitation of an electron at these

two conditions are depicted in Figure 1.1: for a direct gap, the energy of the incident photon of the correct energy is absorbed, exciting the electron to the conduction band; in an indirect gap material, the absorption of a photon must be accompanied by an additional particle, such as a phonon (lattice vibration), to facilitate the change in $\mathbf{k}$, as the momentum of the photon is negligible and the overall momentum must be conserved during the transition. The necessity for a three-particle interaction, as opposed to a two-particle interaction in a direct transition, severely reduces the probability of such an excitation occurring – in general, this reduces the absorptivity of the semiconductor, the consequences of which will be discussed in Sections 1.2.3 and 1.2.5.

The second stage of the photovoltaic effect – charge separation – can be performed in multiple ways, but in general requires some gradient, whether electrical/charge-based or thermodynamic, to drive the process. In the next section, we will discuss how a traditional solid-state solar cell is composed and how this facilitates the separation of electron and hole, but other cell types and architectures are discussed in Section 1.3.3.

1.2.1 Structure and Architecture of a solar cell

The first practical solar cells were developed by Fuller, Pearson and Chapin at Bell Laboratories in the 1950's using silicon as the semiconductor basis for a solar cell – in these, the cell was composed of two layers of silicon, one doped p-type through substitutional gallium (leaving the silicon slightly electron deficient) and modulating the Fermi level to a position near the valence band, while the other was doped n-type through interstitial lithium, making it electron rich (a similar effect can be done through substitutional doping of phosphorous). When two opposingly-doped layers such as these are brought together, a $p-n$ junction forms: at the interface of the two layers, there is a diffusion gradient for electrons to move from the electron-rich n-type layer to the electron-poor p-type layer, and *vice versa* for the holes; as the carriers diffuse, the overall Fermi level is equilibrated across the junction. During this process, the movement of electrons from the n-type layer leaves the positively-charged (in the absence of their associated carrier) donor cores at the interface exposed, while there is an equal build up of negative charge on the p-type side; this

potential difference eventually forms an electric field opposing the original electron diffusion at the junction. The area in which this electric field applies is then the 'depletion region' – if a free carrier is generated in this region, it is quickly swept out of the region by the electric field into the corresponding majority-carrier layer (free electrons towards the n-type layer, and holes towards the p-type layer). This process is represented in Figure 1.2.

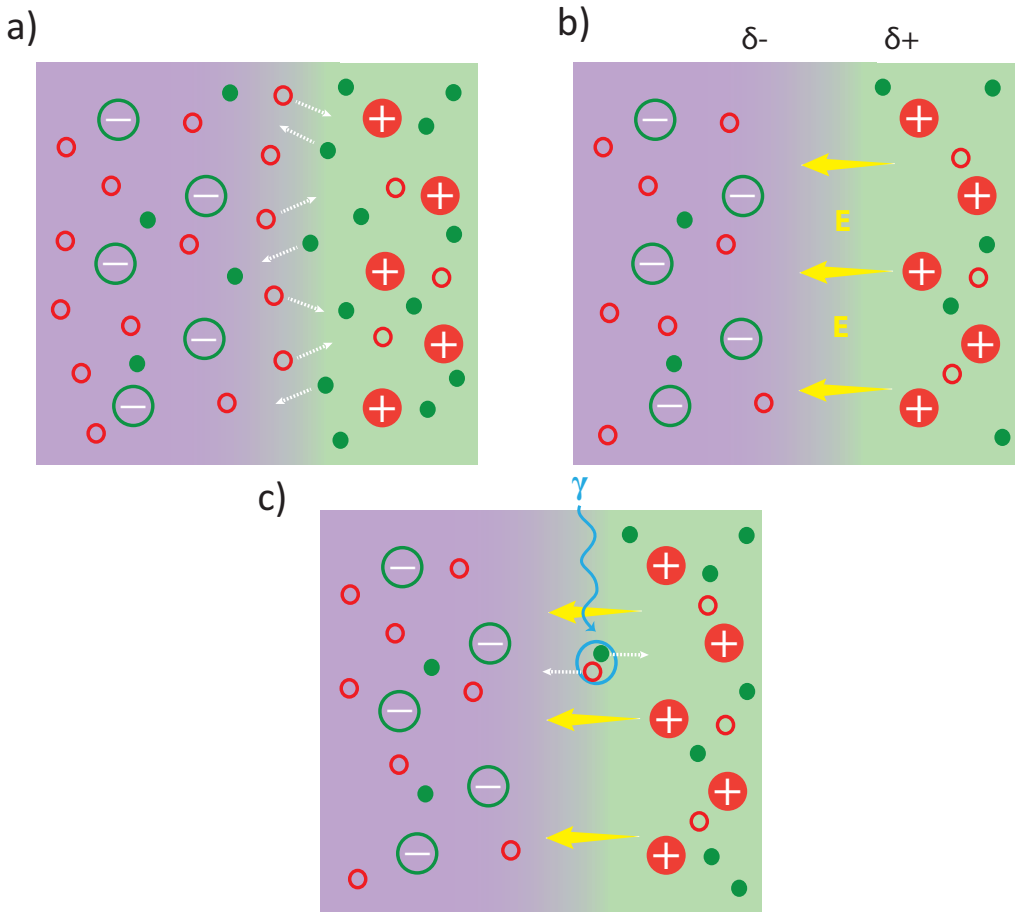

Figure 1.2: Pictorial representation of $p-n$ junction formation and action: a) when p-type (shaded purple) and n-type (shaded green) materials come into contact, majority carriers (holes as small hollow red circles, electrons as small filled green circles) diffuse across into the low concentration opposing material, where they recombine (de-excite). b) the dopant ion cores (filled red circles for donor defects, hollow green circles for acceptor defects) near to the junction are exposed in the absence of free carriers – this forms a small charge difference across the junction, and a resultant electric field (yellow). This field then acts to sweep any additional carriers out of the junction, forming a depletion region. c) An electron-hole pair is generated by the absorption of a photon (blue) in the depletion region – the bias of the field then separates the electron-hole pair, by inducing the hole towards the p-type layer, and the electron towards the n-type.

$p-n$ junctions are used in a variety of other electronic devices, including light-

emitting diodes (which may simplistically be described as a photovoltaic acting in reverse), but in photovoltaics allow for an inherent charge separation when the electron-hole pair is generated within the depletion region. Both layers of a $p-n$ junction need not be constructed from the same base semiconductor; if for example, the particular material cannot easily be doped n-type, then it can be paired with a n-type doped different semiconductor in a *heterojunction* – ideally, the two semiconductors should have similar structures to avoid dislocations and other defects at the interface. A successful example of this type of architecture is p-type CdTe with the efficient electron conductor n-type CdS (see Section 1.3.2 below). Additionally, if a particular semiconductor cannot be easily doped, it can be left as intrinsic, and paired on one side with a p-type material, and an n-type on the other, forming a $p-i-n$ junction across the entirety of the intrinsic layer.

The final process necessary for the solar cell to operate is then, once the charge carriers have been generated and separated, that they must be extracted out of the device and into an external circuit to be of use. So, the complete solar cell must include a highly conductive top and bottom contact on either side of the $p-n$ junction to allow this extraction and to connect to the external circuit. Of these, the back contact is a metal, while the front contact presents an issue – it must be able to extract carriers efficiently but also let light into the device. As such, older devices often had 'strips' of contact material on the front of the device, with the remainder covered by glass, but newer devices have seen the usage of transparent conducting oxides (TCOs) as efficient contacts that can cover the entire frontage of the cell, as they are both transparent to the majority of the solar spectrum (particularly the high IR and visible) while also highly conductive. The overall (simplified) architecture of a typical $p-n$ semiconductor solar cell is thus represented in Figure 1.3.

1.2.2 Extrinsic properties of PV devices: $V_{\mathbf{oc}}$, $J_{\mathbf{sc}}$, FF and efficiency

With our solar cell established, we can now focus on what we can get out of it – the measured outputs and properties of a given cell, and also how these can be compared between cells. The primary target output is power in the form of electricity – as with any energy conversion device the output power will depend on two factors: the input power (in this case, in the form of the intensity of incident photons onto the cell's

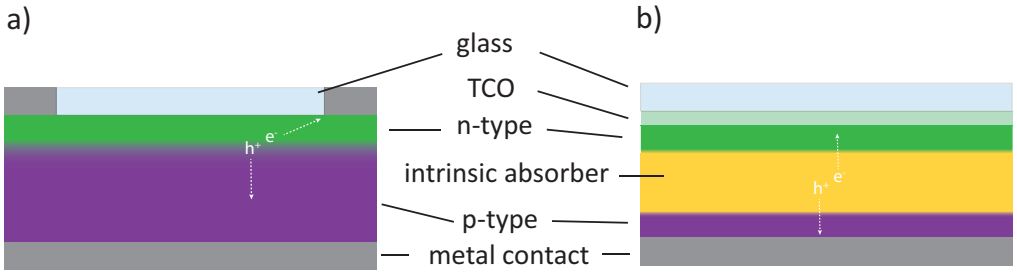

Figure 1.3: Simplified diagram of solar cell architectures: a) a $p-n$ junction architecture traditionally used for silicon-based solar cells, b) a $p-i-n$ architecture, related to those used in 'thin-film' solar cells, including a transparent conducting oxide (TCO) as a contact. Both diagrams show the overall drift pathways for the photogenerated carriers in the depletion region.

surface) and its efficiency in conversion, the percentage of power output to power input. For a solar cell, the former is dependent on the light source, but the most traditional standard assessment to enable comparison between different cells in the laboratory is to use the output of an 'artificial sun': the AM 1.5G spectrum, which describes the global average of spectral irradiance from the Sun's output onto the Earth, if the Sun were at an angle of incidence of 42° to the surface of the Earth and the cell were at sea level, and including losses due to the absorption of molecules in the atmosphere. With this factor fixed, we can directly assess the relative ability for PV devices to convert light through the *power conversion efficiency* (PCE), or η, which is the key factor that we want to maximise for the most optimal PV devices.

The efficiency of a solar cell is given by the ratio of maximum output power to incident power; the former of these, P_{max}, as with other electronic devices, is given by the product of the current and the potential difference. For the case of a photovoltaic, however, we will use a specific current and voltage and also multiply by another variable, the fill factor, giving:

$$\eta = \frac{P_{max}}{P_{in}} = \frac{V_{oc} J_{sc} FF}{P_{in}} \tag{1.1}$$

where V_{oc} is the *open circuit voltage*, J_{sc} is the *short circuit current (density)* and FF is the *fill factor* – all three of these terms relate to extrinsic properties of a solar cell and will be defined further in the following discussion. To ensure parity between values calculated for different devices, solar cell efficiency testing is done under standard conditions: the AM 1.5G spectrum, a temperature of 25 °C and the

incident power density P_{in} is defined as 1 kW/cm^2.[8]

The first of these to discuss is the short circuit current, which is the current through the cell when it is short circuited (i.e. the contacts on either face of the cell are directly connected) and so the output voltage is zero, and so represents the maximum current obtainable within the cell. As discussed above, photocurrent arises from the generation of charge carriers, whether electrons of holes, under illumination, and so J_{sc} is dependent on a number of factors, both internal and external. Two of these, the cell area and the intensity spectrum of incident light, are normalized for comparison between cells; the latter for a terrestrial cell by using the AM 1.5G spectrum, the former generally by quoting the short circuit current (I_{sc}) as a current density (J_{sc}), in units of mA/cm^2. The remaining factors then directly relate to the ability of the entire cell (via the absorber layer) to generate charge carriers – namely the optical absorption and reflection of the cell, the effects of which are considered in section 1.2.3. For ideal cell behaviour, every photon incident on the device that has energy above the band gap of the absorber will be absorbed, producing two charge carriers towards the external circuit, and thus J_{sc} is purely dependent on the band gap. The highest J_{sc} will be then theoretically be obtained when the band gap is minimal (but finite).

The open circuit voltage is the opposing property to the J_{sc}, and is the maximum potential difference across the cell, obtained when the net current through the device is zero. The absolute maximum of the V_{oc} is constrained by the fundamental band gap of the absorber layer, as it is the greatest potential difference between the negatively charged electron and positively charged hole when relaxed to their respective band edges. In actuality, the V_{oc} will be reduced through additional mechanisms: the alignment of the bands in the transport or contact layers with those of the absorber will constrain the V_{oc} further, while the V_{oc} will also necessarily be reduced through electron-hole recombination within the cell. The V_{oc} exhibits this reduction due to its dependence on the *dark current*, J_0 – while the J_{sc} reflects the immediate current on light-induced carrier generation, J_0 is the current that flows through the cell naturally in the dark when connected in an external circuit, purely as a result of thermally-generated carriers, and acts in the opposite direction to the photocurrent. As a solar cell acts as a diode, the V_{oc} can be given by the diode equation for a charge q at $J = 0$:

$$V_{\mathrm{oc}} = \frac{nk_BT}{q}\ln\left(\frac{J_{\mathrm{L}}}{J_0} + 1\right) \tag{1.2}$$

where n is the *ideality factor*, k_B is the Boltzmann constant, T is the temperature and J_{L} is the light-generated current; for most absorbers, $J_{\mathrm{L}} \approx J_{\mathrm{sc}}$. J_0 is highly dependent on the recombination within the material of the solar cell, and will always increase with greater recombination – as radiative recombination (spontaneous emission) will always occur to some degree, V_{oc} will always be reduced from the value of the band gap. Nevertheless, for an ideal absorber, V_{oc} will generally increase with the band gap of the absorber (albeit up until a point in which J_{sc} becomes very small, and the natural logarithm in Equation 1.2 tends back towards to 0.) The ideality factor is also dependent on the mechanisms of recombination present in the cell – their effects will be discussed further in the following section, 1.2.3.

The final extrinsic property is the fill factor, FF, which is most easily observed through the plotting of the *J–V* curve for a hypothetical cell; the *J–V* curve depicts the current-voltage relationship of the cell under illumination, and is the measurement usually required to calculate the efficiency of a synthesised sample solar cell. An example of a *J–V* curve is plotted in Figure 1.4, along with the corresponding definitions of FF and P_{max}.

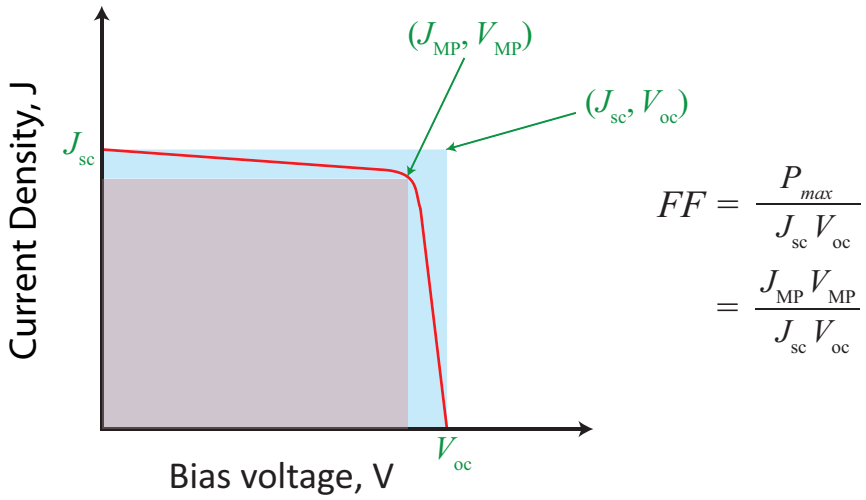

Figure 1.4: *J–V* curve for a hypothetical solar cell, marked by a red line, with the positions of J_{sc} and V_{oc} marked. The fill factor, FF, is represented by the ratio of the areas of the blue rectangle (defined by J_{sc} and V_{oc}) and the pink rectangle (defined by the point of maximal power output, at (J_{MP},V_{MP}))

The fill factor is essentially a measure of the 'squareness' of the *J–V* curve: the

maximum power extractable from the cell occurs at the point of greatest product of J and V, i.e. at the top right corner of the curve. For an ideal cell, there will be no losses to make the curve deviate from the area of the blue rectangle in Figure 1.4, and the maximum power will occur at (J_{sc},V_{oc}). However, in real cells, there will be *parasitic resistances* that cause the curve to deviate from perfect behaviour and follow a path such as the hypothetical red line in Figure 1.4; this then describes a smaller area on the graph (i.e. the pink rectangle). The maximum power is then given by $J_{\mathrm{MP}} \times V_{\mathrm{MP}}$ – the fill factor is then a measure of the ratio of the true area to the ideal area under the *J–V* curve, and so quantitatively represents the loss in power from non-ideal behaviour as a percentage.

With these terms defined, we have a concept of the primary physical properties of a solar cell that can be externally measured and contribute to its overall efficiency. However, we must also consider the ways in which a solar cell can deviate from ideality, and cause losses in efficiency and performance – acknowledgement and understanding of these loss mechanisms is crucial to finding efficient absorber materials for PV.

1.2.3 Losses: recombination, optics and resistances

There are three major loss mechanisms that contribute to the reduction of efficiencies of real-world solar cells: non-radiative recombination in the bulk or at surfaces, optical losses resulting in incomplete absorption of light and parasitic resistances across the cell, and each affect the three extrinsic qualities above in different manners.

Recombination

Recombination in general is simply the mechanism by which separate charge carriers (whether a photoexcited electron or the electron hole created on absorption) in the solar cell can come together through some pathway to de-excite and return to equilibrium conditions. Under all conditions, we may expect higher rates of recombination to negatively affect a solar cell – by recombining, charge carriers can no longer contribute to the photocurrent nor provide potential difference towards the photovoltage. There are three key pathways by which recombination can occur, and each will be discussed in turn – each of them is either radiative, resulting in the

emission of a photon, or non-radiative, a distinction that will become important to their inclusion in certain models used in this thesis. Greater recombination reduces both the J_{sc}, by removing charge carriers, and V_{oc} by increasing the dark current.

As discussed above, *radiative* recombination (spontaneous emission) of electrons and holes will always occur in a solar cell, as it is the reverse process of absorption: in a semiconductor, an excited electron in the conduction band spontaneously decays to the valence band, recombining with a hole, and causes the emission of a photon with energy equal to the band gap (assuming that the electron and hole have relaxed to the band edges). The rate of this band-to-band recombination may be slowed, for instance, by an indirect fundamental gap, however, the process cannot be hindered entirely. Stimulated emission, wherein an incident photon stimulates an electron to decay from conduction and valence band and emit a second photon, is another possible radiative recombination mechanism, however the probability of it occurring is highly dependent on the intensity of incident photons – under standard operating conditions, the probability of its occurrence is negligible compared to that of spontaneous emission.

The remaining recombination pathways are non-radiative, one of which is *Shockley-Read-Hall* (SRH) recombination, also known as trap-assisted recombination. In any macroscopic semiconductor at a temperature above absolute zero, the entropic favourability of defect formation – whether point defects, complexes, dislocations – will ensure that thermodynamically some finite, if low, concentration of defects will exist in the sample. As they are not part of the pure structure, in this dilute limit, the inclusion of defects will cause the formation of isolated electronic states which are not defined by the bulk electronic structure – as such, they can exist within the otherwise forbidden band gap. As these states are spatially localized, unlike the bands defining the free carriers, if a carrier were to enter one of these states, it is 'trapped' and no longer contributes to the overall current. Sufficient thermal energy can release the carriers from the trap state back into their respective band, however, while it remains trapped, if the trap can capture a charge carrier of opposite polarity, the two are then localized in close proximity and are effectively recombined.

The third and final pathway to consider is *Auger* recombination, which is also non-radiative. In this mechanism, two carriers must collide, leading to the excitation

of one to a higher kinetic energy, while the other decays and recombines with a carrier of the opposite charge across the band gap. As it requires an effective three-particle collision, the probability of Auger recombination is, however, usually orders of magnitude less likely to occur than that of the two-particle recombination pathways unless very high carrier concentrations are present. On the other hand, it does become highly relevant in indirect semiconductors when radiative recombination is greatly suppressed – as the collision causes both charge carriers to undergo changes in momentum, this can provide the recombining carrier the change in $\mathbf{k}$ required to cross the indirect gap and recombine with an opposite-polarity charge carrier at the VBM or CBM without the intercession of a phonon, and so Auger recombination is not impeded by an indirect gap.

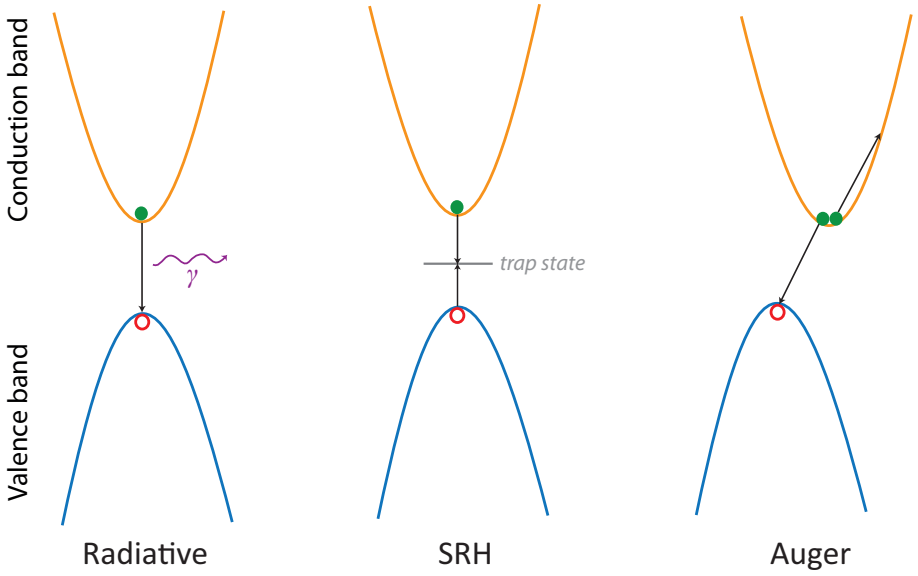

Figure 1.5: A representation of the three primary electron-hole recombination mechanisms in photovoltaic absorbers, with the valence band in blue and conduction band in orange, and electrons and holes represented by filled red and hollow green circles respectively. Electronic transitions are marked by black arrows, while the curved purple arrow represents the emission of a photon.

Which of these three pathways is dominant is highly dependent on the specific circumstances for the solar cell, however a key distinction may be made between those which may be considered 'avoidable', namely those for which the rates can be reduced or effects can be ameliorated through external synthesis, engineering or other methods, and those that are intrinsic to the material and are mostly uncontrollable. Radiative and Auger recombination generally fall into this latter category, while SRH may be considered the former: while defect states, the most significant sites for SRH

recombination, will always be present in semiconductors, their concentrations and behaviour may be changed and even controlled through judicious doping, passivation and synthesis methods. As such, when discussing properties of novel materials, or the improvement of current materials, the suppression of non-radiative SRH recombination is often one of the most significant potential strategies.

Optical losses

In this section, we will consider those losses that result from some reduction in the availability in photogenerated charge carriers from the photons incident on the cell. In general, these losses can be neatly quantified through the cell's *external quantum efficiency* (EQE), which is the ratio of photons within a given frequency range that result in the generation of a charge carrier to the total number of photons incident on the cell; when expressed as a percentage, an EQE of $100\,\%$ thus represents perfect absorption of photons of that frequency, while a lower EQE results when some optical losses are present and causes a reduction in the photocurrent (manifesting externally as a reduction in J_{sc}). The most common source of such losses is incomplete absorption – either through transmission or reflection of the incident light.

One of the most significant optical losses that occurs in cells is that photons with energies below the band gap of the absorber will unavoidably be transmitted in almost all cases (excitonic absorption and other such processes are beyond the simple treatment here), as no allowed electronic transition is available for the photon to stimulate, and so the EQE in that region is 0. Even above the band gap, however, the maximum EQE can be reduced through transmission if the absorption coefficient of the absorber is not high enough to ensure complete absorption within the finite depth of the absorber layer. This becomes particularly significant for indirect-gap absorbers, where absorption coefficients are orders of magnitude lower than their direct-gap counterparts. Additionally, when the profile of absorption is slow to reach full strength above the band gap (again, common for indirect-gap materials), this can result in poor EQE for photon energies slightly above that of the band gap.

Reflection of photons will also result in a reduction in EQE, often to an equal degree across all frequencies, and so it is very common for real world solar cells to incorporate anti-reflective coatings on the front layer to minimize these losses. Any remaining

loss in EQE will arise not from incomplete absorption, but immediate recombination of the photogenerated charge carriers at surfaces in the cell – the charge carriers in this case have been generated, but not 'collected', i.e. they are not able to contribute to the current. The front and back surfaces of the cell are often centres for especially high recombination as they are interfaces between two materials with different crystal structures, and thus can be home to dangling bond and other defect states which aid in SRH recombination.

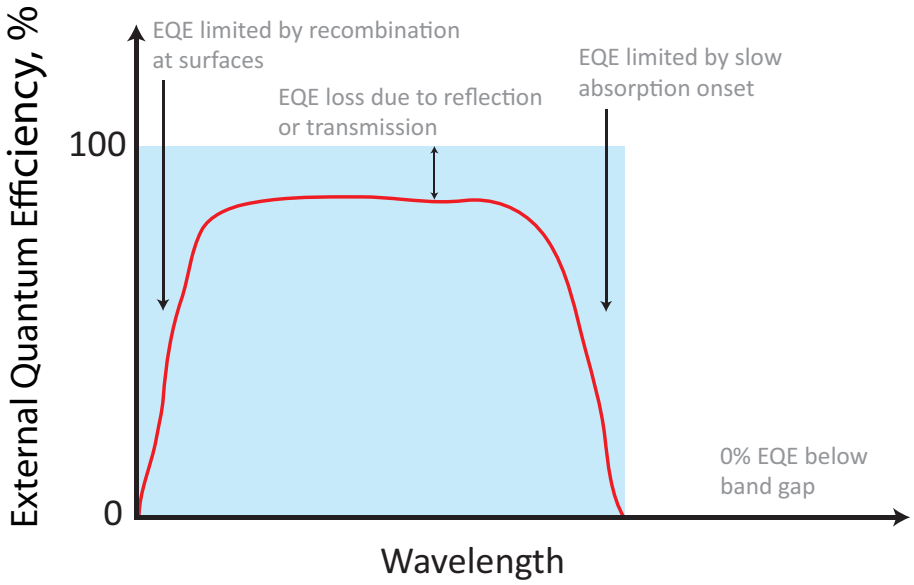

Figure 1.6: A hypothetical external quantum efficiency (EQE) measurement as a function of photon wavelength, marking ideal (blue rectangle) and realistic (red line) behaviour. Parts of the spectrum are notated to demonstrate different ways by which optical losses can occur.

Parasitic Resistances

Parasitic resistances act to reduce the power output of real-world solar cells by impeding the flow of carriers through the cell and the external circuit. They take two primary forms, the first of which is *series* resistance. This occurs due to resistances at the interfaces between the contacts and other layers in the cell, as well as resistance through the layers, contacts and base themselves. *Shunt* resistance is instead the opposition to current leaking through other pathways than the external circuit, or load – this can be through the cell itself or around the edges of the device. As such, a high shunt resistance is desirable to avoid short-circuiting the cell, while a low series resistance is needed to ensure the flow of carriers through the device. When these

resistances are unideal, however, the overall power output of the cell is reduced, and thus the FF is also reduced. While these losses are often crucial to real-world device behaviour, they are primarily developed during the macroscopic manufacture of the cells themselves and so, unlike the above two loss mechanisms, often have little dependence on the intrinsic properties of the absorber; for the purposes of this thesis, the role of parasitic resistances will be only considered in passing.

1.2.4 The Schockley-Queisser limit

Throughout this section, we have contemplated the behaviour of a hitherto qualitative 'ideal' solar cell, representing perfect diode behaviour and minimal avoidable losses. In 1961, Shockley and Queisser applied the thermodynamic principle of detailed balance, where all processes, such as absorption and recombination, are in equilibrium, to the behaviour of a solar cell to find the thermodynamic theoretical limit to the efficiency, η of a single junction solar cell.[9] In this, they considered the incident power on a cell on the surface of the earth from the Sun, as well as the dependencies of both J_{sc} and V_{oc} to formulate an expression for η that depends on only a few factors, in their labels: x_g, the ratio between band gap and thermal energy, x_c, the ratio between the temperature of the cell and that of the Sun, m, the impedance matching (essentially the FF), t_s, which corresponds to the EQE, and f, a factor considering other deviations from ideality, including f_r, the fraction of total recombination that is radiative, as well as the angle of the sun to the cell. This analysis also includes the assumption that only one electron-hole pair is generated from the excitation of one photon (EQE is limited to 100 %), and that the excited carriers with energy in excess of the band gap relax (usually through the intercession of phonons) to the band edges, with the remaining energy lost as heat.

They then fix some of these parameters to ideal values to obtain the detailed balance limit, now also known as the Shockley-Queisser (SQ) limit: a 100 % FF and EQE above the band gap energy, a cell and ambient temperature of 25 °C, entirely radiative recombination and the position of the (unconcentrated) Sun directly normal to the cell surface lead to the dependence of η on solely the band gap, resulting in the curve depicted in Figure 1.7. This curve reaches a maximum of ∼33.7 % for the AM 1.5G spectrum at around 1.34 eV, limiting a single junction solar cell to this

efficiency. No current solar cell has reached this ideal efficiency, although for some materials, it is being approached. Nevertheless, the SQ limit provides a target for developments in photovoltaic systems, as well as a key first target for the proposal of any new solar absorbers – if the band gap of the absorber layer falls outside a 0.9 eV to 1.6 eV range, then the absolute limit on the efficiency of a cell utilising that material will be limited to $<30\,\%$, and thus compare unfavourably to other current absorbers which have band gaps within this range.

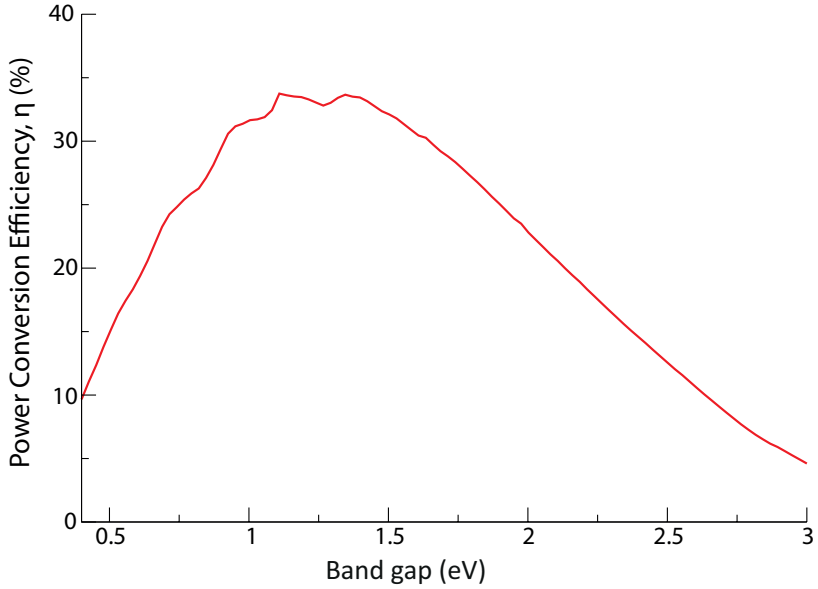

Figure 1.7: The Shockley Queisser limit for a single junction solar cell, given as a function of cell efficiency against band gap of the absorber layer.

We note here that some of the assumptions in the SQ limit are not absolute: for example, concentrators to enable a higher intensity of light are commonplace, and methods of multiple exciton generation (producing more than one carrier pair per photon) such as singlet fission are an active topic of research interest for integration with photovoltaics.[10,11] These directions are, however, beyond the considerations of this thesis.

1.2.5 Intrinsic properties of PV absorbers

In Sections 1.2.2, 1.2.3 and 1.2.4, we established the key extrinsic properties that solar cells demonstrate as well as the key mechanisms by ideal and non-ideal solar cells differ. We have, up until now, only obliquely referenced the intrinsic properties of the absorber layer and how they may affect the macroscopic, external properties

of the cell in general with the exception of the perhaps most crucial: the band gap. Despite this, each of the following highlighted intrinsic properties can have significant impact on photovoltaic performance, and so are further considered here; they are also summarised diagrammatically in Figures 1.8, 1.9 and 1.10. This section is also intended to set out the target values and ranges for these properties to obtain the most optimal solar absorber, as these intrinsic properties will be some of those targeted or calculated in this thesis.

Band gap

The dependence of the external cell properties and the efficiency on the band gap have been discussed relatively comprehensively so far through the construction of the Shockley-Queisser limit, however it is worthwhile to reiterate the specific characteristics that are ideal for potential solar absorber layers. Firstly, as previously discussed, the magnitude of the band gap has significant impact on the overall maximum efficiency available to the solar cell. In general, the optimal range for a single junction solar cell is considered to be where the SQ limit reaches its maximum, around 1.0 eV to 1.5 eV, yet as only a small proportion of proposed solar absorbers have actually demonstrated actual cell efficiencies close to the thermodynamic limit, this guiding range can be somewhat loosely defined. In Figure 1.8 a), 3 champion solar absorbers are marked with their position and current maximum efficiency on the SQ limit: crystalline silicon, GaAs and methylammonium lead iodide, $(CH_3NH_3)PbI_3$ or MAPI. Each of these is significant in different ways: silicon is the dominant material used for commercial solar panels, GaAs has the record single-junction efficiency, while MAPI and the related perovskite family's extremely rapid rise in efficiency will be discussed in Section 1.3.4; nevertheless, all possess a fundamental band gap within or near the ideal 1.0 eV to 1.5 eV range and also record cell efficiencies above 20 $\%$. It is worth noting that the SQ limit only applies to single junction cells – as photovoltaic technologies have developed, the construction of multijunction (containing multiple $p-n$ junctions) cells has become possible, which will be discussed in 1.3.3. For these cells, different criteria exist on the band gaps of the absorbers so as to maximise the absorption of solar spectrum: for example, in a 2-junction cell, the optimal band gaps become 1.1 eV and 1.7 eV for the bottom and top junctions respectively.

The second important quality of the band gap is its nature in reciprocal space, namely whether it is direct or indirect. This primarily affects two factors: the dominant recombination pathway, and the absorption. In general, a direct gap semiconductor is almost always preferable: while an indirect gap material, as discussed in 1.2.3, will display suppressed radiative recombination, this is outweighed by the drastic reduction in absorptivity of the sample at the fundamental gap energy, unless there is an available direct transition close in energy – this will be discussed in greater detail in the next section.

Absorption

Strong optical absorption is understandably a key property for the solar absorber layer to have, as the capture of light and photoexcitation must occur before any of the other processes in the cell can take place. The quantitative property that governs the strength of absorption is the absorption coefficient, α, which is related to the dielectric properties of the semiconductor. The primary contributor to α though is the availability of electronic transitions from occupied to empty states of a given energy – in the ideal absorber, there will be a high density of allowed transitions at energies above the band gap, resulting in an absorption coefficient of $1 \times 10^4\,\mathrm{cm}^{-1}$ to $1 \times 10^5\,\mathrm{cm}^{-1}$ or greater. In terms of the cell, this will allow the absorber layer to be especially thin, on the order of nm which conveys advantages towards carrier transport (discussed in the following sections), while ensuring that losses in the EQE due to transmission are minimized. In Figure 1.8 b), the absorption profiles of c-Si, GaAs and MAPI are all plotted. GaAs and MAPI are both direct semiconductors, and show strong absorption, with a sharp absorption edge (minimal delay in the rise to a high absorption coefficient once above the band gap energy), and so are optimal absorbers, and so act similarly to the ideal absorber nature used for the SQ limit. Si, by contrast, is an indirect gap semiconductor, and so has an absorption coefficient $\sim 1 \times 10^3\,\mathrm{cm}^{-1}$ within the crucial 1 eV to 3 eV spectral range, and so it is generally considered a poor optical absorber.[12] In order to reach high efficiencies, cells using Si as an absorber require a layer thickness on the order of µm, orders of magnitude more than those of GaAs or MAPI. This restricts flexibility in the architecture of the cells themselves, as well as greatly increasing the contribution of the absorber layer to the total cost of the cell.

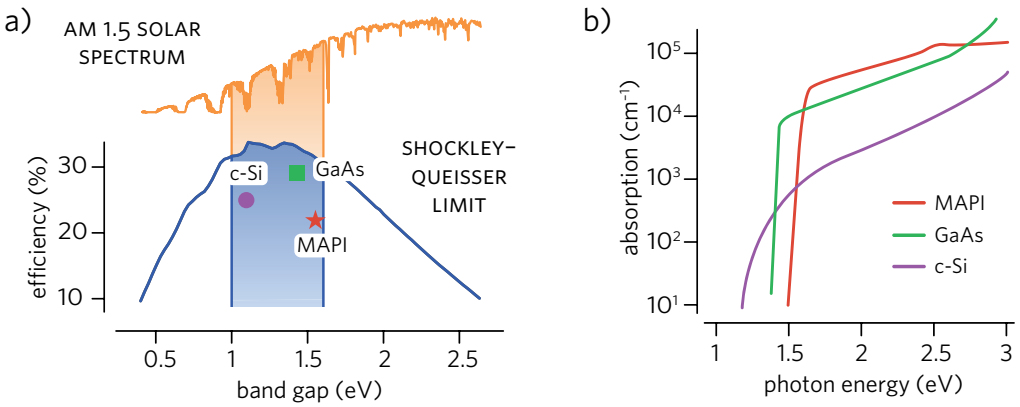

Figure 1.8: a) Depiction of the current record cell efficiencies of three champion absorbers, monocrystalline silicon (c-Si), GaAs and methylammonium lead iodide (MAPI), relative to their positions on the Shockley-Queisser limit and b) Absorption coefficients for those three champion absorbers. Reproduced and adapted with permission from Ganose *et al.*[13]

Carrier transport properties

Once photogeneration has occurred in the absorber layer, the resultant electron-hole pair must separate in order for the carriers to flow through the cell before they can recombine. The primary intrinsic characteristic governing the ability for this separation in semiconductors are the *carrier mobilities*, μ, with higher mobility indicating that the carrier is more freely able to travel through the material. Under almost all considerations, a higher mobility will thus improve photovoltaic device performance: whether enabling electron-hole separation or allowing the carriers to diffuse through the material to other layers, and thus increasing the available current and demonstrating lower resistances. The mobility itself is dependent on a number of external and internal factors, including scattering by defects, phonons and other carriers, however the primary inherent dependency is on the dispersion of the electronic band structure. The method by which this relationship can be derived is discussed in Section 3.2.3, and is represented pictorially in Figure 1.9 a): the more disperse valence band will describe a 'light' hole, which has higher mobility than the 'heavy' hole in a flatter band.

Other transport properties can also be of relevance to specific devices: for example, minority-carrier lifetimes and the related carrier diffusion lengths (essentially the mean free path of the carrier) can be of particular interest, due to often being strongly affected by defect scattering and trapping – long carrier lifetimes can be a strong

indicator of minimal interference by defects and of suppressed SRH recombination, and thus a highly desirable device property. Carrier diffusion lengths, in particular, should ideally be on the length scale of the thickness of the absorber to minimize the risk of recombination.

Defect Tolerance

Defect tolerance is a concept that has been relatively recently developed within the photovoltaic research community but, in general consensus, summarises an ability for a particular material to retain optimal or otherwise desirable properties, which in other materials might be negatively impacted by interactions with defects, regardless of the presence of defects within the material.[14] Defect tolerance itself is thus, to some degree, a collation of multiple beneficial properties, such as higher carrier lifetimes and mobilities, as well as other indicators of low non-radiative recombination, but in theoretical calculations of defects, it is also evidenced by the absence of significant defect states 'deep' within the band gap that could act as centres of SRH recombination.[15] The theory behind defect tolerance is still developing, though a core concept that has been proposed is that the presence of antibonding interactions at the top of the valence band and bonding interactions at the bottom of the conduction band (the opposite trend to that expected by a simple bonding argument in other semiconductors such as silicon) repels defect states that result in dangling bonds (such as vacancies) into the bulk bands and out of the band gap.[14,16] This type of electronic structure (represented in Figure 1.9 b)) has been seen to result as a consequence of either $d-p$ repulsion in the chalcopyrites[17] and Cu_3N[14] or the presence of occupied s states within the valence band, which is characteristic of 'lone-pair' cations such as Sn^{2+},[18] Pb^{2+},[15,19] Sb^{3+} and Bi^{3+};[20,21] as such, these classes of compounds are now key targets for both new materials discovery and renewed interest in formerly studied PV materials.[13]

Another key material property that contributes to defect tolerance is the *dielectric constant*, ϵ, due to its contribution to charge screening. Neutral defects are electronically benign, but charged defect states, where present, will allow the possibility for charge trapping; thus, for semiconductors to be defect tolerant, their interaction with the charge carriers must be suppressed. This can occur by screening the

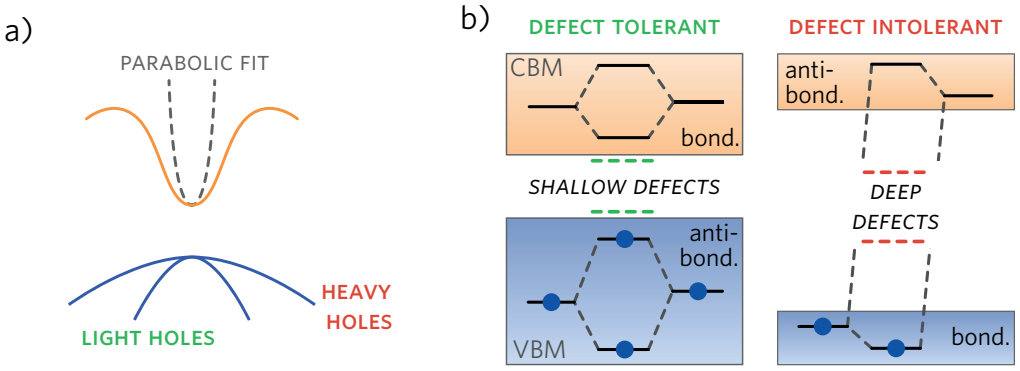

Figure 1.9: a) Band diagram, demonstrating the relationship between carrier effective mass and curvature – lighter carriers (with higher mobilities) will exhibit bands of greater curvature. b) Schematic of the antibonding-VBM/bonding-CBM model of defect tolerance, adapted from Zakutayev *et al.*.[14] Reproduced and adapted with permission from Ganose *et al.*[13]

charged defect from the carrier, if the other bound electrons within the semiconductor are distributed sufficiently to minimize the effect of any electrostatic charge. This is quantified in the dielectric constant, wherein a material with a higher dielectric response will be able to screen defects more efficiently, and so demonstrate greater defect tolerance (observable through e.g. greater carrier lifetimes). This screening effect has been observed to improve mobilities in ferroelectrics from large dielectric constants,[22,23] yet such dielectric properties are also evident in materials containing large polarizable ions such as Pb^{2+} and Bi^{3+}, such as MAPI,[24,25] further encouraging the recent interest in these materials.

Alignment

As discussed above, in a $p-n$ heterojunction, the Fermi level of the two materials equilibrates, and so the conduction and valence bands of the two materials will also come into energetic proximity – allowing the transfer of carriers between the two materials. With new absorbers, care must be taken to ensure that its valence and conduction bands align close in (absolute) energy relative to those of the contacts, heterojunction partner or any other buffer layer to ensure the most amenable contact for charge transport across the interface. If the bands are too dissimilar in energy, poor contacts can result, leading to energetic barriers to charge transport between the two materials and so increasing parasitic resistances at the layer interfaces, reducing the overall device efficiency. Additionally, if the contact layers are aligned poorly,

the overall potential difference of the cell can be limited greatly by the contacts, and not the absorber, leading to a loss in overall V_{oc} – an effect graphically represented in Figure 1.10 a). Where possible, close alignment with ubiquitous or commonly-used contacts, such as the TCO F-doped SnO_2 or the buffer layer CdS, can also be desirable, as it allows integration with cell architectures already in use, which may reduce the difficulty of manufacture and processing.

Band edge and spin-orbit effects

Thus far, we have discussed the significant differences between direct and indirect gap semiconductors, which strongly apply when discussing the difference between, for example, GaAs and Si, the latter of which has no available direct valence-to-conduction band transitions below 3 eV. However, in other indirect semiconductors, the difference is not so clear cut – for some electronic structures, the fundamental band gap is indirect, though (particularly when band dispersion is low) there may be direct transitions that lie only very slightly higher in energy. When this occurs, the absorption coefficient of the material can still be strong, as a result of the direct transitions (albeit with a slightly slower onset), removing one of the major disadvantages of indirect-gap absorbers. These materials may be referred to as *pseudo-direct* semiconductors, and can still be effective absorbers. Another type of electronic structure that can be valuable for photovoltaics are *multivalley* structures, in which there are multiple band maxima and minima close in energy, with moderate dispersion in between them – as these electronic structures combine local dispersion (beneficial for carrier transport) with a relatively high DOS at the band edges (beneficial for strong absorption), they can be highly effective for solar absorber materials.

Figure 1.10 b) represents another band-edge effect that can benefit a solar absorber, namely a local Rashba splitting of the conduction band, which occurs in MAPI. As MAPI contains both lead and iodine, both heavy elements with Z, the atomic number, $>$50, the electronic effect of spin-orbit coupling is large, and the spin-orbit splitting in the conduction band, composed of p orbitals from both Pb and I, approaches 1 eV.[26] Rashba splitting is an associated effect that arises from a break in inversion symmetry in non-centrosymmetric structures, a group to which the tetragonal room-temperature phase of MAPI belongs, and results in a lifting

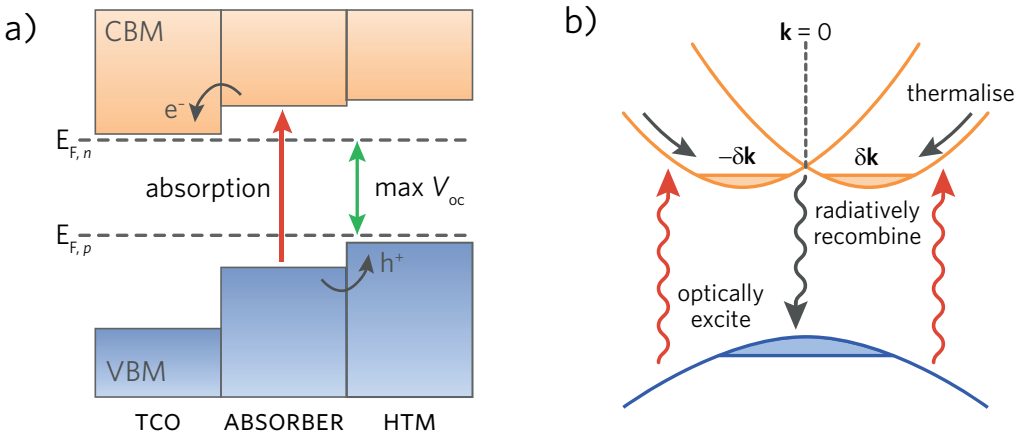

Figure 1.10: a) Representation of band alignment within a solar cell, and potential limitation in V_{oc} as a result. b) Band diagram, depicting the possible mechanism for reduced radiative recombination and direct-indirect character in MAPI. Reproduced and adapted with permission from Ganose *et al.*[13]

of degeneracy in the band edges, causing them to separate slightly in $\mathbf{k}$-space – as occurs in the conduction band depicted in Figure 1.10 b).[27] This instantaneous spin-splitting results in strong absorption, yet also a suppression of radiative recombination upon the carriers thermalizing to different parts of $\mathbf{k}$-space, thus enhancing the carrier lifetimes. Numerically, this has been estimated to inhibit radiative recombination by up to 350 %,[28,29] and thus highly valuable for a potential absorber.

1.3 Current Absorbers

With the internal and external properties that influence photovoltaic capability in materials established, we can now discuss actual solar absorbers within PVs that are in current usage and how they measure up to one another. We will note that, as with the previous section, our review here will be focussed on the absorber layer in the cell; while the other layers, such as TCOs and metal contacts, provide crucial contributions to the overall behaviour of the cell, the absorber layer has the most significant influence on the overall output of the cell, and its intrinsic properties govern the limits of the cell as a whole. In general, this reflects a trend in prior research to describe a particular cell or study in terms of the absorber material, with the other components of the cell usually treated as auxiliaries that can be optimized to fit the particular absorber chosen.

This section is intended to provide a brief overview of the current state of absorber

technologies, which have in prior literature and the community at large, been divided into three 'generations' that broadly reflect the diversifying range of materials that have been trialled as solar absorbers in PVs over the past six decades. Figure 1.11 depicts the highest recorded and validated efficiencies for each of these technologies over this time.

1.3.1 1st generation: Silicon

Silicon-based solar cells currently dominate the market in photovoltaics – across the different architectures available, approximately 90 % of installed modules utilise a form of silicon.[5] Silicon has a number of advantages that have ensured this dominance: it is the second most abundant element in the earth's crust, almost 60 years of scientific and technological development ensure that its electronic and structural behaviour is very well understood, and cells have demonstrated reliable record efficiencies above 15 % for over 20 years,[30] and a current laboratory record of over 26 %.[31] We have elaborated on its primary weakness, however, over the previous sections: its fundamental gap of 1.1 eV, while ideal in principle according to the SQ limit, is indirect and its optical absorption is significantly poorer than other photovoltaic materials.

The inherently poor absorption of silicon requires the use of ∼300 µm thick layers of material within the cell[30] to ensure sufficient photogeneration, as discussed above, but this also results in a number of difficult constraints. If the layer of material in the cell is thick, then carrier diffusion lengths must also be very long, otherwise there is a greater risk that the charge carriers will recombine within the bulk of the material. The two major silicon technologies deal with this in slightly different manners – monocrystalline silicon (mono-Si) is the historical approach and most successful, in which the silicon layers in a cell each consist of a doped single crystal wafer. As the wafer is synthesised together, its doping can be highly controlled, and it made to be otherwise ultra-pure: this ensures that the material has long carrier lifetimes and low recombination, but is associated with a high synthesis cost – both economically and energetically, given temperatures >1000 °C are needed for such crystal growth methods, such as the Czochralski process. The alternative is multi-crystalline silicon, where the layer of silicon consists of a number of relatively

large grains together in a film: the smaller size of grains compared to the overall layer thickness somewhat relaxes the requirements on carrier diffusion lengths, and subsequent purity; multi-crystalline silicon is also generally simpler and less costly to produce, however record cell efficiencies have historically been 5 % below those of monocrystalline silicon cells, with a current maximum efficiency of 22.3 %.[32]

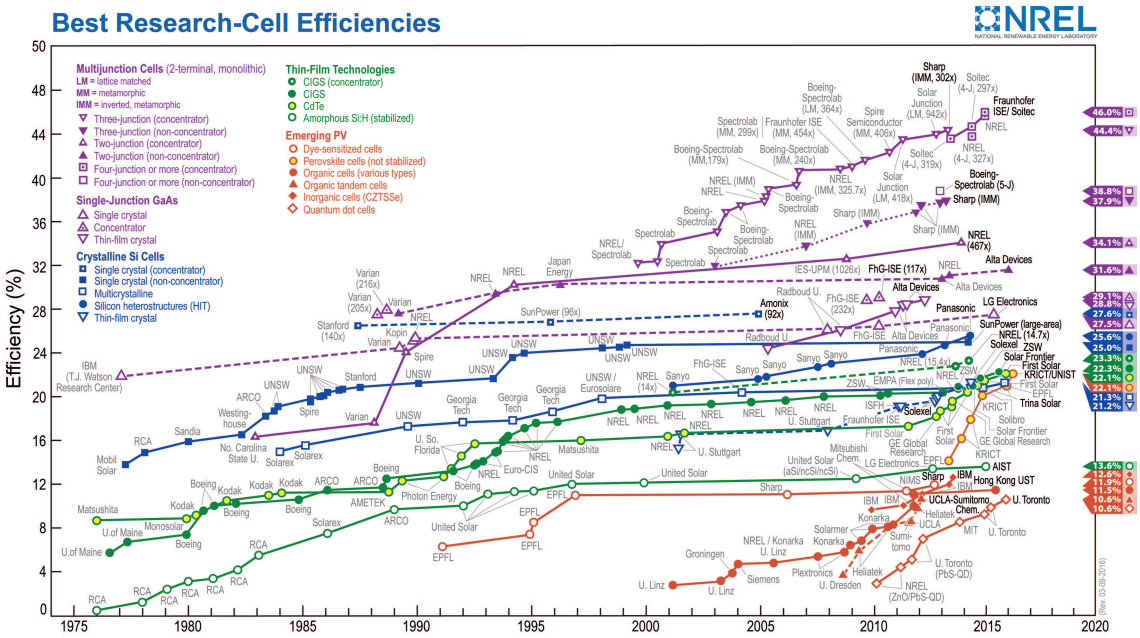

Figure 1.11: Chart depicting the record cell efficiencies for multiple materials families, published as of the end of 2016. This plot is courtesy of National Renewable Energy Laboratory, Golden, CO.

1.3.2 2nd generation: Thin-film Absorbers

The second generation of solar cell materials comprises those developed over the past few decades that do not suffer silicon's primary weakness, instead possessing direct band gaps and strong absorption. As a consequence, the absorber layer within a cell can be significantly thinner while still capturing enough incident light – this thickness can be on the order of 200 nm to 500 nm, and hence cells using these compounds and cell architecture are referred to as 'thin-film' solar cells. There are 3 such compounds that have come to prominence over the last few decades: GaAs, $Cu(In, Ga)Se_2$ (CIGS) and CdTe.

As discussed above, the III-V semiconductor GaAs is used in the absolute highest efficiency single-junction cells; with a 1.4 eV direct band gap, it lies near the maxi-

mum of the SQ limit, and also exhibits strong absorption. Additionally, it benefits from high carrier mobilities[33] (a consequence of its highly ordered zinc blende crystal structure and thus disperse electronic structure), together with consistent development over the past 40 years[34] – as such, the record efficiency of a GaAs cell lies at 28.8 %,[32] and so GaAs is usually the material of choice for extra-terrestrial solar panels, where power to weight ratio (and thus efficiency) is the decisive factor over cost.

CIGS is a solid solution of two chalcopyrites, $CuInSe_2$ (itself popular as a solar absorber) and $CuGaSe_2$, which have band gaps of 1.04 eV and 1.64 eV respectively – by alloying the two compounds, an absorber with an ideal, direct band gap within the SQ limit can result.[35] The chalcopyrite structure is directly related to the zinc blende of GaAs – by replacing half the Ga cations with Cu, and then changing As to Se to balance the stoichiometry – and so the chalcopyrites also tend to have optimal electronic properties as well. The record efficiency of CIGS-based cells is 21.7 %, very close to that of multicrystalline silicon.[32]

CdTe, again belonging to a zinc blende crystal structure, possesses a direct 1.5 eV band gap and strong absorption as with the other compounds above.[36] Of the three thin-film materials discussed here, it has the lowest record efficiency, of 21.0 %, however of the three it is the most commercialisable.[32] In 2013, Peng *et al.* reviewed the current major photovoltaic technologies with an eye on their sustainability, looking at their energy payback time (the length in years for the energy produced by a module to outweigh the energetic 'cost' to manufacture and install it) and greenhouse gas emission rate as a result of manufacture. CdTe performed the best of these, with the lowest average energy payback time (less than 1.5 years) and half the greenhouse gas emission rate per kW h than that of the worst performer, monocrystalline silicon.[37] Additionally, the minimal material required to produce the absorber means that in both 2010 and 2015, CdTe offered the best \$/W ratio of any PV material (\$0.51 versus \$0.74 for mono-Si in 2015).[1,5]

The weaknesses of the traditional thin-film absorbers will be discussed further in Section 5.1, however they are near-universally a question of availability: many of the constituent elements in all 3 of the above compounds are either rare in abundance, and thus compare poorly to highly abundant silicon, require an expensive feedstock

(although the absorber is usually a negligible proportion of the overall cost of a thin-film cell compared to the high processing costs of a silicon wafer) or are potentially toxic, and thus raise concerns over sustainability and recycling. In the case of GaAs, these are its only weakness – however cost and toxicity provide sufficient barriers to marketability that mean GaAs is rarely used in commercial or utility-scale devices. Section 5.1 discusses some of the strategies employed to widen the search for abundant, non-toxic thin-film absorber materials.

1.3.3 3rd generation: Tandems, Organic and Sensitised solar cells

Mostly within the last two decades, a third generation of photovoltaic systems has come to prominence. This encompasses a variety of different systems, but all work to expand the horizons of photovoltaics beyond traditional solid state, single $p-n$ semiconductor junctions – whether it is extending efficiency beyond the SQ limit through *tandem* or multijunction cells, or expanding the variety of PV materials in organic (polymer-based) and *sensitized* solar cells.

Tandem solar cells contain multiple $p-n$ junctions that are connected together in a device stack. This allows the absorption of light at different frequencies – for example, for a two junction cell, one junction will absorb high-frequency blue light, but transmit low frequency photons, some of which will then be absorbed in the bottom junction – and if the band gaps of the absorbers in each case are particularly tuned, a much more reliable absorption coverage of the solar spectrum can be obtained. Through this, conversion efficiencies well above 30 % can be achieved up to a thermodynamic maximum of 68 % (albeit for an infinite number of junctions); the current record cell efficiency for a tandem cell using unconcentrated sunlight is 38.8 %, but used 5 separate junctions.[32] In practice, assembling these cells to attain such outputs is a significant challenge: for a two junction cell, carriers can either be extracted only at the top and base of the complete stack (*two-terminal*) or at either end of each junction (*four-terminal*).[8] Either of these mechanisms introduces complications, however, as four-terminal cells require significant circuit engineering to extract carriers at two separate positions in an often µm scale cell, while two-terminal architectures require careful lattice and current matching, as well as electronic alignment of the buffer layer between the two junctions, otherwise resistances can greatly

inhibit efficiency. In general, these complications have rendered tandem cells historically far too expensive to commercialise, although more recent research directions include integrating low-cost absorbers into tandem cells to reduce overall costs.[38,39]

Organic PV systems use similar concepts to those of semiconductor systems, however there are inherent differences due to molecular nature of the absorbers used. In place of a $p-n$ junction, an organic PV consists of a bilayer of two organic semiconductors – almost always polymers or fullerenes to ensure a suitable band gap – noted as the electron *donor* and *acceptor*.[40] The donor may absorb incident light, generating a localized electron-hole pair; in an organic polymer, the additional localization of charge means that the Coulomb attraction binding these two is stronger than those in semiconductors, and so the exciton diffuses as a unit to the interface with the acceptor. There, instead of the electric field of a $p-n$ junction, the driving force of charge separation is spatial and thermodynamic, with the photogenerated electron donating into the lowest unoccupied molecular orbital (LUMO) of the acceptor molecule via a *charge transfer* (CT) state that is lower in energy than that of the excited donor. A similar process may also occur in the acceptor molecule, with exciton generation and diffusion followed by hole transfer at the interface, while the electron is extracted towards the contact/electrode.

The most efficient polymer PV systems from 2000 onwards[41,42] use a 'bulk heterojunction' architecture (represented in Figure 1.12), where domains of the donor and acceptor molecules greatly interpenetrate, to ensure a much larger interface to allow charge transfer between them, the lack of which had previously greatly limited the overall efficiencies of organic PV. Efficiencies of organic PV now reach above $10\,\%$ due to targeted functionalisation and improvement of both absorbers and buffer layers to improve carrier mobilities and lifetimes (which, due to the localized nature of molecular orbitals, are much poorer than in inorganic equivalents). While organic PV systems are both cheap to produce and often solution processable (allowing for very scalable synthetic techniques, including printing), issues remain regarding their limited efficiency (often due to a high V_{oc} loss from non-radiative recombination and poor absorption/QE at the heterojunction) but also their long-term stability.[43,44]

Dye-Sensitized solar cells (DSSCs) and Solid State-Sensitized solar cells (SSSCs) share a somewhat similar redox-like charge transfer mechanism to organic PV, how-

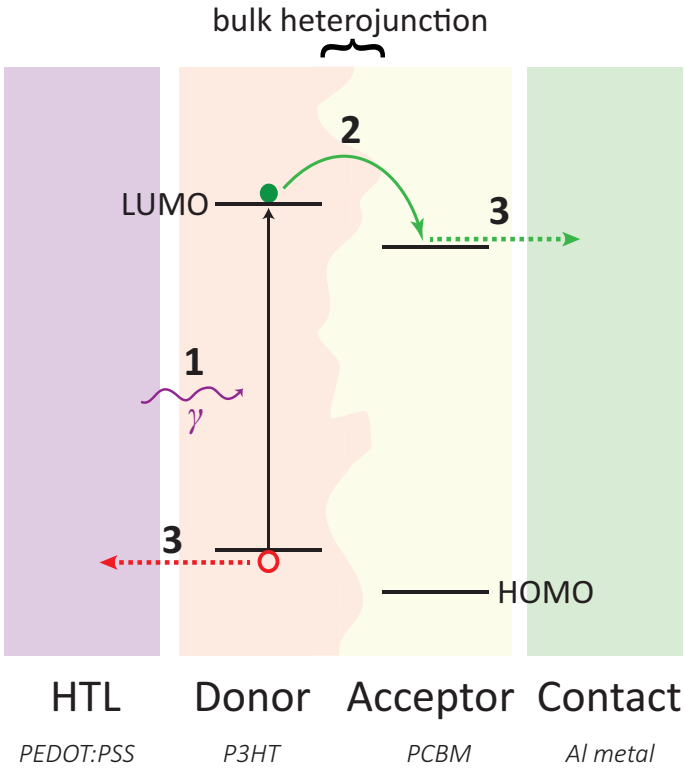

Figure 1.12: Simplified, illustrative diagram of the structure of a typical organic solar cell. The mechanism of photovoltaic action occurs in 3 stages depicted by arrows: 1) Absorption of a photon by the polymer molecule, exciting an electron (green, filled circle) from the highest occupied molecular orbital (HOMO) to LUMO; 2) Charge transfer of excited electron from donor to acceptor molecule; 3) Diffusion of the electron and hole (red, hollow circle) to the contacts for extraction to the external circuit. Example materials for the 4 layers within the cell are given in italics below – abbreviations are defined in the appropriate page of this thesis.

ever arguably are one of the most direct successors of the original Becquerel experiment as photoelectrochemical cells.[45,46] In a DSSC, nanoparticles of an organic, molecular dye is chemisorbed onto a film of a wide band-gap material such as TiO_2 (itself deposited onto a TCO electrode), and then brought into contact with a liquid electrolyte, frequently an iodide. Most of the light incident on the cell is transmitted through the TCO and TiO_2 but is absorbed by the dye, which then injects the photogenerated electrons into the TiO_2 layer (which acts as the electron transporting layer, ETL), and then oxidises the electrolyte (in the case of iodide, to triiodide: $3I^- \xrightarrow{h^+} I_3^-$). The electrolyte is regenerated at the opposite contact/cathode by electrons that have travelled through the external circuit. As with organic PV, there is no depletion region analogous to a semiconductor $p-n$ junction, and so the photovoltage is determined by the alignment of the TiO_2 Fermi level with the reduction

potential of the electrolyte. In a SSSC, the electrolyte is replaced by a solid-state hole transporting layer (HTL), such as CuSCN, which is often still solution processable, however removes the need for potentially fragile or flammable encapsulated liquids in a cell. The structure of an SSSC also begins to mirror that of the $p-i-n$ architecture depicted in Figure 1.3, with the sensitizer taking the place of the absorber, and the TiO_2 (or equivalent) and HTL taking the place of the n- and p-type layers respectively – a detailed example is shown in Figure 1.15 a).

The primary breakthrough that allowed DSSCs to become viable was O'Regan and Graetzel's use of a mesoporous TiO_2 layer, itself composed of nanoparticles with large pores in the structure of the film, greatly increasing the surface area that the dye is deposited on; this effectively increases the depth of the absorbing layer and allows a much greater proportion of light to be absorbed, leading to efficiencies above $7.5\,\%$.[47] Since then, there have been systematic improvements on the design, but the record efficiencies have since plateaued, remaining below $12\,\%$.[32] The architecture, and the advantages of cheap, solution processable materials, have however inspired and influenced two, rapidly developing technologies: quantum dot (QD) sensitized cells, with cells now greatly exceeding $10\,\%$ efficiency[48,49] and discussed further in Section 6.1, and also the unprecedented rise of MAPI and the other lead halide perovskites.

1.3.4 Inorganic-Organic Lead Halide Perovskites: the ideal earth-abundant absorber?

The inorganic-organic hybrid lead halide perovskites ($APbX_3$; $A = Cs$, $(CH_3NH_3)^+$, $(HC(NH_2)_2)^+$; $X = Cl$, Br, I) have, over the course of the past few years, become something of a phenomenon, having risen from just $3\,\%$ efficiency in 2009 to a record of over $22\,\%$ in 2018, equalling or exceeding almost all other competitor materials bar silicon and GaAs[50] (see also Figure 1.11). That this development has occurred in such a short space of time is testament to both the degree of research interest in developing the technology, but also the quite exceptional properties of the material family – it is inarguably the most influential emergent solar absorber of recent times. With the number of research papers published on the family (at the time of writing) exceeding 1000 per year, a complete review of the literature on these materials is

becoming impossible. As such, this section will attempt to go into some detail in reviewing a selection of the key, relevant research on this materials family, its properties – both strengths and weaknesses – and the current research directions that it has influenced.

History and Development

The methylammonium lead halide family ($(CH_3NH_3)PbX_3$, X = Cl, Br, I) were first synthesised and characterized by Weber in 1978,[51] although the origins of their inorganic analogues, the caesium lead halide perovskites lie even earlier, having been first synthesised in 1893 and recorded to exist in (tilted) perovskite structures in the 1950s.[52,53] The general high temperature, cubic structure of all these phases is isomorphic to the classic perovskite mineral, $CaTiO_3$, so can be described by a general formula ABX_3, and the crystal structure of which is depicted in Figure 1.13. In the lead halide perovskite structure, each lead cation is situated in the centre ('B-site') of an octahedron of halide ions ('X'), and these octahedra are corner-sharing with their neighbours; this creates, per octahedron, an interstitial space in the centre of the cell, in which the 1+ cation (methylammonium or caesium) sits ('A-site'). The general ABX_3 formula will be used throughout this thesis to reference the substitutions of certain elements on particular sites within the perovskite structure.

Prior to 2009, the majority of literature on the methylammonium lead halides examined them for their interesting dielectric properties and phase transitions – as with classic oxide perovskites, tilting of the octahedra can easily occur at lower temperatures and form orthorhombic or tetragonal phases, with the structure tending towards cubic at high temperature.[54,55] The rotational freedom of the central methylammonium cation is also associated with the temperature-dependent tilting, for example, in the case of MAPI: in the low-temperature, orthorhombic phase, the methylammonium is fixed in position and aligned along a particular crystal direction; in the high-temperature cubic phase, it appears entirely rotationally disordered on the timescale of XRD experiments, and as the methylammonium cation possesses a permanent dipole moment, this gradual order-disorder transition can affect the dielectric behaviour of the system.[56]

The lead halide perovskites' place in photovoltaics research however began with the

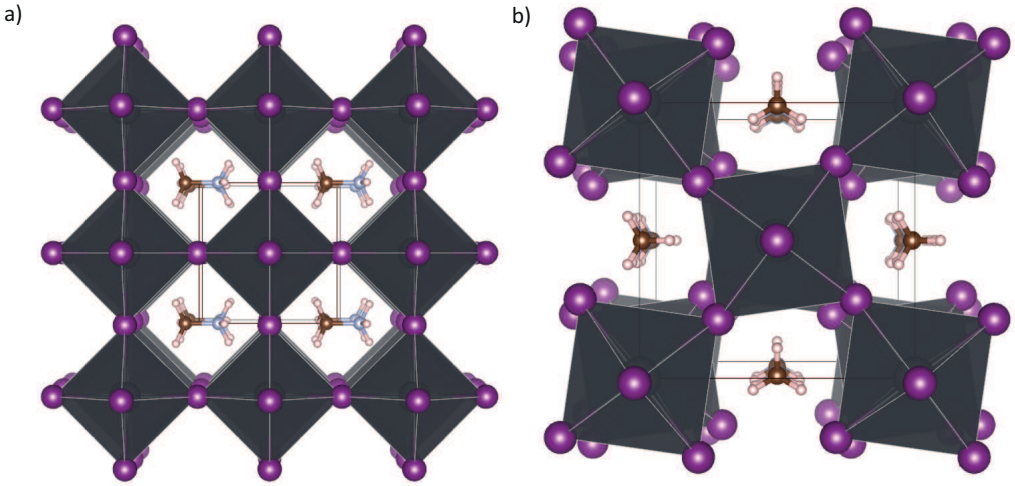

Figure 1.13: Crystal structure of methylammonium lead iodide, MAPI, in a) cubic ($Pm\bar{3}m$), high temperature phase, and b) tetragonal ($I4/mcm$), intermediate/room-temperature phase, displaying the octahedral tilting that occurs. Lead octahedra are marked in dark grey, iodine in purple, nitrogen in blue, carbon in brown and hydrogens in cream. In both diagrams, the methylammonium ions are frozen for clarity – in reality, in both phases there will be dynamic rotation of the ions within the perovskite 'cages', with complete disorder observed in the cubic phase.

report of Miyasaka and co-workers, where $(CH_3NH_3)PbBr_3$ (MAPBr) and MAPI were used as sensitizers to TiO_2 in a dye sensitized cell against a Br^-/Br_2 and I^-/I_2 electrolyte respectively.[57] Both cells attained efficiencies over 3 %, significantly higher than other contemporary QD or inorganic sensitizers, while the MAPBr cell demonstrated a V_{oc} of 0.96 V, exceeding those of the best ruthenium dye-sensitized solar cells. Subsequent work by Park and co-workers improved MAPI-based DSSCs, obtaining higher EQEs and current densities, and raising efficiency to 6.5 %, however noted that the cells were very short-lived, with performance degrading by 80 % in 10 minutes due to the dissolution of MAPI into the electrolyte.[58] The major breakthroughs that sparked the intensive research and excitement around the lead halide perovskites came in 2012, with the publication of the first fully-solid state cell from the groups of Grätzel and Park, using the organic hole transport material *spiro*-MeOTAD (2,2', 7,7' -tetrakis-(N,N-di-p-methoxyphenylamine)9,9'-spirobifluorene) and attaining a PCE of 9.7 %[59] shortly followed by the breaking of the 10 % efficiency barrier by Snaith and co-workers through replacement of the TiO_2 scaffold by the wider-gap Al_2O_3, and seeing an increase in photovoltage.[60]

An added insight in the latter paper was that the alignment of the conduction band of

Al_2O_3 is actually above that of the perovskite, and thus injection of the photoexcited electrons into it is thermodynamically unfavourable – instead it was predicted that Al_2O_3 only acts to structure a layer of MAPI around it, and that the electrons are transported through the perovskite itself to the contact. The key implication of this was that the perovskite can act as an electron transport layer; simultaneously, cells were developed without a specific HTL, inspired by the identification of the caesium perovskite $CsSnI_3$ as a HTL in DSSCs,[61] where the perovskite layer acted as a classic $p-$type layer, transporting holes to the metal contact itself.[62] This has allowed some perovskite-based solar cells to move beyond the 'mesoscopic' architecture of DSSCs and SSSCs, and instead have 'planar' architectures, analogous to the $p-i-n$ structures of traditional inorganic materials, allowing cells to be solution processed, cheaply and at low temperature, while retaining high efficiency.[63,64]

Advances through Alloying

The use of pure MAPI in perovskite-based solar cells eventually reached a record efficiency of 15 %, through adjustments in the HTM and deposition technique, in 2013;[65,66] from this point onwards, alloying, whether of the A-site cation or the X-site halide, between different members of the lead halide perovskite family has resulted in improvements in cell performance beyond that of the base compound. Early cells partially incorporated Cl (in very small concentration to avoid greatly increasing the band gap), forming '$(CH_3NH_3)PbCl_xI_{3-x}$' due to spin-coating syntheses from a $PbCl_2$ precursor;[60,64] the presence of $PbCl_2$ nanoparticles in the product film have since been found to act as nucleation sites improving grain size and film homogeneity,[67] while inclusion of MACl during deposition has lead to similar film, and subsequent V_{oc}, improvements.[68,69] Alloying MAPI with the wider-gap bromide has also been common, as it has allowed band gap tuning of $\sim$0.2 eV, with only a small degradation in performance up to $x = 0.2$ in $(CH_3NH_3)PbBr_xI_{3-x}$.[70] Bromide-alloyed perovskites were used to synthesise a record efficiency 16.2 % fully-solution processed cell in 2014,[71] which also possessed minimal hysteresis – a major problem at the time, and discussed further in following sections.

While halide alloying has been beneficial, alloying on the A-site has lead to the most successful perovskite-based solar cells, originating with the reports by Pellet *et al.*

and Eperon *et al.* on the integration for formamidinium ($(HC(NH_2)_2)^+$, FA) in place of methylammonium into the perovskite structure.[72,73] Formamidinium is one of the few organic cations small enough to fit within the cage of octahedrons in the lead perovskite structure – as can be predicted using an adjustment of Goldschmidt's 'tolerance factor', t:

$$t = \frac{r_A + r_X}{\sqrt{2} r_B + r_X} \tag{1.3}$$

where r_i is the averaged radius of the A, B or X ion respectively. A value of $t \leq 1.06$ has been predicted as the upper limit on perovskite formation when X = Cl, Br, I and so limits the potential size of r_A.[74,75] Pure (FA)PbI_3 itself was first synthesised in 2013, and crystallises in both a tetragonal, tilted perovskite α-phase and hexagonal, one-dimensional δ-phase at room temperature – unfortunately, while the former is recorded to have a 1.48 eV band gap, lower and more ideal than that of MAPI, the latter is yellow, with a wide band gap.[76] While Eperon *et al.* reported a 14.2 % efficiency cell using pure FAPI, Pellet *et al.* noted that alloying of FAPI with MA was necessary to restrict the formation of the δ-phase – both reported high J_{sc} of $\sim$20 mA/cm^2 or above due to the wider spectral range and long carrier diffusion lengths.[72] $FAPbI_3$ was subsequently used as the basis for future record efficiency cells, with the rationale that the lower band gap and increased spectral absorption would improve cell performance;[77] alloying with MA and Br was used to stabilize the structure, and also ensuring that the perovskite film is uniform and thus allowing a broad EQE spectrum above 80 %, J_{sc} >22 mA/cm^2 and V_{oc} >1.0 V.[78,79] The most recent report of a record efficiency single-junction perovskite-based cell to date also used a $(FAPbI_3)_{1-x}(MAPbBr_3)_x$ composition, together with a synthesis environment including additional I_3^- to suppress deep defect states, to break 22 % efficiency and thus firmly establish the lead halide perovskites as equals to other PV materials.[50]

Caesium alloying has also been the subject of intense study, albeit to address a different issue – stability, rather than initial performance (The issue of stability in general will also be further addressed in subsequent sections and Section 4.1). The average ionic radius of caesium is lower than that of both MA and FA, and $CsPbI_3$ occupies a non-perovskite, orthorhombic phase at room temperature, and unlike the hybrid inorganic-organic lead halides, the black, cubic perovskite is not acces-

sible until temperatures above 300 °C – much too high for cell operation.[53] In a photovoltaic context, Cs-alloying has primarily been used as a method to thermodynamically favour the formation of the perovskite phase of $FAPbI_3$ (by shifting the average cation radius towards that needed for an ideal tolerance factor);[80] it was observed to also result in significantly greater retention of PCE over 100 hours of operation in comparison to pure $FAPbI_3$, as well as improved V_{oc} and FF.[81,82] Caesium has also recently been used to form triple-cation mixed perovskites with both MA and FA, further allowing both high efficiency (>20 %) and greater short-term stability in comparison to analogous caesium-free devices.[83] Triple-cation alloying, as well as alloying with Br, has also been used to stabilise specific compositions with fixed band gaps tuned for usage as 'top' absorbers in tandem devices, either with silicon,[84] or even with a low-band gap Sn-alloyed perovskite, to form overall highly efficient (>20 %) cells.[85]

Properties

With efficiencies that now meet or exceed those of other, established absorber materials, it is clear that research effort is not the only driving force of the lead halide perovskites' successes – the materials have some exceptional properties that have allowed them to reach such heights in performance. In particular, we can relate characteristics of MAPI and FAPI to nearly all of the ideal intrinsic properties for absorbers mentioned in Section 1.2.5.

MAPI itself has a band gap of ∼1.55 eV, observed through both optical methods and theoretical calculations,[12,86–88] which still allows for a SQ maximum efficiency >30 %, although as discussed FAPI has a 1.48 eV band gap, bringing it further into the ideal range for use in photovoltaics. In both compounds, the overall electronic structure is similar: the valence band is composed of I p and Pb s orbitals, in accordance with the revised lone pair model for the 2+ oxidation states of group IV cations,[89] and is antibonding in character; the conduction band is composed of I p and Pb p, and so due to the high atomic numbers of both, has an especially strong spin-orbit effect (calculated to be up to 1 eV).[26,90] The organic cation, either MA or FA, has no direct electronic contribution to either band edge, but does lead to implicit effects from the slight changes in structure.[91] An orbital diagram showing

these interactions is included as Figure 1.14. The character of the band gap of the lead halide perovskites is also somewhat complex – as discussed above, the degenerate conduction band is predicted to spontaneously split in $\mathbf{k}$-space through the Rashba effect, as a result of loss of centrosymmetry from the rotation of the (dipolar) methylammonium or formamidinium, and making the gap (otherwise direct at the R point in the cubic phase) temporarily indirect.[28,29] As this splitting is small, the perovskites still behave as pseudo-direct semiconductors,[92] demonstrating very strong ($\sim 1 \times 10^5\,\mathrm{cm}^{-1}$) absorption at 1.5 eV, with a sharp onset similar to GaAs and CdTe.[12]

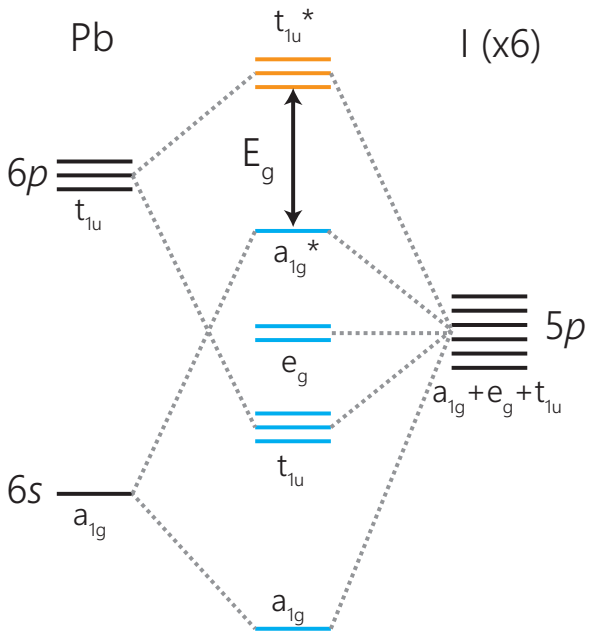

Figure 1.14: Simplified orbital diagram demonstrating the key interactions that make up the bonding within a single lead-iodide octahedron in the lead halide perovskite structure, at the valence and conduction band edges. Only σ interactions from each iodine in the octahedron are considered. The organic cation interacts near-entirely ionically and so is omitted from the diagram.

The carrier dynamics of the methylammonium perovskites have also been under much investigation, as carrier diffusion lengths and lifetimes recorded for both pure and Cl-doped MAPI are generally very high, up to an order of magnitude greater than those of other solution-processed materials, and thus making the planar cell architecture feasible.[93] The monomolecular recombination rate constants (mostly corresponding to trap-assisted recombination) in these materials have been recorded at $\sim 5\,\mathrm{s}^{-1}$ to $20\,\mathrm{s}^{-1}$, corresponding to lifetimes of tens or hundreds of nanoseconds, and bimolecular (radiative recombination) rate constants of $1 \times 10^{10}\,\mathrm{cm}^3/\mathrm{s}$ are com-

parable and lower than those of GaAs.[94,95] Cl-doped MAPI appears to slightly outperform pure MAPI, with the former recorded to have carrier diffusion lengths of $\sim$1 µm while the latter gives $\sim$150 nm,[94,96,97] however both are demonstrative of the relatively minimal apparent effect of traps in the system, despite low-temperature or solution-based synthesis methods which would greatly increase trap density in other systems. Finally, very reasonable carrier mobilities of $\sim 10\,\mathrm{cm^2/V/s}$ in MAPI[95,98] and $>30\,\mathrm{cm^2/V/s}$ in $(CH_3NH_3)PbCl_xI_{3-x}$[99] correspond well with low theoretical effective masses of $0.3\,m_0$ for holes and electrons.[91,100]

These exceptional properties have also sparked research into defect tolerance – even when produced using synthesis methods that would lead to high trap densities, strong SRH recombination and poor carrier diffusion in other materials, the lead halide perovskites still seem to demonstrate exceptional carrier transport – an excellent advantage for their use in photovoltaics. Steirer *et al.* examined MAPI using X-ray photoelectron spectroscopy, observing changes in the binding energies of Pb and I levels over time under the X-ray beam: as the irradiation of X-rays introduced vacancies into the film, the resultant valence band spectrum showed minimal changes in the first few hours before the phase itself started to degrade, indicating that, at least, initially the introduction of defects had minimal overall effect.[25] They proposed that this was due to the pairing of iodide and methylammonium vacancies into a neutral, benign defect complex, agreeing with Walsh *et al.*'s theoretical findings that both 'full' and 'partial' Schottky disorder of this type, resulting in neutral complexes, could allow MAPI to be both highly defective and electronically benign, leading to associated tolerance and high carrier lifetimes.[19] Early theoretical studies of point defects in MAPI also found that almost all vacancies and interstitials were shallow, supporting the antibonding-VB/bonding-CB model of defect tolerance above;[101,102] more recent work has instead found that iodine interstitials or iodine-on-lead antisites could lead to deep defect states, but that I-poor conditions (which may be common in many syntheses) or indeed Br and Cl substitution, will act to 'cure' trap states by shifting them towards the band edges, and could help to explain the superior performance of halide-alloyed perovskites.[103,104]

Interestingly, the area where the lead halide perovskites perform least ideally may be in alignment with other materials. As explained above, in early perovskite cells, Al_2O_3 was a possible replacement for TiO_2 as the scaffolding layer in bulk

heterojunction/DSSC-like architectures but did not aid in electron transport due to misalignment with the conduction band of MAPI; recent research has suggested that TiO_2 may actually act similarly in planar architectures, particularly with narrower-gap FA/MA mixed structures, and that a near-300 meV barrier could exist between the perovskite and TiO_2 layers. Baena *et al.* proposed that SnO_2 may be a more promising replacement, with improved J_{sc}.[105] With regards to the HTL, the ubiquitous usage of spiro-OMeTAD as the hole-transporting material in many of the record perovskite solar cells has also been put under scrutiny, as it requires a multi-step synthesis from relatively expensive starting materials, including palladium-based catalysation.[106] Equally, HTL-free cells have yet to reach the exceptional efficiencies set by those including spiro-OMeTAD,[107] and so there has been a search for alternative, inexpensive organic HTLs that could allow for widespread, commercial development;[108–110] only a small selection of these have been able to generate J_{sc} $>20\,mA/cm^2$ needed to match efficiency with current record cells.[111]

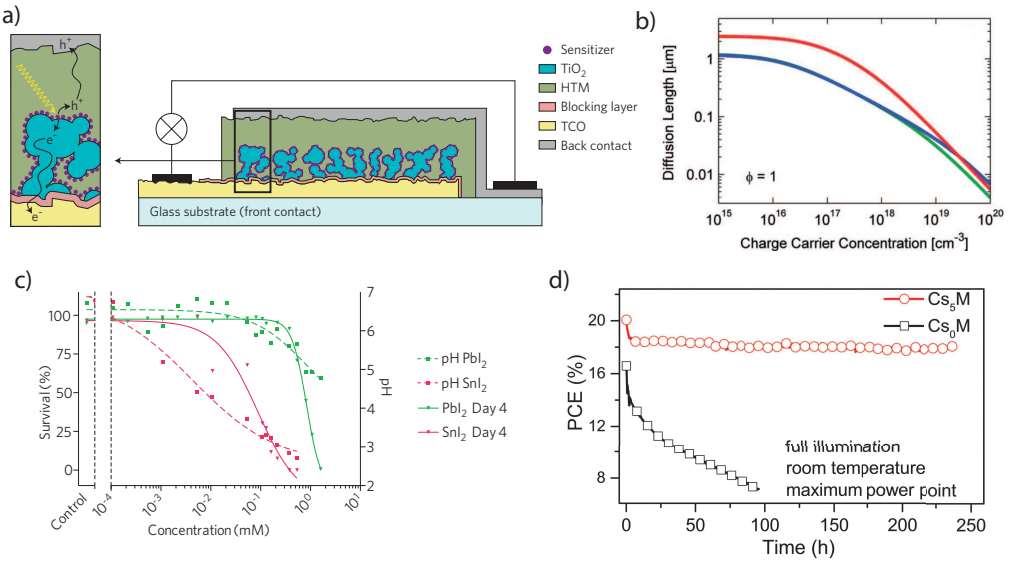

Figure 1.15: a) A diagram of the typical 'mesoscopic' architecture of DSSCs and some methylammonium lead iodide solar cells; reproduced from Grätzel.[112] b) Carrier diffusion lengths of MAPI (green, blue) and $(CH_3NH_3)PbCl_xI_{3-x}$ (red), demonstrating long carrier diffusion lengths over the typical carrier concentrations for absorber layers in PV ($1 \times 10^{16}\,cm^{-3}$ to $1 \times 10^{17}\,cm^{-3}$); reproduced from Wehrenfennig *et al.*[95] c) Survival of zebrafish under concentrations of PbI_2 and SnI_2, decomposition products of perovskite phases; reproduced from Babayigit *et al.*[113] d) Photoconversion efficiency (PCE) of un-doped MAPI (Cs_0M) and 5 % Cs-doped MAPI (Cs_5M) as a function of time, demonstrating the improved stability of hybrid perovskite on Cs alloying or doping; reproduced from Saliba *et al.*[83]

Issues and Challenges

In the discussion of the lead halide perovskites thus far, they may appear to be a near-perfect emergent solar absorber, with exceptional properties and cell efficiencies that match those of well-established technologies. However, there are key issues regarding the use of lead halide perovskites in commercial photovoltaics that have also arisen over the course of the past years that must be addressed for the technology to become a realistic alternative to current absorbers.

The first issue is *device hysteresis* – significant, numerical differences between the *J*–*V* curves generated when measured under forward or reverse bias, and in some cases leading to very different efficiencies.[114] These effects were particularly notable in planar methylammonium lead perovskite devices with minimal mesoporous-TiO_2 and small grain sizes, in which fill factors were seen to decrease by up to 33 $\%$ and leading to similar changes in PCE.[115] This behaviour can be detrimental to large-scale modules as the output properties will not be stabilized, and this can make assessment of performance and power output difficult. Initially, polarization as a result of ferroelectric behaviour (a potential consequence of the methylammonium dipole) was considered as a possible cause of this phenomenon, with a number of reports discussing ferroelectric domains enabling long carrier diffusion lengths, and that their dependence on the direction of applied voltage could lead to hysteresis.[100,116,117] The inconsistency of these reports with conductance measurements and prior reports of a centrosymmetric space group ($I4/mcm$) for the room temperature phase of MAPI has lead to a relative consensus that mixed ionic and electronic conduction is a more likely source for the hysteresis.[118–120] Both MA[121] and I[122] vacancies have been reported to be relatively mobile through the structure of MAPI, with activation energy barriers of $\sim$0.5 eV – under the presence of a current, defects are hypothesised to migrate towards the contacts, opposing the photogenerated electric field and reducing performance; if beginning at open-circuit conditions (no current) instead, the voltage acts against defect migration, and the resultant *J*–*V* scan will appear unaffected, thus leading to a difference between scans. The issue of hysteresis has become less prominent as mixed-halide and mixed-cation perovskites have become popular, and generally show less hysteresis[69,71] – a possible consequence of additional disorder disrupting ion diffusion, or simply the variation in synthesis

conditions.[123]

The second issue, previously highlighted, and perhaps the most impactful, is *device stability*. In order to realistically compete with currently established absorber technologies, photovoltaic modules generally need to demonstrate a lifespan over $>$20 years, and show minimal degradation in performance over that time; even with the photovoltaic market moving beyond solely long-timescale building-mounted modules, devices will still need to have sufficient longevity to ensure production is worthwhile. Unalloyed and unprotected MAPI cells, however, have had a poor track record of stability, with devices reported to degrade under atmospheric moisture,[124,125] oxygen (through the generation of superoxide defects),[126,127] heat,[128] and even UV-light,[129,130] with absorption and cell performance often degrading by at least 50 % on a timescale of hours. There have also been numerous reports on the intrinsic thermodynamic instability of MAPI, particularly possessing a positive formation enthalpy from PbI_2 and $(CH_3NH_3)I$, through both theoretical calculations and experimental testing, including calorimetry.[131–133] This is clearly a significant barrier to the widespread application of the technology, and efforts are being made to counteract this – the caesium alloying described above has shown improvements, although sometimes at the cost of an increased band gap, while recently doping with rubidium (itself never forming a cubic perovskite when in a compound with lead and iodine) has also produced improved lifetimes under operating conditions.[134] The perovskite layer itself is not the only troublesome component in the classic device structures described above, with TiO_2 identified as the source of UV-instability due to its photocatalytic properties, while organic HTLs such as spiro-OMeTAD also demonstrate poor stability to water; efforts to improve these include replacing the ETL with benign alternatives[135] and replacing the HTL with stable inorganic equivalents such as CuI[136] or partially encapsulating or protecting vulnerable layers using buffer layers.[130,137] Nevertheless, the poor general stability of the perovskite family has motivated the search for related, but less fragile, photovoltaic materials, as discussed further in Section 4.1.

The final major issue is the *toxicity* of lead, and is intensified by the poor device stabilities: if the perovskites themselves were sufficiently stable, the danger that lead might leach into the environment would be minimized, and discussion surrounding the ecological impact of the technology might be limited to initial production and

recycling at the end of module lifespans, as is primarily the case for the water-insoluble CdTe.[138] Lead itself has well-known neurodegenerative effects over both intensive exposure, and small-dose long-term exposure, particularly in children,[139,140] and solvated $(CH_3NH_3)PbI_3$ has been reported to have cytotoxic effects on a variety of human cells.[141] As such, the potential leaching of lead from damaged cells has been of particular concern: Hailegnaw *et al.* simulated rainfall on unprotected cells and found that the majority of lead within was lost into solution;[142] Babayigit *et al.* predicted that such concentrated leakage from a module, even under heavy rainfall, would be enough to induce defects or even death in zebrafish.[143] Replacement of Pb with Sn within the ABX_3 perovskite structure as been proposed, however all-tin cell efficiencies have historically been far lower than their lead counterparts ($<10\,\%$), and are prone to instability with respect to Sn(IV), with devices degrading within hours.[144,145] Even should they be stabilised, in some reports Sn-based cells have been predicted to have a worse environmental impact than their lead counterparts, particularly in water due to the release of HI on the solvation of SnI_2,[143] as well as poorer energy payback (given the lower efficiency) and the mining and extraction of a less abundant element.[146] With this, researchers have suggested either fail-safe encapsulation of cells (with associated manufacturing costs) or exploring beyond Pb and Sn for other, less toxic materials.[113]

1.4 Motivation and Aims

The success of the organic-inorganic lead halide perovskites, both just prior and concurrent to this project, has rejuvenated the search for alternate photovoltaic absorbers, whether those that might share similar structures and properties to the lead halide perovskites, but also those earth-abundant non-toxic materials that have perhaps been overlooked in the past few decades. In this project, we have studied a number of materials using theoretical methods to calculate their electronic and optical properties, with the intent to examine their suitability as solar absorbers to be used within photovoltaic devices. Chapters 2 and 3 detail the theoretical basis and methodology used, with particular focus on how important properties for PV, such as a semiconductor band gap or optical absorption may be obtained *ab initio* – purely predicted from theoretical principles alone, without the need for

fitting or adaptation to empirical, experimentally-recorded values. Accurate *ab initio* prediction of materials properties can be of immense value, allowing the obtaining of properties that may be difficult or resource-intensive to obtain through experiment, but also, through comparison with experiment, can provide atomistic rationale and explanation for trends and results that are obtained.

In this thesis, we will focus on the calculation of three families of materials, to accurately predict their electronic properties and, ultimately, assess whether they may be useful as emergent solar absorbers in photovoltaics. In Chapter 4, we consider the caesium silver bismuth halides, a family of compounds whose recent discovery was directly inspired by the search for less toxic alternatives to the lead halide perovskites. Here, we critically discuss their electronic structure in comparison with their lead-based analogues with particular focus on how orbital character can directly affect bonding, and subsequently, optical behaviour, and thus an outlook for the possibility of lead-free perovskite PV materials. Chapter 5 discusses the silver copper sulfides, in the context of recent developments in the search for inorganic chalcogenide materials as 'thin-film' absorbers. In our research, we use *ab initio* calculations together with experimental support to discuss the potential pitfall in suggesting materials as novel solar absorbers purely on the basis of band gap, and the associated SQ efficiency. Finally, in Chapter 6, we attempt to bring the recently-developed knowledge of lead and bismuth-based materials in PV with the stability of inorganic chalcogenides in the *ab initio* prediction of the properties of the little-studied ternary lead bismuth sulfides. Within that research, we have also performed intensive investigation of a candidate absorber, including *ab initio* calculations of defect properties, and demonstrate how these results can be used to inspire potential cell architectures.

Throughout this research, we have attempted to explore the structure-property relationships of these emergent materials, and provide some contribution towards the understanding of heavy-metal compounds within the context of photovoltaics. Concurrently, we aim to further demonstrate that *ab initio* calculations can provide chemical insight and accurate prediction at the atomistic level towards such emergent materials, developing the future of the crucial and promising energy-generation technology that is photovoltaics.

Chapter 2

Theory

2.1 Quantum Mechanical Methods

Computational chemistry encompasses a wide variety of methods, allowing the calculation of a wide variety of properties and processes through a variety of different methods. For the assessment of optoelectronic properties, the aim of this thesis, perhaps the most important quality of computational chemistry is the prediction, *ab initio*, of the electronic structure of solid state materials through the theory of quantum mechanics (QM). While classical or empirical methods are highly valuable, when studying emerging materials and compounds that may be poorly characterised, or with minimal extant literature coverage, accurate *ab initio* methods can give useful insights and predictions that can guide future experimental and theoretical work on such systems.

The primary goal for the quantum mechanical methods used in theoretical chemistry is the solution of the (time-independent) Schrödinger equation (TISE),

$$\hat{H}\Psi = E\Psi \tag{2.1}$$

where $\hat{H}$ is the Hamiltonian operator, which for an electronic system may be split into $\hat{T}$, the kinetic energy contribution, and $\hat{V}$, the potential energy contribution; Ψ the wavefunction and E the energy eigenvalue(s). The obtaining of the energy of a given system is the most crucial in determining the form of the ground state of that system, as once the exact wavefunction of a system – which solves the equation above – is obtained, a number of properties may be obtained through other operators. Difficulty arises however, when obtaining the form of such a wavefunction for any multi-electron system: while the energy levels (and associated wavefunctions/atomic orbitals) of a hydrogenic atom may be solved exactly, once there are more than one electron in a system, the combination of electron-electron and nuclear-electron interactions ensure that the problem becomes mathematically intractable to solve. As such, for any polyatomic system, such as a molecule or a solid semiconductor, approximations must be used in order to simplify our Hamiltonian or wavefunction to enable their solution.

The theories used as the basis for this work all utilise the Born-Oppenheimer (BO) approximation as a first degree of simplification. The Born-Oppenheimer approxi-

mation postulates that, given the relative difference in masses between an electron and the protons and neutrons of a nucleus (∼5 orders of magnitude), the nuclei are effectively immobile on the timescale of electron motion – essentially, that the electrons can be treated as travelling within a field of fixed nuclei. This allows the decoupling of the electronic and nuclear wavefunctions from each other, such that the total wavefunction becomes:

$$\Psi = \psi_{electronic} \times \psi_{nuclear} \tag{2.2}$$

The practical implication of this for computation is that the electronic wavefunction may be solved separately, greatly reducing the dimensionality of the problem, and that the electron-nuclear potential interaction becomes a mean field interaction, while the nuclear-nuclear potential is constant. While there are situations under which the BO approximation will no longer be valid, such as highly excited vibrational states and conical intersections, where vibronic coupling (between nuclear and electronic motion) is especially strong, these are not generally of particular importance to the description of the electronic structure of ground state semiconductors.

2.2 Hartree-Fock (HF) Theory

The Hartree-Fock (HF) method originated in the work of Hartree in the 1920's,[147,148] where a solution to the Schrödinger wave equation was proposed by simplifying the full TISE to solely a 1 electron Hamiltonian, and thus solving for separate one electron wavefunctions (orbitals). In this manner, we treat the electrons as non-interacting (a problem that will be adjusted for later), but by doing so, remove much of the mathematical complexity of the physical problem, and make a theoretical description tractable. Within this approximation, the reduced one-electron Hamiltonian operator is, in atomic units*, and for a system of P nuclei and N electrons:

$$\hat{h}_i = \hat{t}_i + \hat{v}_i = -\frac{1}{2}\nabla_i^2 - \sum_p^P \frac{Z_p}{r_{ip}} \tag{2.3}$$

*Atomic units are a convention in computational chemistry where, for simplicity, a number of fundamental constants, such as $\hbar$ and the elementary charge are treated as unity

where ∇_i^2 is the Laplacian operator (here, the sum of second derivatives along each cartesian direction) Z_p the charge on nucleus p and r_{ip} the distance between electron i and nucleus p. In this, we have already assumed the Born-Oppenheimer approximation to remove the terms associated with the nuclei alone to obtain an 'electronic' Hamiltonian (we shall use Ψ as the shorthand for the electronic wavefunction, rather than total wavefunction from now on). The solution to this will then satisfy the equation:

$$\hat{h}_i \chi_i(x_i) = \epsilon_i \chi_i(x_i) \tag{2.4}$$

with ϵ_i as the single-electron energies for the single spin orbital χ_i(x$_i$), with x_i as a generalized coordinate including all degrees of freedom (i.e. position along each of 3 cartesian directions, and spin). The total energy of this non-interacting system is thus the sum of these one electron energies, while the total electronic wavefunction is given by the Hartree Product:

$$\Psi(x_1, x_2, \ldots, x_N) = \chi_1(x_1)\chi_2(x_2)\ldots\chi_N(x_N) \tag{2.5}$$

Unfortunately, as this model neglects all electron interactions, including exchange and correlation, it is a poor description of realistic systems. The Hartree product also does not obey the Pauli exclusion principle – that the wavefunction must undergo a change in parity under the interchange of two fermions:

$$\Psi(x_1, x_2) = -\Psi(x_2, x_1) \tag{2.6}$$

Further work from Hartree then included the Coloumbic electron-electron interaction through the mean-field approximation. Rather than ignoring electron-electron interaction entirely, but not considering the individual relative motions of every electron with each other, we can instead treat an individual electron moving in a potential field created by the presence of all the other electrons in the system – similar to that of the 'stationary' nuclei. Unlike the nuclei, however, our electrons are in motion, but we can attain an average interaction by using the probability distribution of the *electron density*, which in the Born interpretation of QM, is simply given by the

square of the wavefunction. In a simple 1-nucleus, 2-electron system, the Hamiltonian in our eigenequation for electron 1 thus includes the terms in our previous Hamiltonian above, plus the interaction of electron 1 with the mean field of electron 2 over *all space* (throughout this thesis, this is given by an integral with respect to $\mathrm{d}\tau$, which is equivalent to $\iiint \mathrm{d}x\,\mathrm{d}y\,\mathrm{d}z$):[†]

$$\hat{H}_1\chi_1(x_1) = \left[-\frac{1}{2}\nabla_1^2 - \frac{Z}{r_1} - \int \frac{[\chi_2(x_2)]^2}{\mathbf{r_{12}}}\mathrm{d}\tau \right]\chi_1(x_1) = \epsilon_1\chi_1(x_1) \tag{2.7}$$

We can note that although we are trying to evaluate the solution for electron 1, our Hamiltonian includes the eigenfunction of electron 2; in order to do this, we must solve the problem in a self-consistent manner. By making an initial guess at $\chi_2(x_2)$ (and $\chi_1(x_1)$ for the equivalent eigenequation for electron 2), we can obtain the respective electron-electron interactions, and produce a new eigenset. Notably, these, when replaced into equation 2.7, could produce a different electron-electron interaction – we can then repeat our solution of the equation to obtain another set of orbitals. These steps can be repeated until our input and output orbitals are the same, and a converged solution is obtained, making it a *self consistent field* (SCF) method. We can expand this method to higher-electron (or nuclear) systems by simply adding additional potential terms to our Hamiltonian, each considering the interaction of electron 1 with a given field of another electron. Our electron-electron interaction is still solely Coulombic, however, and our total wavefunction does not obey the Pauli exclusion principle.

In order to solve this problem, Fock and Slater[149,150] noted that instead of solely composing our electronic wavefunction from individual spin orbitals, we can instead represent our system in a single Slater determinant, e.g. for a two-electron system:

$$\Psi(x_1, x_2) = \begin{vmatrix} \chi_1(x_1) & \chi_1(x_2) \\ \chi_2(x_1) & \chi_2(x_2) \end{vmatrix} = \chi_1(x_1)\chi_2(x_2) - \chi_1(x_2)\chi_2(x_1) \tag{2.8}$$

[†]From this point, we will use the Dirac's bra-ket shorthand notation to simplify integrals involving wavefunctions – this simplifies the inner product of two wavefunctions $\int \chi_1^*\chi_2\,\mathrm{d}\tau$ to $\langle\chi_1|\chi_2\rangle$; the total energy of a system is given by the expectation value $\langle E\rangle = \int \Psi^*\hat{H}\Psi\,\mathrm{d}\tau \equiv \langle\chi_1|\hat{H}|\chi_2\rangle$

Our wavefunction needs to satisfy orthonormality and so should then be normalised with a constant of $\frac{1}{\sqrt{N!}}$.[‡] We can then also check that this obeys the Pauli principle:

$$\begin{aligned}\Psi(x_2, x_1) &= \frac{1}{\sqrt{2}}[\chi_1(x_2)\chi_2(x_1) - \chi_1(x_1)\chi_2(x_2)] \\ &= -\frac{1}{\sqrt{2}}[\chi_1(x_1)\chi_2(x_2) - \chi_1(x_2)\chi_2(x_1)] = -\Psi(x_1, x_2)\end{aligned} \tag{2.9}$$

Here, there is the implicit assumption that electronic systems are describable by a single Slater determinant: in reality, the possibility of excited states means a linear combination of multiple Slater determinants is required to describe a system fully, however a single determinant can make for a good first approximation. 'Post-HF' methods such as Configuration Interaction often work to improve on this by including more determinants, but often at exorbitant computational cost (as each determinant is an N×N dimensional object),[151] limiting their potential usage to generally small systems, although increases in computational power are making these far more viable.

As the Slater determinant represents all electrons in the system, we can now formulate an expectation value for the total electronic energy of the system:

$$\begin{aligned}\langle\Psi(1,2)|\hat{H}|\Psi(1,2)\rangle = &\langle\Psi(1,2)|\hat{h}_1|\Psi(1,2)\rangle + \langle\Psi(1,2)|\hat{h}_2|\Psi(1,2)\rangle \\ &+ \langle\Psi(1,2)|\frac{1}{\mathbf{r_{12}}}|\Psi(1,2)\rangle\end{aligned} \tag{2.10}$$

where $\hat{h}_1$ and $\hat{h}_2$ are the non-interacting one-electron Hamiltonians as in Equation 2.3, while the final term considers the through-space interaction between two electrons. The first two terms can be reduced to terms analogous, but not identical, to the single-electron energies ϵ_1 and ϵ_2 above by expanding the slater determinant, separating out variables (noting that, for example, $\hat{h}_1$ solely acts upon x_1) and considering the orthogonality of χ_1 and χ_2:

[‡]Orthonormality is guaranteed if a set of eigenfunctions are to be well-behaved solutions of a Hermitian operator such as the Hamiltonian; mathematically, it ensures that the inner products satisfy $\langle\chi_i|\chi_i\rangle = 1$ and $\langle\chi_j|\chi_i\rangle = 0$

$$\begin{aligned}
\langle\Psi(1,2)|\hat{h}_1|\Psi(1,2)\rangle &= \frac{1}{2}\langle\chi_1(x_1)\chi_2(x_2)-\chi_1(x_2)\chi_2(x_1)|\hat{h}_1|\chi_1(x_1)\chi_2(x_2)-\chi_1(x_2)\chi_2(x_1)\rangle \\
&= \frac{1}{2}\langle\chi_1(x_1)\chi_2(x_2)|\hat{h}_1|\chi_1(x_1)\chi_2(x_2)\rangle + \frac{1}{2}\langle\chi_1(x_2)\chi_2(x_1)|\hat{h}_1|\chi_1(x_2)\chi_2(x_1)\rangle \\
&\quad - \frac{1}{2}\langle\chi_1(x_1)\chi_2(x_2)|\hat{h}_1|\chi_1(x_2)\chi_2(x_1)\rangle - \frac{1}{2}\langle\chi_1(x_2)\chi_2(x_1)|\hat{h}_1|\chi_1(x_1)\chi_2(x_2)\rangle \\
&= \frac{1}{2}\cancelto{1}{\langle\chi_2(x_2)|\chi_2(x_2)\rangle}\langle\chi_1(x_1)|\hat{h}_1|\chi_1(x_1)\rangle + \frac{1}{2}\cancelto{1}{\langle\chi_1(x_2)|\chi_1(x_2)\rangle}\langle\chi_2(x_1)|\hat{h}_1|\chi_2(x_1)\rangle \\
&\quad - \frac{1}{2}\cancelto{0}{\langle\chi_2(x_2)|\chi_1(x_2)\rangle}\langle\chi_1(x_1)|\hat{h}_1|\chi_2(x_1)\rangle - \frac{1}{2}\cancelto{0}{\langle\chi_1(x_2)|\chi_2(x_2)\rangle}\langle\chi_2(x_1)|\hat{h}_1|\chi_1(x_1)\rangle \\
&= \frac{1}{2}\langle\chi_1(x_1)|\hat{h}_1|\chi_1(x_1)\rangle + \frac{1}{2}\langle\chi_2(x_1)|\hat{h}_1|\chi_2(x_1)\rangle \cong \epsilon_1
\end{aligned} \tag{2.11}$$

The final term of the Hamiltonian then comprises the electron-electron interactions:

$$\begin{aligned}
\langle\Psi(1,2)|\frac{1}{\mathbf{r_{12}}}|\Psi(1,2)\rangle &= \frac{1}{2}\langle\chi_1(x_1)\chi_2(x_2)|\frac{1}{\mathbf{r_{12}}}|\chi_1(x_1)\chi_2(x_2)\rangle + \frac{1}{2}\langle\chi_1(x_2)\chi_2(x_1)|\frac{1}{\mathbf{r_{12}}}|\chi_1(x_2)\chi_2(x_1)\rangle \\
&\quad - \frac{1}{2}\langle\chi_1(x_1)\chi_2(x_2)|\frac{1}{\mathbf{r_{12}}}|\chi_1(x_2)\chi_2(x_1)\rangle - \frac{1}{2}\langle\chi_1(x_2)\chi_2(x_1)|\frac{1}{\mathbf{r_{12}}}|\chi_1(x_1)\chi_2(x_2)\rangle
\end{aligned} \tag{2.12}$$

As the electron-electron operator depends on both x_1 and x_2, the integrals in Equation 2.12 are not separable, and four terms result. The first two terms reflect the classical Coulomb interaction between electrons 1 and 2 – the terms are positive, reflecting the repulsive nature of the interaction. The second two terms, however, are uniquely present due to the antisymmetry of the Slater determinant (these cross terms would not appear from e.g. the Hartree product). These are termed the 'exchange' integrals, and represent a purely quantum mechanical interaction between electrons of similar spin. This interaction is crucial to the accurate prediction of electronic energies (and is indeed the basis for chemical principles such as e.g. Hund's 2nd rule), and in Hartree-Fock (HF) theory, it is formulated exactly.

While the example method above was enumerated with a 2-electron system in mind, the method is easily extendable to molecular and larger systems by additional Hamiltonian terms and extension to the Slater determinant, allowing the calculation of any multi-atomic or multi-electronic system. As with the Hartree model above, the HF equations themselves can be solved iteratively to obtain a converged self-consistent solution for the atomic orbitals of a system. Importantly, such a solution is also a

reliable approximation to the ground-state energy of a system as a *variational principle* applies. The variational principle ensures that the acquired expectation value of the total energy is an upper bound for the true ground state energy, E_0:

$$\langle \Psi | \hat{H} | \Psi \rangle = \langle E \rangle \geq E_0 \tag{2.13}$$

With this established, the solution of the wavefunctions (here, the Slater determinant) can be iterated such that the resultant energy is minimized at every step – in doing so, the solution will approach that for the true ground state energy, and so we expect that our trial wavefunctions approach (but do not necessarily equal) the 'true' wavefunction of the system. Additionally, this iteration is still done self-consistently; with the electron interaction still being treated as an interaction between *average* electron positions, the energy expectation value still depends on the probability of the electron density, and so the method can be continued until a converged solution is reached.

In all, the Hartree-Fock method can provide surprisingly accurate energies and properties, despite its assumption of mean field behaviour, and as a result, a neglect of all electron correlation; it remains a popular first-choice method for the calculation of molecules in particular. A major drawback, however, for solid state systems is that the neglect of correlation leads to poor descriptions of semiconductor electronic structures – HF band gaps are often substantially overestimated, sometimes by several electronvolts. However, its exact treatment of exchange has lead to its usage as the basis of numerous higher-level methods, one of which is detailed in the Section 2.4.4.

2.3 Density Functional Theory

Density Functional Theory (DFT) approaches the problem of the TISE in a somewhat different manner to Hartree-Fock theory and its derivatives, primarily its usage of the 3-dimensional electron density as the primary source/basis for information on an electronic system, in opposition to the 3N-dimensional wavefunction. The description of an electronic system using the density alone dates to the 1920's, in the work of Thomas and Fermi,[152] which represented the first attempts to use the

observable electron density, rather than the more complex, abstract wavefunction for this basis. In their work, the model system used to formulate such ideas behind was the homogeneous or uniform electron gas (UEG), also known as jellium, which comprises an infinite volume of electrons, surrounded by an equally-distributed positive charge (representing the nuclei). Notably, unlike the orbital-centred atomic or molecular picture of HF, the UEG closer to the representation of a solid, in particular metals. In the Thomas-Fermi model, the kinetic energy of the UEG could be defined by a functional (a function of a function, the latter, in this case being the electron density), which could be combined with the repulsive electron-electron interaction described by the classical Hartree energy (see the mean field description above, and E_{e-e} in Equation 2.14 below), and the attractive Coulomb interaction between the electrons and the nuclei (V_{N-e}). However, by including only classical terms, and the rough approximations in T_{TF}, such an expression is poor in describing the properties of real systems.

$$E_{TF}[\rho(\mathbf{r})] = \underbrace{\frac{3}{10}(3\pi^2)^{\frac{2}{3}}\int \rho(\mathbf{r})^{\frac{5}{3}}\mathrm{d}\mathbf{r}}_{T_{TF}} - \underbrace{\int \frac{Z\rho(\mathbf{r})}{r}\mathrm{d}\mathbf{r}}_{V_{N-e}} + \underbrace{\frac{1}{2}\iint \frac{\rho(\mathbf{r})\rho(\mathbf{r}')}{|\mathbf{r}-\mathbf{r}'|}\mathrm{d}\mathbf{r}\mathrm{d}\mathbf{r}'}_{E_{e-e}} \quad (2.14)$$

The key fundaments of DFT, however, were laid out in the 1960's, within the context of this prior work on the UEG, in the work of Hohenberg, Kohn and Sham – it was their work that set up the theoretical grounding, and then the self-consistent computational approach that would both underpin the workings of DFT today. Hohenberg and Kohn's work in 1964 set out two key proofs that form the framework of DFT that allows it to solve for physical, electronic systems. First, they proved that for any group of electrons moving under the influence of an external potential $\nu_{ext}(\mathbf{r})$, the external potential defines a functional of the electron density, $\rho(\mathbf{r})$, and that, as $\nu_{ext}(\mathbf{r})$ also defines the general Hamiltonian, $\hat{H}$, (H = U + T + V, where U is the electron-electron interactions, T the kinetic energy and V the interactions with external potential) the ground state energy of the system must also be a functional of the electron density.[153] Secondly, they showed that a variational principle exists for this energy functional, $E[\rho(\mathbf{r})]$, such that for the correct ground state electron density, the energy functional is minimal and as such, equal to the total, exact

ground state energy of the system. From these two proofs, the total energy of a system can then be defined by:

$$E[\rho(\mathbf{r})] \equiv \int \nu_{ext}(\mathbf{r})\rho(\mathbf{r})d\mathbf{r} + F[\rho(\mathbf{r})] \tag{2.15}$$

where the first term is the system-dependent interaction between the electrons and an external potential created by the nuclei, and $F[\rho(\mathbf{r})]$ is the Hohenberg-Kohn *universal functional* – it contains all information about the electron-electron interactions and kinetic energies, and is solely a functional of the electron density. Should we know the form of this universal functional, then we could also know the exact ground state energy of any system; however, the form of this functional is not known, nor was it provided by Hohenberg and Kohn, who then considered the correspondence of this method with the Thomas-Fermi model in the UEG. Nevertheless, these formal proofs are the important groundwork that demonstrate that the formalism of what would become DFT is physically valid.

Kohn and Sham's work the following year[154] provided an approach to compute an approximation to $F[\rho(\mathbf{r})]$. Their work initially considers a system of non-interacting electrons with an electron density $\rho(\mathbf{r})$, *which is identical to the electron density of the true system of interacting electrons*, and that the universal functional may be separated as follows:

$$F[\rho(\mathbf{r})] \equiv E_{e-e}[\rho(\mathbf{r})] + T_S[\rho(\mathbf{r})] + E_{xc}[\rho(\mathbf{r})] \tag{2.16}$$

where E_{e-e} is the classical Hartree energy from above, T_S is the kinetic energy of the non-interacting electrons, and that E_{xc} is then the sum of both the non-classical electron-electron interactions and the correction to the kinetic energy T_S that accounts for these non-classical interactions (thus giving the correct total kinetic energy, T). Importantly, our system of *non-interacting* electrons, as in the HF method above, are *exactly* defined by Slater determinants, containing sets of single-electron molecular orbitals, ϕ_i. As such, T_S can be given exactly by the Lorentzian expression seen in Equation 2.3 – and thus our reference system can also satisfy a set of single-electron time-independent Schrödinger equations, resulting in the Kohn-Sham equations:

$$\left(-\frac{1}{2}\nabla^2 + \int \frac{\rho(\mathbf{r})}{r_{12}} d\mathbf{r_2} - \sum_n^N \frac{Z_n}{r_n} + V_{xc}(\mathbf{r})\right)\phi_i = \epsilon_i \phi_i \tag{2.17}$$

where V_{xc} is the potential generated by the functional E_{xc}, and where Equation 2.16 and Equation 2.17 must define the same overall external potential. As the potential section of the Hamiltonian still depends on the (unknown) electron density, and hence on these Kohn-Sham molecular orbitals, we can apply an iterative approach to solve these equations: by beginning with an initial guess of the orbitals, the electron density could be calculated, and a new set of orbitals calculated such that the energies are minimized; the process is then repeated until convergence is obtained. This self-consistent cycle is near-identical in concept to the Hartree SCF cycle detailed above, however with the total density as one of our variables. As the second H-K theorem determines that a variational principle applies to the electron density, and that the first theorem determines that the exact electron density is *uniquely defined* for a given external potential, in principle, this method could attain an exact ground state energy – however, the problem resides in the exact exchange-correlation term V_{xc}, the exact form of which we do not know. As such, any DFT calculation requires the approximation of the exchange-correlation functional: Kohn and Sham introduced the first of these, which is detailed in the next section; the work in this thesis, however, uses multiple, more complex exchange-correlation functionals in order to obtain the best approximation to the true energies of the systems we study, as described below.

2.4 Exchange-Correlation Functionals

2.4.1 LDA: Local Density Approximation

Hohenberg, Kohn and Sham's work formed the basis for the first exchange correlation functional: they noted that for a slowly varying electron density, the exchange-correlation functional can be given by the inner product of the *local* electron density and the exchange-correlation energy for the uniform electron gas (ϵ_{xc}), which, as a model system, could be predicted (while assuming that this was sufficient to include all exchange and correlation effects of the system in question):

$$E_{xc}[\rho(\mathbf{r})] = \int \rho(\mathbf{r})\epsilon_{xc}d\mathbf{r} \tag{2.18}$$

In this way, the exchange-correlation energy solely depends on the density local to the point considered – hence, the methods utilising this as the basis for the exchange and correlation in DFT are known as the Local Density Approximation (LDA). The chemical potential of exchange for the uniform electron gas was then predicted, following the method of Kohn and Sham, to be:

$$\mu_x = \frac{1}{\pi}(3\pi^2\rho(\mathbf{r}))^{1/3} \tag{2.19}$$

Notably, this formulation neglected correlation of the UEG, for which a simple expression such as the above does not exist. Instead, the majority of current practical implementations of LDA use the empirical correlation energy predicted by Vosko, Wilk and Nusair,[155] calculated through interpolation of data from quantum Monte Carlo simulations for the correlation energy density of the UEG. Despite its simplicity, LDA has been widely used to predict the structural, thermodynamic and electronic properties of many systems, to a reasonable degree of accuracy. Notably, however, it fails in systems with highly varying electron density, given the assumption that leads to its derivation – and most real systems will be, to a given extent, not slowly varying in the electron density. It also poorly describes systems with high degrees of correlation, such as elements with highly localized orbitals (e.g. 1st row transition elements). Most importantly for ab initio prediction of photovoltaic materials, it is well known to substantially underestimate band-gaps for semiconductors and insulators in this manner, sometimes by up to 40 %.[156]

The last two of these issues, the poor description of strongly correlated materials and underestimation of band gaps, are actually known to be fundamental issues in DFT itself, set apart from the choice of exchange-correlation functional. The first of these arises from the 'self-interaction error' (SIE): we can note that the formulation of Equation 2.17 does not forbid the interaction of a density with another density at the same point. In HF, the possibility of an electron occupying the same position and spin is mathematically forbidden through the Exchange integrals and the basis of the Slater determinant (this area of zero-probability occupation is known as the

exchange, or Fermi, hole). In DFT, the exact formulation of V_{xc} would ensure that this self-interaction would be cancelled, however, as our exchange-correlation functional in reality is always an approximation to the true functional, the self-interaction is never fully cancelled. This effect is particularly strong in highly localized orbitals such as the $3d$ electrons in 1st row transition metals, where the limited range of the orbital means the probability of electrons being closer in proximity is high. In practice, in solids, this usually leads to an unphysical delocalisation of electrons away from the metal centres in order to reduce the total energy, and resultant metal electronic states lie higher in energy than without the SIE.

The band-gap underestimation has been thought to arise since the Kohn-Sham exchange-correlation functional ($E_{xc}[\rho(\mathbf{r})]$) is independent of energy[156] – the exact exchange-correlation energy of a semiconductor is expected to have discontinuities in the derivative ($\frac{dE_{xc}}{d\rho(\mathbf{r})}$) on an integer change in the electron number, and it is indeed the magnitude of this discontinuity that relates to the band gap. LDA, however, and K-S DFT in general, does not provide for energy-dependent exchange-correlation, and thus cannot describe these discontinuities (even on improvements to E_{xc}, as long as it remains local). An error specific to LDA, though, is its relative 'overbinding' of crystal structures, resulting in predicted lattice parameters that are smaller in comparison with experiment, by up to 4 $\%$.[157] The primary cause of this overbinding is due to the electron density of real molecules and solids being more inhomogeneous than the local UEG basis of LDA: the exchange hole predicted by LDA lies further from the atomic nucleus than in real atoms, and as a consequence, when atoms are brought together to form bonds, LDA predicts a greater exchange energy than needed – thus, we may improve upon LDA by considering alternative strategies to describe this inhomogeneity.

2.4.2 GGA: Generalized Gradient Approximation

To improve upon the LDA, especially in systems with more widely variant densities, one could, instead of solely using the local density for the description of our functional, include an expansion of increasing-order gradients around a point to garner greater information about the behaviour of the density at that point (with the density itself being the first term in the gradient expansion). Performing this expansion

for Equation 2.18 leads to:

$$E_{xc}[\rho(\mathbf{r})] = \int [\rho(\mathbf{r}), \nabla\rho(\mathbf{r}), \nabla^2\rho(\mathbf{r}), \ldots]\epsilon_{xc}d\mathbf{r} \tag{2.20}$$

By using the gradient, and in some cases higher derivatives, of the electron density, the resultant functional would then be expected to more accurately describe the wider variation of electron density in real systems, i.e. the non-uniformity where they deviate from similarity to the UEG. With a more accurate description of the inhomogeneity of the true electron density, we might thus expect such a functional to more accurately predict structural and thermochemical properties. In practise, using such a direct expansion of the density gradients (called the gradient expansion approximation, GEA) can lead to poorer descriptions of properties in the local density limit,[158] and so gradient terms are often used to correct initial LDA energies. There have been many and various varieties of such corrections proposed, and collectively they are referred to as Generalised Gradient Approximation (GGA) functionals. In general, they may be divided into 'semi-empirical' functionals, which involve adjustable parameters that may be tuned to accurately predict the properties of a certain subset of systems by fitting to experimental data, and those that remain '*ab initio*' and solely use expansions of the density. While the former can be highly accurate for systems similar to which they are parameterized, they can often lack the wide applicability of the latter – as many empirical functionals have been parameterised using small molecules, they can tend to perform poorly for solids, which are the subject of the work in this thesis, and so the GGA functionals we will consider primarily fall in the latter category.

Perdew, Burke and Ernzerhof devised the functional now referred to as PBE in 1996,[159] refining the GGA description of a previous functional, PW91, in order to correct its behaviour for close-to-linear density response (where LDA behaves best) while removing parameterization. While the resulting functional form is still somewhat too complex to detail here, it fits the general form:

$$E_{xc}^{PBE} = \int \rho(\mathbf{r}).\epsilon_x^{UEG}(\rho(\mathbf{r})).F_{xc}(r_s, \zeta, s)d\mathbf{r} \tag{2.21}$$

where r_s is the local Seitz radius (a reflection of the reciprocal of the electron spin

density of the system), ζ the relative spin polarization and s is a dimensionless density gradient. We can recognize the similarity with Equation 2.18 in the first terms, with F_{xc} acting as the scaling ('enhancement') factor that includes the gradient terms (with the LDA limit recurring as $s \to 0$). PBE is able to attain similar accuracy to other, parameterized functionals, while being considerably more simple in form, and has lead to its popular and widespread application. The gradient expansion in PBE also generally tends to lead to slight underbinding compared to experimental values, and so lattice parameters are often overestimated by $1\,\%$ to $2\,\%$.[160]

More recently, Perdew and co-workers have adapted the PBE functional for a better description of solids[161] – they note that in order to attain more accurate atomisation energies (and resultant dissociation energies in molecules) the coefficient of the second term in the gradient expansion (that in s, above) is, in PW91 and PBE and other functionals, weighted at double that for the UEG so as to more closely match the highly accurate, equivalent expansion that can be made of atomic exchange in terms of the nuclear charge, Z. This weighting, however, violates UEG behaviour and particularly deviates for slowly-varying densities, which solid systems tend to possess; as such, cohesive energies for solids tend to be relatively inaccurate for those functionals. The functional now-termed PBEsol restores the UEG-like behaviour in the gradient expansion, and so generally performs more accurately, in both energies and lattice parameters of solids, than PBE – given its greater similarity with LDA in form, it tends to overbind slightly in comparison to experiment, and lattice parameters are often shorter, but improve upon those of LDA.[160]

While improving on properties such as binding energies and structural description, all GGAs, however, still suffer from those problems identified in DFT as a whole such as the self-interaction error, particularly strong in highly correlated systems, and underestimation of semiconductor band gaps. To attempt to rectify these, two possible methods both reach beyond the basic principles of DFT: adding a Hubbard U parameter, or introducing some Hartree-Fock component into our DFT energy in so-called 'hybrid DFT'.

2.4.3 DFT+U

The DFT+U method attempts to address the problem of spurious electron delocalisation in highly correlated solids that arises from the self-interaction error by introducing an energetic penalty to recreate the correct localization. Acting somewhat analogously to the U parameter in the theoretical model of Mott-Hubbard insulators such as NiO, where a conventional tight-binding model would predict metallic behaviour, instead a band gap is opened due to the strength of the Coulomb interaction (U) between the highly localized valence 3d electrons, preventing the charge from delocalising. In the DFT+U model, a repulsive interaction (again, given as U) is added to the total DFT Energy for particular orbitals (i.e. the $3d$ in the 1st row transition metals in question) that is maximized when the electron count is a non-integer, but 0 when the electron occupation is an integer value. This then acts directly against the additional stabilisation that unmodified DFT would get from delocalising charge to avoid self-interaction and reaching non-integer occupations; with a sufficiently large energetic correction in U, the correctly localized electronic structure will be obtained.

In terms of the electronic band structure, DFT+U will result in said highly-correlated states usually lowering in energy, and thus can open/widen a band gap where DFT previously predicted metallic/narrow gap behaviour, leading to more accurate band gap predictions. The U parameter itself can be dependent on both the element in question, but also its chemical environment, and so careful choice is required – often, U values can be fit through comparison of key localized state energies to those measured in experimental X-ray photoelectron spectroscopy (XPS) analysis. DFT+U has seen substantial usage where higher-level methods were too computationally expensive, due to the relative inexpense of adding the U interaction: the method has been particularly popular in supercell calculations for defect property prediction.

The specific DFT+U method used in this report is the rotationally invariant form of Dudarev's correction:[162]

$$E_{DFT+U} = E_{DFT} + \frac{U-J}{2}\sum_{\sigma}[(\sum_{j}\hat{\mathbf{n}}^{\sigma}_{jj}) - (\sum_{j,l}\hat{\mathbf{n}}^{\sigma}_{jl}\hat{\mathbf{n}}^{\sigma}_{lj})] \tag{2.22}$$

where $\hat{n}$ is the density matrix of d electrons, with eigenvalues equal to the occupation

numbers of the individual d states with spin σ, and the magnitude of the correction is determined by the two parameters U (Coulombic) and J (Exchange). The second term in this expansion, with dependence on l, allows the correction to be orbital dependent, however also cancels exactly in the limit of integer occupation numbers, allowing the corrected DFT+U energy to still be suitable for calculating cohesive energies of solids. For the methods and examples used in this thesis, we assume a purely Coulombic correction, and so J = 0.

2.4.4 Hybrid DFT

While DFT+U can work to correct the self-interaction error, it does not rectify the underestimation of semiconductor band gaps in all cases. Instead, a more recent innovation in the field of DFT has been the introduction of 'hybrid' functionals, which combine exchange and correlation from DFT methods with the exact exchange calculated from HF theory, with the aim that including this exact exchange will counteract at least some of the inaccuracy in the 'semilocal' LDA or GGA approximations. However, the inclusion of HF exchange will greatly increase computational demand and hence their application, particularly in solid systems has been limited until recent developments in computational power. The idea of utilising exact exchange is not novel, and indeed Kohn and Sham acknowledged the possibility of the treatment of exact exchange, while correcting for correlation effects, within the framework of the exchange-correlation functional, however noted that such a non-local operator would be too complicated to solve.[154]

The current format of hybrid functionals rose from the empirical parameterized approach to the approximation of exchange and correlation, and the first hybrid functionals contained multiple parameters determining the proportions of HF, GGA exchange and correlation. However, it was noticed that fixing the ratio of HF to GGA (specifically PBE) exchange to $\frac{1}{4}$ while combining with DFT correlation still lead to accurate molecular bond lengths, intermolecular interactions, and derived properties, leading to the construction of the wholly not-parameterized PBE0 functional:[163]

$$E_{xc}^{PBE0} = E_{xc}^{PBE} + \frac{1}{4}(E_x^{HF} - E_x^{PBE}) \tag{2.23}$$

The use of $\frac{1}{4}$ HF exchange has been justified non-empirically by Perdew *et al.* for most molecules by noting that the proportion of hybrid exchange can be linked to the reciprocal of the order of perturbation theory required to provide a description of the dependence of the exchange correlation functional on electronic interactions.[164] In molecules, *fourth*-order Møller-Plesset perturbation theory, with the Hartree-Fock Hamiltonian as the zero-order term, was noted to perform highly accurate predictions for atomization energies, and so the authors noted that the $\frac{1}{4}$ coefficient represents the most suitable choice for molecules (while also noting that an ideal hybrid functional form could optimize this factor for each system). More recently, Heyd, Scuseria and Ernzerhof discussed the truncation of the HF exchange interaction with range as a method for improving the computational efficiency of hybrid DFT while maintaining accuracy.[165] The HSE functional form resulted:

$$E_{xc}^{HSE}(\alpha,\omega) = \alpha E_x^{HF}(\omega) + (1-\alpha)E_x^{PBE,SR}(\omega) + E_x^{PBE,LR}(\omega) + E_c^{PBE} \quad (2.24)$$

In this form, α is the parameter defining the proportion of exchange, while ω defines the range at which HF exchange is truncated, with solely GGA exchange being considered beyond it. The HSE06 functional specifically uses $\alpha = \frac{1}{4}$ and $\omega = 0.11\,\text{bohr}^{-1}$;[166] in this way, the functional reduces to PBE0 as $\omega \to \infty$, and PBE as $\alpha \to 0$. Both HSE06 and PBE0 have seen substantial success with solid systems, as well as molecular. In particular, they are able to more accurately reproduce highly localized d states than DFT, as the exact exchange from HF, where self-interaction is forbidden by the exchange hole, helps to counteract the SIE. Most importantly, by balancing the underestimation of DFT with the overestimation of HF, PBE0 and HSE06 are able to accurately predict the band gaps of semiconductors, often to within 0.1 eV of low-temperature experimental gaps: in wide-gap insulators, long-range exchange is more dominant, and, of the two, PBE0 performs better, while in narrow-gap insulators, particularly within the ideal 1.0 eV to 1.5 eV range for photovoltaic absorbers, the range-dependence of HSE06 means it tends to predict more accurately.[167] As such, while it is still worth benchmarking functionals, hybrid DFT does allow the possibility of highly accurate *ab initio* prediction of semiconductor electronic structures and properties.

Chapter 3

Computational Methodology

In the previous chapter, we have discussed the fundamental theory that underlies the quantum mechanical calculations that will be performed. In this chapter, we will discuss first the specific considerations that are taken when performing QM calculations on condensed matter – in the case of this thesis, crystalline solids. We will also summarise the key techniques and methods used to obtain information on the electronic structure and optical properties of solid systems, that will be relevant for studying them within the frame of assessing their photovoltaic capability.

3.1 Quantum Mechanical calculations in solids

One key area that was not discussed regarding the implementation of the theories covered in the previous chapter was the choice of the *form* of Ψ (whether the Hartree-Fock electronic wavefunctions or the Kohn-Sham wavefunctions in DFT) and the mathematical functions that make it up – the *basis set* of eigenvectors for the TISE, our eigenequation. In the modelling of molecules in a vacuum, it is very common to use a basis set generated through the Linear Combination of Atomic Orbitals (LCAO): the finite number of elements in the molecule are each represented by a combination of basis functions dependent on their electronic configuration, and these are then combined to form the overall molecular energetic states. A number of additional factors, however, arise when describing the states of a crystalline solid, most notably that a solid can be described by a near-infinitely repeating units of atoms, and hence the description of every atom individually becomes a computational impossibility. All the quantum mechanical calculations in this thesis use the Vienna Ab initio Simulation Package (VASP) computational code, which implements a number of methods common to many solid-state QM codes that make the solution of the Schrodinger equation for solids tractable.[168–171]

3.1.1 Unit cells and periodic boundaries

The structure of crystalline solids are defined by their (conventional) *unit cell*, the lowest volume parallelopiped that contains lattice points at its vertices: as such, it reflects both the periodicity of the lattice, and the structural/chemical motif that is then repeated to create the structure. The lattice, and the structure itself, are

periodic, and are treated to repeat infinitely in each cell dimension. This periodicity provides a unique opportunity for calculations however – rather than treating each atom in the solid individually, instead we can calculate the wavefunction of just a single unit cell under the constraints of periodic boundary conditions, and this wavefunction can then be replicated identically for each cell to produce a wavefunction for the entire solid structure. This now allows the computationally tractable solution of solids and indeed VASP and all the calculations performed for this thesis use periodic DFT. This constraint does restrict our calculations to crystalline solids – for amorphous solids, which do not exhibit periodicity in the same way, other methods must be used. All crystal structures in this thesis were plotted using the aid of the program *VESTA*, designed by Momma and Izumi.[172]

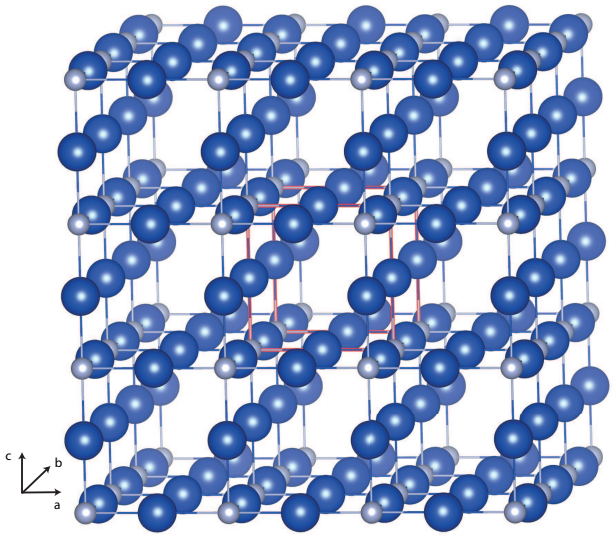

Figure 3.1: Crystal structure of Cu_3N, with Cu atoms in blue and N atoms in grey and the conventional unit cell is marked in red. Surrounding atoms and bonds are included to demonstrate the periodicity of the structure. The lattice vectors, $\mathbf{a}$, $\mathbf{b}$ and $\mathbf{c}$ are annotated – as Cu_3N possesses a cubic crystal structure (space group $Pm\bar{3}m$), these are all symmetry equivalent, and the cell shape can be described by a single lattice parameter, *a*.

3.1.2 The Reciprocal lattice, Bloch's Theorem and the Brillouin zone

Solid systems can be described using LCAO or similar methods to construct the wavefunction in terms of constituent atomic orbital basis sets, however periodicity can once again be exploited again to simplify and make calculations more efficient by instead describing the wavefunction as a combination of plane waves. To implement this, we first need to understand the concept of the *reciprocal lattice* and how it

embodies the periodicity of our real space lattice. If our real space lattice (assuming, for now, an orthorhombic lattice) is described by the lattice vectors **a**, **b** and **c**, then any particular translation between lattice points, $\mathbf{l}$ can be described by:

$$\mathbf{l} = l_x\mathbf{a} + l_y\mathbf{b} + l_z\mathbf{c} \tag{3.1}$$

where l_x, l_y and l_z are integers. If we wish to have a function that describes a physical property of the crystal system, such as the electron density, then that function must in itself be periodic – i.e. it must satisfy the equation:

$$f(\mathbf{r} + \mathbf{l}) = f(\mathbf{r}) \tag{3.2}$$

Periodic functions can also be written in terms of a Fourier series, a sum of sine and cosine waves that can be, via Euler's formula, expressed as a sum of complex exponentials; noting that **a**, **b** and **c** are the periods of the function in the x, y and z directions, we can then express $f(\mathbf{r})$ as (n_i being integer values):

$$f(\mathbf{r}) = f(\mathbf{r} + \mathbf{l}) = \sum_{n_x,n_y,n_z} A(n_x, n_y, n_z)e^{2\pi i(\frac{n_x x}{a} + \frac{n_y y}{b} + \frac{n_z z}{c})} \tag{3.3}$$

Instead, we can then express this series in terms of *reciprocal* lattice lengths, rather than our conventional, real-space unit cell parameters:

$$a^* = n_x\frac{2\pi}{a} \qquad b^* = n_y\frac{2\pi}{b} \qquad c^* = n_z\frac{2\pi}{c} \tag{3.4}$$

This then implies the existence of a *reciprocal lattice*, with any given reciprocal lattice vector translation, $\mathbf{k}$, in analogy to $\mathbf{l}$, given by the reciprocal lattice vectors, $\mathbf{a}^*$, $\mathbf{b}^*$ and $\mathbf{c}^*$:[†]

$$\mathbf{k} = n_x\mathbf{a}^* + n_y\mathbf{b}^* + n_z\mathbf{c}^* \tag{3.5}$$

[†]It is notable that the reciprocal lattice vectors have two separate definitions: here we use the definition that includes the factor of 2π, while in crystallography it is more common to define, for an orthorhombic system, $\mathbf{a}^* = \frac{1}{\mathbf{a}}$ while the factor of 2π remains in the exponential of the Fourier series; this crystallographic convention is also used when describing the coordinates of special $\mathbf{k}$-points in the Brillouin zone below. The fundamental meaning of these points, however, is unchanged.

This reciprocal lattice is itself periodic and has a number of properties that reflect those of the real-space lattice: its volume is inversely proportional to the real space lattice, and its lattice vectors are normal to a set of lattice planes in real space. This latter property is then key in crystallography, as the constructive interference of X-rays scattering from sets of lattice planes leads to Bragg peaks in a diffraction spectrum. These Bragg peaks are indexed according to the particular set of lattice planes from which they originate by Miller indices, which are necessarily identical to individual points on the reciprocal lattice. For example, the complete set of (100) Miller planes for an orthorhombic crystal corresponds to the point at $1\mathbf{a}^*$ on the reciprocal lattice. We can now write our Fourier series in terms of $\mathbf{k}$, also known as a wavevector:

$$f(\mathbf{r}) = \sum_k A(k) e^{i\mathbf{k}\cdot\mathbf{r}} \tag{3.6}$$

Our function expressed this way will still satisfy the periodicity criterion we given in Equation 3.2, so long as we realise that the dot product of $\mathbf{k}$ and $\mathbf{l}$ will give an integer multiple of 2π, and thus $e^{i\mathbf{k}\cdot\mathbf{l}}$ is unity:[173]

$$\begin{aligned} \mathbf{k}\cdot\mathbf{l} &= (k_x a^* l_x a + k_y b^* l_y b + k_z c^* l_z c) \\ &= \frac{2\pi n_x}{a} l_x k_x a + \frac{2\pi n_y}{b} l_y k_y b + \frac{2\pi n_z}{c} l_z k_z c \\ &= 2\pi \times [integer] \end{aligned} \tag{3.7}$$

$$f(\mathbf{r}+\mathbf{l}) = \sum_k A(k) e^{i\mathbf{k}\cdot(\mathbf{r}+\mathbf{l})} = \sum_k A(k) e^{i\mathbf{k}\cdot\mathbf{r}} e^{i\mathbf{k}\cdot\mathbf{l}} = \sum_k A(k) e^{i\mathbf{k}\cdot\mathbf{r}} = f(\mathbf{r}) \tag{3.8}$$

To extend this argument to a non-orthorhombic lattice, we only need to redefine the reciprocal lattice vectors as:

$$\mathbf{a}^* = 2\pi \frac{\mathbf{b}\times\mathbf{c}}{\mathbf{a}\cdot\mathbf{b}\times\mathbf{c}} \qquad \mathbf{b}^* = 2\pi \frac{\mathbf{c}\times\mathbf{a}}{\mathbf{b}\cdot\mathbf{c}\times\mathbf{a}} \qquad \mathbf{c}^* = 2\pi \frac{\mathbf{a}\times\mathbf{b}}{\mathbf{c}\cdot\mathbf{a}\times\mathbf{b}} \tag{3.9}$$

From these results, we can see that it is possible to define a periodic real-space function in terms of a reciprocal lattice vector, $\mathbf{k}$. We should now consider how this will apply to the representation of our basis set. The Schrodinger equation for our given crystalline solid must be invariant under a lattice translation – i.e. the

potential at a given position $\mathbf{r}$ must be the same as at the position $(\mathbf{r}+\mathbf{l})$. In 1928, Bloch showed in order to satisfy this condition, the wavefunction that satisfies the TISE can be defined by a wavevector $\mathbf{k}$ such that translation by a lattice vector, $\mathbf{l}$ is identical to multiplying by a phase factor $e^{i\mathbf{k}\cdot\mathbf{l}}$; where $\mathbf{k}$ itself belongs to the reciprocal lattice, then this is equivalent to multiplication by 1.[174] In practice, this means that an electronic state, or band, that still satisfies the TISE, with index n of a crystalline solid can be described by a Bloch wave: a periodic function $u(\mathbf{r})$, which is itself a Fourier series (as in 3.6) in a reciprocal lattice wavevector, $\mathbf{G}$, with the *same* periodicity as the real-space solid, combined with any plane wave $e^{i\mathbf{k}\cdot\mathbf{r}}$:

$$\psi_{n,\mathbf{k}} = u_{\mathbf{k}}(n,\mathbf{r})e^{i\mathbf{k}\cdot\mathbf{r}} = \sum_{G} A_{Gk}e^{i(\mathbf{G}+\mathbf{k}).\mathbf{r}} \tag{3.10}$$

Our energetic ground state, satisfying the TISE, is thus found by a sum over Bloch waves with the periodicity of the lattice that minimizes the total energy of the system. We can simplistically and qualitatively express how this wavefunction describes the system by noting that $u(\mathbf{r})$ contains the information describing the variation of potential *within* each unit cell, while $\mathbf{k}$ reflects the periodic phase relationship *between* cells. We should note here, that, as currently stated, our wavevector is not uniquely defined: as $\mathbf{k}$ has the same dimensions as the reciprocal lattice vectors, an identical solution is obtained for any wavevector $\mathbf{k}'$ that differs from $\mathbf{k}$ by integer units of the reciprocal lattice vectors. We can exploit the periodicity of the reciprocal lattice to this effect: if we note that $\mathbf{k}$ repeats every unit of $\frac{2\pi}{n}$ (with n one of the 3 lattice parameters), then all $\mathbf{k}'$ can be reduced to a certain point in the region of the reciprocal lattice such that:

$$-\frac{\pi}{n} < \mathbf{k} \leq \frac{\pi}{n} \tag{3.11}$$

This region is called the first *Brillouin Zone*, and by noting the above, we need only calculate $\mathbf{k}$-points within the Brillouin zone to obtain our wavefunctions for all $\mathbf{k}$. In practice there are still an infinite number of $\mathbf{k}$-points even in this reduced scheme for a perfect crystal, and so for practical computation, we approximate integration over the entire Brillouin zone by a sum of sampled, equally spaced $\mathbf{k}$-points. The total energy obtained using our set of $\mathbf{k}$-points (our $\mathbf{k}$-mesh) must thus be converged for each

system to ensure we are using a sufficiently dense $\mathbf{k}$-mesh to describe the energetics accurately. In all the calculations in this thesis, the $\mathbf{k}$-meshes were centred at Γ – the defined (0, 0, 0) point, or centre, of the reciprocal lattice (a unique property not shared by the real space lattice, where the assignment of an origin is somewhat arbitrary). As this point represents the completely in-phase interaction of a cell with its periodic images along all three reciprocal lattice vectors (or, alternatively, where the system in question can be described by a wave of infinite wavelength), Γ can often be the point at which energetic maxima and minima occur, and so its inclusion is often crucial for accurate electronic structures.

One of the key benefits of using a basis set of plane waves over atom-centred basis sets is that the only other adjustable parameter to be converged is then the *energy cutoff*. We note that the energy of the plane waves used to construct $u_{\mathbf{k}}(n, \mathbf{r})$ are defined by the relation for a free electron wave:

$$E_G = \frac{\hbar^2 |\mathbf{G}|^2}{2m} \tag{3.12}$$

Like $\mathbf{k}$, there are infinite allowed $\mathbf{G}$ vectors, and higher energy plane waves allow the description of more rapid variations in potential, although as E_G increases, the respective coefficients in the Fourier series A_{Gk}, decrease and their contribution is lessened. Thus, to avoid an infinite sum of plane waves of increasing energies being used to describe our periodic potential in $u_{\mathbf{k}}(n, \mathbf{r})$, a cutoff in E_G is enforced, with energies above this not used to ensure the calculation is tractable. In practice, the energy cutoff is dependent on the particular elements used in the structure and the potentials they generate; like the $\mathbf{k}$-mesh, it must be converged to ensure accurate calculations. In the calculations in this thesis unless otherwise specified, the energy cutoff was converged for each system such that the total energy differed by no more than 10 meV per atom, while the $\mathbf{k}$-mesh convergence criterion was 1 meV per atom; in general, convergence to this extent would result in no change to the electronic structure on further increase in basis. Having only 2 such parameters to converge is highly favourable in comparison to multiple parameters in atom-centred basis sets. Other advantageous properties of plane wave basis sets for solids include efficient calculations and a broad applicability to a variety of systems – the plane wave description is independent of the particular atoms within the unit cell.

3.1.3 Core electrons and Pseudopotentials

One area that plane waves are less efficient at describing are core electrons in atoms: close to the nucleus, the wavefunctions of core electrons oscillate far more than those of valence electron states, and often have multiple nodes. In order to describe these states, numerous, very high energy plane waves would be needed to fit such oscillations in $u_{\mathbf{k}}(n, \mathbf{r})$, making the calculation of the wavefunction very difficult. A number of solutions have been proposed to alleviate this – VASP uses the projector-augmented wave (PAW) method,[175] which combines elements of the *pseudopotential* and *augmented plane wave* methods. The pseudopotential method involves replacing the core potential in the Schrodinger equation by a smoothly varying function that has fewer nodes than the true potential – by doing so, the core is treated as 'frozen', and essentially treated together with the nucleus and not calculated explicitly; the valence electrons, now smoothly varying, are computationally inexpensive to calculate, and feel the same approximate effect from the core potential through the pseudopotential. By removing this information, pseudopotentials must be carefully fitted for individual elements, and often demonstrate poorer accuracy. A diagrammatic representation of this treatment is included in Figure 3.2.

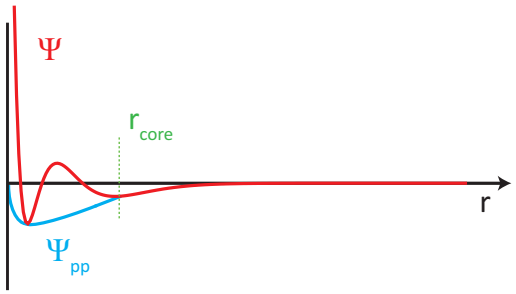

Figure 3.2: Illustrative depiction of how pseudopotential methods describe the wavefunction of valence electrons within the core region (r_{core}). Ψ represents the 'true' form of the wavefunction, while Ψ_{pp} is the pseudopotential that replaces the potential within the core region.

The augmented plane wave method directly separates the structure into 'core' and 'interstitial' regions: the wavefunction in the core is usually described by symmetric 'muffin-tin potentials' while between the spheres representing the ion cores, plane waves are used to describe the potential of the interstitial region. As such, two separate functions are used, and a continuous transition between the core and interstitial regions must be established. The resulting wavefunction is expensive to

calculate, especially for heavy atoms, as all the electrons are calculated explicitly, but the method can be highly accurate. The PAW method, however, compromises between the two by retaining the use of pseudopotentials but also calculating the overlap integral of each valence partial wavefunction by a radial 'projector' function, which augments the wavefunction within the core region, giving it the same scattering properties as an all-electron potential, while retaining the form of a plane wave. It has been shown that the accuracy of all-electron methods can be replicated with pseudopotential-like cost using the PAW method, making it a powerful computational method.[176]

3.1.4 Structural relaxation

When preparing to perform calculations on a system, some method must be used for finding a starting nuclear configuration within the unit cell, from which to start the electronic SCF cycles, whether using HF or DFT methods. In practice, *ab initio* crystal structure prediction methods are still very much an active area of development, and are as yet still quite complex and expensive to perform, especially for the more complex stoichiometries present in some emerging PV materials. As such, we still rely on experimental methods as our source for unit cell information, through databases such as the Inorganic Crystal Structure Database (ICSD) which contains records of crystallographic data on the majority of experimentally determined or refined inorganic crystal structures in prior literature, usually determined through X-ray, neutron or electron diffraction. Usually, these records are reliable and accurate measurements of such structures, and hence are a reliable starting configuration that reflects the reality of how the given compound crystallizes. However, these crystal structures are usually determined at or near room temperature and ambient conditions, whereas *ab initio* calculations are attempting to predict the equilibrium ground state of the material, in the absence of any temperature – the structure of a given compound under these two conditions can be very different. So, before electronic structure calculations for the purposes of the methods below are performed, the structure must first be *relaxed*, that is finding the equilibrium geometry by calculating the residual forces on each atom in the unit cell, and perturbing the atoms slightly to reduce these forces, then recalculating the forces and continuing until they are within a certain threshold.

The force for a given nuclear coordinate, q are given by the negative derivative of the system energy with respect to that coordinate, as in the first equality of Equation 3.13. To avoid a potentially complicated perturbation of the system along every possible nuclear coordinate to obtain the forces, we can instead use the Hellmann-Feynman theorem. If the wavefunction, ψ, is variational, which it is for both HF and DFT, then all the following equalities hold:

$$\mathbf{F}_q = -\frac{\partial E(\mathbf{r})}{\partial q} = -\frac{\partial \langle \psi(\mathbf{r}) | \hat{H}(\mathbf{r}) | \psi(\mathbf{r}) \rangle}{\partial q} = -\langle \psi | \frac{\partial \hat{H}(\mathbf{r})}{\partial q} | \psi \rangle \tag{3.13}$$

This is due to the derivatives of ψ with respect to q reducing to 0, leaving solely the derivative of $\hat{H}$, which is tractable and fixed for the given Hamiltonian we are using – this means we solely need the wavefunctions that we have obtained in the SCF cycle to determine the forces in an efficient manner. The Hellmann-Feynman theorem also holds for the derivative with respect to any general parameter, so can be extended to the derivative with respect to the strain tensor to also give the stress tensor. Calculating the external stresses on the unit cell in this way also allows the relaxation of the unit cell dimensions, shape and volume as well as the atoms within, allowing the complete determination of the equilibrium unit cell over the course of multiple relaxation steps (each requiring an SCF cycle) by the minimisation of both forces and stresses. The method by which the atomic perturbations are chosen in each relaxation step to reduce the forces overall is a gradient optimization problem, and are determined by algorithms integrated in VASP; while multiple algorithms are available, all the structures in this thesis were relaxed using one of either the quasi-Newton-Raphson RMM-DIIS or conjugate-gradient algorithms.[177] Unless otherwise specified, the convergence criterion for geometric relaxations for calculations in this thesis was that the forces be below 0.01 eV Å^{-1} on each atom.

One issue that arises during the full relaxation (including the change of cell volume) of structures using a plane-wave basis set is *Pulay stress*. When the volume of the cell changes during the relaxation, the basis set is no longer complete, and this results in small errors in the stress tensor unless complete convergence has already been obtained with respect to the basis set – these errors are referred to as Pulay stress.[178] There are two approaches to reducing this error: either one can perform a number of fixed-volume relaxations and then fit the total energies to an equation

of state to obtain the equilibrium volume; alternatively, one can ensure that the energy cutoff during the relaxation is much larger than that required to generally converge the total energy, in which case the Pulay errors become negligible. In all the relaxations in this thesis, the latter approach was used, and so the cutoff energy was increased by 30 % to 40 % during the relaxation on top of the converged cutoff stated.

3.2 Electronic Structure Methods

Once the equilibrium geometry of a material is found, the electronic structure can then be calculated and characterised to obtain a number of different properties and relationships, many of which can be highly useful in determining a compound's suitability for use in photovoltaic devices.

3.2.1 Density of States

The density of states (DOS) is a measure of the number of energy levels, or states that occur within an infinitesimal energy range – between E and E + dE – per unit of volume of a sample. It is generally spherically averaged, and so it is simply a measure of relatively how many electronic states in the bulk system are within that given energy range, with no specific information as to directionality within real space. The DOS can however give some qualitative insight into the energetics and bonding of a material: highly localized states with minimal interaction with other electronic states will manifest as narrow, intense peaks in a DOS, reflecting a high density of bands with minimal dispersion, while strong hybridization or interaction between states will result in a wide, flatter DOS, reflecting that such bands will vary greatly in energy with $\mathbf{k}$ and be highly disperse. The formulation of the DOS is given by the following summation over all $\mathbf{k}$, with the Kronecker delta being 0 if the state n is not within the infinitesimal range, and 1 if it is:

$$D(E) = \frac{1}{4\pi^3} \sum_n \int \delta(E - E_n(\mathbf{k}))d\mathbf{k} \tag{3.14}$$

In additional to the total density of states, VASP can also calculate the partial

projected densities of states for each atom and orbital within the unit cell. This is done by projecting the calculated wavefunction within a given Wigner-Seitz radius (that essentially defines the volume of the total cell occupied by each atom) onto the spherical harmonics for that atom – in essence comparing the overall density to that of atomic orbitals. This is a qualitative comparison without any external reference, and does have a degree of error to the apportioning of charge, but is valuable to allow use to determine the dominant character of particular bands or energy ranges. For example, the DOS of the semiconductor compound Cu_3N is included in Figure 3.3, with the most dominant partial DOS marked. The valence band appears to be dominated by Cu d and N p states, which corresponds with the highest energy occupied orbitals in the Cu^+ and N^{3-} ions. It also displays the effect of bonding – as the Cu ions are linearly coordinated to N in the anti-ReO_3 structure of Cu_3N, we might expect from a symmetry perspective that only one of the d-orbitals per Cu will interact strongly with the N p, while the remainder remain non-bonding (a similar bonding argument is considered for AgCuS in Section 5.1). The non-bonding Cu d orbitals form the large peaks around -3 eV, while the d_{z^2} or $d_{x^2-y^2}$ (depending on the definition of the cartesian axes) hybridizes with the N p and forms the top of the valence band, making a more disperse and wide DOS.

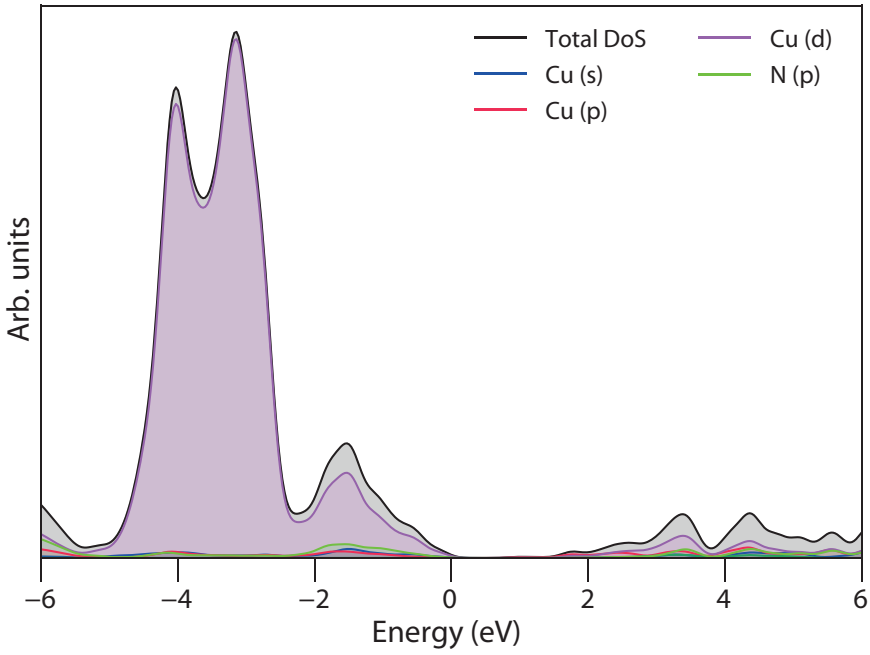

Figure 3.3: Total and Partial Density of States diagrams of Cu_3N, calculated with the HSE06 functional. Energy $= 0$ eV is set to valence band maximum.

All the DOS depicted in this thesis display some smearing in energy – this is a result of the method used to determine the occupancies of the bands. Unless otherwise discussed, a Gaussian smearing of 0.2 eV width is used for the DOSes displayed, which helps to replicate some of the spectral broadening that would be present in any experimental result, but also to improve legibility, albeit at the cost of some accuracy. Given the relatively qualitative information garnered from the DOS, this loss in accuracy was judged to be acceptable.

3.2.2 Band structure

Another crucial representation of the electronic structure of a solid is the depiction as a plot of band energies in $\mathbf{k}$-space – the electronic band structure. The ultimate goal of electronic structure prediction may be to be able to plot band energies across the entirety of $\mathbf{k}$-space within the first Brillouin zone, and thus be able to pinpoint each band's energy for any $\mathbf{k}$-point and a full description of the band dispersions along any reciprocal direction. In practice, calculating this would be very expensive without providing much additional information, while plotting a 3D surface for multiple bands becomes highly complex and difficult to plot. As such, electronic band structures are generally shown as a two-dimensional plot of band energy against $\mathbf{k}$, with $\mathbf{k}$ following a path between the 'high-symmetry' $\mathbf{k}$-points for the given Bravais lattice of the material; these special $\mathbf{k}$-points lie on the vertices or centres of faces of the Brillouin zone, and are positions at which the wavefunction is invariant under certain symmetry operations of the crystal; for example, in the Brillouin zone of a face-centred cubic cell, there are 8 'L'-points, each lying in the centre of one face, which are related to each other through 4-fold rotation axes and so are equivalent. As the wavefunction describing such a system obey the symmetry relations of the cell (in the absence of any symmetry-breaking mechanism), the energy of a band at one 'L' point will be the same as at the others.

We can rationalise, from a tight-binding perspective, that these special $\mathbf{k}$-points also tend to represent the maximal and minimal interactions in terms of bonding, and so represent the greatest difference in *orbital* periodicity: to demonstrate this, we can consider a hypothetical 1D chain of H atoms, with one atom in the centre of each unit cell, with length a. At $\mathbf{k} = 0$, the plane wave that could describe the

wavefunction of the valence electron has infinite wavelength, and so corresponds to an LCAO description in which $1s$ atomic orbitals on all the H atoms interact in-phase with each other, and so represents the maximal bonding interaction for those states. At $\mathbf{k} = \frac{\pi}{a}$ (the 1D Brillouin zone boundary), however, the wavefunction now has a periodicity of one unit-cell length, and so corresponds to an LCAO picture where alternate $1s$ orbitals are out of phase with each other – the most anti-bonding configuration for those states.

The $\mathbf{k}$-points between these points are also calculated to then provide a description of the band dispersion – the curvature of the band variation between points – and have to be sampled at a relatively high density to produce a smooth band structure. For some structures, band maxima or minima will lie on the path between high-symmetry points – this is more likely to occur for particularly low-symmetry or complex structures, but can occur in any (for example, the conduction band minimum of silicon). So, the band structure path is chosen to maximise the number of points, and paths between them, albeit at the balance of remaining cost effective, as the greater number of $\mathbf{k}$-points calculated, the more expensive the calculation. The high-symmetry points and their labels used for each Bravais lattice in this thesis are taken from Bradley and Cracknell[179] – a full list of the Brillouin zones and point definitions are included in the Appendix.

An example of a semiconductor band structure, again of Cu_3N, is depicted in Figure 3.3, calculated using the HSE06 functional, and we shall discuss here some of the key features that can be extracted from such a diagram. The valence band is depicted in blue, while the conduction band is in orange – this representation will be consistently used for the band structures in this thesis. As discussed in Section 1.2.5, our key interest in the electronic band structure, when in the context of assessing materials for potential use in photovoltaics, is examining the band edges, the magnitude of the band gap, and whether it is direct or not – all of which will impact strongly on a materials ability to absorb light. Like the DOS, due to the lack of a definitive Fermi level position, we align the band structure such that the valence band maximum is at 0 eV in energy.

Using Cu_3N as an example, we can examine what information a band structure can give us: the maximum in the valence band occurs at the R point – (0.5, 0.5, 0.5)

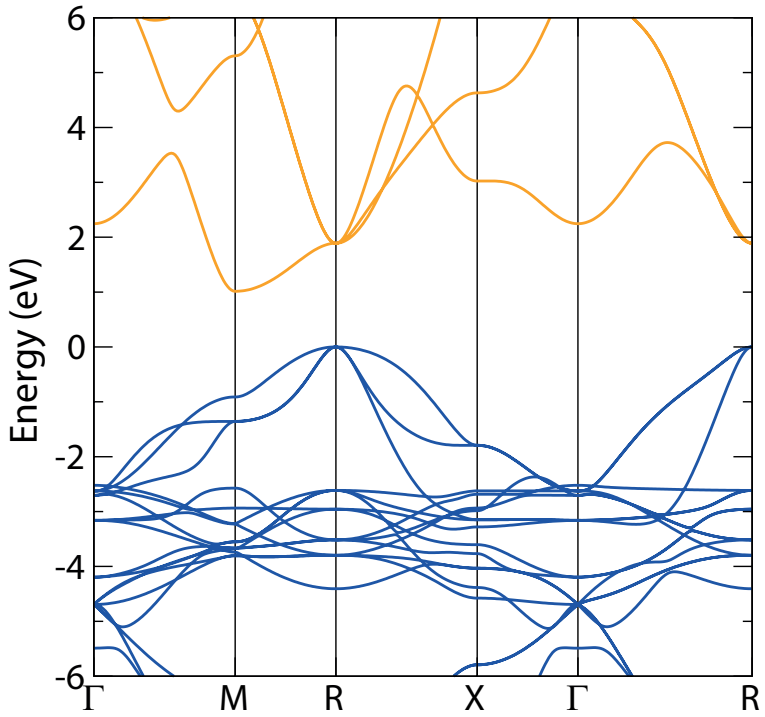

Figure 3.4: HSE06 electronic band structure of Cu_3N with valence band in blue, and conduction band in orange. Valence band maximum (VBM) is set to 0 eV.

in reciprocal space coordinates – which would be consistent with the fully antiphase interaction between N p in neighbouring cells in all 3 dimensions, connected via Cu d. The top three occupied bands (between 0 eV to -2 eV) are relatively disperse, showing high curvatures. This contrasts with the set of bands around -3 eV, which are relatively densely packed and flat – as predicted from the DOS above, these appear to be the bands composed from the non-bonding Cu d states, and so show localized behaviour and low dispersion. The conduction band minimum occurs at the M point instead (0.5, 0.5, 0), making Cu_3N an indirect semiconductor, and the conduction band in general shows significant dispersion. As discussed in Section 1.2.5, indirect semiconductors demonstrate much weaker absorption of photons, due to the necessary intercession of a phonon to conserve the change in crystal momentum (the change in $\mathbf{k}$), although strong absorption can occur if a direct transition of higher, but close, in energy is available. In Cu_3N, the indirect gap predicted with HSE06 is 1.01 eV while the lowest direct VB to CB transition occurs at a point along the R–M path, with energy 1.73 eV. While this $>$0.6 eV separation is not ideal, it does mean that Cu_3N could strongly absorb within the visible region of the EM spectrum; this information is valuable for predicting such microscopic

properties, but is also useful on a wider scale, aiding to explain why a particular material is a strong, appropriate absorber.

3.2.3 Carrier Effective massses

Band edge information is not the only valuable information that can be derived from an electronic band structure. Above, we discussed the relative dispersion of different bands in a structure, and how localized states tend to have lower dispersion, or less curvature, of the bands that describe them. We can also view this quantitatively through the concept of effective mass: above, we noted that the basis set for our solid state QM calculations can be constructed from the product of a periodic potential and plane waves, and as such our resultant bands will share some qualities with those of free-electron waves ($e^{\mathbf{k}\cdot\mathbf{r}}$), including resembling their shape. The relationship between E and $\mathbf{k}$ for a free-electron plane wave is well defined in terms of the electron mass, as a model quantum system:

$$E(\mathbf{k}) = \frac{\hbar^2\mathbf{k}^2}{2m_e} \tag{3.15}$$

Differentiating this expression twice with respect to $\mathbf{k}$, we can obtain:

$$\frac{d^2E(\mathbf{k})}{d\mathbf{k}^2} = \frac{\hbar^2}{m_e} \tag{3.16}$$

We can see that this now gives the electron mass directly as the reciprocal of the second derivative, or curvature, of the E-$\mathbf{k}$ relationship. By equating the bands in our band structure to parabolic free-electron waves such as the above, we can calculate the *effective* electron mass within the band when the curvature of a particular band is numerically determined from our determined eigenvalues. A more disperse band with high curvature will thus have a lower electron effective mass, while a flatter band will have a high electron effective mass – we can further relate this to electron transport properties by noting the classical relationship between mass and mobility, μ:

$$\mu = \frac{qt_e}{m_e} \tag{3.17}$$

where t_e is the electron scattering time (this is highly dependent on the carrier and defect concentrations in a sample – for our static electronic structure calculations, it is effectively constant) and q is the elementary charge. In this way, a lower effective mass for a given band will generally lead to a higher carrier mobility; for photovoltaics, as discussed in Section 1.2.5, a high carrier mobility is desirable as it will facilitate electron hole separation and improve device characteristics. We can calculate effective masses for holes in the valence band similarly, with the holes acting as electrons but with negative effective masses due to the inverted curvature of the valence band edge. In general, we are most interested in the effective masses at the VBM and CBM, and so to obtain numerical electron and hole effective masses, we fit this parabolic behaviour to the few $\mathbf{k}$-points closest to the VBM or CBM along each dimension in $\mathbf{k}$-space, and obtain values in units of m_0, the mass of an electron in the free-electron wave (in a vacuum, with no external potential). We can also establish the relative directionality of the likely carrier mobility: the effective masses can either be isotropic, such as the hole effective masses in Cu_3N which are all $\sim$0.2 m_0, or anisotropic. The electron effective masses in Cu_3N are the latter, with the conduction band showing much higher curvature along the M to Γ direction than M to R, and this is reflected in the values of the effective masses, which are $0.16\,m_0$ and $1.60\,m_0$ respectively. In real space (noting that for a cubic system, $\mathbf{a}$ and $\mathbf{a}^*$ correspond to the same direction), this suggests that electron mobility could be poorer along the individual dimensions than towards the diagonal faces of the Cu_3N crystal.

3.2.4 Band Alignment

A disadvantage of periodic DFT calculations is the lack of any external reference energy, and so in VASP, all eigenvalues for a bulk calculation are given with respect to an assumed Fermi level mid-gap. This does mean that without a second calculation, while the levels of the conduction and valence bands are consistent with respect to each other, we do not know their position with respect to the vacuum level, which is necessary for the determination of the ionization potential (IP) and electronic affinity (EA). These measures of band position are themselves crucial for aligning a photovoltaic absorber with partner layers – if, for example, the conduction band of our absorber layer lay significantly lower in energy than that of a neighbouring

TCO layer in a hypothetical cell, then there will be a large thermodynamic barrier for the carrier electrons to transfer into the TCO and the cell resistance will be very high, limiting performance. If we know the relative conduction band positions of the absorber and TCO however, we can select a more suitable partner layer, as discussed in Section 1.2.5. Comparing ionization potentials and electron affinities is useful as a first approximation for determining band alignments of cell layers – alignment could be determined more accurately by constructing a heterojunction of the given material with any candidate partner layers and examining the band bending at the junction, however this can become highly computationally expensive due to structural reconstructions at the interface. As the work in this thesis primarily deals with the first screening of materials for use as solar absorbers, however, this simple alignment with literature values is usually of sufficient accuracy to aid in cell development.

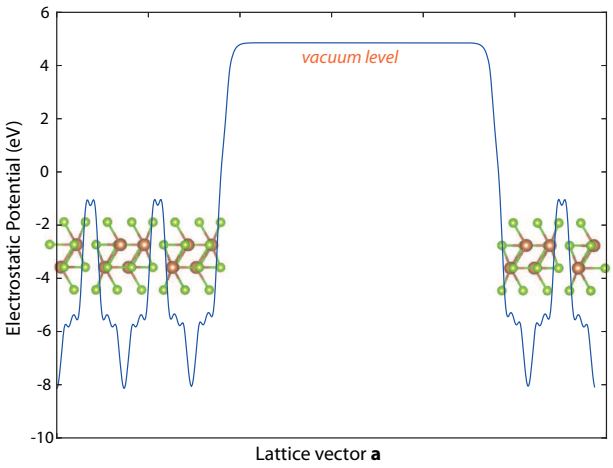

Figure 3.5: Electrostatic potential of a slab model of Sb_2Se_3 with **a** used as the dimension extended for the construction of a supercell. The plateau in the electrostatic potential represents the simulated vacuum level relative to the eigenvalues in the calculation. The crystal structure is underlaid to demonstrate how the atomic positions give rise to the variation in the electrostatic potential.

To obtain the band alignment of a material to the vacuum, we must perform a *slab* calculation, in which we include both a section of the crystal structure and then a large volume of empty space within the unit cell to be calculated, forming a 2D slab of solid surrounded by vacuum along one side. As periodicity is enforced, there are an infinite number of stacked slabs, however the volume of vacuum is chosen such that there are negligible interactions between a slab and its periodic image (usually this requires ∼30 Å separation between slabs). The electrostatic potential should

plateau in the vacuum space, as seen in Figure 3.5, and while the slab valence band energy is not meaningful due to the presence of the surface termination, this plateau can be compared in energy to the energy of a chosen core state on an atom that is deep in the slab, to approximate 'bulk-like' behaviour. The vacuum-core level separation can then be compared to the VBM-core level separation from the bulk calculation to obtain the vacuum-VBM separation, which is the ionization potential of the bulk:

$$\mathrm{IP} = E_{\mathrm{vac}} - E_{\mathrm{VBM,\ bulk}} = (E_{\mathrm{vac}} - E_{\mathrm{core,\ slab}}) - (E_{\mathrm{VBM,\ bulk}} - E_{\mathrm{core,\ bulk}}) \quad (3.18)$$

The EA can then be approximated by using the fundamental Kohn-Sham band gap in the equation E_g = IP - EA. This core-level alignment method was developed by Wei and Zunger,[180] and is used for all band alignments in this thesis. The planar average of the electrostatic potential calculated by VASP is obtained using the PlanarAverage code as part of the MacroDensity package produced by Butler *et al.*[181,182]

3.3 Optical Methods

In the previous section, we have discussed the methods, and valuable information that they can provide, that describe the static electronic structure of a solid semiconductor. Just as important for an optimal absorber material in a solar cell, however, are the optical properties – the material must be able to strongly and efficiently absorb light, ideally across as much of the IR and visible spectrum as possible, to most efficiently harvest the incident light onto the solar cell and be able to convert that energy into an electrical current. In actuality, truly accurate calculations of optical properties and treatment of excited states necessitates moving beyond the single-particle theories discussed so far towards many-body techniques, such as the Bethe-Salpeter equation.[183] In practice, however, these methods remain very computationally intensive for any solid system beyond the most simple unit cells, and so instead we can obtain moderately accurate optical properties through the calculation of the static dielectric matrix from the ground state eigenvalues alone.

3.3.1 Dielectric Spectra

Obtaining the dielectric matrix, the response of a material to an electric field (ϵ), requires the calculation of the microscopic energy-dependent polarizability of the system and also the electronic transition dipole moments between valence and conduction band states. The method by which this is done within the PAW formalism used by VASP is not trivial, and its original implementation is discussed thoroughly in Gajdoš *et al.*[184] The calculation of the transition dipole matrix elements however, is of interest due to their proportional relationship to the transition probability (here from valence state 'v' to conduction state 'c') as given by Fermi's golden rule:

$$P_{vc} = \frac{2\pi}{\hbar} |\langle \psi_c | \tau | \psi_v \rangle|^2 D(E_c) \tag{3.19}$$

where τ is the transition dipole moment operator, and $D(E_c)$ the density of states in the conduction band. Through the calculation of these transition dipole moment magnitudes/amplitudes, we can see whether certain valence to conduction band features are allowed (high transition probability) or forbidden (formally $P_vc = 0$, although a proportionally very small matrix element will essentially be forbidden), which is crucial for the absorption at that energy. Often, transitions are forbidden due to symmetric constraints on the wavefunction (for example, the Laporte selection rule in atomic spectroscopy), and such symmetry forbidden transitions will require the intercession of some perturbation to break the symmetry and become allowed. This reduction in probability means that direct, but forbidden transitions can be as detrimental to optimal absorption in a photovoltaic semiconductor as an indirect gap. We note here that the method of Gajdoš *et al.* only concerns contributions from direct (same $\mathbf{k}$) interband transitions, as the inclusion of indirect transitions would require additional perturbations. Due to the greatly reduced probability of indirect transitions, this is a reasonable omission, especially for thin films of materials, and excellent qualitative agreement to experiment can be achieved, even in indirect semiconductors such as Cu_3N.[185]

Perhaps the most important derivable optical property however is the attenuation or absorption coefficient, α, which is the primary indicator of the strength of optical absorption as a function of the incident photon energy. α itself is a measure of the

reciprocal of the penetration depth of radiation into a sample; as the penetration depth will be shorter for a more absorbing material, a higher absorption coefficient corresponds to a material that absorbs light more strongly. As discussed in Section 1.2.5, for an optimal photovoltaic material, an absorption coefficient of the order of 10×10^4 cm^{-1}, or better 10×10^5 cm^{-1}, would be considered strongly absorbing and so suitable for thin-film applications. It is also generally desirable for the absorption coefficient to be highly absorbing within the smallest energy delay above the band gap as possible, leading to a sharp absorption edge. The absorption coefficient is calculated from the dielectric through the following relationship to the complex refractive index, n:

$$n = n' + in'' = \frac{(\epsilon' + i\epsilon'')}{\epsilon_0} \qquad \alpha(E) = \frac{4\pi n''}{\lambda} \tag{3.20}$$

where ϵ_0 is the permittivity of free space and λ is the wavelength of energy considered.

3.3.2 SLME

Spectroscopic Limited Maximum Efficiency (SLME) is a metric recently proposed by Yu and Zunger for the screening of photovoltaic absorbers using first principles calculations,[186,187] and presents an interesting tool for use in the studies in this thesis as a numerical comparison of the materials studied in terms of their intrinsic properties. The Shockley Queisser limit was discussed in Section 1.2.4 as a theoretical thermodynamic limit on the efficiency of single junction solar cells as a function of the absorber's band gap. SLME mostly follows the 'detail balance' thermodynamic formalism of the SQ limit, although it differs in two key areas where assumptions are made regarding the optical behaviour of the absorber in question.

The first of these is in the treatment of recombination: in the original SQ method, factors representing the transmission and the effect of non-radiative recombination are combined into a single factor – while Shockley and Queisser considered the effect of multiple values of this factor, the limit is most often quoted in the highest efficiency limit, where this factor is 1, representing perfect blackbody behaviour of the absorber and solely radiative recombination. For direct band gap materials such

as GaAs, this is a reasonable assumption, however in materials where the direct gap is forbidden or with an indirect fundamental gap, as discussed in Section 1.2.3, radiative recombination can be much more limited and other recombination pathways such as Shockley-Read-Hall or Auger recombination can make up a much larger proportion of losses. As a result of greater non-radiative recombination, the efficiency will be reduced from the SQ limit. SLME accounts for this non-radiative recombination by treating the fraction of total electron-hole recombination that is radiative (f_r) as:

$$f_r = e^{-\Delta/k_B T} \tag{3.21}$$

where k_B is the Boltzmann constant, T, the temperature, and Δ is the difference between the lowest direct allowed transition (E_g^{da}) and the fundamental band gap (E_g). For allowed direct-gap materials, $\Delta = 0$ and $f_r = 1$, restoring the radiative limit; for $\Delta > 0$, f_r is reduced, and non-radiative recombination is increased. As the non-radiative recombination increases, the SLME reduces, representing the increased total recombination (from both radiative and non-radiative sources) impacting the overall available charge carrier concentration, and thus the reduction of the short-circuit current.

The second adjustment present in SLME relates to the photon absorptivity, $a(E)$, which is essentially identical to the external quantum efficiency. In the SQ limit, this is treated as a step-wise function, with 0 below the band gap and 1 above, with the absorber behaving as a perfect blackbody. In SLME, it is instead approximated by Beer-Lambert behaviour, with the absorptivity being a function of both the calculated absorption coefficient, $\alpha(E)$, and the thickness of the material, L:

$$a(E) = 1 - e^{-2\alpha(E)L} \tag{3.22}$$

A stronger absorption coefficient will tend to have a lower overall exponential factor, and thus draw closer to black body behaviour above the band gap (with a(E) still 0 below the band gap, as in our calculations, there is no sub-gap absorption and so $\alpha(E)$ is also 0). The inclusion of the material dependent optical absorption in SLME further helps to distinguish between absorbers which, although possessing the same band gap, will actually be hampered by optical losses in actual applications.

Overall, SLME is a useful tool for the theoretical examination of potential thin-film solar absorbers due to the inclusion of intrinsic properties (band gap nature, absorption coefficient) into the impact on potential cell efficiencies. SLME is still far from a perfect theoretical model of cell efficiency, however: like the SQ limit, SLME does not address defect properties, and the large effects they can have on both carrier mobilities and recombination in real systems; there is also no treatment of interfaces between layers in the cell and the potential series resistance that can occur. Very recently, Blank *et al.* have detailed how the lack of inclusion of the refractive index in SLME oversimplifies the relationship between internal properties such as α and the external efficiencies that would be experienced in devices.[188] Nevertheless, SLME's usefulness lies as a screening metric: it is inexpensive (purely relying on calculable static optical properties), does not rely on empirical models (and thus is useful for emergent materials on which there is often little prior characterization or study in the literature and is particular applicable to thin-film absorbers, where optical losses from, for example, indirect gap behaviour, can be severe.

3.4 Ab Initio Point Defect Calculations

As has been mentioned in both this and the previous chapter, the defect behaviour of photovoltaic absorbers can be critical to their electronic, optical and transport properties, and thus have significant impact on their behaviour within a photovoltaic device. While the affected properties such as carrier lifetimes and concentrations or conductivity can often be recorded easily through multiple experimental characterization methods, the intrinsic thermodynamics of defect levels and their formation can be difficult to probe without specific spectroscopic techniques such as Deep Level Transient Spectroscopy (DLTS). Theoretical methods, however, can allow the calculation of defect thermodynamics within relatively simple formalism: while defect formations have been calculated using cluster-based semi-empirical methods since the pioneering work of Mott and Littleton in the 1930's,[189] more recently a formalism for the *ab initio* calculation of defects in semiconductors has been developed using supercells.[190–193]

In a typical semiconductor, defects will always be present, albeit usually in low concentrations and distributed randomly through a pure sample. To attempt to mimic

this distribution in a calculation, a supercell (an expansion of the unit cell by an integer multiple in any of the three cell dimensions, and which is still periodic) can be constructed and a defect constructed within. The ideal is for the defect within to simulate the concentration in the bulk and not interact with any neighbouring periodic image – in practice, however, the size of supercells manageable even under inexpensive *ab initio* methods (<500 atoms) usually do not eliminate such interactions altogether, and corrections must be made to recreate the dilute limit.

In reality, the formation of a defect, like any thermodynamic process, is governed by the Gibbs free energy ($\Delta_f G = \Delta_f H$ - T$\Delta_f S$), although a number of approximations reduce this. Firstly, *ab initio* calculations are *athermal*, and in the absence of any temperature, the entropic contribution is negated – this is often small under typical, dilute defect concentrations at room temperature regardless. Secondly, another implicit approximation often made for *ab initio* thermodynamics of solids is that the work done by changes in pressure and volume are negligible and so $\Delta_f H \approx \Delta_f E$, the change in internal energy, which is the total energy that we can calculate through DFT. The energy of the defective supercell can be compared with that of the pristine bulk, to obtain a formation energy, as detailed below.

Unlike the formalism of Kröger and Vink, defect formation is not necessarily treated in terms of balanced equations, instead the formation of defects is treated through a grand canonical description – through the removal and addition of atoms and electrons with an external reservoir. The notation of defect charge states, using the value q, is equivalent to Kröger-Vink: a neutral defect has $q = 0$, while if an electron is added to the defect site $q = -1$, and if an electron is removed to the external reservoir, $q = +1$. Equally, the three major types of intrinsic point defect use similar notation, e.g. in our sample semiconductor Sb_2Se_3: a selenium *vacancy* is given by V_{Se}, a *substitutional* defect of a selenium atom on an antimony site in the structure is given as Se_{Sb}, and an antimony atom in an *interstitial* position in the structure, Sb_i. In Sb_2Se_3 there are two crystallographically distinct antimony sites, with differing symmetries, and so defects on these sites are distinguished using a superscript: Se^1_{Sb} and Se^2_{Sb} are selenium on the first and second antimony sites respectively.

3.4.1 Thermodynamic formalism

The formation energy of a defect X in charge state q is given by:

$$\Delta_f E(q) = [E_X(q) - E_H] + q(E_H^{VBM} + \Delta E_F + \Delta V_{el}) + \sum_i n_i(E_i^0 + \Delta\mu_i) + E_{corr} \tag{3.23}$$

Together, these terms represent the overall free energy change on defect formation, and will be discussed individually. The first term is the energy change between the defective supercell (E_X^q) and a pristine (non-defective) bulk supercell of the same cell dimensions, E_H. The second is then the change in chemical potential (molar free energy) of the electrons being exchanged; the chemical potential of the electron is given by the Fermi energy, E_F, which for our calculations is defined in reference to the host valence band energy, E_H^{VBM}, such that $\Delta E_F = E_F - E_H^{VBM}$ (ΔV_{el} is one of the correction terms, associated with the change in electrostatic potential for a charged defect, and is discussed below). The third term represents the exchange of n atoms of element i with the reservoir (noting that $n_i > 0$ for atoms *removed* from, and $n_i < 0$ for atoms *added* to the host when the defect forms), where E_i^0 are the calculated elemental reference energies (i.e. the elements at 0 K), and $\Delta\mu_i$ are the elemental chemical potentials (defined with respect to those elemental references) under which the material is formed, i.e. its growth conditions. The final term, E_{corr} then covers the final corrections, band-filling and image charge, to recreate a dilute limit. Both of these last two terms will be discussed in greater detail in the following sections. We can also note that in the case of neutral defects, equation 3.23 is simplified:

$$\Delta_f E(q = 0) = [E_X^0 - E_H] + \sum_i n_i(E_i + \Delta\mu_i) + E_{corr} \tag{3.24}$$

This has the important implication that neutral defects have no dependence on Fermi level position, and that their formation solely depends on the chemical potential environment.

3.4.2 Chemical Potential Limits

We can note that there are two major variables in Equation 3.23: ΔE_F and $\Delta\mu_i$ under which our defect formation energies can vary. The latter of these, the elemental chemical potentials are together actually an N-dimensional variable, where N is the number of different elements in the system at hand. As such, describing defect formation thermodynamics as a full function of $\Delta\mu_i$ is rarely done, instead it is customary to solely treat the limits of the chemical potential space under which the system in question is formable; usually these limits resolve to be the most n or p-type conditions for the semiconductor, and thus are generally the most useful for real-world applications. To calculate these limits, we must consider the elemental chemical potentials when bounded by the formation of the standard elemental states and the formation of the compound or any of its competing phases.

We shall use the binary semiconductor Sb_2Se_3 as an example, and first note that the formation of it is defined by the reaction $2\,Sb + 3\,Se \rightleftharpoons Sb_2Se_3$. Equally, under constant temperature and pressure, the chemical potential per species, μ_i is defined by the derivative of the Gibbs free energy with respect to the number of particles of that species, N_i, and thus the sum over all species entails the total infinitesimal change in Gibbs free energy:

$$dG = \sum_i \mu_i dN_i \tag{3.25}$$

For the point at which the formation reaction is in equilibrium, $dG = 0$, and so, for Sb_2Se_3:

$$2\mu_{Sb} + 3\mu_{Se} - \mu_{\mathrm{Sb_2Se_3}} = 0; \qquad 2\mu_{Sb} + 3\mu_{Se} = \mu_{\mathrm{Sb_2Se_3}} \tag{3.26}$$

We must then note that for our calculations, the chemical potentials must be defined to the respective elemental reference energies, just like E_F above, such that $\mu_i = E_i^0 + \Delta\mu_i$. Integrating this into 3.26, we obtain an expression that in the reference energies, that can be rearranged to give the Gibbs formation energy of Sb_2Se_3:

$$2(E^0_{Sb} + \Delta\mu_{Sb}) + 3(E^0_{Se} + \Delta\mu_{Se}) = (E^0_{\mathrm{Sb_2Se_3}} + \Delta\mu_{\mathrm{Sb_2Se_3}})$$
$$2\Delta\mu_{Sb} + 3\Delta\mu_{Se} = \underbrace{(E^0_{\mathrm{Sb_2Se_3}} + \Delta\mu_{\mathrm{Sb_2Se_3}}) - 2E^0_{Sb} - 3E^0_{Se}}_{\Delta_f G(\mathrm{Sb_2Se_3})} \tag{3.27}$$

$\Delta_f G(\mathrm{Sb_2Se_3})$ itself, within our athermal model with minimal entropic and pressure changes, we can approximate to $\Delta_f E(\mathrm{Sb_2Se_3})$, the calculable formation energy of Sb_2Se_3. With this equality now established, we can now consider the limitations on the chemical formation space of Sb_2Se_3. The first limitation is to avoid the formation of Sb and Se in their standard states, so we must first constrain:

$$\Delta\mu_{Sb} \leq 0, \qquad \Delta\mu_{Se} \leq 0 \tag{3.28}$$

Finally, in the equality in 3.27, $\Delta_f E(\mathrm{Sb_2Se_3})$ has a fixed value, and as such, either of $\Delta\mu_{Sb}$ and $\Delta\mu_{Se}$ are dependent on the other. If only $\Delta\mu_{Sb}$ is considered, it is the independent variable, and we see that the equality in 3.27 defines the second limiting inequality on $\Delta\mu_{Sb}$:

$$2\Delta\mu_{Sb} \geq \Delta_f E(\mathrm{Sb_2Se_3}) \tag{3.29}$$

Combining Equations 3.28 and 3.29, we can obtain the limits on the independent chemical potential $\Delta\mu_{Sb}$:

$$\frac{\Delta_f E(\mathrm{Sb_2Se_3})}{2} \leq \Delta\mu_{Sb} \leq 0 \tag{3.30}$$

From this, we have found that for a binary, the chemical potential space can be defined solely by a 1-dimensional phase space of $\Delta\mu_{Sb}$. There are no thermodynamically stable competing phases to Sb_2Se_3 and so, noting our calculated $\Delta_f E(\mathrm{Sb_2Se_3})$ of 1.5 eV, the chemical potential limits (per atom) of Sb_2Se_3 are then the Sb-rich/Se-poor boundary ($\Delta\mu_{Sb} = 0$, $\Delta\mu_{Se} = -0.5$ eV) and the Sb-poor/Se-rich boundary ($\Delta\mu_{Sb} = -0.75$ eV, $\Delta\mu_{Se} = 0$).

The above formalism works for any binary compound – for ternary systems and above,

the number of independent variables, and equations defining their limits increases. Equally, competing phases put further limits on the chemical potentials; however, the problem remains a number of simultaneous linear equations in a number of variables, and so is soluble. However, it does become more difficult to solve by hand, and so we use the Chemical Potential Limits Analysis Program (CPLAP) to automate the solution.[194]

While these limits, when presented as numerical values, can be highly useful in determining defect formation energies, their chemical meaning is not immediately apparent. We can attempt to translate the behaviour of the Sb-rich/Se-poor and Sb-poor/Se-rich by noting that in the former, our defect environment is Sb_2Se_3 in equilibrium with only elemental Sb, while in the latter condition, Sb_2Se_3 is in equilibrium with elemental Se alone. From this, we can construct the Kröger-Vink formation equations of the neutral ($q = 0$) antimony vacancy, selenium vacancy and selenium interstitial in the two chemical potential conditions, Se-rich and Sb-rich, respectively:

Se-rich	**Sb-rich**
$\mathrm{Sb}_{\mathrm{Sb}}^{\times} + \frac{3}{2}\mathrm{Se}_{(\mathrm{s})} \rightarrow V_{\mathrm{Sb}}^{\times} + \frac{1}{2}\mathrm{Sb}_2\mathrm{Se}_{3(\mathrm{s})}$	$\mathrm{Sb}_{\mathrm{Sb}}^{\times} \rightarrow V_{\mathrm{Sb}}^{\times} + \mathrm{Sb}_{(\mathrm{s})}$
$\mathrm{Se}_{\mathrm{Se}}^{\times} \rightarrow V_{\mathrm{Se}}^{\times} + \mathrm{Se}_{(\mathrm{s})}$	$\mathrm{Se}_{\mathrm{Se}}^{\times} + \frac{2}{3}\mathrm{Sb}_{(\mathrm{s})} \rightarrow V_{\mathrm{Se}}^{\times} + \frac{1}{3}\mathrm{Sb}_2\mathrm{Se}_{3(\mathrm{s})}$
$\mathrm{Se}_{(\mathrm{s})} \rightarrow \mathrm{Se}_i^{\times} + \mathrm{Se}_{(\mathrm{s})}$	$\frac{1}{3}\mathrm{Sb}_2\mathrm{Se}_{3(\mathrm{s})} \rightarrow \mathrm{Se}_i^{\times} + \frac{2}{3}\mathrm{Sb}_{(\mathrm{s})}$

Through these examples, we can see how the formation equations drastically change between the chemical potential environments, as different phases balance the formation of the defect. This argument also allows us to think about how these limits reflect experimental conditions – for example, if the amount of selenium were to be restricted during a synthesis of Sb_2Se_3, then the formation of an antimony vacancy during that process is more likely to follow the equation in the right hand column (as Se is not required as a reagent), and so the formation energy required to form the vacancy (and its resultant bulk concentration) will more closely reflect the Sb-rich conditions of our calculations.

3.4.3 Corrections

As discussed in previous sections, defect formation energies calculated using the supercell model require corrections in order to create the dilute limit approximation that neighbouring point defects do not interact with each other. The three primary corrections are detailed below. Additionally, there can be the requirement for a fourth correction: as supercells can contain many more atoms than a regular primitive cell, it can become too expensive to calculate using a hybrid DFT functional, and GGA functionals are used instead. As such, the calculated band gap of the semiconductor is underestimated, however the accurate positions of VBM and CBM are crucial for determining the relative Fermi level position, an important quality for the description of defects. So, historically, it has been common to use a *band edge* correction to calculate more accurate VBM and CBM positions for a GGA supercell – as computational power has increased, however, hybrid functionals or +U methods have become more approachable. Nevertheless, it was necessary to perform the point defect calculations in Section 6.3.4 of this thesis using PBEsol, although the band-edge correction in this case was negligible due to fortuitous cancelling of the underestimation with the additional omission of spin-orbit coupling from the defect calculations.

Potential Alignment

Neutral defect supercells have the same reference for the electrostatic potential as the bulk supercells, and so the valence bands of both the pristine and defective supercells will align. Problems arise, however, in the description of positive and negative charge states. In periodic DFT codes, the crystal itself must be neutral, and thus to describe charged cells, the defect is treated as a point charge while it is compensated by a background jellium (HEG) that neutralises the charge. As a result, the total energy no longer becomes well-defined and the background electrostatic potential is shifted with respect to that of the bulk, and as a result, so are all of the eigenvalues. Thus, in order to ensure all the defects have the same reference energy, we must align the potentials of the charged cells to that of the neutral. This is performed by a simple shift, ΔV_{el}, defined:

$$\Delta V_{el} = V_{core,X} - V_{core,H} \tag{3.31}$$

Where $V_{core,X}$ and $V_{core,H}$ are the average potential across all core levels in the defective and host supercells respectively.[195,196]

Band-filling

In all defect supercells, the electronic states from the periodic images of the defect will interact, together forming a defect band. In the case where this defect band lies deep within the band gap of the semiconductor, then it remains localized and has minimal effect on the surrounding electronic structure. If, however, the defect band is *shallow*, lying within k_BT of the band edges ($\sim$0.02 eV for room temperature), then this can result in additional electronic population of the conduction band (or depopulation of the valence band) in accordance with the Fermi-Dirac distribution– as partial occupancies do not count towards the total energy of the system, the effect of this *band-filling* must be accounted for. The band-filling correction developed by Lany and Zunger is given for donor states by:

$$\Delta E_{bf} = -\sum_{n,\mathbf{k}} \Theta(e_{n,\mathbf{k}} - e_H^{CBM})(w_{\mathbf{k}}\eta_{n,\mathbf{k}}e_{n,\mathbf{k}} - e_H^{CBM}) \tag{3.32}$$

where $e_{n,\mathbf{k}}$ are the eigenvalues for band n, e_H^{CBM} is the conduction band minimum energy in the host supercell, $w_{\mathbf{k}}$ is the $\mathbf{k}$-point weighting, and $\eta_{n,\mathbf{k}}$ is the band occupation. Θ is the Heaviside step function, ensuring that ΔE_{bf} is only non-zero for eigenvalues above the CBM. An equivalent expression (replacing $-e_H^{CBM}$ for $+e_H^{VBM}$) is used for calculating the band-filling effect of acceptor states on the valence band.

Image Charge Correction

Charged defect sites will interact electrostatically with their periodic images, as the Coulomb interaction decays with $\frac{1}{\mathbf{r}}$, and supercells are rarely large enough for this interaction to decay entirely. As such, to restore a dilute limit, in which electrostatic interactions between defects are infinitesimally small, an *image charge correction* is

required. Numerous forms have been proposed for this correction, although most derive from the expression for the interaction between point charges in the presence of a background jellium, the Madelung energy:

$$E_{Madelung} = \frac{q^2\alpha}{2L} \tag{3.33}$$

where α is the structure-dependant Madelung constant, and L the distances between the charges (for a cubic system, the supercell length). In reality, however, defects rarely behave as point charges, with some of the charge density distributed around the defect site, or onto neighbouring atoms. For such diffuse distributions, Makov and Payne derived a third-order expression,[197] which also includes charge screening by the host structure through the dielectric constant, ϵ:

$$\Delta E_{icc}^{MP} = \underbrace{\frac{q^2\alpha}{2\epsilon L}}_{\Delta E_{MP1}} - \underbrace{\frac{2\pi qQ}{3\epsilon\Omega}}_{\Delta E_{MP3}} \tag{3.34}$$

The second term in this expansion, ΔE_{MP3} is the interaction between the point charge q and the quadrupolar moment of its images' charge density, ρ_i, where Ω is the cell volume, and Q is the quadrupolar moment, given by:

$$Q = \iiint_{\Omega} d^3r\rho_i(\mathbf{r})r^2 \tag{3.35}$$

Lany and Zunger proposed the calculation of $\rho_i(\mathbf{r})$ through the difference between the total charge densities of the defective and host supercells,[195] and found that in this instance, the charge density difference was dominated by the screening response of the host structure outside of the defect. This allows the simplification of Q in terms of this screening factor, leading to the ΔE_{MP3} term also becoming proportional to $\frac{q^2}{L}$ and becoming pseudo-first order. As such, the image charge correction can be formulated as the modification of the first-order screened Madelung energy, ΔE_{MP1}:[198]

$$\Delta E_{icc}^{LZ} = [1 + c_{sh}(1 - \frac{1}{\epsilon})]\frac{q^2\alpha}{2\epsilon L} \approx \frac{2}{3}\Delta E_{MP1} \tag{3.36}$$

where c_{sh} is the shape factor, and varies on the crystal packing. In the conditions that ϵ is sufficiently large and the supercell is relatively isotropic, which is the case for the cases included in this thesis, the pre-factor in the Lany-Zunger correction in Equation 3.36 can be approximated by $\frac{2}{3}$. The calculations in this thesis use the simplified Lany-Zunger correction, modified by the method of Murphy and Hine to include anisotropy in the dielectric constant.[199]

3.4.4 Transition level diagrams

Once the defect formation energies have been calculated, the remaining step is to display this information in a meaningful manner. As discussed above, for each of the chemical potential limits, the defect formation energies are generally plotted as a function of Fermi level position (above the VBM), demonstrating both the thermodynamics of the defect, and its electronic behaviour given by Equation 3.23 – neutral defects are electronically benign, and appear as horizontal lines, while donor defects (those with positive charge states) slope upwards from left to right, while acceptor defects (negative charge states) slope downwards. In practice, however, displaying all the charge states for every defect will lead to a crowded diagram, and so for a particular defect, it is most thermodynamically informative to only include the charge state with the lowest formation energy for that Fermi level position. The points in energy at which two charge states intersect, and the defect changes behaviour, are termed thermodynamic *transition levels* (TL); the TL (denoted $E(q/q')$, energy relative to the VBM) between one charge state, q, and another, q', for a given defect X is given by the following expression, where the defect formation energies are defined as in Equation 3.23:

$$E(q/q') = \frac{\Delta_f E_X(q') - \Delta_f E_X(q)}{(q - q')} \tag{3.37}$$

An example transition level diagram is given in Figure 3.6, showing examples of a selection of acceptor and donor defects in Sb_2Se_3. We also note that the position of the TLs within the band gap of a semiconductor are crucially important to its behaviour as a photovoltaic. *Shallow* defects, as defined above with TLs within $\sim$0.02 eV of band edges, will primarily contribute to conduction through the thermal

generation of carriers, and are crucial to forming p or n-type behaviour and a p-n junction where appropriate. *Deep* defects, those further within the gap, however, can be detrimental to photovoltaic ability as they can act as recombination centres in SRH recombination, as discussed in Section 1.2.3. The transition level of a particular defect centre is central to this as it represents the change in charge state that the defect could undergo when trapping one or multiple charge carriers, and its distance from the band edges then reflects the thermal energy that is required for a trapped carrier to be released back into the valence or conduction bands, with more energy required if the TL is deeper. An *ultra-deep* defect, that is distant in energy from both band edges and sits near to mid-gap, is then most debilitating to photovoltaic ability, as it can easily trap both holes and electrons and efficiently act as a centre for SRH recombination.

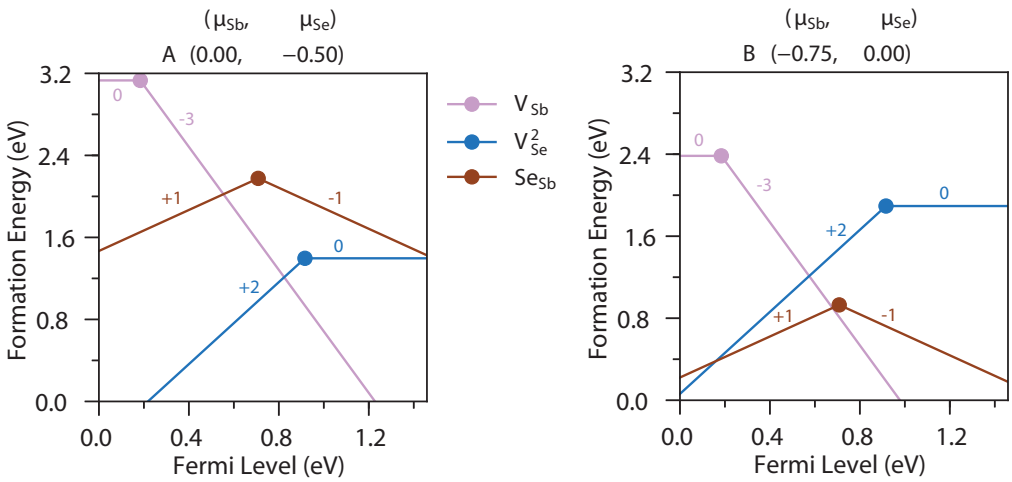

Figure 3.6: Transition level diagram of defects in Sb_2Se_3 at the two chemical potential limits A and B, calculated using HSE06. Individual defect charge states are labelled by the number close to the slope in question, and transition levels are marked by dots. The Fermi level is given in reference to the valence band maximum, which is set to 0 eV.

Finally, we must also briefly consider how individual defect formation energies link to macroscopic concentrations. Omitting vibrational entropic effects (which would cause in considering our $T = 0$ K model, the concentration of defects in a volume of sample, n_X obeys an Arrhenius-like dependence on the formation energy (A is the number of atoms per unit volume):

$$N_X = Ae^{\frac{-\Delta_f E_X}{k_B T}} \tag{3.38}$$

This exponential behaviour means that, at non-zero temperatures, lower formation energy defects are significantly more likely to impact the bulk electronic behaviour than higher formation energy ones due to their much higher concentration: a defect of formation energy 1.5 eV will have a concentration $\sim 10^{15}$ greater than a defect with formation energy 2.5 eV under the same Fermi level and chemical potential. As a result, in our discussion of relevant defects for photovoltaics, usually only defects with formation energy of $<$1.5 eV are considered.

With this information, we can analyse the behaviour of the three defects included in Figure 3.6 as an example of how this information can be relevant to photovoltaic behaviour and enable our results to inform the potential construction of devices. Two of the defects depicted are vacancies: the antimony vacancy, V_{Sb} and the selenium vacancy on the second of 3 crystallographic sites, V^2_{Se}. The former of these acts as an acceptor, with the -3 charge state operating for the bulk of the Fermi level range, while the latter acts as a donor with the $+2$ charge state – these states reflect the inverse of the original oxidation state of the absent ion, and so are 'fully ionised', in which the carriers generated on the creation of the defect are fully donated to the bulk reservoir. A half-equation representative of this process in Kröger-Vink notation might be:

$$\mathrm{Sb_{Sb}} \rightarrow \mathrm{Sb} + V'''_{\mathrm{Sb}} + 3h^{\bullet} \tag{3.39}$$

Both, however, have deep transition levels, with the $+2/0$ for V^2_{Se} being 0.55 eV below the CBM while the 0/-3 TL of V_{Sb} lies shallower at 0.19 eV above the VBM. The third defect, a selenium-on-antimony antisite (Se_{Sb}), is also predicted to give a deep TL, with $+1$/-1 lying directly mid-gap; this defect can act as either an acceptor or donor, and so is known as *amphoteric*. As this defect is equidistant and deep from both band edges, this is likely to be the most harmful defect for PV operation, as it could trap both holes and electrons with approximately equal probability, and thus be a major recombination centre. We can also see the effect of chemical potential on the defect formation energies by looking between the limits given by A ($\mu_{Sb} = 0$, Sb-rich) and B ($\mu_{Se} = 0$, Se-rich). Moving from Sb-rich to Se-rich conditions, we can see that the formation energies of V_{Sb} and Se_{Sb} fall as the thermodynamic penalty to removing an Sb atom from the structure falls, while the formation energy of V^2_{Se}

rises inversely. Relating this to their relative defect concentrations, we could suggest that, within our thermodynamic formalism, Sb-rich conditions would be less harmful for the synthesis of Sb_2Se_3 devices than Se-rich, as the formation energies of the most harmful defect transition levels are maximised, and thus their concentration, and impact on the carrier dynamics of the system are minimised.

Chapter 4

Results I: Bismuth Halide Double Perovskites

4.1 Introduction: Moving on from MAPI

As stated in the Section 1.3.4, the inorganic-organic lead halide perovskites have soared in efficiency to give cell efficiencies of over 22 %, matching champion current technologies such as CdTe, and multicrystalline Si,[83,111] while Perovskite/Si monolithic tandem cells reach efficiencies of >23 %.[39] However, the lead perovskites still present significant drawbacks in some areas: degradation and instability to moisture or even in open air is common and often rapid, limiting their widespread usage;[126,127,131,132] the inclusion of lead in an inherently unstable material also brings concerns around toxicity and the potential for leaching into the environment unless otherwise encapsulated.[113]

A number of different strategies to get around either of these problems have been proposed and studied. As previously discussed, the methylammonium lead halide perovskites can be stabilized through alloying with caesium or formamidinium on the A site, or bromine on the X site, while having only a relatively small impact on the overall structure and the resultant promising photovoltaic properties.[84,200] However, both cationic and anionic substitutions can act to increase the band gap of the system, often leading to overall lower efficiencies, or the necessity to combine with silicon to effectively harvest the solar spectrum. Thus, many studies have examined moving beyond the fixed 3-dimensional perovskite structure of MAPI altogether. In place of retaining the entire perovskite structure, some success has been met by moving to layered or '2D' perovskites, where the crucial corner-sharing lead halide octahedra are retained in two dimensions, but capped in the third by either a different anion or a much larger organic cation that separates the inorganic layers. For anions, these will generally be pseudohalides, and the lead thiocyanate iodide compound $(CH_3NH_3)_2PbI_2(SCN)_2$ (MAPSI) has seen substantial interest due to increased stability, particularly to moisture, and improvement of hysteresis,[201–205] although more recent studies have found its band gap to also be too large for ideal absorption in a single junction. Work from within our group, to which I have contributed, has examined the family of related pseudohalides and demonstrated that they are possess tuneable, stable electronic structures with minimal deep defects, making them strong candidates for top cells in tandem devices.[133,206]

When exchanging the organic cation, replacing methylammonium entirely with any

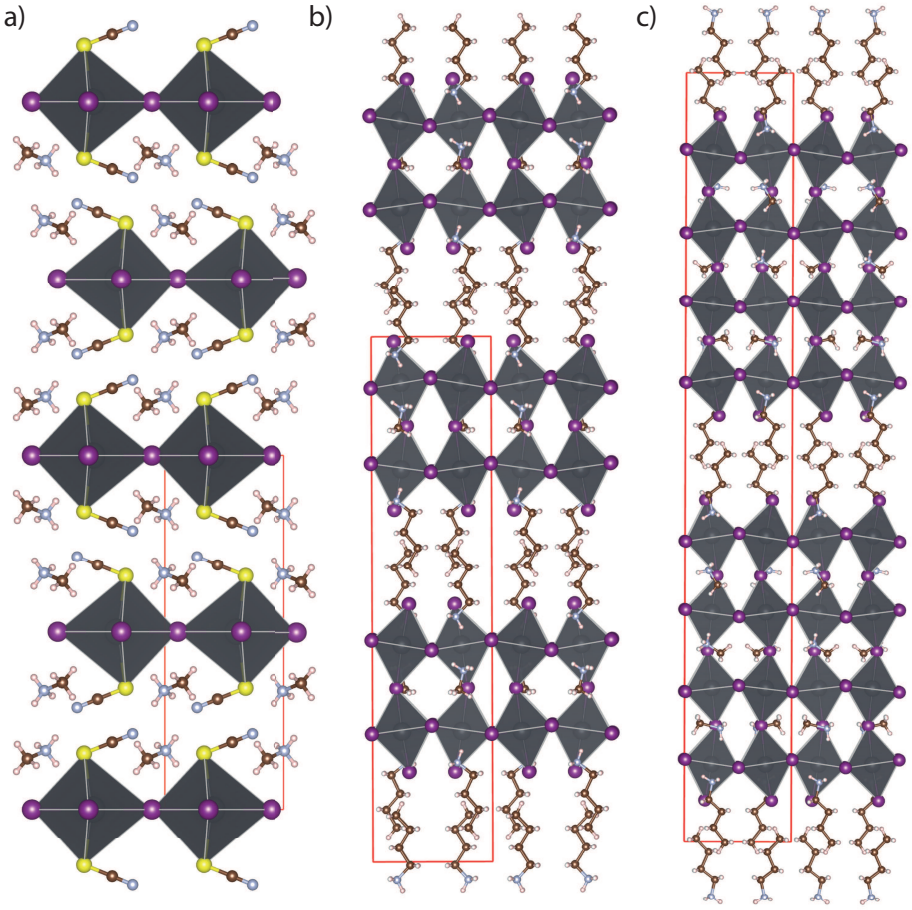

Figure 4.1: Crystal structures of the 'layered' a) $(CH_3NH_3)_2PbI_2(SCN)_2$ (MAPSI) and $(CH_3(CH_2)_3NH_3)_2(MA)_{(n-1)}Pb_nI_{(3n+1)}$ with b) n = 2, c) n = 4, demonstrating the increasing proportion of MAPI-like within the overall layered structure. A single unit cell is marked in red for each, and lead octahedra (distorted, especially in the case of MAPSI) are depicted in grey, iodine atoms are in purple, carbon in brown, nitrogen in blue, hydrogen in cream, and sulfur in yellow.

cation other than formamdinium or caesium generally results in the complete break-up of the inorganic perovskite network and the degradation of the excellent properties that provides. Instead, much research interest has considered compounds where the methylammonium is partially substituted, giving a structure with layers of $MAPbI_3$ sandwiched between those of a large organic cation, giving the general formula $(A)_2(MA)_{(n-1)}Pb_nI_{(3n+1)}$. The two most successful alternative organic monocations that form layered lead halide perovskites in this form have been butylammonium ($(CH_3(CH_2)_3NH_3)^+$, or BA^+) and phenylethylammonium ($(C_6H_5(CH_2)_2NH_3)^+$, or PEA^+).[207–210] In both of these cases however, there have been recorded improvements in stability, with cell performance often only degrading by $\sim 1\,\%$ on time scales of hundreds or thousands of hours; in a similar or even shorter timescale,

unstabilised methylammonium lead iodide cells could see a efficiency loss of over 50 %.[127,209] Additionally, these materials are tuneable through the 'n' parameter – the ratio between A and MA cations – by varying synthesis conditions, a wide range of n can be obtained, with values of 1 – 60 being reported.[209,211] As a result of the limitation of structural and electronic connectivity in one dimension through the inclusion of these large cations, the band gap of the 2D materials is often much higher; by increasing n, the band gap can be adjusted to conform more closely with that of MAPI, and thus access improved cell performance. By doing so, however, the effect of the dimensionality reduction on the stability is often greatly reduced.[209]

These '2D' materials also do not tend to display the hysteresis associated with many planar methylammonium-based cells – this is likely a result of the observed lack of facile ion diffusion,[210] which a number of reports have implicated as the primary cause behind cell hysteresis in the methylammonium lead halides.[118,122] However, ion diffusion has also been highlighted to result in some of the exceptional properties of the methylammonium lead halides as well, including a giant dielectric constant and ferroelectric self-poling (the accumulation of ions at ends of the device causing a strengthened electric field across the $p-n$ junction),[212,213] and so losing these properties presents a further cost for increased stability. Research in this area is however ongoing and promises to be an enticing new direction for the photovoltaic community,[214] especially with the recent report of a mixed 2D/3D perovskite using protonated aminovaleric acid as the organic cation demonstrating both long-term stability ($>$1 year) and high efficiencies.[215]

These approaches do not however address the inclusion of Pb in often highly soluble halides, and hence the environmental danger of leaching into the environment through moisture or degradation.[113] An interesting new direction in the perovskite PV field has been cation mutation of Pb^{II} to Ag^{I} and Bi^{III}, moving from the single ABX_3 perovskite to a $A_2B^{I}B^{III}X_6$ double perovskite, removing lead from the structure entirely (and also, in most cases, replacing MA for Cs). This structure-type retains the cubic symmetry of the single perovskite, but with the substitution of Ag and Bi onto alternate B sites, the unit cell is doubled along each axis and the cell becomes face-centred (space group $Fm\bar{3}m$), as depicted in Figure 4.2. In early 2016, two articles were published reporting the synthesis of members of this family of materials. Slavney *et al.* first reported the synthesis of $Cs_2AgBiBr_6$, finding an

indirect optical band gap of 1.95 eV through UV-Vis spectrometry and also record its time-dependent photoluminescence behaviour: from this, they were able to extract a primary decay lifetime of 660 ns.[216] This decay reflects the overall recombination lifetime – given the indirect gap, the authors suggest that this value is dominated by non-radiative processes, and this long lifetime is comparable to the >1 µs seen in some MAPI solar cells. McClure *et al.*, publishing just a few weeks later, synthesised both $Cs_2AgBiCl_6$ and $Cs_2AgBiBr_6$, finding optical band gaps of 2.77 and 2.19 eV respectively.[217] While neither of these studies attempted to manufacture a solar cell, they still provided an impetus for the direction of research into further Pb-free perovskites, including our own study, with a goal to replace Pb and form a stable structure, while maintaining some of the properties that make the hybrid lead halide perovskites so successful.

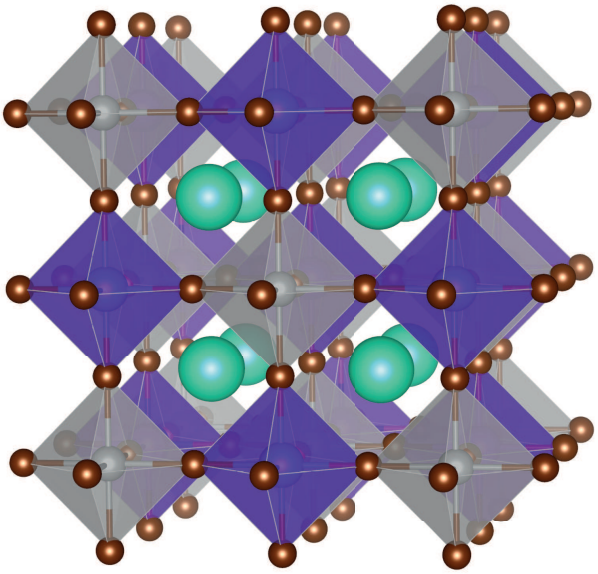

Figure 4.2: Crystal structure for the Cs_2AgBiX_6 family, exemplified here with X = Br. Cs atoms are in turquoise, silver atoms in light grey, bismuth in purple and bromine in brown, with the silver- and bismuth-based octahedra also depicted.

While our research was underway, there were numerous further reports examining these systems. The groups of Giustino and Snaith have performed a screening of this family of double perovskites with DFT, including all where M^{I}= Cu, Ag, Au, M^{III} = Bi, Sb and X = Cl, Br, finding band gaps that span a range from 0 eV to 2.7 eV, however those predicted to be within the 1 eV to 1.5 eV limited to the hypothetical $Cs_2AuBiBr_6$, $Cs_2AuSbCl_6$ and Cs_2SbAgI_6, and the authors acknowledge that expense of precursors would strongly limit the ability for large quantities of Au

compounds.[218] Further work from these groups examined the extant members of the family, $Cs_2AgBiBr_6$ and $Cs_2AgBiCl_6$ using many body GW theory, and finding band gaps of 1.8 and 2.4 eV, in reasonable agreement with the variable experimental values.[219] Cheetham and co-workers have taken an alternative synthetic approach – they first synthesised $(CH_3NH_3)_2KBiCl_6$,[220] using a alkali metal cation in place of the noble metal for M^I; this is, in fact, in closest analogy to an older family of halide double perovskites, the elpasolites, with the general formula $Cs_2M^IM^{III}X_6$, with M^I= Na and M^{III} = Sb, Bi. These compounds were characterised in the 1970's and 1980's, but mostly only gathered attention for their low temperature ferroelectric phase transitions, distorting away from the fully cubic structure.[221–224] An amplified distortion is seen in $(CH_3NH_3)_2KBiCl_6$ due to the large disparity in ionic radius between K^+ and Bi^{3+}, and as a chloride, the band gaps was still high and indirect, through both optical measurement and DFT prediction, reaching above 3 eV. Later, their investigations highlighted $(CH_3NH_3)_2TlBiBr_6$, which possesses a direct band gap, albeit still wider than ideal at 2.16 eV.[225] A theoretical study of the intrinsic defects of $Cs_2AgBiBr_6$ using the PBE functional found that while $Cs_2AgBiBr_6$ was stable with respect to decomposition and alternate competing phases, V_{Bi} (in Br-rich conditions), and Ag_{Bi} (under all conditions) possess formation energies below 1 eV and have mid-gap charge transition levels, which could allow them to act as detrimental recombination centres.[226]

Given the potential promise of these materials, especially should an iodide be found, which is more likely to have a band gap ideal for solar absorption within PV devices, our aim in this work was to investigate these materials thoroughly with hybrid DFT to accurately assess their capability for usage in applications. The Cs_2AgBiX_6 family also posed interesting questions: why, when performing the cation mutation, did the band gap become indirect, despite the retention of cubic symmetry; also the lack of a synthesised iodide was conspicuous, especially given that Slavney *et al.* had found no decomposition of their material under N_2, while McClure *et al.* had seen degeneration in their reflectance signal after a month of storage under ambient air. We attempted to answer these in our following work.

4.2 Methodology

Geometry optimizations of all structures were performed using the PBEsol functional. Further electronic structure and optical calculations were performed with the HSE06 functional, with the explicit addition of spin orbit coupling (HSE06+SOC), due to the presence of the heavy elements Bi and/or I. Recent studies have used the HSE functional with the α parameter, percentage of HF exchange, adjusted to 43 $\%$ (herein denoted HSE43) to correctly recreate the band gap of the hybrid lead halide perovskites when combined with spin-orbit coupling.[227,228] Volonakis *et al.* utilised PBE0+SOC (on top of LDA relaxed structures) for their computational screening,[218] while McClure *et al.* used HSE06+SOC, finding agreement within 0.1 eV of their experimental band gaps.[217] HSE43+SOC was used in addition to HSE06+SOC to separately calculate the band structure of $Cs_2AgBiBr_6$ in this study as a benchmark – it was found that the band gap was significantly overestimated compared to the highest reported experimental value in both cases (0.4 eV – and the error would be expected to be higher if PBE0 were used) leading us to conclude that HSE06 was the best functional to accurately assess band gaps for this family of compounds, given the agreement with both experiment and the GW calculations of Filip *et al.*.[219] Scalar relativistic pseudopotentials were used, and 5d electrons were treated as valence for Bi. For all electronic calculations, a plane wave cutoff of 400 eV and a k-point mesh of 3×3×3 were used for all double perovskites, as these were sufficient to convergence the total energy to within 1 meV. A tighter k-mesh of 4×4×4 was used for optical calculations to ensure relevant k-points were included and SLME was converged. The forces on each atom were converged to below 0.01 eV Å^{-1} in optimizations.

Disorder was simulated using a regular solution model: this considers the mixture of one species with another, with given enthalpic and entropic contributions to the total free energy of mixing. In this study, we are examining the free energy change from Ag/Bi order to disorder, and to find the temperature at which disorder will occur, we must satisfy the inequality:

$$\Delta G = \Delta H - T\Delta S \leq 0 \tag{4.1}$$

The ΔH of disorder is given, within an approximation of constant volume (reasonable considering a solid), by the difference in energy between the ordered and disordered supercells. ΔS can be taken solely as a configurational entropy ($S = k_B \ln W$) arising from the exchanging of two atoms, such that:

$$\Delta S = -k_B(x_1 \ln x_1 + x_2 \ln x_2) \tag{4.2}$$

with k_B the Boltzmann constant (in eV), and x_1 and x_2 here are the fractions of the individual components – in this case, a 50:50 mixture of Ag and Bi on the cation sites means that x_1=0.5=x_2.

4.3 Results and Discussion

4.3.1 Structure and Relaxation

The structures of the 2 halide double perovskites were relaxed using the PBEsol functional, giving the lattice parameters in Table 4.1, with both systems retaining their $Fm\bar{3}m$ symmetry. The lattice parameters for both systems are $<1\,\%$ deviant from their experimental values (both taken from McClure), and the cell volume also demonstrates good agreement, although the values are underestimated in both cases likely due to the underbinding of the PBEsol functional. In general, however, these were considered sufficient as the basis for further electronic calculations.

Table 4.1: Optimized lattice parameters of Cs_2AgBiX_6 (X = Cl, Br), with percentage difference from experiment[217] in parentheses

Compound	a/Å	volume/Å^3
$Cs_2AgBiCl_6$	10.6959 (–0.75%)	1223.64 (–2.25%)
$Cs_2AgBiBr_6$	11.2011 (–0.43%)	1405.342 (–1.29%)

As the intent was to examine the properties and trends of the entire family of compounds however, this necessitated the prediction of the structure of Cs_2AgBiI_6, despite the lack of available experimental verification. We had initially generated a structure of Cs_2AgBiI_6 using the Materials Project 'Structure Predictor' – which attempts to predict crystal structures for a given set of elements and stoichiometry through insertion of chosen atoms within known crystal structures of the same

stoichiometry, and ranking the resultant structures using an electrostatic Ewald summation.[229] While it had given the same $Fm\bar{3}m$ double perovskite structure as its most likely prediction, the lattice parameters were close to those of $Cs_2AgBiBr_6$, seemingly unlikely given the larger ionic radius of I^- compared to Br^-. As a result, the double perovskite lattice of $Cs_2AgBiBr_6$ was used, but the initial lattice parameters adjusted using the SPUDS program of Woodward and co-workers.[230] As this program includes the ionic radii of common ions, it could be used to obtain a more accurate estimate of the lattice parameter of a given hypothetical double perovskite. This hypothetical structure for Cs_2AgBiI_6 was then fully optimized (with relaxation of cell volume, shape and atomic positions), and again cubic symmetry was retained. During the study, it became clear that further hypothetical perovskites would need to be constructed, with the formula $A_2M^IM^{III}X_6$, with M^I= In, Tl, M^{III} = Bi and X = Cl, Br; these structures were constructed and optimized identically to Cs_2AgBiI_6 (appropriate substitution into the $Cs_2AgBiBr_6$ structure, adjustment of lattice parameters in line with ionic radii, then full optimization).

Table 4.2: Lattice parameters of hypothetical Cs_2MBiX_6 (M = Ag, In, Tl; X = Cl, Br, I) compounds within the cubic double perovskite structure type, optimized using PBEsol

Compound	a/Å	volume/Å^3
Cs_2AgBiI_6	11.9312	1698.448
$Cs_2InBiCl_6$	11.2017	1405.568
$Cs_2InBiBr_6$	11.6677	1588.385
$Cs_2TlBiCl_6$	11.3199	1450.534
$Cs_2TlBiBr_6$	11.8052	1645.205

4.3.2 Electronic Structure

After relaxation, the electronic properties of the Cs_2AgBiX_6 compounds were calculated with HSE06+SOC. First, the electronic calculations were benchmarked against other functionals to assess whether HSE06+SOC was the most accurate for predicting band gaps, and thus subsequent optical properties. The fundamental band gaps for $Cs_2AgBiBr_6$ from our calculations are compared in Table 4.3.

As explained in the methodology, HSE43+SOC appears to greatly overestimate even the highest recorded experimental measurement by at least 0.4 eV, HSE06+SOC in comparison is no more than 0.4 eV underestimated from the highest experimental

Table 4.3: Indirect band gaps of $Cs_2AgBiBr_6$, comparing different theoretical methods, with all values in eV.

Compound	HSE06+SOC	HSE43+SOC	GW[219]	Experiment
$Cs_2AgBiBr_6$	1.79	2.67	1.83	1.89,[219] 1.95,[216] 2.19[217]

value of 2.19 eV, and is within 0.2 eV of the other two experimental measurements. It is also in very good agreement (0.04 eV) of the calculated GW gap of Filip *et al.*, providing good agreement between theoretical measurements (as experimental optical gaps may be higher than the fundamental due to temperature effects or others, such as Moss-Burstein filling). As a result, HSE06+SOC was chosen for the prediction of all electronic and optical properties in this study.

The electronic band structures of $Cs_2AgBiCl_6$ and our hypothetical Cs_2AgBiI_6 structure are plotted in Figure 4.3, while that of $Cs_2AgBiBr_6$ is included with further analysis in Figure 4.4. From these, it is evident that all the compounds in the family possess indirect band gaps, with the VBM in all cases at the X point, while the CBM is variable, either being at Γ (X= Cl), or L (X= Br, I). It is also of note that in all cases, the conduction band as as whole is relatively flat and thin with low dispersion, and also only limited dispersion in the valence band as well, especially between W and X. This is in direct contrast to the band structure of the methylammonium lead halide perovskites shown in the Introduction, which have highly disperse, wide conduction and valence bands, with a direct band gap (the additional absence of Rashba splitting in the CB is unsurprising given the substitution of the symmetry-breaking MA cation for isotropic Cs). The lowest direct VB–CB transition in all 3 compounds occurs from the VBM, at X. Moving down the halides from Cl to I, the most notable trend is the reduction in band gap as a consequence of the raising of the halide valence p orbitals in energy, decreasing from 2.35 eV in $Cs_2AgBiCl_6$ to 1.08 eV and is a similar trend to that seen in the methylammonium and caesium lead halides. Also of note, as the halide valence p is raised, the overlap in the conduction band appears to improve, and the conduction band widens, while the valence band correspondingly narrows slightly. This in turn, however, leads to the difference between the fundamental indirect and lowest direct gaps increasing as X is close to the maximum in energy of the conduction band (this is quantified in Table 4.4). Yu and Zunger have recently highlighted the importance of the spacing of the indirect

and lowest direct allowed transitions in assessing materials for PV, noting that a larger spacing of this sort can lead to poorer absorption and increased non-radiative recombination.[186,187]

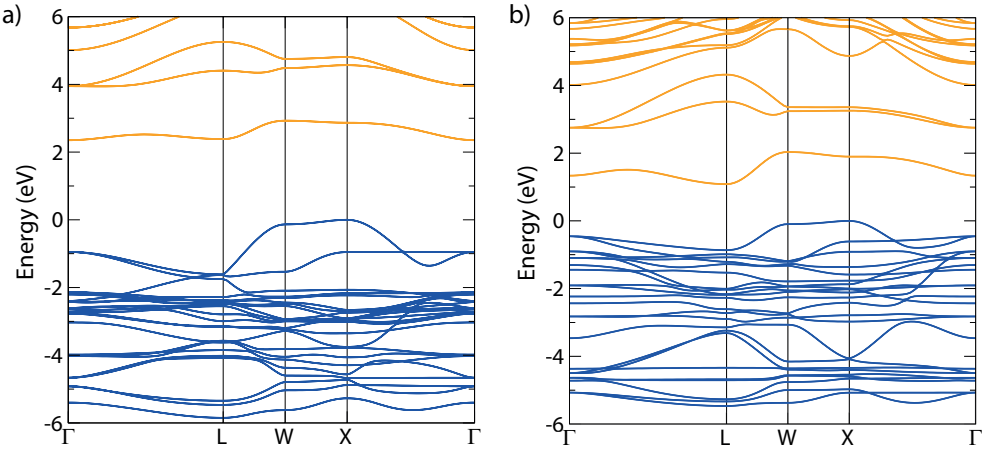

Figure 4.3: HSE06+SOC band structures of a) $Cs_2AgBiCl_6$ and b) Cs_2AgBiI_6, with valence band in blue, and conduction band in orange. Valence band maximum (VBM) is set to 0 eV.

To identify the reason for such a discrepancy between the Cs_2AgBiX_6 and the related lead halide perovskites, we looked to a establishing more direct, quantitative comparison. $CsPbBr_3$ is the closest lead halide analogue to $Cs_2AgBiBr_6$, with the sole difference in structure being the cation mutation of Pb to Ag and Bi, and so would not include any of the potential exotic effects of methylammonium and contains the same halide that the cations interact with. Sadly, at room temperature, $CsPbBr_3$ in fact exists in an orthorhombic crystal structure as a result of octahedral tilting, but can transition to a fully cubic structure at high temperature in a similar fashion to the phase transitions and tilting seen in the traditional oxide perovskites, like $CaTiO_3$. So, to obtain a direct analogy with $Cs_2AgBiBr_6$, we constructed a '$Cs_2Pb_2Br_6$' double perovskite by replacing Ag and Bi with Pb in the primitive cell of $Cs_2AgBiBr_6$. By using the same structure as $Cs_2AgBiBr_6$, this structure also has the same symmetry and reciprocal lattice, and, as such, allows direct comparison of the two band structures, which are depicted in Figure 4.4, along with charge density isosurfaces of both conduction and valence bands at specific k-points in the Brillouin zone.

The band structure of our '$Cs_2Pb_2Br_6$' is in contrast to that of $Cs_2AgBiBr_6$, and much more similar to those of $CsPbI_3$ or MAPI: the conduction band and valence

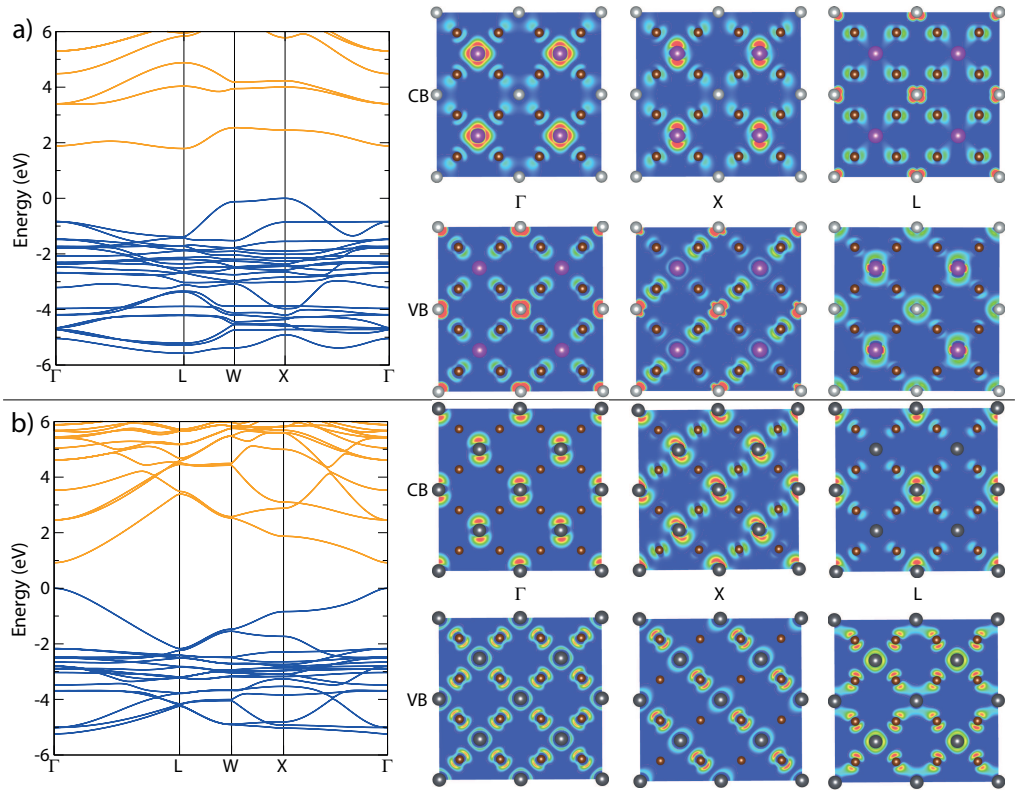

Figure 4.4: HSE06+SOC band structures of a) $Cs_2AgBiBr_6$ and b) '$Cs_2Pb_2Br_6$' ($CsPbBr_3$ in the double perovskite structure), with respective charge density isosurfaces of VBM and CBM, pictured along (110) of the primitive cell and at specific k-points. Silver atoms are in light grey, bismuth in purple, lead in dark grey and bromine in brown. VBM is set to 0 eV, isosurface level set to 0.002 eV $Å^{-1}$.

band are both highly disperse, particularly around the VBM and CBM, which both lie at Γ; both bands are also wider, but especially the conduction band (2.47 eV compared to 0.75 eV in $Cs_2AgBiBr_6$), leading to a narrow band gap of 0.9 eV as well. This increase in bandwidth appears to be the dominant factor in the change in band gap, as half the change in CB width (∼0.86 eV) is roughly equal to the difference in fundamental band gaps (0.87 eV). Thus, two questions arise concerning the double perovskites – why does cation mutation lead to such a reduction in band width and why do the VBM and CBM occur at different points in reciprocal space? To attempt to answer these questions, we must look at the charge densities at each point, as these provide insight into where the electrons in a band will reside, constructing a visual representation of the bonding for a given position and energy. The charge densities, plotted as isosurfaces on the (110) plane of the primitive cell, for the particular k-points Γ, (0, 0, 0) in reciprocal space, X (0.5, 0, 0.5) and L (0.5, 0.5, 0.5), are included in the second half of Figure 4.4.

Table 4.4: Lowest indirect (E_g^i) and direct allowed (E_g^{da}) transitions, with conduction band widths (CBW, determined by the difference in band energy between that at the CBM and at W) and spectroscopic limited maximum efficiencies (SLME) for a film thickness of 200 nm, predicted using HSE06+SOC of Cs_2AgBiX_6 (X = Cl, Br, I) and $CsPbBr_3$ within the cubic double perovskite structure ('$Cs_2Pb_2Br_6$')

Compound	E_g^i/eV	E_g^{da}/eV	CBW/eV	SLME/%
$Cs_2AgBiCl_6$	2.35	2.87	0.58	3.90
$Cs_2AgBiBr_6$	1.79	2.45	0.75	7.92
Cs_2AgBiI_6	1.08	1.79	0.95	12.37
'$Cs_2Pb_2Br_6$'	–	0.92	2.47	17.15

Looking at Γ, which corresponds to fully symmetric interaction in all 3 dimensions, the distribution of the charge density between cation neighbours begins to demonstrate the fundamental differences between these two compositions (in most of the isosurfaces, the charge density contains some contribution from the Br p orbitals – in general, they mostly appear to act as the interaction 'bridge' between cations). In the VBM of $Cs_2Pb_2Br_6$, the bonding pattern appears clearly dominated by the s-like contribution from all neighbouring Pb cations, bridged by Br p. In $Cs_2AgBiBr_6$, on the other hand, the valence band has contribution from the Ag cation, but no contribution from Bi, limiting the interaction to next-nearest neighbouring cations. This similarly occurs in the conduction band – interestingly that of $Cs_2Pb_2Br_6$ appears to purely comprise 'non-bonding' Pb p orbitals, but on every neighbouring cation, while that of $Cs_2AgBiBr_6$ resembles the VBM, but with solely contribution from Bi (with Br p), and none from Ag. This pattern then continues across both X and L, given their symmetry constraints, with contributions from either Bi or Ag, but never both. In terms of the electronics, this appears to be the cause of the narrow band width of $Cs_2AgBiBr_6$ – with only next-nearest neighbour cation contributions, the strength of the interaction will be much reduced and the band energies at Γ and L are similar, leading to the formation of a band with low dispersion in comparison to the strong concomitant interaction in the fully Pb compound.

Looking at the valence band of $Cs_2AgBiBr_6$ at X also aids to explain the alteration in VBM position: unlike the weak interaction at Γ, the VBM at X exhibits electron density on the Ag very reminiscent of a d_{z^2} orbital – which corresponds with the in-phase interaction in 1 dimension, out of phase in the other 2 symmetry at X – together with strong contribution from Br p, but also some Bi s. This much-stronger,

but highly directional, interaction, in comparison to those at Γ, lead to it becoming an extremum in energy, and thus the valence band maximum. So, it appears that by not having a valence s cation on both cation sites, the Ag d and Bi s valence orbitals on the cations are mismatched, and can no longer form strong interactions of the same symmetry, leading to an enforced indirect (and wide) band gap. As these features similarly appear in the electronic structures of the chloride and iodide, this mismatch is inherent to the family, and indeed, may be expected for other d/s combinations such as Au and Sb.

4.3.3 Restoring the direct gap

Given our hypothesis above, one solution to obtain a more suitable electronic structure for solar absorption could be to match valence s cations, thus retaining a direct analogy with the lead halides, as in $Cs_2Pb_2Br_6$, and restoring a direct band gap. Our attention thus fell on the Group 13 elements In and Tl: while both can exist in the 3+ oxidation state, they can (particularly Tl) exhibit 1+ chemistry, with a lone pair similar to that in Pb^{2+} and Bi^{3+}, and so would make excellent candidates to replace Ag and be combined with Bi. With, at the time, no synthesised examples of In or Tl double perovskites, hypothetical structures were constructed by substitution into the $Cs_2AgBiBr_6$ structure and adjustment of the lattice parameters to reflect the new composition, as described in the Methodology for this chapter. The electronic structures of Cs_2MBiX_6 (M = In,Tl; X = Cl,Br) were calculated with HSE06+SOC as with the other double perovskite structures, and the band structures are plotted in Figures 4.5 and 4.6.

It is immediately noticeable that, unlike the Ag/Bi double perovskites, the In and Tl double perovskites all possess direct band gaps at Γ, like $Cs_2Pb_2Br_6$ and the actual hybrid lead halide perovskites. This, as with $Cs_2Pb_2Br_6$, comes from the recurrence of the VBM at Γ – the reasons of which can be made clear when taking $Cs_2TlBiCl_6$ as an example in Figure 4.5 and plotting the charge density isosurfaces in the same manner to Figure 4.4. From these, we can see the clear similarities in the density at Γ to $Cs_2Pb_2Br_6$: while not equal in intensity, the VBM contains contributions from all neighbouring cations, both Tl and Bi, forming a strong cooperative interaction via the Br p and leading to a much higher energy valence band than the interrupted

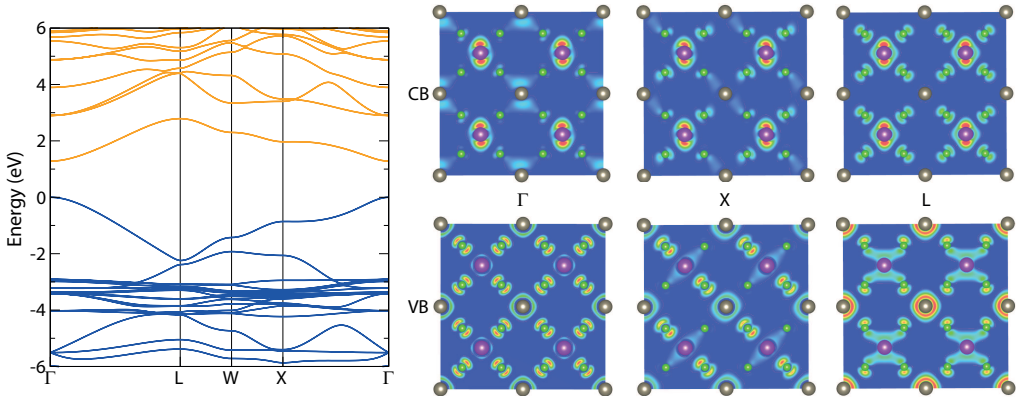

Figure 4.5: HSE06+SOC band structures of $Cs_2TlBiCl_6$, with charge density isosurfaces of VBM and CBM, pictured along (110) of the primitive cell and at specific k-points. Thallium atoms are in light grey, bismuth in purple, chlorine in green. VBM is set to 0 eV, isosurface level set to 0.002 eV $Å^{-1}$.

interaction in $Cs_2AgBiBr_6$, and helping to confirm our hypothesis. Of similar note is the much lower band-gaps seen across the In and Tl halides, in comparison with the silver compounds. Again, this seems a consequence of the restored VBM at Γ but also the much wider conduction band, itself also a result of the stronger interactions available; while the band widths (numerated in Table 4.5) are not quite as large as that of $Cs_2Pb_2Br_6$, possibly due to the slight energy mismatch in In/Tl and Bi states, they are still all 1 eV larger than in the silver bismuth double perovskites, contributing to the lower band gaps. Equally, the higher energy In states in the valence band appear to lead to a further reduced band gap still for $Cs_2InBiCl_6$ and $Cs_2InBiBr_6$ – although the accuracy of these low band gaps must be taken with caution due to the hypothetical determination of their crystal structures. Nevertheless, these band structures demonstrate that within the double perovskite structure, the matching of similar-angular momentum valence orbitals on the B cation sites is crucial for a suitable, direct band gap, and that the indirect gaps of the Cs_2AgBiX_6 compounds are inherent to the family.

To further illustrate the effect this may have on the actual suitability of these materials for photovoltaic applications, we calculated the optical absorption for all the In, Tl and Ag double perovskites, and used this to obtain the spectroscopically limited maximum efficiency (SLME), introduced in Section 3.3.2, which works as a metric for assessing the relative capability of thin film PV materials. The SLME percentages calculated for each double perovskite are included in Tables 4.4 and 4.5. For reference, a target SLME value would be that of $CuInSe_2$, as given in the original

Table 4.5: Lowest indirect (E_g^i) and direct allowed (E_g^{da}) transitions, with conduction band widths (CBW) and spectroscopic limited maximum efficiencies (SLME) for a film thickness of 200 nm, predicted using HSE06+SOC, of Cs_2MBiX_6 (M = In, Tl; X = Cl, Br)

Compound	E_g^i/eV	E_g^{da}/eV	CBW/eV	SLME/%
$Cs_2InBiCl_6$	–	0.28	2.17	10.25
$Cs_2InBiBr_6$	–	0.36	2.03	10.43
$Cs_2TlBiCl_6$	–	1.28	2.24	15.87
$Cs_2TlBiBr_6$	–	0.71	2.22	17.72

paper of Yu and Zunger at 20 % for a film thickness of 200 nm;[186] above this value would indicate a strongly absorbing material and thus a promising candidate for PV. Like the Shockley-Queisser limit that it is based off, the band gap value is one of the key contributing factors to the overall SLME, and hence band gaps outside of the 1.0 eV to 1.7 eV ideal range tend to have low SLMEs, as is the case for $Cs_2AgBiCl_6$ and Cs_2InBiX_6. However, it is notable that even though its indirect gap is only slightly above the ideal, the SLME for $Cs_2AgBiBr_6$ is lower than that of both indium perovskites, despite their very small band gaps – this is a likely consequence of the large separation between the direct and indirect gaps in $Cs_2AgBiBr_6$ weakening absorption. Similarly, even the hypothetical Cs_2AgBiI_6, despite possessing a band gap predicted well within the ideal range, has a lower SLME than both thallium perovskites as a result of a poor absorption coefficient. While these values may not reflect the absolute likely efficiencies for cells, given the approximations involved, they do strongly illustrate the detrimental effect that the inherent indirect gap of the Cs_2AgBiX_6 family can have. Shortly after the publication of the work depicted in this chapter, Xiao *et al.* published their work on lower dimensional and lead-free perovskites, coming to a very similar conclusion to ours on the applicability of the Cs_2AgBiX_6 family: the silver/bismuth compounds are electronically '0D' due to the mismatch between silver and bismuth, while the indium or thallium perovskites with bismuth would be electronically '3D' through the cooperative nearest-neighbour cation interactions, leading to better properties for photovoltaics.[231] The thallium, or indium, double perovskites with bismuth could be stronger solar absorbers however they themselves present additional problems: thallium is itself highly toxic, and thus not an appealing replacement for lead, while indium in the 1^+ state is relatively rare, with oxidation to In^{3+} common. As such, our next consideration would

be thermodynamic stability.

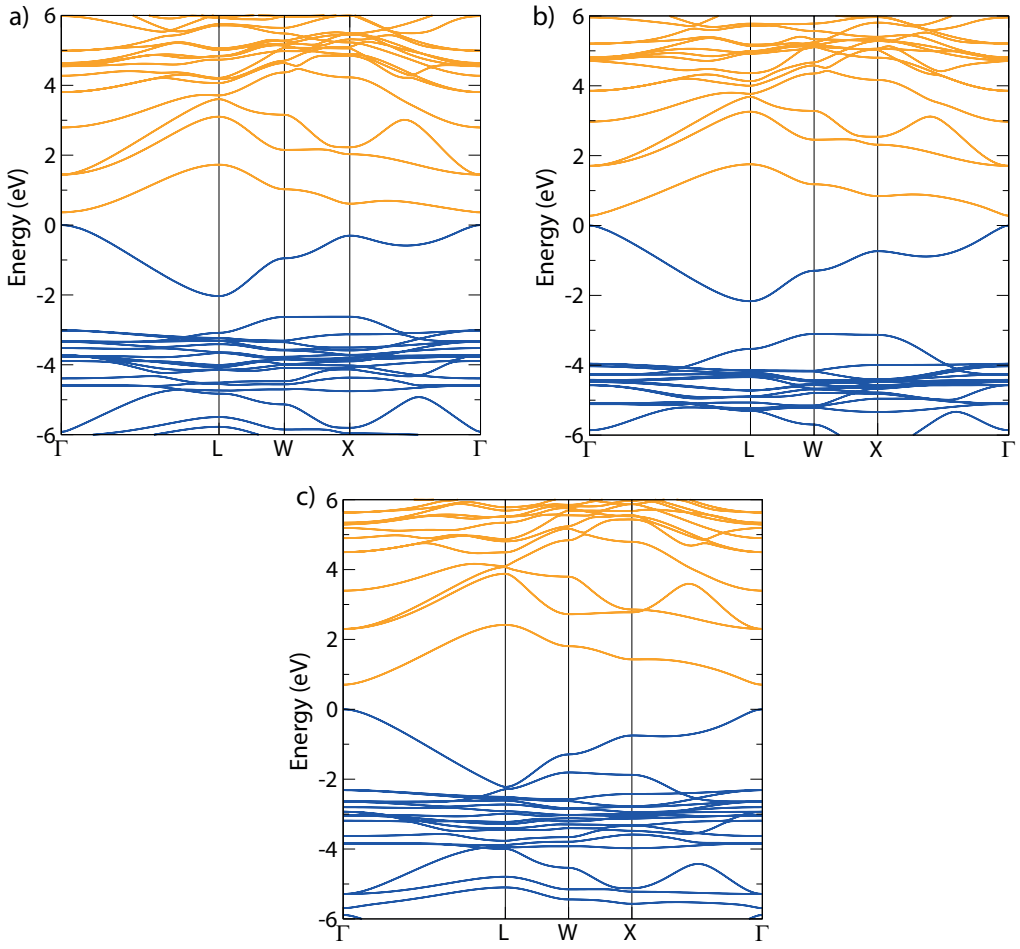

Figure 4.6: HSE06+SOC band structures of a) $Cs_2InBiCl_6$, b) $Cs_2InBiBr_6$ and c) $Cs_2TlBiBr_6$, with valence band in blue, and conduction band in orange. Valence band maximum (VBM) is set to 0 eV.

4.3.4 Methylammonium: A help or hindrance?

In their article on the survey of lead free double perovskites, on noting the indirect band gap of $Cs_2AgBiCl_6$, Volonakis *et al.* suggested that the reinsertion of methylammonium in place of caesium in the double perovskite structure might break symmetry restrictions and allow a direct band gap.[218] In the course of our study on these materials, we also sought to examine the potential effect of methylammonium substitution in these structures. Two approaches were attempted: the first was to recreate the substitution performed by Volonakis *et al.*, although using a supercell of the orthorhombic $Pnma$ structure of $(CH_3NH_3)PbI_3$ (which has a fixed methylammonium position) as the starting structure. This substitution is performed

by replacing Pb in said structure with Ag and Bi, alternating on nearest-neighbour cation sites, and obtaining a hypothetical '$(CH_3NH_3)_2AgBiI_6$' – by doing this we hope to observe whether the Ag-Bi substitution affects (using the iodide rather than chloride structure allows us to compare to the more substantial theoretical characterisation efforts devoted to MAPI than the chloride equivalents). Our second approach was to substitute into the cubic double perovskite structure of $Cs_2AgBiBr_6$, replacing the Cs manually with a methylammonium ion to obtain a '$(CH_3NH_3)_2AgBiBr_6$' structure. This second substitution instead examines the effect of MA in the cubic double perovskite, rather than equivalence with MAPI.

The band structures for these hypothetical compounds were calculated, also using HSE06+SOC, and are plotted in Figure 4.7. Both structures experience loss of symmetry as a result of the substitutions:$(CH_3NH_3)_2AgBiI_6$ lowers from $Pnma$ (which has a single Pb site) to $C2/m$ as a result of the alternate substitution of Ag and Bi, while $(CH_3NH_3)_2AgBiBr_6$ lowers to $P\bar{1}$, as a result of the fixed methylammonium position ($Pm\bar{3}m$ assignment for the high temperature $(CH_3NH_3)PbI_3$ structure relies on a fully rotationally-free methylammonium cation), but to more easily compare to the caesium equivalent, we also calculate its band structure within the special k-points (and appropriate labels) of the original $Fm\bar{3}m$ space group (Figure 4.7b).

From the band structures of '$(CH_3NH_3)_2AgBiBr_6$' we can see that the direct impact of the methylammonium substitution is small – this is perhaps unsurprising given repeated findings that the methylammonium or caesium A cation has very little impact on the bulk electronic structure of the lead halide perovskites, as noted in section 1.3.4, and only generally manifests in more exotic and local properties such as ferroelectric domains or Rashba splitting.[233,234] The (time-reversal) symmetry breaking effect of the methylammonium does appear to remove the degeneracy present in many of the bands, including the conduction band, however the splitting is small, and the band gap remains wide and indirect at 1.75 eV, although the VBM does also swap from X to W.

Unlike the band structure presented by Volonakis *et al.*, we find that our hypothetical '$(CH_3NH_3)_2AgBiI_6$' is predicted to retain an indirect gap of 1.38 eV, with the VBM at A_0 and the CBM at D; however, the direct transition at Γ is fully-symmetry allowed, which is in conjunction with their findings, and at 1.59 eV, does present a

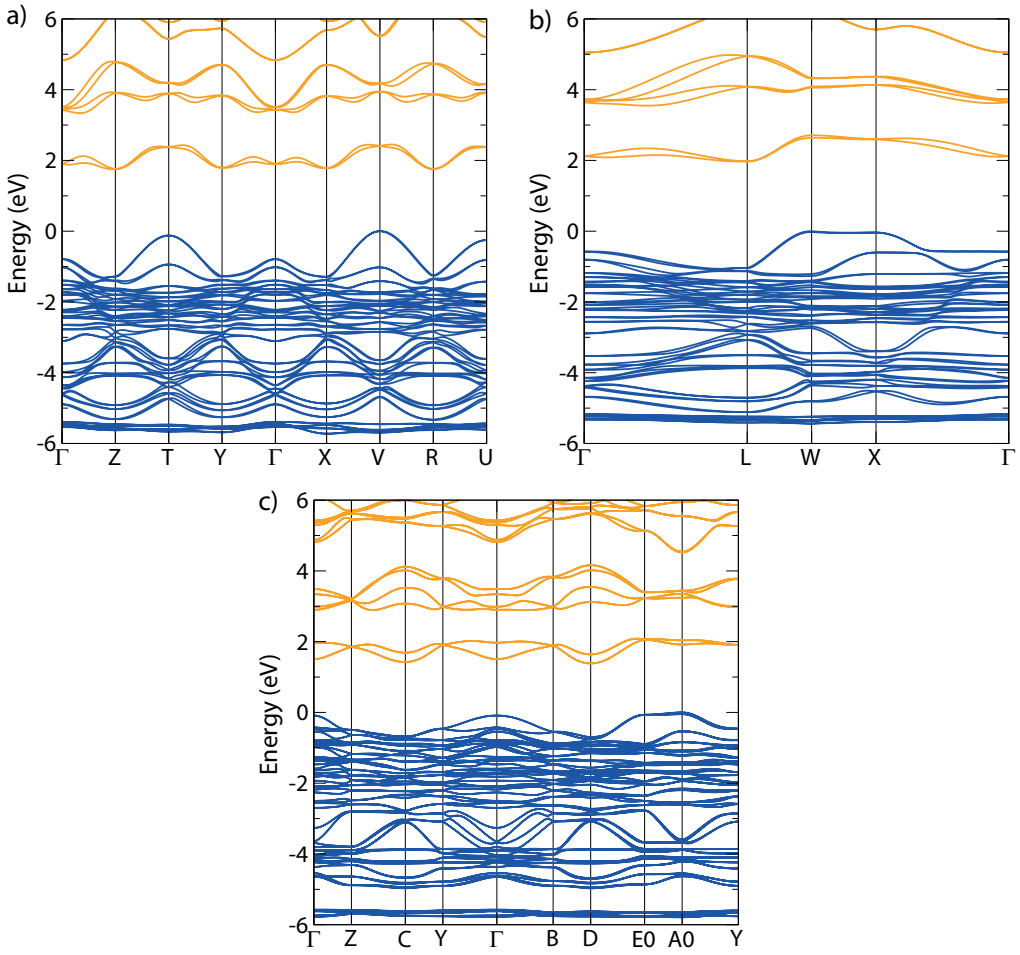

Figure 4.7: HSE06+SOC band structures of a), b) '$(CH_3NH_3)_2AgBiBr_6$' (substitution of MA for Cs in the primitive cell of the cubic $Cs_2AgBiBr_6$ structure),[217] and c) '$(CH_3NH_3)_2AgBiI_6$' (substitution of Ag and Bi for Pb in the $Pnma$ low temperature structure of $(CH_3NH_3)PbI_3$)[232] with valence band in blue, and conduction band in orange. a) uses the $\mathbf{k}$-point path and labels of the lowered primitive triclinic space group, while b) uses the F-centred cubic high-symmetry lines (in analogy to $Cs_2AgBiBr_6$) for $(CH_3NH_3)_2AgBiBr_6$; c) uses the k-points from the lowered C-centred monoclinic space group of the relaxed '$(CH_3NH_3)_2AgBiI_6$' structure. VBM is set to 0 eV.

somewhat viable electronic structure for a PV absorber. As such, it does appear that the direct band gap of the already symmetry-broken orthorhombic MAPI structure is not strongly affected by substitution of Pb for Ag and Bi. Nevertheless, the utility of this approach for predicting a real-world compound is predicated on that particular octahedral tilting being viable for the Ag/Bi double perovskite at operating temperatures, whereas all currently synthesised examples appear to occupy a fully cubic (non-tilted) structure. Overall, these results do however support our electronic argument in the light of the report of $(CH_3NH_3)_2TlBiCl_6$ from Deng *et al.*[225] – the

direct band gap that Deng *et al.* observe is a result of the matching of ns^2 cations, and not related to methylammonium substitution into the cubic double perovskite structure.

4.3.5 Stability

As highlighted in the introduction, poor long-term stability has been a major drawback to the widespread application of the methylammonium lead halides in devices and a significant obstacle to overcome. Additionally, despite inherent indirect gaps, both of our hypothetical iodides constructed in this report do present band gaps within the appropriate range for use as absorbers – however at the time of study, neither moiety had been experimentally realised. As such, the assessment of thermodynamic stability was essential to confirming whether the Cs_2AgBiX_6 family could present an improvement on the lead halides in sustainable and long-term applications and also as to whether such iodides might be synthesisable.

The total energies of all known and crystallographically characterised competing phases of the Cs_2AgBiX_6 were calculated using PBEsol, and the program CPLAP[194] was used to compare the formation energies of the silver-bismuth double perovskites with those of the competing phases to determine whether they were thermodynamically stable. $Cs_2AgBiCl_6$ and $Cs_2AgBiBr_6$ were both found to be stable, however the hypothetical cubic Cs_2AgBiI_6 was unstable with respect to decomposition, reflecting the synthetic observations of the chloride and bromide, but not the iodide. On closer examination of the relative energies, this difference in stability appeared to primarily result from the decomposition pathway:

$$2\,\mathrm{Cs_2AgBiX_6} \xrightarrow{\Delta \mathrm{E}_r} \mathrm{Cs_3Bi_2X_9} + 2\,\mathrm{AgX} + \mathrm{CsX} \tag{4.3}$$

with a $\Delta E_r = -0.41\,eV$ per formula unit. Notably, the shift from X = Cl, Br to X = I coincides with a major structural change in the relative $Cs_3Bi_2X_9$ structure – while $Cs_3Bi_2Cl_9$ and $Cs_3Bi_2Br_9$ both occupy a defect perovskite structure (analogous to the lead halide structure, but with 1 in 3 Bi cations missing due to the higher valence), $Cs_3Bi_2I_9$ occupies a '0D' structure with dimerised $[Bi_2I_9]^-$ ions – and it appears that the energy of the double perovskite to the $Cs_3Bi_2X_9$ structure is much

higher in the iodide.

Table 4.6: Decomposition energies of the double perovskites, using the pathway in Equation 4.3

Compound	ΔE_r/eV
$Cs_2AgBiCl_6$	+0.57
$Cs_2AgBiBr_6$	+0.38
Cs_2AgBiI_6	–0.41
$(MA)_2AgBiI_6$	–0.10
$Cs_2InBiCl_6$	+0.01
$Cs_2InBiBr_6$	–0.04
$Cs_2TlBiCl_6$	–0.05
$Cs_2TlBiBr_6$	–0.21

While thermodynamic instability does not necessarily discount the potential kinetic stabilisation and synthesis of Cs_2AgBiI_6, as with $(CH_3NH_3)PbI_3$, it is likely to lead to significant issues with decomposition in ambient or working conditions, and poor longevity of devices without additional modification. The decomposition energies for the other double perovskites considered in this study are also included in Table 4.6. It is evident that, unfortunately, while possessing more ideal electronic structures than the silver-bismuth double perovskites, the In and Tl double perovskites are unlikely to be formable due to their instability towards this decomposition pathway. Similarly, the hypothetical $(MA)_2AgBiI_6$ is also unstable, again indicating that the double perovskite iodides in general, while potentially possessing band gaps in the range viable for PV, are less likely to be formable, and even if they can, may well suffer similar stability problems to MAPI. Since this work was performed, Xiao *et al.* have further examined the stability of the hypothetical In/Bi perovskites experimentally and theoretically, finding that further thermodynamic competition with In(III) compounds mean that the In(I)/Bi double perovskites are all likely to undergo reduction and thus unlikely to be synthesisable,[235] further supporting our conclusion here that In(I) double perovskites will not be viable. The groups of Snaith and Giustino have also studied this area, noting the necessity to use In and Bi to obtain electronic structures suitable for PV, and proposing that In(I) perovskites might instead be stabilised through cation alloying between caesium, methylammonium and formamidinium, as in the lead perovskites.[236]

4.3.6 Disorder

One final consideration to be made was that with somewhat similar ionic radii (115 pm for the Shannon ionic radius of Ag^{+} and 103 pm for Bi^{3+})[237] and identical coordination environments, Ag/Bi cation disorder may be possible in these materials. McClure *et al.* did note the lack of observable signatures for cation disorder in their refinements of $Cs_2AgBiBr_6$, however such disorder is highly common in oxide double perovskites.[238,239] Cation disorder has been predicted to have significant effects on band gaps, and also V_{oc}, in solar absorbers such as $ZnSnN_2$,[240,241] $ZnSnP_2$,[242] and most notably Cu_2ZnSnS_4, where it has previously been cited as a major contributor to the large V_{oc} deficit experienced in cells via large Urbach tailing and deep antisite defects, and is thought to be a major obstacle to further improvement.[243–245] In order to estimate the relative effect of cation disorder in the silver bismuth halide double perovskites, we constructed two 3×3×3 supercells of $Cs_2AgBiBr_6$: one with the alternate ordering seen in the recorded crystal structures, and the other a 'special quasirandom structure' (SQS), representing a 'maximally disordered' cell.[246,247] Unlike randomly generated alloy structures, an SQS closely replicates the local correlation functions of the true disordered phase, and so provides the best approximation of the fully disordered state in a single periodic supercell. Despite atomic correlations only being considered over the first few coordination shells, the calculation of an SQS can still give relatively accurate properties for disordered semiconductor alloys.[248,249] The ordered and SQS cells were internally relaxed using the PBEsol functional and their energies compared. Of the two, the ordered supercell was lower in energy and can thus be assumed to be the ground state, supporting the conclusion of McClure *et al.* that their sample of $Cs_2AgBiBr_6$ demonstrated no cation disorder. The difference in energy between the supercells was only $\Delta E = 29\,meV/atom$, which is close to kT at room temperature (25.7 meV) and indicates that disorder could be a possibility when the negative entropy associated with disorder is included.

Using analogy with a regular solution model, as described in the Methodology, it was possible to calculate an approximate order/disorder temperature, at which the entropic contribution will win out as disorder will be thermodynamically favourable, and the structure will undergo a phase transition. This was calculated to be 477 K – while this is low enough to suggest that the structure will not spontaneously dis-

order under normal working conditions, it is sufficiently low to be accessible under many synthesis conditions, such as in a furnace or post-processing annealing steps. To assess how this might affect the electronic structure of $Cs_2AgBiBr_6$, we calculated the direct VBM-CBM transition at Γ for both supercells using PBEsol+SOC (HSE06+SOC was not possible for supercells of such size, while PBEsol is likely to consistently underestimate the band separation to a similar amount in both structures). In the ordered supercell, this transition was found to be at 1.504 eV, while in the disordered supercell, it was 0.256 eV: this is a significant reduction – applied to the HSE06+SOC gaps above, this change would result in the gap of $Cs_2AgBiBr_6$ narrowing to less than 0.5 eV. We could thus suppose that, if different samples of $Cs_2AgBiBr_6$ might contain different levels of cation disorder depending on their synthesis conditions, this could lead to large differences in band gap, and could partly explain the 0.24 eV variance seen in the reported experimental values for $Cs_2AgBiBr_6$.

4.4 Conclusions and Impact

In this chapter, we have examined the Cs_2AgBiX_6 family of compounds, and calculated their electronic structures using hybrid density functional theory, enabling us to thoroughly assess their suitability as nontoxic, stable replacements for the methylammonium lead halides. Our investigation of their orbital makeup has revealed a fundamental mismatch of Ag d and Bi s orbitals at the valence and conduction band edges in these double perovskites, causing their band gaps to be inherently indirect and large due to a reduction of the conduction bandwidth and displacement of the VBM in comparison with a analogous Pb compound. Our replacement of the Ag by ns^2 1+ ions such as In^+ or Tl^+, demonstrates that the matching of I/III ns^2 cations is able to restore a more suitable, direct band gap for PV through the s–s concomitant nearest-neighbour cation interactions. Substitution of Cs by $(CH_3NH_3)^+$ does not lead to a restoration of the band gap through symmetry breaking in the two structure types that we have investigated. The calculated SLME for these structures (synthesised and hypothetical) follows these trends in band structures, and the value for the indirect silver-bismuth double perovskites are low. In addition, we have calculated the full thermodynamic stability of the Cs_2AgBiX_6 family, and find that the extant members $Cs_2AgBiBr_6$ and $Cs_2AgBiCl_6$ are stable, while Cs_2AgBiI_6 is predicted to

decompose to ternary and binary constituent iodides, perhaps explaining current inability to synthesise it. Equally, many of the hypothetical compounds examined in the report are also predicted to be unstable to a similar decomposition pathway, potentially limiting further efforts to expand the lead-free double perovskites. Finally, the energy change in Ag/Bi disorder is calculated and used in a regular solution model: while full disorder is not predicted at room temperature, it may be accessible during synthesis. With complete Ag/Bi disorder predicted to cause a $\sim$1 eV reduction in band gap, this may need to be an additional consideration for the application of these materials. Considering all these factors, it is evident that the Cs_2AgBiX_6 family possess a number of inherent limitations that strongly impact their potential to replace the methylammonium lead halides as solar absorbers; to do so either matching of ns^2 cations on the perovskite B site, or potentially moving beyond the double perovskite structure altogether may be necessary.

Since the publication of our work, the rapid nature of the field has lead to a number of further publications on the topic since, as noted in the sections above. Some interest has also arisen in newly synthesised $Cs_2InAgCl_6$, which uses more stable In(III) in place of bismuth, and also has a direct band gap from the matching of valence d^{10} cations in place of ns^2 to similar effect, albeit with low valence band dispersion from the localised d orbitals and a wide gap of 3.3 eV.[250,251] However, it appears to be understood that the search for Pb-free perovskite solar absorbers must move beyond the Cs_2AgBiX_6 family.

The results included in this chapter were written up as a paper, which was accepted and published in ACS Energy Letters.[252] *A selection of the figures in this chapter have been adapted from those included in this paper.*

Chapter 5

Results II: Silver Copper Sulfides

5.1 Introduction: Thinking about thin film photovoltaics

As mentioned in Section 1.3.2 of the introduction, thin-film materials such as CdTe, GaAs and $Cu(In, Ga)Se_2$ (CIGS) comprise the so-called 'second-generation' PV materials and have seen an increase in market share within the last two decades as cell efficiencies have been raised to approach or even exceed those of silicon:[1,35] over 21 % for CdTe and CIGS, and 28.8 % for GaAs.[32] All of these materials possess direct band gaps, leading to higher absorption than indirect-gap Si, not only leading to much thinner layers of absorber material and thus cheaper production costs, but also allowing much greater freedom in both synthesis/deposition techniques and cell architecture – both CdTe and CIGS have been used to produce solar cells on flexible polymer substrates,[253,254] opening the way to lightweight, bendable PVs as well as numerous other potential applications beyond those of fixed, roof-bound panels.

The advantages of thin-film materials over silicon are finite, however. While historically, the high energetic cost of producing silicon has meant thin-film materials have had a significant cost advantage, this gap has narrowed in recent years as silicon feedstock has become cheaper and cell engineering has improved.[4,5] Additionally, with the photovoltaic industry expanding rapidly, questions remain over the availability and sustainability of the component elements required to synthesise the thin-film compounds. Cd and As are both toxic elements,[255,256] and hence provide concerns over the widespread usage of materials containing them. Recent efforts are still being made, however, to reduce the environmental impact of CdTe production, such as the replacement of the dopant material $CdCl_2$ with the benign and cheap $MgCl_2$ with minimal efficiency loss.[257] In and Te (and to a lesser extent, Ga) are both very low in abundance in the earth's crust;[258] this can lead to higher feedstock costs for those elements, but also raise the question – are current sources and production methods sufficient to account for the growing demand for PV?[259]

For this reason, there is still a high degree of research and industrial interest in finding other *non-toxic*, *earth-abundant* and highly efficient solar absorber materials.[13] While the hybrid lead halide perovskites have become some of the most widely studied materials fitting these target properties (and those elaborated on in Section 1.2.5) due to their rapid and unprecedented success, their instability is still a major barrier towards widespread commercialisation, and partially results from their halide

nature, which tend to be highly soluble in water and other solvents, and hence can lead to degradation.[124,260] This instability is, in general, much less common for inorganic sulfides, selenides and nitrides, which are also generally abundant and non-toxic, and represented some of the most popular inorganic earth-abundant absorbers prior to the rise of the lead halide perovskites. Compounds such as the zinc tin pnictides ($ZnSnN_2$, $ZnSnP_2$),[240,242] the copper bismuth and antimony chalcogenides ($CuSbS_2$, Cu_3BiS_3)[261–263] and bismuth chalcohalides (BiOI, BiSI)[264,265] have all been proposed and studied for their optical absorption and electronic structure through both theoretical and experimental methods, however, in general, cell efficiencies remain low, often less than 5 %.[13] These materials are of current research interest within the group, and have been the subject of publications, though these studies will not be detailed further here.[21,185,241,266,267]

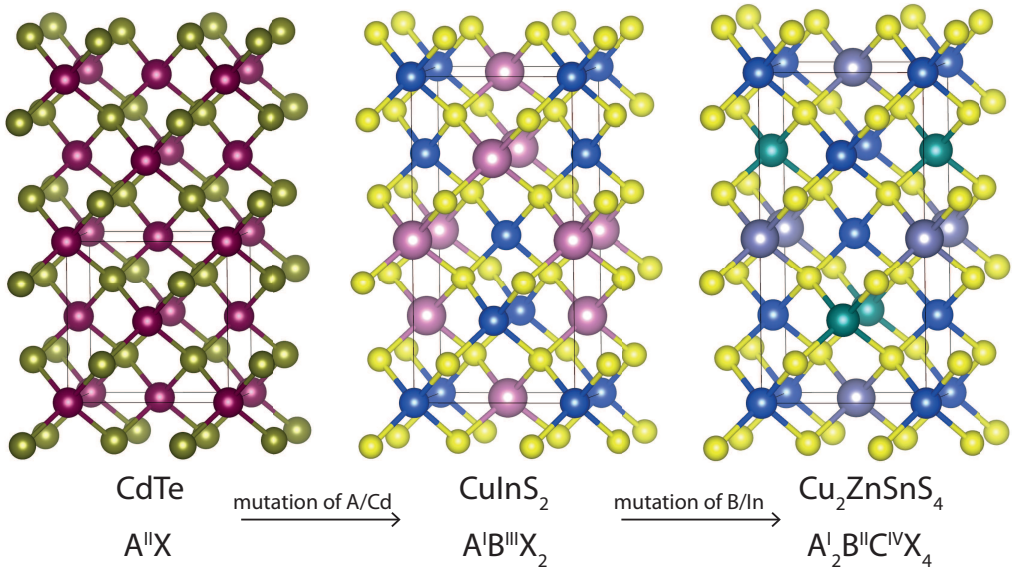

Figure 5.1: Diagram representing how cation mutation results in the formation of CZTS (kesterite) from the basic II-VI zinc blende structure, while retaining the same anionic lattice in all 3 compounds. A single unit cell is marked in black in each structure, and the following atom colours are used: Cd in maroon, Te in olive, Cu in blue, In in pink, Zn in teal, Sn in mauve and S in yellow.

Some thin-film materials, however, have seen more substantial development in efficiencies. The champion 3rd-generation PV absorber prior to the rise of the hybrid lead halide perovskites was Cu_2SnZnS_4 (CZTS), which for the highest efficiencies is often alloyed with selenium to give $Cu_2SnZn(S,Se)_4$ (CZTSSe) : after cell efficiencies of 9.6 % were reported by IBM in 2010,[268] it drew significant research attention for its capacity as a high efficiency absorber with all its constituent elements being

earth-abundant and relatively non-toxic. From a theoretical standpoint, its successful electronic structure is inherited through cation mutation from the already successful $CuInSe_2$ (itself similarly analogous to the highly successful III-V semiconductors) – by replacing In(III) in the chalcopyrite structure with Sn(IV) and Zn(II), you can obtain the 'kesterite' CZTS structure (Figure 5.1), retaining tetrahedral coordination for all cations, and thus, the electronic structure remains similar, with a $\sim$1.5 eV direct band gap, suitable for absorption.[243,269] Despite further improvement studies breaking the 10 % barrier, the record efficiency for CZTSSe plateaued for nearly 4 years at the publication, also from IBM, of a 12.6 % efficiency cell achieved through optimizing J_{sc} by modulating the thickness of buffer and TCO layers together with targeting, Cu-poor and Zn-rich conditions in a hydrazine solution-based synthesis.[270] The major barrier towards improving CZTS efficiencies has been roundly considered to be the V_{oc} deficit – the difference between the cell's V_{oc} and the theoretical limit determined by the band gap of the absorber – which has been at least in excess of 0.5 eV in many cells. Even in such record-efficiency cells, V_{oc} has been less than 50 % to 60 % of the expected value from the Shockley-Queisser limit; in comparison, J_{sc} could be >85 %.[270] The cause of this V_{oc} deficit has thus been of great interest, and a number of explanations have been proposed, including Cu/Zn disorder and resultant recombination centres or Urbach tailing, poor contacts with either Mo or the CdS buffer layer and the presence of further defect complexes or domains of competing secondary (non-kesterite) phases.[245,271,272] Recent studies have suggested some of these issues, particularly disorder and band tailing, can be improved upon extrinsic passivation through Cd or Na doping[273,274] and there has been recent report of an unpublished cell efficiency of 13.8 %;[272] nevertheless, these barriers, even in champion materials, do strongly indicate that there is still great interest in the search for new non-toxic earth-abundant solar absorbers with fewer drawbacks.

The silver copper sulfide Ag_3CuS_2, also referred to as the mineral jalpaite, was recently the subject of investigation in a ITO/ZnO/Ag_3CuS_2/P3HT/Pt cell as the absorber layer, achieving an efficiency of 2.01 %, a significant improvement on the bare ZnO-nanotube electrode.[275] Interestingly, both the ZnO nanorod arrays and the Ag_3CuS_2 layer were both deposited entirely in a low-temperature solution synthesis, demonstrating the possibility for relatively scalable and inexpensive manufacture. However, the fill factor of the cell was still relatively low at only 0.57, indicating the

presence of parasitic resistances and recombination limitations on the V_{OC}. Another study also reported the preparation of a ITO/Ag_3CuS_2/P3HT cell, albeit reporting n-type Ag_3CuS_2, and utilising an Ag back contact – the resulting cell had a poorer efficiency of 0.79 %, primarily resulting from a low V_{OC} of 260 meV and fill factor of 0.43.[276] Nevertheless, these reports were promising for a newly developed solar absorber material, and encouraged our interest and investigation of these materials as potential thin-film photovoltaics.

AgCuS, an alternative Ag-Cu-S moiety to Ag_3CuS_2 and called stromeyerite in its mineral form, has been examined for a high temperature phase transitions to the ionically conductive α and δ phases, with mobile copper and silver ions,[277] and has also been the subject of crystallographic interest for this reason: Baker *et al.* confirmed the assignment of the room-temperature (β) phase space group of $Cmc2_1$ through electron diffraction while also discovering the existence of a lower-symmetry low temperature phase below 120 K,[278] while Trots *et al.* further examined the thermal expansion and superionic transitions between 361 K to 439 K.[279] Jansen and co-workers have also examined the behaviour of AgCuS under pressure – finding two high pressure phases, supported with DFT calculations. More recently, the high-temperature phase transitions of AgCuS have been of interest for device applications due to giant observed p–n–p type conduction and Seebeck coefficient switching through these structural transitions, present in the bulk material, but absent in nanocrystals.[280,281] The study by Guin *et al.* also found β-AgCuS to be a semiconductor with a band gap of 0.9 eV from optical diffuse reflectance, and their theoretical prediction using PBE+U of 0.92 eV.[280] The room temperature structure of AgCuS itself possess some interesting features, and is depicted in Figure 5.2. The Ag^+ ions exhibit the linear coordination to sulfur somewhat typical of the oxidation state (found in both aqueous complexes[282] and pseudohalide solids[283]) in a 'zig-zag' like pattern; the Cu^+ meanwhile form the remainder of the sulfurs' coordination sphere, being coordinated itself in a trigonal planar arrangement perpendicular to the Ag-S chains. This unusual linear coordination environment, or distortion of an octahedral environment towards two of the ligands, is relatively common in Ag^+ compounds, and was rationalised by Orgel to be a result of $s - d$ hybridization – hybrid orbitals with density concentrated along the one axis may be formed through the combination of d_{z^2} and s orbitals.[284]

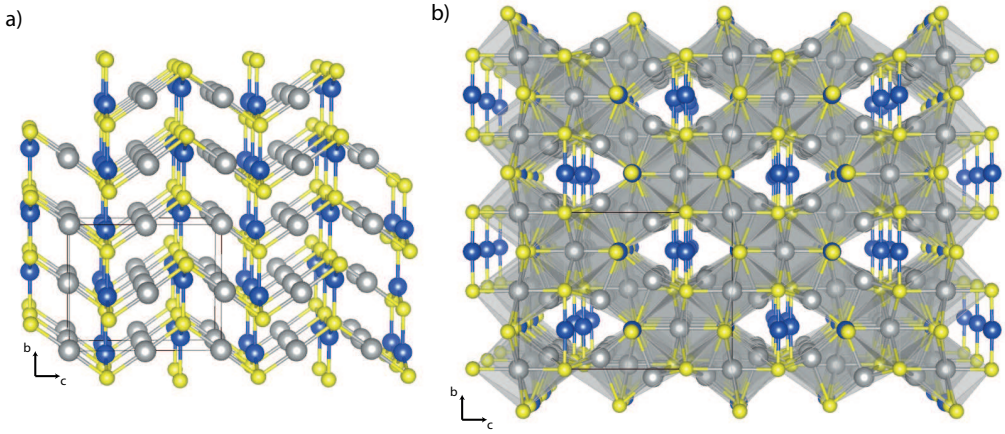

Figure 5.2: Crystal structures of a) RT-AgCuS and b) RT-Ag_3CuS_2. A single unit cell is marked in each, and the following atom labels are used: Ag atoms in grey, Cu in blue and S in yellow.

Ag_3CuS_2 has also been the subject of multiple crystallographic studies: Baker *et al.* determined the tetragonal structure of room-temperature phase through powder XRD, finding an $I4_1/amd$ space group, while finding that, like AgCuS, both cations disorder and it becomes ionically-conducting;[285] Trots *et al.* further investigated its full phase behaviour with temperature using a combination of neutron and synchrotron diffraction, finding further low and high temperature phases – notably, that Ag_3CuS_2 transitions to an $I4_1/a$ phase at 250 K.[286] As a sulfur-rich stoichiometry on the phase boundary between Ag_2S and Cu_2S, it follows that the Ag_3CuS_2 structures have a increased Ag-S coordination, while lower Cu-S coordination: the $I4_1/amd$ phase of Ag_3CuS_2 (from here, denoted RT-Ag_3CuS_2 has two silver environments – Ag1 sits in a [4+2] coordination site, forming an octahedron with neighbouring sulfur atoms that is distorted by a tilted axis, while Ag2 sits in a distorted tetrahedral site that face-shares with the Ag1 octahedron. Together, these environments form an "X" shaped structure, which can be viewed along (010) in Figure 5.2, and the Cu lie in the interstitial spaces, linearly coordinating to sulfur. The low temperature $I4_1/a$ phase (LT-Ag_3CuS_2) forms a very similar structure, with identical Cu sites, but with both Ag sites further distorted from regular polyhedra. While only RT-Ag_3CuS_2 is relevant for general cell operating conditions (room temperature and above), and so will solely be referred to as Ag_3CuS_2 in this chapter, LT-Ag_3CuS_2 was still examined in this study to provide some context on how the distorted environment of Ag could affect the electronic structure.

We considered both AgCuS and Ag_3CuS_2 to be emergent materials that could possess advantageous properties for photovoltaics, and with potential low-temperature synthesis method and containing non-toxic elements, could become emergent materials for solar absorption. Thus, this chapter features our investigation into predicting the electronic structures and optical behaviour of both silver copper sulfides and examining their relative potential to be part of a photovoltaic device.

5.2 Methodology

All structures examined in this chapter were studied using multiple density functionals, both at the GGA and hybrid DFT levels: PBEsol, PBEsol+U, HSE06 and PBE0 were all used to first relax the structure towards equilibrium geometry and then to calculate the electronic structure. A range of functionals were used due to the minimal prior theoretical study of the silver copper sulfides, and so there was necessity to judge which method might be most suitable through comparison with the work of our experimental collaborators. As copper is a first row transition metal, its strongly localised and correlated $3d$ electronic states are most susceptible to self-interaction error inherent in DFT, and so can often have particularly significant errors in their energetics. The GGA+U method is commonly used to circumvent this error, by installing an energetic penalty that acts against electron delocalisation, analogous to the Hubbard U parameter, on those particular d states, which then acts to lower them in energy and achieve a more accurate predicted band gap. For this study, we utilised a U value of 5.17 eV for the Cu $3d$ states and Ag $4d$ states, a magnitude which has been used to accurate effect previously in both Cu(I) and Ag(I) materials.[287,288] Santamaria-Perez *et al.* also used a U value of 5 eV in their supporting PBE+U calculations on the high pressure phases of AgCuS, albeit finding a systematic overestimation of lattice parameters.[289] Alternatively, as explained in Chapter 2, by including exact Hartree-Fock electron exchange, hybrid functionals such as HSE06 or PBE0 have been observed to counteract some of the self-interaction error from DFT even in highly localised systems, and give accurate measurements of band gaps for transition metal semiconductors.[290,291] Each structure was geometrically optimized using the 4 functionals above and then electronic structures calculated from those relaxed structures. Convergence testing was per-

formed across the 3 structures (AgCuS, RT-Ag_3CuS_2 and LT-Ag_3CuS_2) and it was found that a cutoff energy of 350 eV and a k-point mesh density of 0.02 Å along each reciprocal cell length was sufficient to give total energies within 1 meV per atom. For the geometry optimizations, the forces on each atom were reduced until below 0.01 $Å^{-1}$. The optical properties of both AgCuS and Ag_3CuS_2 were calculated using the Furthmüller method to calculate the high-frequency dielectric function, from which the absorption coefficient is derived.[184] The valence band alignment of AgCuS was performed using the core-level alignment approach developed by Wei and Zunger,[180] as further described in Section 3.2.4.

Details of the experimental methods used to obtain results included in this chapter are included in the Appendix.

5.3 Results and Discussion

5.3.1 Theoretical Investigations

Structural Optimization

The crystal structures of AgCuS and Ag_3CuS_2 were obtained from the ICSD, using the recorded structures from the studies by Trots *et al.* in both cases.[279,286] These structures were then optimized using a Quasi-Newton algorithm to reduce the forces within the structure using the 4 functionals PBEsol, PBEsol+U (with correction on both Ag and Cu), HSE06 and PBE0. The resultant lattice parameters for AgCuS and RT$-Ag_3CuS_2$ are detailed in Tables 5.1 and 5.2.

Table 5.1: Calculated lattice parameters of AgCuS, percentage difference from experiment or experimental error in brackets. All cell angles are retained at 90°

	a (Å)	b (Å)	c (Å)
PBEsol	3.9262 (−3.37 %)	6.6847 (0.85 %)	8.0361 (0.81 %)
PBEsol+U	3.9489 (−2.81 %)	6.5864 (−0.63 %)	7.9567 (−0.18 %)
HSE06	4.0422 (−0.52 %)	6.7522 (1.87 %)	8.4311 (5.77 %)
PBE0	4.0399 (−0.58 %)	6.7404 (1.69 %)	8.4181 (5.61 %)
Experiment[279]	4.0633(2)	6.6281(4)	7.9713(4)

For the structure of AgCuS, all four functionals have issues: PBEsol and PBEsol+U both underestimate the a parameter significantly (usually, PBEsol has been able to

reproduce lattice parameters to within 1 % to 2 %), and while PBEsol slightly overestimates the other two parameters, the U correction results in an overall improvement in the magnitude difference from the experimental value on all 3 parameters. Both hybrid functionals perform similarly, matching the experimental value of a well, but overestimating b and c, the latter by a substantial margin. It is difficult to rationalise such differences from experiment, especially when the most deviant lattice parameter in each case differs by functional. We can note that Guin *et al.* published a phonon dispersion curve of AgCuS in their study on the bulk material, finding multiple low energy modes, and a number of negative frequency, or imaginary, modes – these can represent potential pathways for the structure to distort to reach an otherwise lower-energy nuclear configuration. Guin *et al.* note that one of these is reflective of the low temperature phase transition, while the other two reflect weak instabilities, suggesting a shallow potential energy surface; a soft material such as this will then be difficult to replicate exactly at near-room temperature given the absence of any temperature effects in the DFT simulations.

Table 5.2: Calculated lattice parameters of Ag_3CuS_2, percentage difference from experiment or experimental error in brackets. All cell angles are retained at 90°

$I4_1/amd$	a (Å)	c (Å)
PBEsol	8.2279 (−4.85 %)	12.2428 (3.86 %)
PBEsol+U	8.2578 (−4.51 %)	12.1745 (3.28 %)
HSE06	8.8350 (2.17 %)	11.8013 (0.11 %)
PBE0	8.7969 (1.73 %)	11.8239 (0.30 %)
Experiment[286]	8.6476(5)	11.7883(8)

The structure of Ag_3CuS_2 on the other hand sees a clearer distinction between the DFT and hybrid methods. PBEsol severely underestimates the a parameter while overestimating the c parameter by almost the same percentage difference (even more similarly in terms of the actual cell length, deviating by 0.42 Å and 0.45 Å respectively). PBEsol+U, as with AgCuS, improves upon the PBEsol values albeit by a smaller margin and still represents a much less accurate recreation of the structure than the two hybrid functionals, which only overestimate the a parameter by no more than 2.2 %, and the c parameter by less than 0.5 %. As such, the minimum of the hybrid functional PES appears to more accurately coincide with the experimentally determined structure for Ag_3CuS_2.

In all, none of the four functionals or methods appears to offer a systematically more accurate description of both silver copper sulfide structures simultaneously, despite the DFT and hybrid methods varying from the experimental values in contrasting manners. Further testing was performed with uncorrected LDA and PBE functionals, however when relaxed, these were even more divergent from the experimental lattice parameters than PBEsol and HSE06 respectively. As a result, given the lack of a consistent structural description and for internal consistency, for each functional the following electronic structures were calculated on the structure optimized using that same method.

Densities of States

The electronic density of states can be particularly useful when studying compounds with relatively little prior research in the literature, as the determination of which electronic states dominate both the conduction and valence band edges can provide important information on how the crystal structure and the individual elements within it contribute to the overall electronic behaviour of the system. The DOS of AgCuS, calculated with the four different theoretical methods, is plotted in Figure 5.3. The most notable features in all 3 diagrams are the localized d states of both Ag and Cu in the valence band, which appear as narrow, high intensity peaks characteristic of localized states, as they will only weakly interact with other orbitals (particularly the S p) and lead to a relatively tight distribution of band energies. Another notable behaviour is the variation of these peaks in energy, which reflect the relative strength of the different methods to alleviate the self-interaction error, as explained above: PBEsol has no correction, and so the bulk of d states are high in energy; when adding the U parameter, this 5 eV energy penalty to delocalisation causes a more correct energetic behaviour to be realised, and the peak in the d states in the valence band reduces in energy by over 1 eV; the hybrid functionals only partially adjust for the self-interaction (with only 25 $\%$ exact HF exchange) and so the d orbitals are reduced in energy, but by less than in the U correction.

Overall, even with the variation in d state behaviour, the overall partial DOS contributions to the bands are consistent between the four methods: the valence band is dominated by the Ag and Cu d states, with significant S p contribution at the

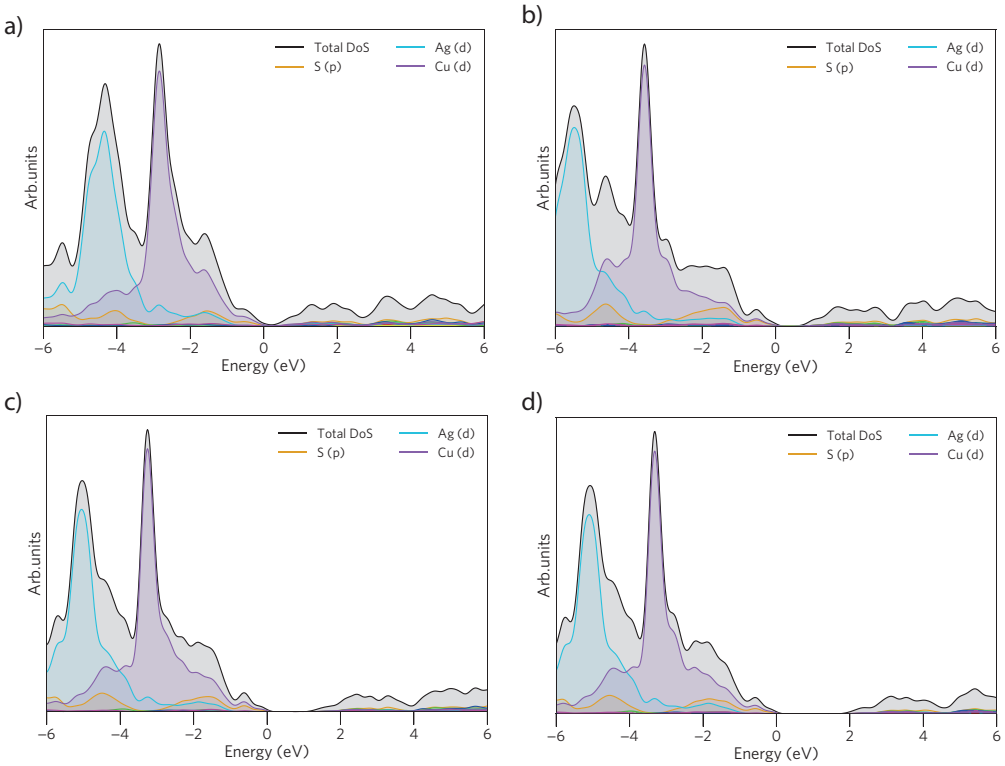

Figure 5.3: Total and Partial Density of States diagrams of AgCuS, using a) PBEsol, b) PBEsol+U, c) HSE06 and d) PBE0; individual partial DoS are labelled in legends, Energy $= 0$ eV is set to valence band maximum.

valence band edge (but notably, much weaker contribution where the d states are at their most-localized, helping to confirm our judgement that those states are relatively non-bonding). At the valence band maximum itself, the Ag contribution becomes minimal, and those states appear to be purely a mixture of Cu d and S p. The conduction band contributions are more disparate and equal between the elements: a combination of Cu d, S s and Ag s states make up the conduction band minimum, but other states also appear to be involved. These representations are consistent with the valence contributions that would be expected from Ag^+ and Cu^+ (both with a filled 3/4 d^{10} valence shell) and S^{2-}, with a filled valence $3p$. The contribution of both Ag s and d to the band edges is also consistent with Orgel's aforementioned bonding prediction for linear Ag coordination.[284] The density of states for Ag_3CuS_2, depicted in Figure 5.4 shows similar trends to those in AgCuS.

Like AgCuS, the general shape of each DOS is similar, with the primary difference between functionals being the position of the non-bonding Ag/Cu d states. The shift of these states to lower in energy in both the PBEsol+U and hybrid functionals

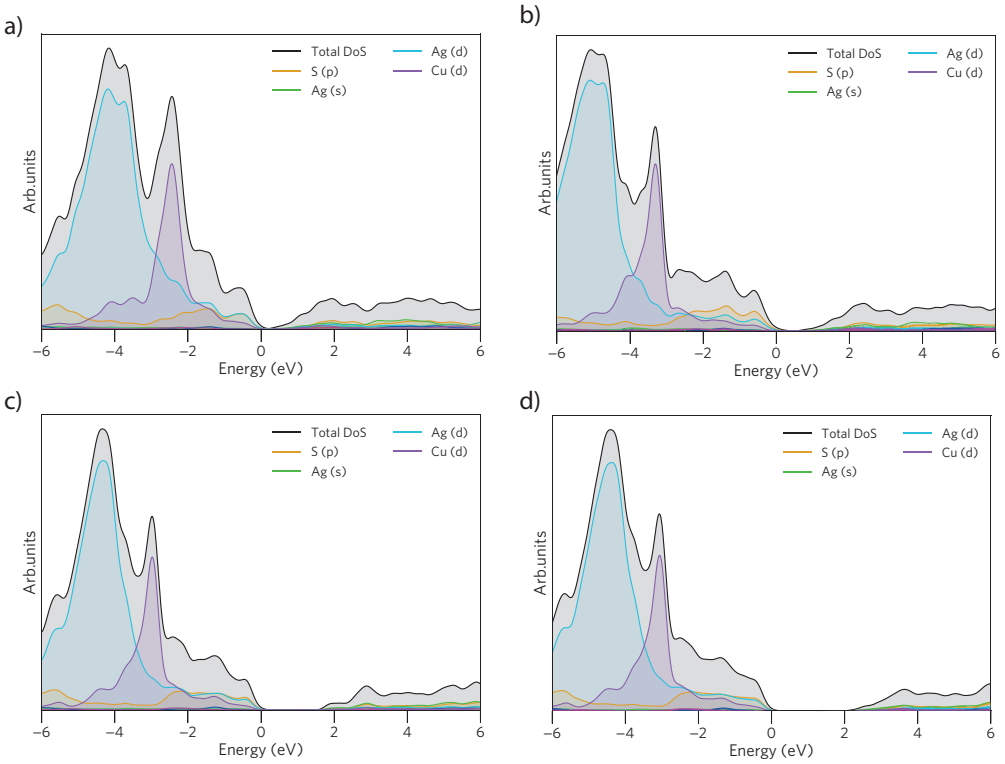

Figure 5.4: Total and Partial Density of States diagrams of RT-Ag_3CuS_2, using a) PBEsol, b) PBEsol+U, c) HSE06 and d) PBE0; individual partial DoS are labelled in legends, Energy = 0 eV is set to valence band maximum.

does also lead to a wider valence band than in the PBEsol DOS, which can indicate a more disperse band. The valence band of Ag_3CuS_2 is also dominated by Ag d, Cu d and S p; given the change in stoichiometry, it is unsurprising to see that Ag contributes more in Ag_3CuS_2 than AgCuS, but it is notable that, in Ag_3CuS_2, Ag contributes to the very top of the valence band as well. The conduction band is also relatively similar, being a mixture of Ag, Cu and S states in more equal contributions.

Electronic band structure

The electronic band structures of AgCuS and Ag_3CuS_2 are plotted in Figures 5.5 and 5.6 respectively, again with all four functionals displayed to enable comparison.

The electronic structures of AgCuS in Figure 5.5, while sharing an overall similarity in shape, do also show some differences between the functionals. While the valence band maximum occurs at Γ in all four methods, the conduction band minimum occurs between Γ and Y in the PBEsol band structure, but in PBEsol+U and the hybrid structures it occurs at Γ as well. Outside of the Γ to Y path, the structure of

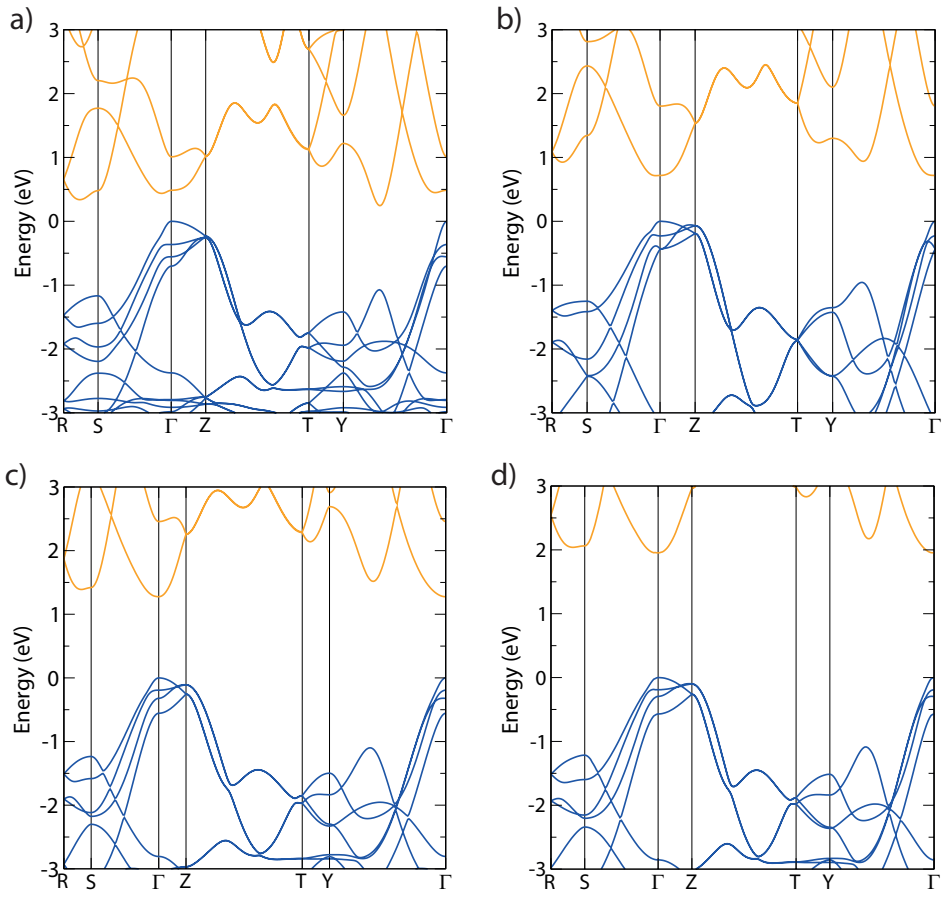

Figure 5.5: Electronic band structure diagrams of AgCuS, using a) PBEsol, b) PBEsol+U, c) HSE06 and d) PBE0; valence band marked in blue, conduction band marked in orange, Energy = 0 eV is set to valence band maximum.

the conduction band remains relatively consistent across the methods, however that particular path contains an off-Γ feature that varies – it is likely, given this feature is solely lower in energy than at the Γ point in the PBEsol structure, that this is another consequence of the poor description of the Cu d in normal DFT, and that the other methods, by correcting for the self-interaction error, provide the correct CBM. The major distinction between all four methods is then the magnitude of the band gap: 0.25 eV for PBEsol, 0.72 eV for PBEsol+U, 1.27 eV for HSE06 and 1.95 eV for PBE0, providing a wide range (>1.5 eV of values. Of these, two are unlikely to be realistic: without any correction for DFT's well-known underestimation of band gaps (explained in Chapter 2), the PBEsol result is a significant underestimation; similarly, with a 1.1 eV difference between this and the experimental optical gap of 0.9 eV determined by Guin *et al.* suggests a large overestimation (although the

difficulty in comparing experimental, room temperature optical gaps with theoretical fundamental gaps will be discussed later, band-gap overestimation of narrow band gap materials by PBE0 is known). Of the remaining two methods, the PBEsol+U value of 0.72 eV bears the closest resemblance to the optical measurements and PBE+U predictions of Guin *et al.*,[280] although we note the change in GGA functional is likely to lead, especially given the variance of results in Table 5.1, to differences in crystal structure, and the electronic structure as a consequence.

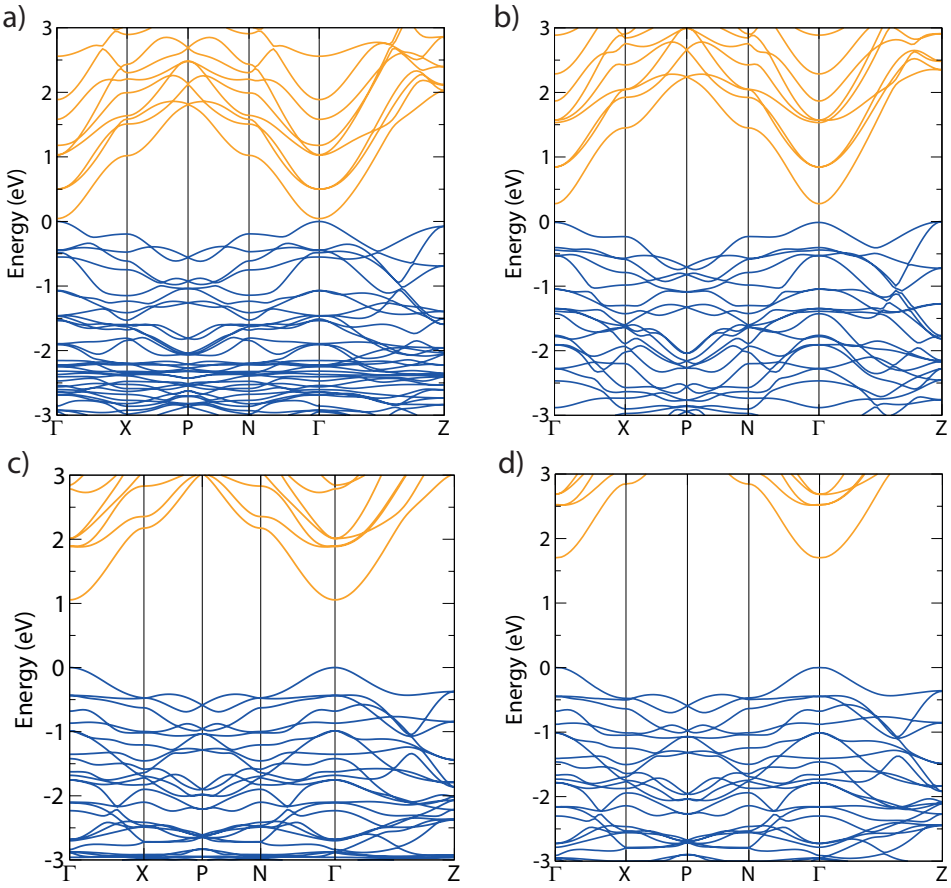

Figure 5.6: Band structure diagrams of RT-Ag_3CuS_2, using a) PBEsol, b) PBEsol+U, c) HSE06 and d) PBE0; valence band marked in blue, conduction band marked in orange, Energy = 0 eV is set to valence band maximum

The electronic band structures of Ag_3CuS_2 show more obviously the effect of reducing SIE when either including a U value or using a hybrid functional through the position of the large concentration of densely-packed flat states, which, in the PBEsol band structure, lie between -2 eV to -3 eV. These are hallmark of localized d states and correspond to the intense DOS that was in that region in Figure 5.4. In the structures of all other functionals, these states are shifted much lower in energy,

beyond the range of the plots, demonstrating the large effect of SIE. The overall shape of the band edges is again very similar across all four functionals, with both the VBM and CBM occurring at Γ forming a direct band gap. Compared to the valence band structure of AgCuS though, Ag_3CuS_2 shows a generally more dense collection of bands (reflective of the greater number of atoms in the primitive cell), but with lower local dispersion, potentially indicating weaker interactions between the cation d and S p orbitals. The variance in the magnitude of the band gap is similar to that in AgCuS though, spanning 0.04 eV for PBEsol to 1.70 eV for PBE0; again, these two extremes are likely to be inaccurate, and the values of either the PBEsol+U 0.28 eV or HSE06 1.05 eV are more likely to be representative of the true gap. Of these, the HSE06 value seems the more reliable as a gap of 0.28 eV would severely limit open circuit voltage, even as a sensitizer to ZnO, which is not seen in either of those published in the literature – both extant cells were reported to produce photovoltages of $>$0.25 eV. The low value for PBEsol+U could be a function of the poor structural description as a significantly underestimated a parameter could result in artificially short Ag-S and Cu-S bonds, leading to a narrowed gap, or potentially the fixed U value does not correspond well for the Ag_3CuS_2 structure. It was however clear that experimental validation of our predictions could strongly help confirm our findings and verify which method provides the most suitable electronic structure for the silver copper sulfides.

5.3.2 Experimental validation

All experimental work depicted in this section was performed by Dr. Will Travis and Ria Atri, working with Dr. Rob Palgrave at UCL. The discussion of the experimental results in this section was written by the author, with the aid of an initial description by Dr. Will Travis, as these key results link directly with the theoretical findings described in this thesis.

XRD and structure

To further develop the theoretical work above, experimental work was carried out by our collaborators at UCL to synthesise and characterise both compounds, and to aid in the verification of the theoretical predictions above. Both silver copper sulfides

were synthesised from a mixture of their constituent elements,[292] as described in the Experimental Methods included in the Appendix. The Ag–Cu–S products were obtained as black powders, and identified using powder X-ray diffraction; the resulting patterns were indexed in the space groups of $Cmc2_1$ for AgCuS and $I4_1/amd$ for Ag_3CuS_2, obtained in the studies of Trots *et al.*,[279,286] and are shown in comparison to patterns simulated from those literature structures in Figure 5.7. Lattice parameters obtained by least squares refinement of the powder XRD peak positions were a = 4.0623(1) Å, b = 6.6254(2) Å, c = 7.9692(2) Å for AgCuS, and a = 8.6370(2) Å, c = 11.7688(5) Å for Ag_3CuS_2. A clear match between the simulated and experimental patterns (with $<0.2\,\%$ difference in any lattice parameter), and the lack of any Bragg peaks that could arise from crystalline impurity phases, indicates that the powders obtained were sufficiently single-phase and pure for further analysis.

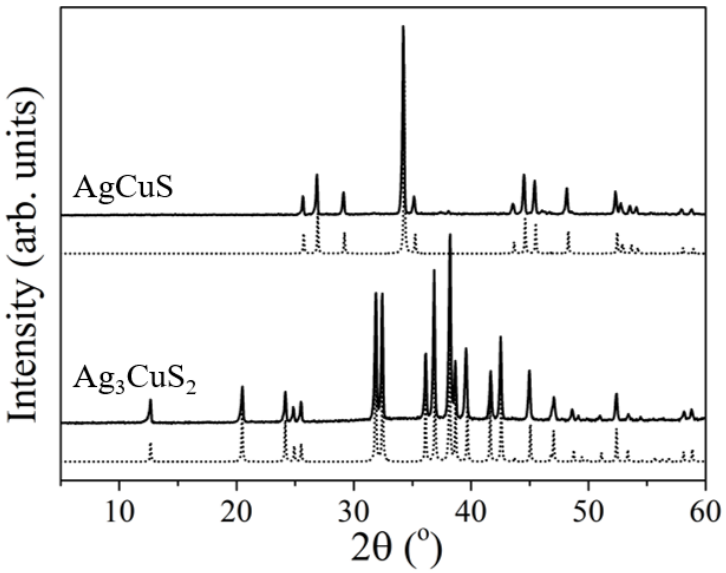

Figure 5.7: X-ray diffraction patterns of AgCuS and Ag_3CuS_2: solid lines are recorded patterns, dotted lines are patterns simulated from previous crystal structures (λ = 1.540 46 Å).[279,286]

XPS

X-ray photoemission spectroscopy (XPS) can be a valuable tool for the identification and characterization of solid state materials. XPS focussing on the core levels of the constituent elements is particularly adept for the accurate determination of composition and stoichiometry: the XPS spectra in Figures 5.8 and 5.9, for example,

demonstrate that the synthesised Ag-Cu-S samples are indeed phase-pure and with minimal other elements beyond trace samples. Both synthesised samples produced XPS survey spectra that demonstrated the presence of Cu, Ag, S with oxygen and adventitious carbon – after etching with 2 keV Ar^+ ions, the latter two elements were no longer detectable and so compositions (within a known error of 10 %) were recorded to be $Ag_{0.93}CuS_{0.96}$ and $Ag_{3.01}Cu_{1.03}S_{2.01}$, matching well with the intended stoichiometries.

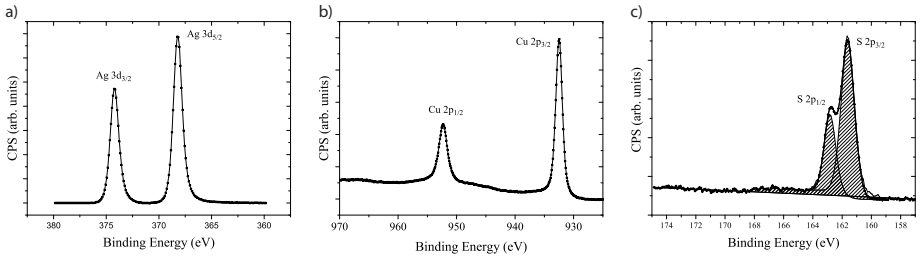

Figure 5.8: XPS core levels of Ag $3d$, Cu $2p$ and S $2p$ in as-synthesised powder of AgCuS.

To confirm the oxidation states of the elements in the samples the core-level XPS of Figures 5.8 and 5.9 can be compared to similar standard phases. The Ag 3d peak, for example, occurs in both samples (indeed the XPS of the two phases are near-identical indicating the same make-up in each) and is split by spin-orbit coupling into a J $= \frac{3}{2}$ and J $= \frac{5}{2}$, with the latter occurring at 368.2 eV – this is also consistent with previous XPS reports on Ag_2S.[293] With no additional loss features, that would manifest as peak asymmetry, which could indicate Ag metal, this seems to confirm the presence of Ag^+. Similarly, the Cu $2p$ states in both compounds show similar spin-orbit coupling splitting, and the peak values of 932.5 eV and 932.7 eV for J $= \frac{3}{2}$ in AgCuS and Ag_3CuS_2 match strongly to those recorded in Cu_2S.[294,295] As Cu^{2+} states will tend to show satellite peaks and Cu metal would show the peak asymmetry mentioned above, the clear spectra in Figures 5.8 and 5.9 demonstrate that Cu is also in the $+1$ oxidation state. This is also significant for our calculations, as the presence of any Cu^{2+} or Ag^{2+} would necessitate the consideration of potential magnetic orderings. The S 2p peaks are also consistent with the literature,[294] and the absence of any higher energy peaks (that could be characteristic of sulfate species) in the etched samples indicates that any of the oxidation seen in the initial survey is limited to the surface layer.

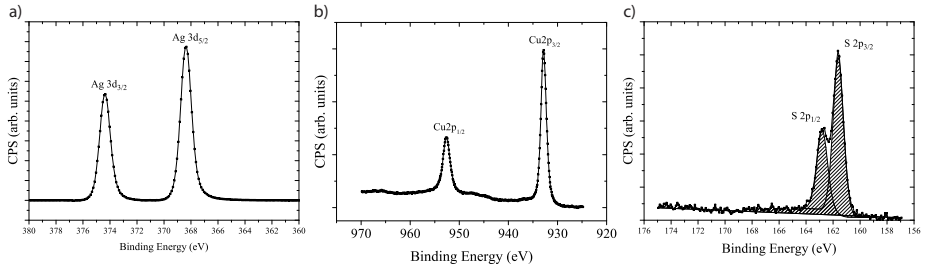

Figure 5.9: XPS core levels of Ag $3d$, Cu $2p$ and S $2p$ in as-synthesised powder of Ag_3CuS_2.

Valence band XPS can also be highly informative, albeit for a slightly different reason: the valence band XPS should directly reflect the density of states of the valence band of a chosen material, and so should thus also be directly comparable to a theoretical density of states. We note that in pseudopotential calculations, as the core states are only treated implicitly, they will not be suitable for direct comparison. By tracking intense valence states that are explicitly included however, such as the Ag and Cu d states, we can more firmly assess which method is most suitably at describing these highly-correlated states. In order to compare directly to experiment, however, the theoretical total density of states must be adapted to reflect the conditions of the experiment: firstly, while the ratio of partial densities of states in the theoretical spectrum is purely dependent on the number density of each element within the unit cell, the intensity in the XPS spectrum will also depend on how strongly each orbital scatters X-rays, and so the theoretical PDOS are each scaled by the photoionization cross-section for the particular orbital at the 1.5 keV (Al kα) incident X-ray energy. These photoionization cross-sections have previously been calculated by Yeh and Lindau within certain approximations.[296] To simulate the effect of experimental lifetime broadening, the theoretical DOS is also convolved with Gaussian and Lorentzian lineshapes, with widths given in the caption to Figure 5.10, and finally the positive XPS binding energies are changed in parity to give negative total energies. This comparison, and the plotting thereof, was performed using the aid of GALORE (https://github.com/SMTG-UCL/galore), a package developed by members of the group.[297]

None of the resulting comparisons between theory and experiment gave perfect alignment of all the peaks in both spectra, however the scaled HSE06 DOS in Figure 5.10 appeared to give the most consistent description of all the major peaks in the

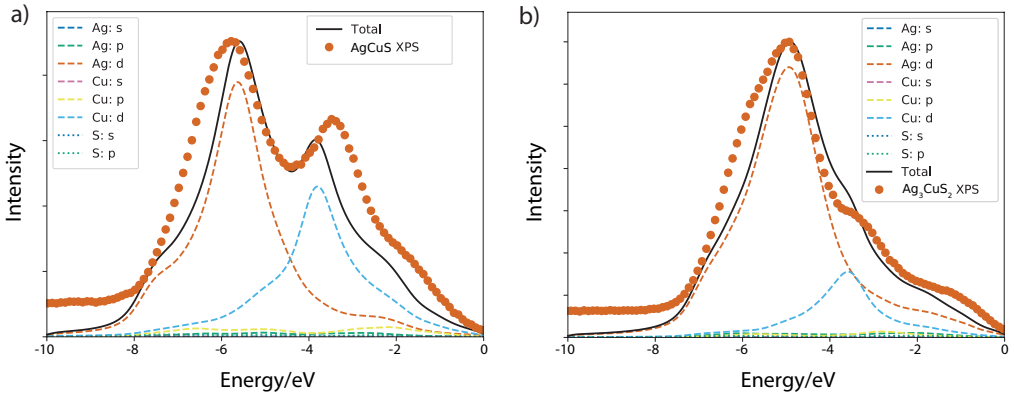

Figure 5.10: Comparison of valence band XPS and HSE06 total density of states (scaled by photoionization cross sections) for a) AgCuS and b) Ag_3CuS_2. The DOS were broadened by: a) a 0.4 eV width Gaussian and 0.5 eV width Lorentzian, b) a 0.3 eV width Gaussian and 0.5 eV width Lorentzian respectively.

VB XPS of both silver copper sulfides, indicating that it is a reliable method for the *ab initio* prediction of the properties of these systems.

Optics

Diffuse reflectance measurements were also recorded on the synthesised powders of both AgCuS and Ag_3CuS_2: the Kubelka-Munk plots that can be derived from the reflectance should then reflect the optical band gaps of each system at the intersection of the background and absorption edge, and are plotted in Figure 5.11.

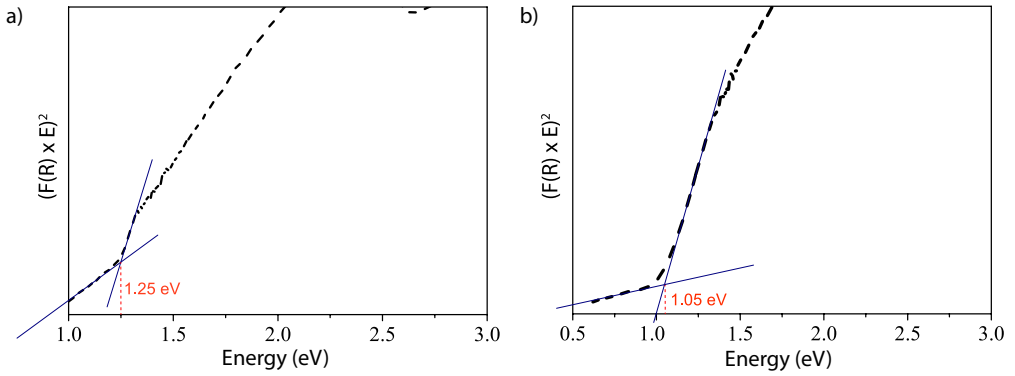

Figure 5.11: Kubelka-Munk plot from diffuse reflectance measurement of a) AgCuS and b) Ag_3CuS_2. Intersections of background and absorption marked, giving the optical band gaps, in red.

The experiment optical gaps of 1.25 eV for AgCuS and 1.05 eV for Ag_3CuS_2 that our collaborators obtained correlate surprisingly well with the HSE06 fundamen-

tal direct gaps from the band structures that we calculated (1.25 eV and 1.05 eV respectively), although this agreement is very likely fortuitous as this comparison ignores temperature effects and other electronic effects that might vary an optical gap, such as Burstein-Moss shifts. Nevertheless, this seems to indicate that the PBEsol+U results above, especially for Ag_3CuS_2 are indeed underestimations, and together with the fit to the valence band XPS, that HSE06 is, overall, the most accurate method for the prediction of the electronic structure and properties of the silver-copper sulfides.

Electronic Transport Properties

The band gap is not the sole measure of capability as a photovoltaic absorber, as explained in Section 1.2.5. An ideal photovoltaic absorber layer should also demonstrate disperse valence and conduction band edges, as it can be important that both majority and minority carriers are mobile within the structure, and thus able to separate and enter the other layers of the solar cell before recombining. We can calculate the electron and hole effective masses by considering the curvature of the conduction and valence band edges, and as explained in Chapter 3, the effective masses are then inversely proportional to the carrier mobility. The carrier effective masses, in units of the mass of an electron in a vacuum, are calculated from the theoretical HSE06 band structures and detailed in Table 5.3.

Table 5.3: Calculated effective masses of AgCuS and $I4_1/amd$ Ag_3CuS_2 from HSE06 band structures

	Valence Band (m_0)			Conduction band (m_0)		
AgCuS	$\Gamma \rightarrow$ S	$\Gamma \rightarrow$ Y	$\Gamma \rightarrow$ Z	$\Gamma \rightarrow$ S	$\Gamma \rightarrow$ Y	$\Gamma \rightarrow$ Z
	-0.311	-0.242	-1.795	1.362	0.736	0.493
	Valence Band (m_0)			Conduction band (m_0)		
Ag_3CuS_2	$\Gamma \rightarrow$ N	$\Gamma \rightarrow$ X	$\Gamma \rightarrow$ Z	$\Gamma \rightarrow$ N	$\Gamma \rightarrow$ X	$\Gamma \rightarrow$ Z
	-0.522	-0.598	-0.279	0.281	0.322	0.206

The effective masses in both the conduction and valence band of AgCuS show some anisotropy, but most notably in the valence band, where the effective masses along $\Gamma \rightarrow$ S and $\Gamma \rightarrow$ Y are both low ($<$0.35 m_0, indicative of high mobility and easily within the target range of even candidate TCOs[298]), however the effective mass along $\Gamma \rightarrow$ Z is 1.795 m_0, significantly higher and potentially problematic for carrier

transport. The low dispersion along this direction can be rationalised as $\Gamma \rightarrow$ Z corresponds to the direction of the **c** axis in real space: given that the DOS at the valence band edge shows solely Cu d and S p character, but there is no Cu-S connectivity along **c** making a pseudolayered Cu-S network, we would expect that the states at the VBM would have high dispersion in the directions in which there is connectivity (i.e. the **ab** plane), while poor dispersion along **c**. This could indicate that careful lattice matching and alignment control may be necessary to ensure a viable cell architecture with AgCuS. The effective masses of Ag_3CuS_2 are much more isotropic, reflecting the 3-dimensional connectivity and high symmetry of its structure, equally the effective masses are all quite low with the electron effective masses all also $<0.35\,m_0$. Effective masses of this magnitude are comparable to those predicted in CZTS and other identified candidate PV materials, and so are highly promising for potential applications.[299–301]

We also wished to see how the theoretical effective masses could translate into reality, and our collaborators were able to perform Hall effect measurements on a pressed pellet of synthesised AgCuS, and these results are detailed in Table 5.4, and contrasted with values from studies in the literature on highly successful absorbers CZTS and MAPI. The positive Hall coefficient indicates p-type conductivity, agreeing with the thermoelectric measurements of Guin *et al.*, and thus affirming the importance of the low predicted hole effective masses. Our synthesised pellet also demonstrated a moderately high carrier concentration given the targeted stoichiometry and no extrinsic doping. As a result, the observed mobility of $2.237\,cm^2/V/s$ does compare poorly with more intrinsic, lower concentration samples but it is on par with samples of similar or equal concentration magnitudes – an encouraging result for a sample that we might expect to contain grain boundaries and other defects that could lower mobilities, that would not be present in the high-grade thin films needed for PV devices. Unfortunately, with a sheet resistivity of $11.57\,\Omega/sq$, comparable Hall effect measurements on the Ag_3CuS_2 pellet were not possible.

Table 5.4: Electronic characterisation of AgCuS, compared to other photovoltaic materials (stoichiometric, bar *, where S content ranges from 0 – 90%, and Cu, Zn and Sn ratios are variable)

Material	Hall Coefficient ($cm\,C^{-1}$)	Bulk Concentration (cm^{-3})	Mobility ($cm^2\,V^{-1}\,s^{-1}$)	Resistivity ($\Omega\,cm$)
AgCuS	0.2304	1.7×10^{18}	2.237	1.678
CZTS[302]	–	8×10^{18}	6.0	0.13
CZTS[303]	160	3.9×10^{16}	30	5.4
CZT(S,Se)*[304]	–	$17.3 - 1.4\ \times10^{15}$	0.46 – 1.32	774 – 3300
MAPI[76]	–	$\sim10^{9}$	66	5.1×10^{7}
MAPI[98]	–	2.8×10^{17}	3.9	–

5.3.3 SLME and Alignment: Towards a cell architecture

Optical Calculations

In the previous sections, HSE06 has appeared to be the most reliable functional for the calculation of the silver copper sulfides, and so we have used it for all further theoretical analysis. The fundamental band gaps for both silver copper sulfides are within the ideal range for high theoretical efficiencies, and the electronic transport properties of AgCuS at least appear to be almost as good as current earth-abundant champion absorber materials. So, with the general electronic structure of both compounds assessed, we can now move towards looking at properties specifically relevant for usage in photovoltaic cells, namely the optical absorption and the alignment of the valence and conduction bands to other materials – the latter allowing us to predict a cell architecture with minimal barriers to carrier transport, which could significantly ease the construction of future cells. The optical absorption coefficient, α, of both AgCuS and Ag_3CuS_2 were calculated from the theoretically predicted dielectric spectrum and are plotted in Figure 5.12, with the fundamental band gaps marked on in bold lines.

As explained in previous chapters, high absorption is usually defined by an absorption coefficient on the order of $10^4\,cm^{-1}$ to $10^5\,cm^{-1}$, and so Figure 5.12 is plotted on this scale. Here, we can note that despite their direct fundamental band gaps, the absorption remains $<10^4\,cm^{-1}$ until 1.7 eV for AgCuS, and until 2.2 eV for Ag_3CuS_2 – ideally, an optimally absorbing material will have a sharp absorption edge, and this is not the case here, especially for Ag_3CuS_2 which only attains strong absorption

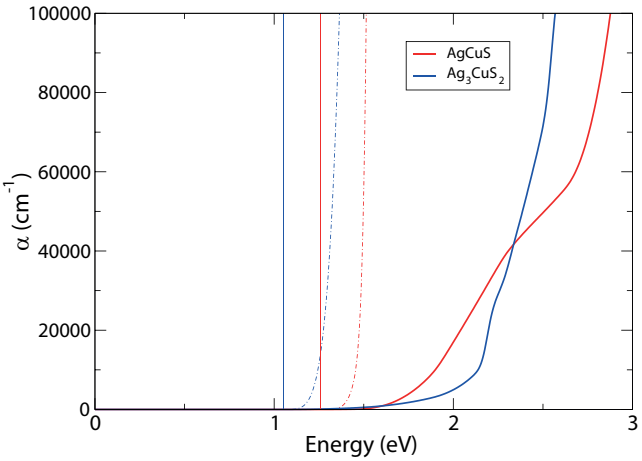

Figure 5.12: Calculated HSE06 optical absorption of AgCuS and Ag_3CuS_2, with: absorption coefficients marked as bold lines; fundamental band gaps marked by vertical lines; $(\alpha h\nu)^2$, representative of the predicted optical band gap, is marked as alternating dot-and-dash lines.

for high photon energies. This delayed absorption, in other systems such as silicon, can be due to an indirect band gap, and thus a reduced probability of optical transitions occurring and weak absorption until the spectrum reaches a lowest-energy direct transition; although in this case, the silver copper sulfides are predicted in our calculations to be direct gap semiconductors. $(\alpha h\nu)^2$ is also plotted in the same diagram, as this reflects the direct 'optical gap' in analogy to those obtained from experiment (its form is identical to the frequently used Tauc method, and is analogous to the Kubelka-Munk method in that the reflectance function F(R) and α are similar). These optical gaps are both greater than the fundamental band gaps, and in this case, are perhaps more ideal for comparison to our experimental optical results – they are both within 0.2 eV of their respective experimental band gaps, a difference that could then be explained through thermal effects (especially in structures that soft, such as these, the extension of lattice parameters with temperature could lead to a relatively large decrease in the band gap). These theoretical optical gaps do also demonstrate that although strong absorption is only present at higher-than-anticipated photon energies, there is absorption just above the band gap, albeit weak.

To attempt to investigate why the silver copper sulfides do not demonstrate strong absorption despite being predicted to have direct band gaps, the transition amplitudes for given energies were calculated. VASP outputs the transition dipole mo-

ment matrix elements for given valence to conduction band transitions at individual k-points – as, given Fermi's Golden rule, the probability of a transition occurring (its amplitude) is proportional to the square of the transition dipole moment, we can obtain relative amplitudes for these transitions from a square of the matrix elements. Doing so for the silver copper sulfides reveals that in both compounds, the lowest direct transition at Γ (VBM to CBM) has an amplitude 10^3 weaker than other transitions: while non-zero (hence the presence of some above-band gap absorption), this could be considered 'forbidden' in comparison, and will result in a low dielectric spectrum in that region of energy and thus, a low absorption coefficient. In AgCuS, the next direct transition (from VBM-1 to CBM, marked in Figure 5.13) is 'allowed' in comparison, and so the strong absorption onset occurs earlier than in Ag_3CuS_2, where the 3 lowest energy direct transitions at Γ are all forbidden, and the high local dispersion of the bands means that almost all off-Γ transitions are high in energy. Transitions such as these can often be forbidden due to disobeying the Laporte selection rule ($\Delta l = \pm 1$) – here, in both compounds, the valence band maximum to conduction band minimum transitions are primarily between states primarily composed of Cu d ($\Delta l = 0$); the transition amplitudes in the silver copper sulfides are non-zero, however, likely due to some mixing with S s, p or Ag states, leading l to become a less well-defined quantum number for these electronic states. Nevertheless, the primary $\Delta l = 0$ character of these transition means that their amplitudes will be orders of magnitude lower than others, and so they are only weakly 'allowed'.

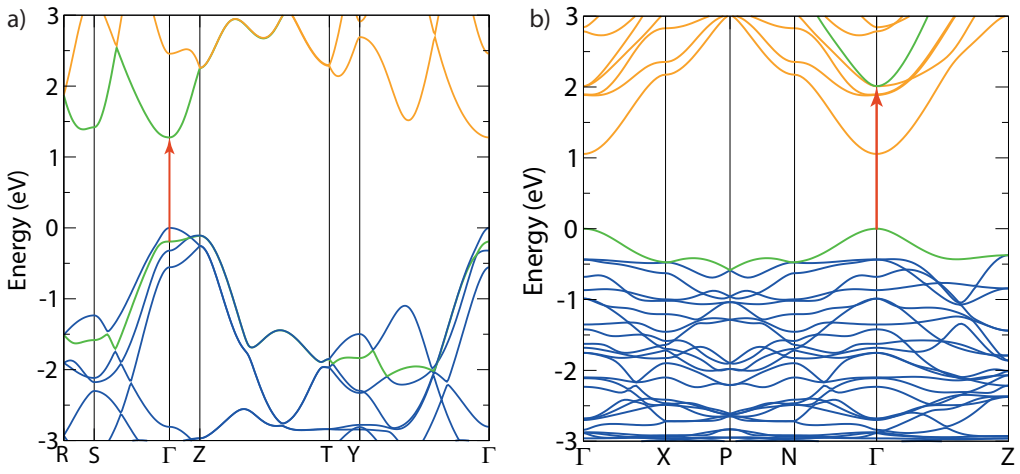

Figure 5.13: HSE06 Band structures of a) AgCuS and b) Ag_3CuS_2, with the lowest direct "allowed" transition (Relative transition amplitude >0.001) marked and the bands involved coloured green.

A slow absorption onset and forbidden transitions such as these will impact upon the performance of a solar absorber, and we can supplement the results above by the calculation of the spectroscopically limited maximum efficiency (SLME),[186,187] as also used in Section 4.3.3. As SLME directly incorporates forbidden optical transitions into its treatment of non-radiative recombination (the Δ factor discussed in Section 3.3.2), the metric will qualitatively reflect the negative impact that these optical losses may have on the potential efficiency of a solar cell (although, with a relatively simple model of the physical processes, not necessarily quantitatively). Calculating for the benchmark film thickness of 0.2 µm and using the HSE06 calculated absorption coefficients, the SLME of AgCuS is 20.6 %, just above the 'high-SLME' threshold originally proposed by Yu and Zunger, and can be increased to 27 % in the limit of infinite thickness. Thus, AgCuS appears to not be too negatively impacted by the forbidden transition and weaker absorption. Ag_3CuS_2, on the other hand, has an SLME of 0.2 % for the same film thickness – a significantly poorer result. In this case, SLME is not quantitatively reflective of the maximum efficiency – given the reports of cells with conversion efficiencies above this value – however it does indicate that Ag_3CuS_2 may be significantly more limited than AgCuS as a thin-film PV absorber by a combination of its weak absorption below 2 eV and forbidden transitions leading to larger non-radiative recombination and other optical losses. As a result, AgCuS appears to be the more promising candidate for further theoretical and experimental study in this area.

Band Alignment

The above results indicate that AgCuS is perhaps the better candidate than Ag_3CuS_2 as a PV absorber material, but as there have been no previous reports on its use in this way, it may be highly useful to calculate its band alignment with other materials that can be used as partner layers in a solar cell. In this way, we can theoretically predict potential device architectures that will be optimal for AgCuS and so aid future experimental and theoretical research on this material. The valence band alignment was calculated using the core level alignment approach described in Section 3.2.4: by constructing a non-polar (001) slab of AgCuS with sufficient vacuum, we can use the PlanarAverage code developed by Walsh and co-workers[181] to obtain the average of the electrostatic potential in the vacuum, and thus quantitative energy

separation between the vacuum level and a particular (S $1s$) core state, which can then be aligned to the VBM from a bulk calculation. This resulted in a calculated ionization potential (IP) of 4.6 eV – we then compare this to other solar absorber materials as well as potential contact layers in Figure 5.14.

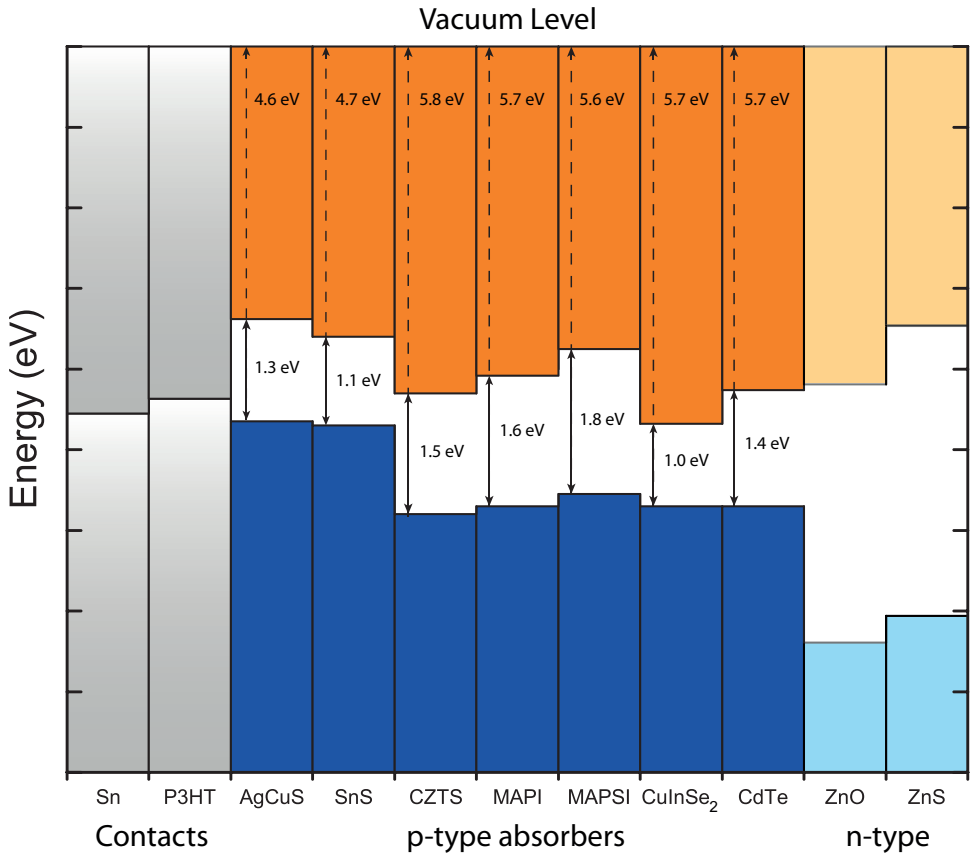

Figure 5.14: Valence band alignment of AgCuS with a number of other materials. Ionisation potentials, band gaps and workfunctions of other materials have been taken from the literature.[133,305–310]

At first, it is notable from this figure that an IP of 4.6 eV puts AgCuS at a 1 eV higher valence band position than a number of other popular solar absorber materials, like CZTS and MAPI, and hence any attempt to fit AgCuS with comparable partner layers to those used with these materials is likely to be highly limited. A low IP does support the highly p-type behaviour demonstrated in this and other reports – defect states, both extrinsic and intrinsic, are more likely to align close in energy to a higher VB, and thus demonstrate acceptor behaviour. Given that CZTS also has a valence band dominated by Cu d and S p states, it is perhaps surprising to see a much lower IP in AgCuS, and instead see a more comparable match with another recently studied absorber, SnS. Structural distortion, resulting in a change

in cation coordination sphere, was proposed as a possible reason for the low IP of SnS,[305] and indeed the variation of IPs in different TiO_2 polymorphs has also been rationalised through different local Madelung potentials[311,312] – themselves defined by the coordination environment of atoms in a structure. As such, it is possible that the variance in IP between AgCuS and CZTS, despite similar orbital make-up, is a result of the unusual lower coordination of Cu in the AgCuS structure, being trigonal planar instead of tetrahedrally coordinated to sulfur as in CZTS.

The goal of this alignment was to find a cell architecture for AgCuS – with synthesised samples appearing to be natively p-type, we will need either a p-type buffer layer or metal contact, and then a partner n-type layer to form a heterojunction. The high VB position of AgCuS does mean that it matches well to the workfunction of P3HT, as used in the previous literature cells of Ag_3CuS_2, but for an entirely-inorganic cell, Sn could also be used as the back metal contact, with only a 0.1 eV offset that could likely form a low barrier to hole transport. For the n-type partner, the conduction band alignment was constructed using the HSE06 band gap on top of the calculated VBM position, giving an electron affinity (EA) of 3.3 eV. ZnO, as used with Ag_3CuS_2, is poorly aligned with such a CB position; instead the lower EA ZnS could create a better aligned (again, within 0.1 eV) n-type material for an efficient cell structure.

5.4 Conclusions

In this chapter, we have studied the room temperature phases of the silver copper sulfides AgCuS and Ag_3CuS_2 as potential solar absorber materials. We find, through comparison with experimental work performed by our collaborators, that HSE06 appears to present the most accurate theoretical prediction of the equilibrium structures and valence band electronic structure of these systems. We find that both systems possess direct band gaps within the ideal region for single junction absorbers: 1.05 eV for Ag_3CuS_2 and 1.27 eV, along with suitably disperse conduction and valence band with low carrier effective masses in some directions. While thus possessing excellent electronic structures for photovoltaic absorption, theoretical optical properties predict multiple forbidden transitions in Ag_3CuS_2, resulting in weak absorption in the IR-range of the EM spectrum, as well as a poor SLME. AgCuS,

however, is predicted to have a high SLME and stronger absorption, as well as being measured to have mobilities on par with other champion absorber materials, and thus is the better candidate for future studies into these materials in photovoltaics. Band alignment of AgCuS with potential contact and partner layers then allows us to provide valuable information to aid further research into this material.

The results included in this chapter were written up as a paper, which was accepted and published in the Journal of Materials Chemistry A.[313] *Figures 5.7, 5.8 and 5.9 were all produced by Dr. Will Travis and Dr. Robert Palgrave, while 5.11 was adapted from their results, and these figures are reproduced here with their permission. Some of the figures in this chapter have also been adapted from those included in this paper.*

Chapter 6

Results III: Lead Bismuth Sulfides

6.1 Introduction: Building upon Binaries

The binary chalcogenides lead sulfide, PbS, and bismuth sulfide, Bi_2S_3, have both experienced interest from the field of optoelectronics, especially over the past two decades, albeit in different contexts. Bulk PbS, in the $Fm\bar{3}m$ rock-salt structure,[314] is a narrow-gap semiconductor with a band gap of 0.28 eV at 4.2 K, measured through reflectometry, increasing to 0.3 eV to 0.4 eV at room temperature.[315] The entire PbCh family (Ch = S, Se, Te) has seen substantial success as thermoelectrics: PbSe-PbTe and PbS-PbTe alloys, when nanostructured, possess some of the highest zT (figure of merit for thermoelectric devices) of all semiconductors, ∼1.8 at 800 K.[316–319] Of more significance to photovoltaic applications has been the increased availability of air-stable, high absorption PbS colloidal quantum dots (QDs), which can be used as sensitizers for solid state and dye solar cells.[320] Strong quantum confinement effects ensure that the band gap of the QDs is highly tuneable between 1.0 eV to 1.3 eV,[321] enabling usage in Near-IR detectors, but also potential for significantly higher theoretical maximum photovoltaic efficiencies within the detailed balance limit than the bulk. PbS QD cells have rapidly developed in efficiency, exceeding 10 % in 2016 through judicious iodide passivation of deep trap states at the PbS surface.[48,322]

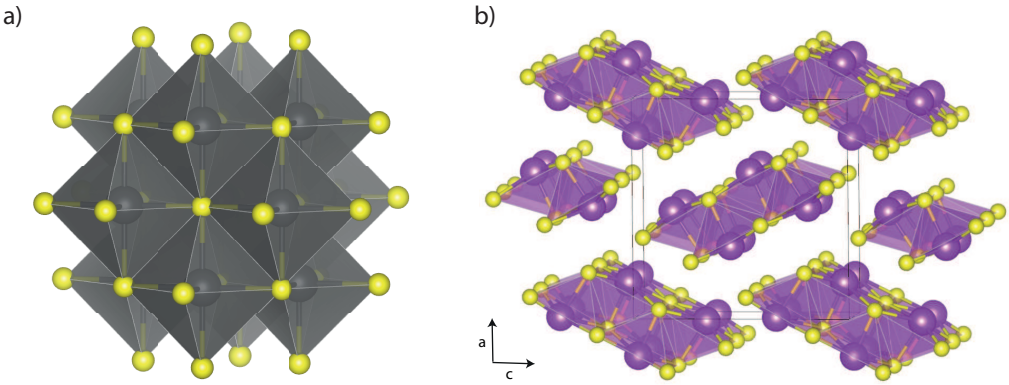

Figure 6.1: Crystal structures of a) PbS and b) Bi_2S_3. Lead polyhedra are in grey, bismuth polyhedra in purple and sulfur atoms in yellow.

Bismuth sulfide has had an extensive research history in thin-film devices, with studies published from the 1980's discussing its photoelectochemical behaviour.[323] Bi_2S_3 occupies a much less regular structure than PbS due to the realization of the 'stereochemical lone pair': the structure comprises 'Bi_4S_6' units that are connected in an edge-sharing pattern down one dimension to form ribbons.[324] These ribbons are then

surrounded by interstitial space into which the lone pairs on the bismuth atoms are directed – the ribbons then stack such that there are close Bi-S distances between ribbons, but longer than conventional bonds, indicating longer-range interactions. This leaves an overall '1D' structure, with lower dimensional connectivity than in PbS, which is depicted in Figure 6.1. Bi_2S_3 is intrinsically n-type, and its band gap of 1.3 eV to 1.6 eV and high absorption coefficient ($\sim 1 \times 10^4\,\mathrm{cm}^{-1}$)[325,326] both suggest its potential as a solar absorber material. Cell efficiencies have been relatively low, however, with recent advances leading to nano-crystalline Bi_2S_3 as a sensitizer on TiO_2 providing 2.5 % PCE,[327] and in combination with the organic absorber P3HT, 3.3 %.[328] As an n-type material, Bi_2S_3 may also be combined with p-type PbS QDs, and in 2012, Konstantatos and co-workers developed a 'bulk nano-heterojunction' architecture to combine these two materials; the resultant devices showed near 400 % improvement in J_{sc} from a standard heterojunction, and a maximum cell efficiency of 4.9 %, improving upon Bi_2S_3 alone.[329]

Despite the success of these two materials, and the numerous compounds within the phase space, relatively little research has focused on the ternary lead bismuth sulfides ($Pb_xBi_yS_z$) beyond initial characterization with XRD. Five individual phases by composition have been identified and characterised crystallographically in the Pb-Bi-S series,:[330] $Pb_6Bi_2S_9$ (heyrovskyite),[331] $Pb_3Bi_2S_6$ (lillianite, xilingolite),[332] $Pb_2Bi_2S_5$ (cosalite),[333] $PbBi_2S_4$ (galenobismutite)[334] and $PbBi_4S_7$.[335] Of these, $PbBi_2S_4$ and $Pb_3Bi_2S_6$ have been examined for thermoelectric behaviour by Ohta *et al.*, finding low lattice thermal conductivities and moderate zT without attempting to optimize the carrier concentrations.[336] Electronic and optical characterization was performed on thin films of the lead bismuth sulfides by Malika *et al.*, however the phases were only identified by virtue of reagent ratios, making direct comparison difficult, however all films were observed to have high absorption coefficients and band gaps within the 0.3 eV to 1.6 eV range bounded by the binaries.[337]

Structurally, the mixed lead bismuth sulfides offer characteristic motifs of both binaries. The structure of $Pb_6Bi_2S_9$ (space group $Cmcm$) consists primarily of layers of edge-sharing Pb-S octahedra – the motif of PbS – which are bridged by Bi-S octahedra, forming an overall 3-dimensionally connected structure. $Pb_3Bi_2S_6$ ($C2/m$) is homologous, however with the elemental ratio moving further towards bismuth, the layers of Pb-S octahedra are thinner. In the structure of $Pb_2Bi_2S_5$ ($Pnma$), the

PbS-like octahedra are localised in a chain along b, bonded now to both Bi-S octahedra and 7-coordinate Pb-S capped trigonal prisms. This 7-coordinate environment is reminiscent of Bi_2S_3, where bismuth atoms are bonded to sulfur in a pseudo-square pyramid with 2 additional long interactions between the layers. $PbBi_2S_4$ ($Pnam$) continues in this paradigm, with all the lead atoms occupying 7-coordinate environments, and 1 bismuth in each of 6 and 7-coordinate polyhedra; while finally $PbBi_4S_7$ ($C2/m$) also contains further proportion of 7-coordinate cation sites, as we approach the Bi_2S_3 limit. All of these structures are depicted in Figure 6.2.

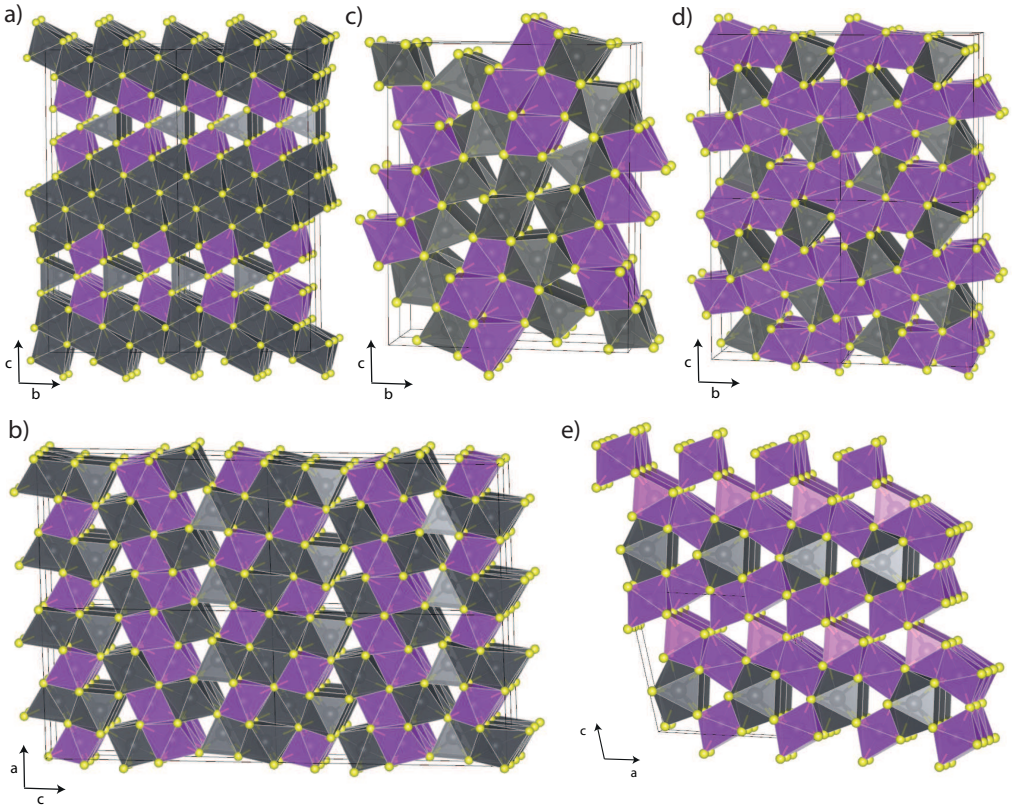

Figure 6.2: Crystal structures of the five Pb-Bi-S compounds studied: a) $Pb_6Bi_2S_9$, b) $Pb_3Bi_2S_6$, c) $Pb_2Bi_2S_5$, d) $PbBi_2S_4$ and e) $PbBi_4S_7$ (using our lowest energy obtained ordering of Pb and Bi). Lead polyhedra are in grey, bismuth polyhedra in purple and sulfur atoms in yellow.

As well as reflecting the motifs of whichever cation is in greater proportion in the structure, these structures also present an interesting possibility for electronic dimensionality. A defining limitation of Bi_2S_3 in solar cells is its low dimensional nature – charge transport is strongly restricted along the non-ribbon cell dimensions ($\mathbf{a}$ and $\mathbf{c}$ in Figure 6.2) and this tends to hinder the overall cell performance. The mobility in PbS is, in contrast, very high[338] due to the highly symmetric, 3-dimensionally

connected structure; however, the bonding within both compounds leads bismuth sulfide to have a near-ideal band gap for photovoltaics, whereas that of bulk PbS is much narrower. We can also note the detrimental effect of low electronic dimensionality that was seen in our discussion of the caesium silver bismuth halides, where the inability for those compounds to from strong interactions between nearest-neighbour cations limited band dispersion and the possibility of strong absorption from a direct gap. Here, though, the combination of both of the structural motifs of the binaries as well as two ns^2 cations, could open possibilities for both facile charge transport and a band gap close to the ideal limit in the ternary mixed systems, fulfilling two major criteria for successful solar absorbers.

6.2 Methodology

Geometry optimizations of all structures, including those of all ordered polymorphs of $PbBi_4S_7$ (a function of determining its most likely ground state ordered structure, and detailed in Structure and Relaxation), were performed using the PBEsol functional due to the large size of some of the cells. Further electronic structure and optical calculations were performed with the HSE06 functional, with the explicit addition of spin orbit coupling (HSE06+SOC), due to the presence of the heavy elements Bi and Pb. Scalar relativistic pseudopotentials were used, and 5d electrons were treated as valence for both Bi and Pb. For all electronic calculations, a plane wave cutoff of 350 eV and a k-point mesh density of 0.02 $Å^{-1}$ were used for all 5 compounds, determined to be sufficient to achieve convergence of the total energy to within 1 meV. During optimizations, the forces on each atom were converged to below 0.01 eV $Å^{-1}$.

The ionization potential (IP) of $PbBi_2S_4$ was calculated using the core-level alignment approach of Wei and Zunger.[180] A vacuum-slab model was constructed and a single-point calculation using HSE06+SOC is used to obtain the electrostatic potential. This can then be averaged using the MacroDensity package to align the vacuum level with a chosen core level, which can be compared to the bulk, and the valence band-vacuum level separation (IP) can be found.[181]

The intrinsic defect formation energies of $PbBi_2S_4$ were calculated through the use

of a $1 \times 1 \times 3$ (84 atom) supercell, using geometry optimisation with the PBEsol functional, a Γ-centred $2 \times 2 \times 2$ k-point mesh and cutoff energy of 350 eV for all calculations. Four corrections were included to account for the effect of the finite-size supercell. Three of these are the Potential level alignment, Band-filling and Image Charge corrections that are described in the defect methodology in Section 3.4. In addition, as we use PBEsol in place of HSE06+SOC for the calculation of these defective supercells, we must correct the band edges to match those of HSE06+SOC using a scissor-like correction – due to fortuitous error cancellation (the underestimation of PBEsol compared to HSE06 is offset by the reduction in band gap from spin-orbit effects), this correction was small ($\sim$0.05 eV). We also use a self-consistent Fermi level calculator, as developed by John Buckeridge (https://github.com/jbuckeridge/sc-fermi) which uses the calculated transition levels and formation energies to find the equilibrium position of the Fermi level at a given temperature. It does this through calculating the concentrations of donor (N_d) and acceptor (N_a) defects (see Equation 3.38) and the carrier concentrations as a result of those levels (n_d for electrons and p_a for holes) through:

$$n_d = \frac{N_d}{\frac{1}{2}e^{\beta(\epsilon_d - E_F)} + 1}; p_a = \frac{N_a}{\frac{1}{2}e^{\beta(E_F - \epsilon_a)} + 1} \tag{6.1}$$

where ϵ_d and ϵ_a are the donor and acceptor defect energy levels respectively, and β is the thermodynamic factor $\frac{1}{k_B T}$. Finally, the free carrier concentrations (n_c and p_v for electrons and holes respectively) can be extracted from the bulk electronic structure, and then noting that at thermodynamic equilibrium, these carriers will charge balance:

$$n_c + n_d = N_d - N_a + p_v + p_a, \tag{6.2}$$

these equations can be solved self-consistently to find the equilibrium Fermi energy at a chosen temperature T, usually 300 K.

6.3 Results and Discussion

6.3.1 Structure and Relaxation

Firstly, before the calculation of their electronic structure, the crystal structures of $Pb_6Bi_2S_9$, $Pb_3Bi_2S_6$, $Pb_2Bi_2S_5$, $PbBi_2S_4$ and $PbBi_4S_7$ were all relaxed using the PBEsol functional to ensure atoms were in the ground state, equilibrium positions. In addition, for benchmarking purposes, the structures of the binaries PbS and Bi_2S_3 were also included. Of note here is the assignment of lead and bismuth and the problem of cation disorder. When the (often mineral) samples were originally characterised in the 1970's with XRD, it could often be difficult to distinguish elements with similar atomic numbers, such as lead and bismuth, as the X-ray scattering factor of the two is very similar, and limits on the accuracy of determining atomic positions could make separating atomic environments near-impossible. Nevertheless, the on-average longer Pb-S bond length enabled the assignment of Pb and Bi to individual sites in the reports of $Pb_2Bi_2S_5$ and $PbBi_2S_4$. While original studies on $Pb_6Bi_2S_9$ and $Pb_3Bi_2S_6$ reported structures with static Pb/Bi disorder on the cationic sites, more recent studies have been able to distinguish or suggest fully ordered structures (with ordered-$Pb_3Bi_2S_6$ noted to be a homologue of the disordered lilianite $Pb_3Bi_2S_6$ studied previously). However, the only reported structure refinement of $PbBi_4S_7$ in the Inorganic Crystal Structure Database (ICSD) is that of Takeuchi and Takagi, with static disorder of Pb and Bi throughout. While a completely disordered polymorph is plausible, the appearance of ordered phases for all 4 other Pb–Bi–S compositions suggested that this could be an artefact resulting from the limited methods and equipment available. So, in order to obtain a structure for the compound on which calculations of bulk properties could be performed, all 27 possible symmetry-inequivalent ordered structures of the $PbBi_4S_7$ unit cell were generated using the Site-Occupancy Disorder program (SOD).[339] These structures (with the static disorder on one sulfur position averaged) were then relaxed using the PBEsol functional and their energies compared. The lowest energy ordering was then selected as representative of the most likely ordered polymorph for the compound, as it was >0.05 eV per formula unit more stable than the next lowest-energy structure, and hence the other orderings were unlikely to be thermally accessible at 300 K. Nevertheless, the possibility for low-level or dilute Pb/Bi disorder on individ-

ual sites needs to be accounted for, even in the other Pb–Bi–S phases, and so its effect on the electronic structure is considered later, when we consider the behaviour of antisite point defects.

The lattice parameters from the geometry optimizations of all compounds are depicted in Table 6.1, with comparisons given to the original experimental crystal structures. In all cases, the agreement between PBEsol-relaxed structures and experiment appears to be close, with the majority of lattice parameters differing by no more than $1\,\%$ of the original value, and none of the the lattice parameters in the Pb-Bi-S systems deviating by $>1.5\,\%$. This agreement was considered sufficient for these structures to then be used as the basis for subsequent electronic structure calculations.

Table 6.1: Optimized lattice parameters of PbS, Bi_2S_3 and all calculated Pb–Bi–S systems, (primitive cells for $Pb_6Bi_2S_9$ and $Pb_3Bi_2S_6$) with percentage difference from experiment in parentheses

Compound	a/Å	b/Å	c/Å	$\alpha/^\circ$	$\beta/^\circ$	$\gamma/^\circ$
PbS [314]	5.897	—	—	—	—	—
$(Fm\bar{3}m)$	(–0.57%)	—	—	—	—	—
$Pb_6Bi_2S_9$ [340]	4.095	7.106	31.191	—	—	106.748
$(Cmcm)$	(–1.22%)	(–0.99%)	(–0.98%)	—	—	(–0.04%)
$Pb_3Bi_2S_6$ [341]	4.052	7.029	20.766	92.80	89.92	106.77
$(C2/m)$	(–0.81%)	(–0.40%)	(+0.57%)	(+0.81%)	(–0.09%)	(–0.05%)
$Pb_2Bi_2S_5$ [333]	4.028	19.176	23.916	—	—	—
$(Pnma)$	(–0.81%)	(+0.39%)	(+0.01%)	—	—	—
$PbBi_2S_4$ [334]	4.056	11.622	14.455	—	—	—
$(Pnam)$	(–1.084%)	(–1.426%)	(–0.924%)	—	—	—
$PbBi_4S_7$ [331]	13.253	3.977	11.992	—	105.20	—
$(C2/m)$	(+0.043%)	(–1.31%)	(–0.41%)	—	(+0.17%)	—
Bi_2S_3 [324]	10.931	13.260	15.619	—	—	—
$(Pbnm)$	(–1.67%)	(–0.54%)	(–0.25%)	—	—	—

Further to this, as the five Pb-Bi-S compounds represent a continuous series across the range of PbS to Bi_2S_3, and so, during synthesis, each of the ternary compounds could act as a competing product or phase to the others. As a result, it is useful to determine their relative stability, to see which is most energetically stable and, potentially, most likely to form. We perform this by finding the so-called 'convex hull' between PbS and Bi_2S_3, which is a mathematical construct that encloses the lowest energy configurations in a given phase space; so, the most stable configurations will lie on the convex hull, while less energetically stable phases are given with respect

to how high in energy they are above it. This representation is advantageous over solely presenting the formation energies, as it allows the direct identification of the most thermodynamically stable compositions/structures within a given phase space. The relative energies from the relaxed structures with PBEsol are given in Table 6.2.

Table 6.2: Energy above convex hull (per formula unit) for all Pb–Bi–S compounds, calculated with PBEsol. Elemental energies are 0 eV above hull by definition.

Compound	Energy above convex hull/eV
PbS	0
Bi_2S_3	0
$Pb_6Bi_2S_9$	+0.0128
$Pb_3Bi_2S_6$	+0.0081
$Pb_2Bi_2S_5$	+0.0262
$PbBi_2S_4$	0
$PbBi_4S_7$	+0.0091

From these results, we can see that only $PbBi_2S_4$ of the mixed lead-bismuth sulfides lies on the convex hull, and is thus fully thermodynamically stable with respect to the binary compounds and other ternaries. However, all the other phases lie within 0.026 eV of the convex hull, which is approximately the value of k_BT at 300 K, and so we may expect that all these phases are metastable at room temperature, which corroborates Craig's report of several isolable phases within the Pb–Bi–S phase diagram.[330] From this, we can then move on to calculate the electronic structures of all five ternary compounds, with any of them potentially attainable and synthesisable for device conditions.

6.3.2 Electronic Structure

Given the lack of direct experimental assessment of the band gaps of the ternary lead bismuth sulfides, our calculations of their electronic structure would have to act predictively and accurately. Thus, it was crucial to properly benchmark our choice of functional using the well-characterised binary systems prior to calculation of the Pb–Bi–S compounds. HSE06 was selected due to its recorded ability to accurately replicate the electronic structure of narrow and moderate gap semiconductors, including previous studies on sulfides from this group and others.[290,342,343] The addition of spin-orbit coupling is necessitated by the presence of the heavy elements lead and bismuth, the electronic effect of which has been observed to be on the

order of 0.7 eV to 1.0 eV in the lead halide perovskites.[26,344] The electronic band structures of PbS and Bi_2S_3 were calculated with HSE06+SOC, and are depicted in Figure 6.3.

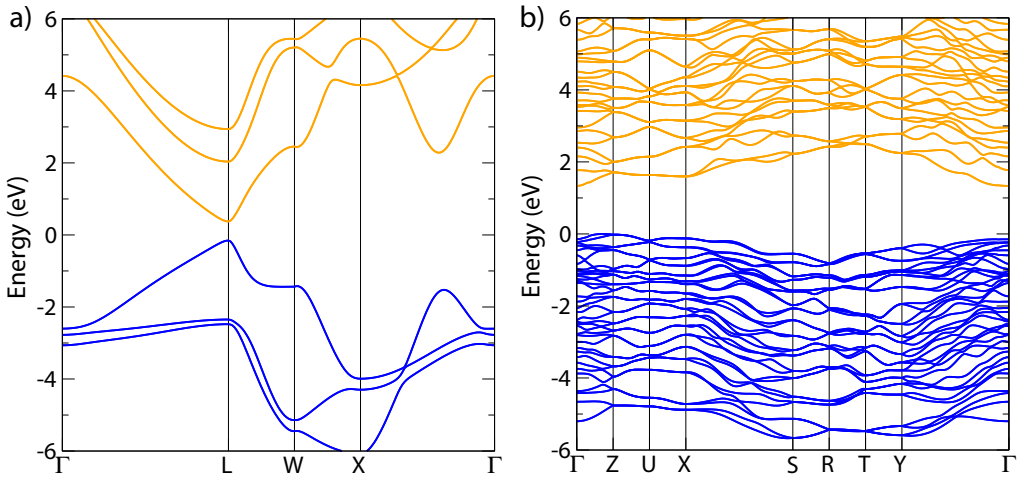

Figure 6.3: HSE06+SOC band structures of a) PbS and b) Bi_2S_3. The valence band is depicted in blue, conduction band in orange, and the valence band maximum is set to 0 eV.

From our HSE06+SOC calculations, PbS is a semiconductor with a narrow gap of 0.279 eV, with both the VBM and CBM occurring at the L point (0.5, 0.5, 0.5). This value for the band gap is very close to that of experiment, 0.286 eV recorded from magnetoabsorption at 4.2 K,[315] and 0.31 eV from highly accurate, but expensive, quasiparticle GW calculations.[345] Bi_2S_3, on the other hand, possesses a moderate, indirect gap of 1.469 eV, which can be compared favourably to a GW+SOC band gap of 1.42 eV,[346] and variable experimental measurements, ranging from 1.4 eV from optical transmission at 77 K[347] to 1.55 eV from UV-vis absorption at room temperature.[348] With these benchmarks established, it appears that HSE06+SOC is able to replicate the band gaps of lead and bismuth sulfides to at least within 0.1 eV and so can be used accurately for the assessment of the ternary materials.

It is important to discuss here how the structural motifs of the binaries influence their electronic structure. The narrow gap of PbS appears to result from large bandwidths (>2 eV) of both conduction and valence band, with noticeably high dispersion in both bands. This reflects how, in the highly symmetric octahedral coordination environment for both species, the atoms are correctly positioned to allow strong interactions between Pb s, p and S p orbitals. In the electronic structure of Bi_2S_3, however, the bands are relatively narrow, with low curvature and the band

gap is indirect: the CBM occurs along Γ to X at (0, 0.111, 0), while the VBM occurs along the path through k-space between Γ and Z, specifically at the point (0, 0, 0.294). This also appears to be a direct result of its structure – all the bismuth atoms occupy an anisotropic coordination environment with 5 bonds to neighbouring sulfurs, and two longer interactions to sulfur atoms on the next 'layer' along **b**, forming an overall highly distorted capped-trigonal prismatic environment. This lack of local symmetry in general and especially the anisotropy appears to prevent strong, symmetric interactions between bismuth and sulfur orbitals, shifting the band maxima off Γ and especially along the **b** axis, results in low dispersion and mobility. However, the narrowing of the bands in Bi_2S_3 enables a wider band gap, and importantly, at around 1.4 eV, this is much closer to the ideal band gap range for high theoretical efficiencies from the S-Q limit than the narrow gap of PbS, making it much more suitable for an absorber layer in a PV device.

The electronic band structures of all five ternary Pb–Bi–S compounds are shown in Figure 6.4, calculated using HSE06+SOC. Due to the large unit cells in all cases, the band structures are noticeably dense with electronic states, making them more reminiscent of Bi_2S_3 than PbS, however the large density of states, and correspondingly the large number of available direct transitions, in many cases will help to strengthen absorption. Equally, when viewing the structural features moving across the series from $Pb_6Bi_2S_9$ (most Pb-containing) to $PbBi_4S_7$ (most Bi-containing), individual trends appear to emerge. Both $Pb_6Bi_2S_9$ and $Pb_3Bi_2S_6$ are direct semiconductors, with the gaps occurring at S and B respectively, which for their space groups (N.B. $Pb_3Bi_2S_6$ uses a reduced symmetry P monoclinic path in order to capture the correct band edges) both correspond to the Brillouin zone boundary at (0, 0.5, 0). As we move further towards Bi_2S_3, however, the band gaps become indirect: the CBM (and lowest direct transition from CB to VB) of $Pb_2Bi_2S_5$ remains at Γ, but the VBM shifts very slightly off, at (-0.082, 0, 0); $PbBi_2S_4$ is becomes further indirect, with the VBM at (0, 0, 0.231) and CBM, and lowest direct transition, at (-0.01, 0.5, 0); finally, $PbBi_4S_7$ becomes the most indirect in energy with the VBM at (0.157, 0.157, 0) and CBM at (0, 0, 0.312). A summary of the band gaps of the materials is given in Table 6.3.

As we move across the series, the ternaries seem to reflect the expected change in electronic structure between the binaries – with the inclusion of more bismuth

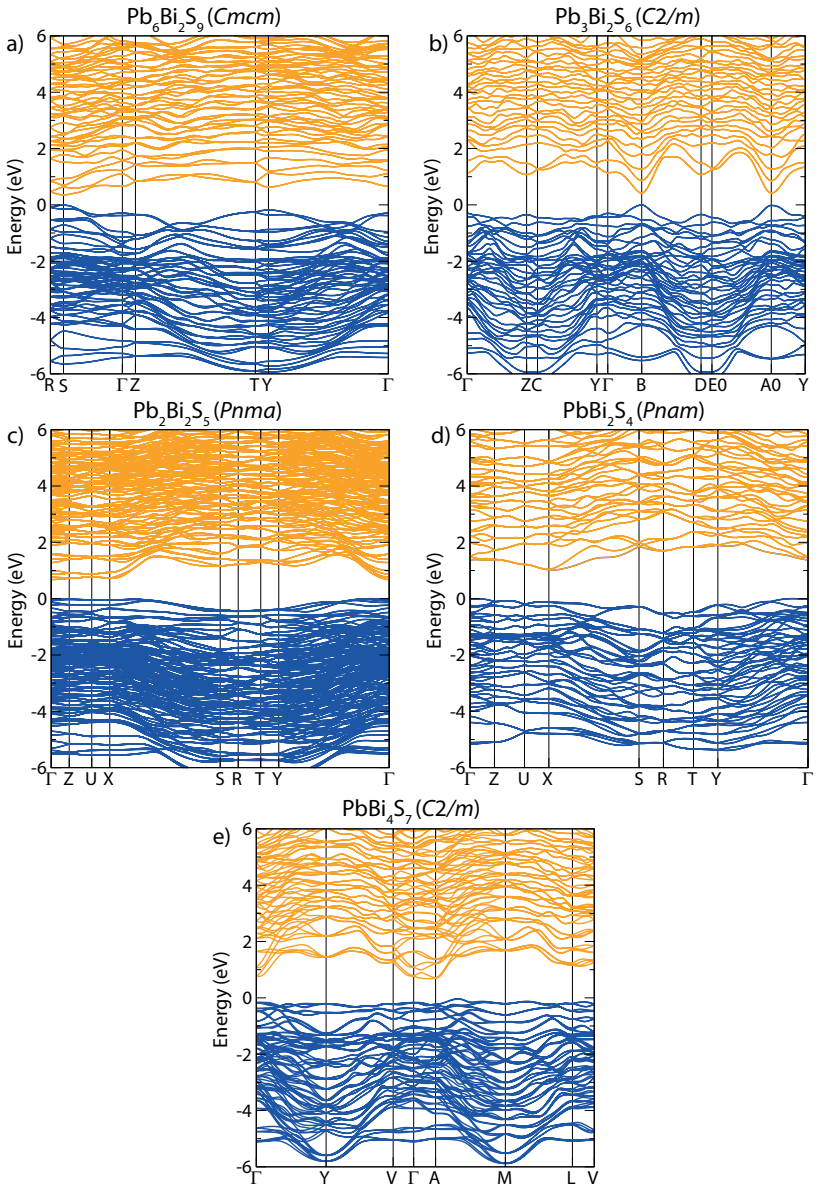

Figure 6.4: HSE06+SOC Electronic band structures of a) $Pb_6Bi_2S_9$, b) $Pb_3Bi_2S_6$, c) $Pb_2Bi_2S_5$, d) $PbBi_2S_4$ and e) $PbBi_4S_7$. Valence band is in blue, conduction band is in orange and VBM is set to 0 eV.

into the structure, the band gap increases from narrow, like PbS, to much, but also becomes more indirect. In the case of $PbBi_2S_5$ in particular, the difference in energy between the fundamental indirect gap (E_g^i) and the lowest available direct transition between valence and conduction bands (E_g^{da}) is $<$0.01 eV, which is so close as to be considered 'near-direct'. For such compounds, while absorption will be hindered at the fundamental gap, the availability of a nearby direct transition means that the overall absorption will be negligibly affected, and thus it acts essentially as a direct semiconductor, which is beneficial for use in solar devices. For $PbBi_2S_4$ and

Table 6.3: Indirect (E_g^i) and lowest direct allowed (E_g^{da}) fundamental band gaps/transitions of PbS, Bi_2S_3 and all calculated Pb–Bi–S systems

Compound	E_g^i/eV	E_g^{da}/eV
PbS	—	0.279
$Pb_6Bi_2S_9$	—	0.253
$Pb_3Bi_2S_6$	—	0.414
$Pb_2Bi_2S_5$	0.678	0.685
$PbBi_2S_4$	1.225	1.323
$PbBi_4S_7$	0.710	0.866
Bi_2S_3	1.469	1.500

$PbBi_4S_7$, the energy difference between E_g^i and E_g^{da} is greater, however no larger than 0.16 eV, and so absorption will still likely be strong – indeed, this is reflected in the high absorption coefficients ($10^5\,cm^{-1}$) seen in all the mixed Pb–Bi–S thin films recorded by Malika *et al.*[337] This is particularly important for $PbBi_2S_4$, the band gap of which lies directly in the ideal range for a high theoretical maximum cell efficiency.

In addition to the direct character of the fundamental gap, moving across the series understandably affects the relative contributions to the conduction and valence bands. The density of states diagrams for the ternary compounds are plotted in Figure 6.5.

The valence band of all 5 ternaries is dominated by S p, but the VBM has appreciable contributions from both Pb s and Bi s, with p states included deeper in energy; the CBM is a mixture of S p, Pb p and Bi p. This make-up is characteristic of post-transition metal oxides and sulfides, where the nominally deep cation s orbitals are able to contribute to the valence band structure via interaction with mixed cation p-anion p orbitals to form antibonding states with s contribution at the very top of the valence band, in the 'lone-pair effect';[89,291] this was pictorially represented for the analogous lead halide perovskites in Figure 1.14. As mentioned previously, this particular electronic structure has been implicated as a major contributor to ideal properties for solar absorption such as defect tolerance, and a large density of states at the VBM, leading to strong absorption.[14,15,20] Trivially, as the proportion of Bi is increased within the structure, the ratio of Bi s to Pb s at the VBM (and similarly for p contribution to the CB) shifts in favour of Bi. A notable exception to

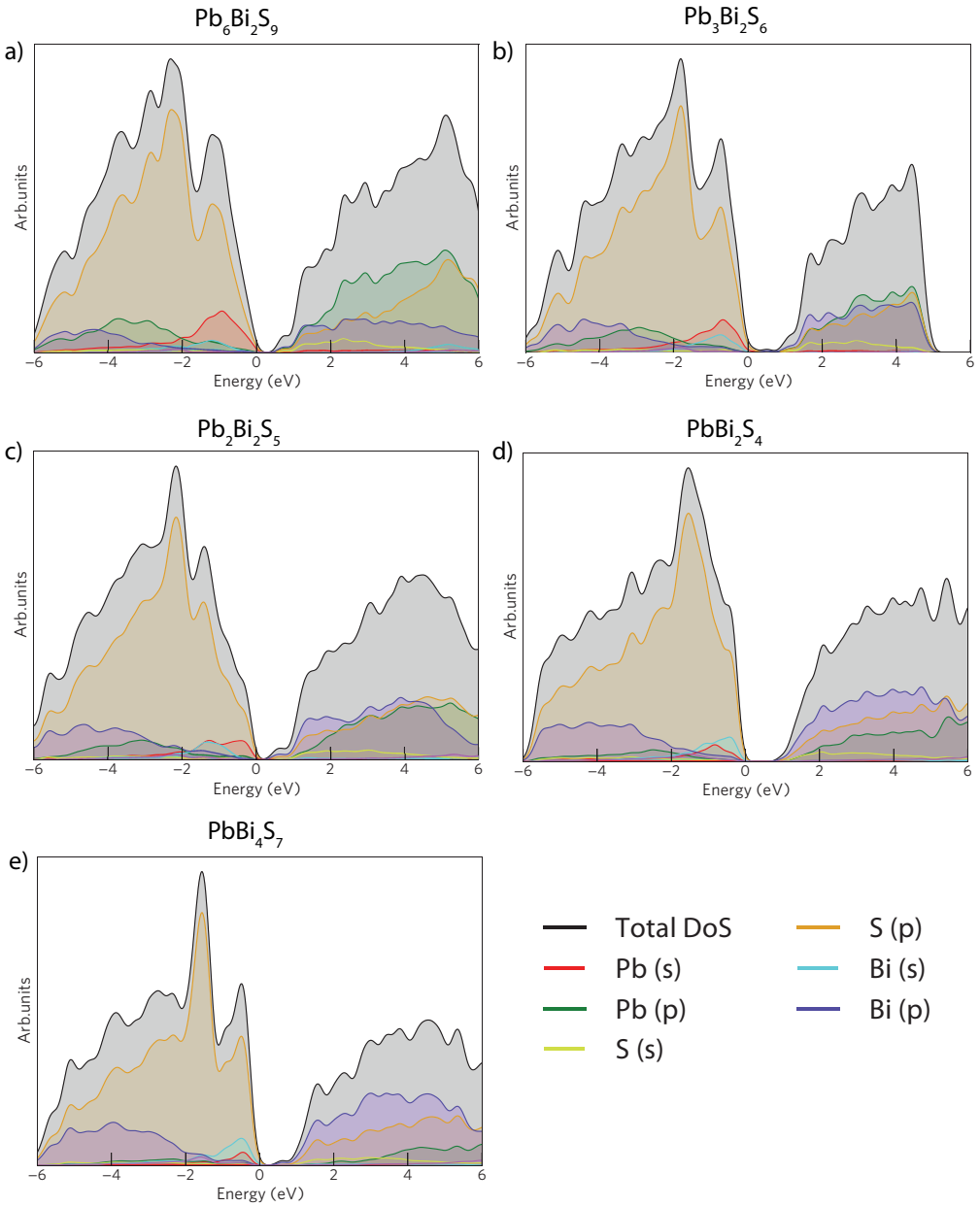

Figure 6.5: HSE06+SOC Density of States (DOS) of a) $Pb_6Bi_2S_9$, b) $Pb_3Bi_2S_6$, c) $Pb_2Bi_2S_5$, d) $PbBi_2S_4$ and e) $PbBi_4S_7$. VBM is set to 0 eV.

this, however, is $PbBi_2S_5$, in which the very top of the valence band is still highly dominated by Pb s, with Bi s lower in energy – the reasons for this will become clear when determining the local electronic structure later.

Equally of note when discussing the trends in electronic structure across the series is the change in band dispersion around the band extrema, which was notably variant between PbS and Bi_2S_3. While the overall band structures of $Pb_6Bi_2S_9$ and $Pb_3Bi_2S_6$ are somewhat 'flat', the dispersion local to the band extrema in both cases is,

in fact, relatively high. To quantify this, the band effective masses (taken as an isotropic average over all calculated directions – despite the anisotropy of the crystal structures, the effective masses for each compound were within 10 % to 20 % of each other) for the VBM (m_h) and CBM (m_e) for all the ternary Pb–Bi–S compounds, as well as those of the binaries for comparison are given in Table 6.4.

Table 6.4: Isotropically averaged hole and electron effective masses for all Pb–Bi–S compounds, calculated using HSE06+SOC.

Compound	m_h/m_0	m_e/m_0
PbS	0.174	0.168
$Pb_6Bi_2S_9$	0.214	0.169
$Pb_3Bi_2S_6$	0.253	0.130
$Pb_2Bi_2S_5$	2.472	0.574
$PbBi_2S_4$	0.682	0.351
$PbBi_4S_7$	0.364	2.004
Bi_2S_3	0.776	0.839

The high curvature around the VBM and CBM for $Pb_6Bi_2S_9$ and $Pb_3Bi_2S_6$ leads to effective masses of $<0.3\,m_0$ for holes and $<0.2\,m_0$ for electrons, indicating the potential for very high mobility of charge carriers in both cases, and on the same order as PbS. In $Pb_2Bi_2S_5$, however, while the conduction band is somewhat disperse along Γ to Y, the valence band has minimal curvature, and this is demonstrated in a moderate electron effective mass of $\sim 0.6\,m_0$, but a hole effective mass of $>2\,m_0$, which is likely to ensure very poor carrier mobility. $PbBi_4S_7$, on the other hand, has a high electron effective mass, as while there is good dispersion in the conduction band along A to M, the A to Γ curvature is minimal – while the valence band is also relatively flat, the VBM itself however is a small pocket of isolated curvature, leading to comparatively mobile holes. $PbBi_2S_4$ appears to offer a more anomalous result, with moderate effective masses for both holes and electrons, and though the dispersion in both conduction and valence bands is significantly less than that in PbS, it is still appreciable; this leaves it the strongest candidate for applications, combining an ideal band gap magnitude with potentially good mobilities.

While the electronic structures of the ternary Pb–Bi–S in general demonstrate a somewhat monotonic progression from 'PbS-like' to 'Bi_2S_3-like', $PbBi_2S_5$ and $PbBi_2S_4$ both offer unusual features that can only be rationalised by examining in greater depth the connection between local structural motifs and bonding. Cation coordi-

nation in particular has been noted in other works to be highly influential on the electronic structure,[312,349] and this is no different in the Pb–Bi–S compounds. To do so, we plot charge density isosurfaces of the valence band maximum for each compound in Figure 6.6.

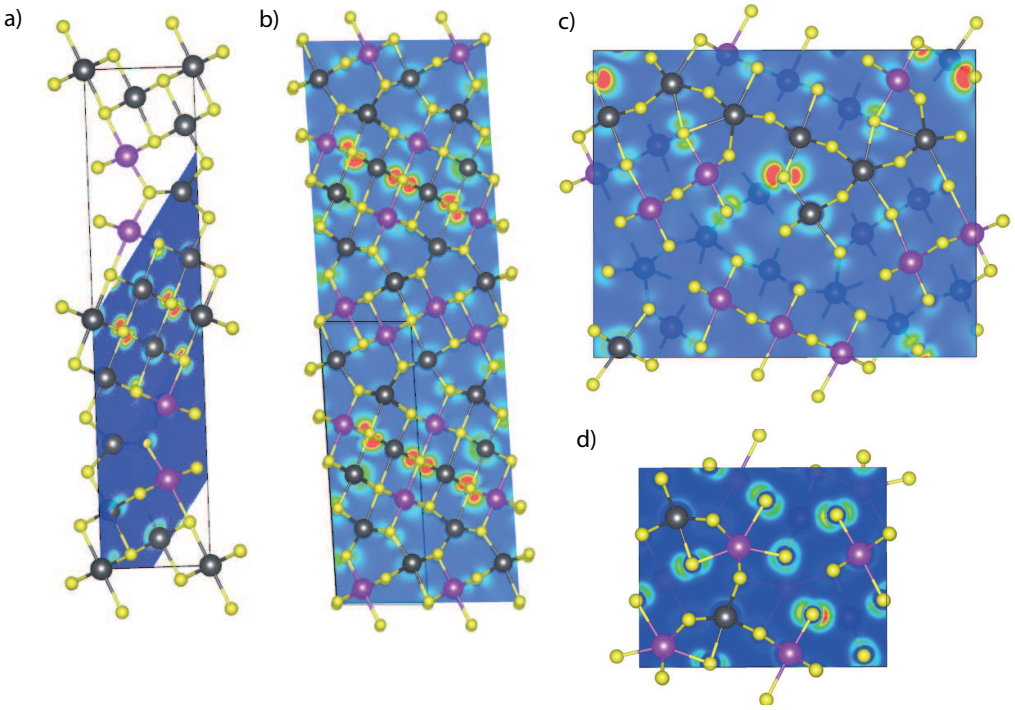

Figure 6.6: Partial charge density isosurfaces of the valence band maxima of a) $Pb_6Bi_2S_9$, b) $Pb_3Bi_2S_6$, c) $Pb_2Bi_2S_5$ and d) $PbBi_2S_4$. Lead atoms are in grey, bismuth atoms in purple and sulfur atoms in yellow, and the isosurface level is set to 1 meV Å^{-1}.

The charge density of the VBM of $Pb_6Bi_2S_9$ is in keeping with the contributions shown in the density of states above – S p orbitals dominate the density picture, with supporting contribution from s-like density on Pb, and a small input from Bi s. What is notable is *where* these sit in the structure, since the majority of the density is focussed on the 'PbS-like' layers of edge sharing octahedra, with minimal density on the bridging bismuth sulfide octahedra, and none on the distorted Pb environment between the layers. Qualitatively, this trend continues with $Pb_3Bi_2S_6$, where again the majority of the electron density sits on edge-sharing PbS octahedra, with only a little more from the bridging Bi-S. This reinforces the electronic structures above – we can hypothesise that strong Pb-S interactions lead to a higher valence band (and narrower gap), and overall high dispersion at the VBM, as the 'PbS-like' environments propagate in two of the crystal dimensions. Moving to $Pb_2Bi_2S_5$, the

electron density remains on the edge-sharing PbS octahedra, however these are no longer occupy an entire layer within the structure; instead, they are confined to a central chain along **b**, and bordered by distorted bismuth sulfide octahedra, which do not appear to interact with the Pb-S. This confinement appears to lead to a highly localised VBM, and thus corroborates the density of states, with localized Pb s states above that of Bi s, and a resultant minimally disperse band and a high hole effective mass. Comparatively, the charge density of the VBM in $PbBi_2S_4$ demonstrates cooperative interaction from both Bi s and Pb s in roughly equal measures, and also in all 3 crystallographic dimensions. Considering the previous compounds, it appears that the complete removal of any Pb-S edge-sharing octahedra from the structure, i.e. the 'PbS-like' motif, results in the VBM instead deriving primarily from the 7-coordinate distorted capped trigonal prismatic arrangement, which Pb and Bi share. The reduction in symmetry in this interaction would likely be the cause of the VBM moving off a high symmetry point, and the weaker interaction overall leads to a lower valence band, leading to a higher band gap, similar to Bi_2S_3. Unlike Bi_2S_3 however, as these Bi and Pb environments appear to retain connectivity in all 3 dimensions, the dispersion in these directions at the band edges remains high, and the effective masses are significantly lower. It is clear that in $PbBi_2S_4$ the relative proportion of Pb and Bi is enough to balance the structural motifs of PbS and Bi_2S_3 and prevent the PbS motif from dominating the electronic structure, and thus form a structure with a more ideal mix of properties for use as a PV absorber layer.

6.3.3 Optical properties and SLME

So far we have highlighted the strong impact that structural motifs have on the electronic structure of the Pb–Bi–S series. Optical absorption, however, is crucial for PV applications, and while $PbBi_2S_4$ appears to possess the most promising electronic structure, it is important to assess the impact that the indirect band gap could have. The optical absorption coefficient, α, for all the Pb–Bi–S compounds was obtained via the calculation of real and imaginary high-frequency dielectric constants, and are plotted in Figure 6.7.

We can see that despite its indirect band gap, $PbBi_2S_4$ has perhaps the sharpest absorption edge of all the ternary compounds, with α rapidly increasing to a high value

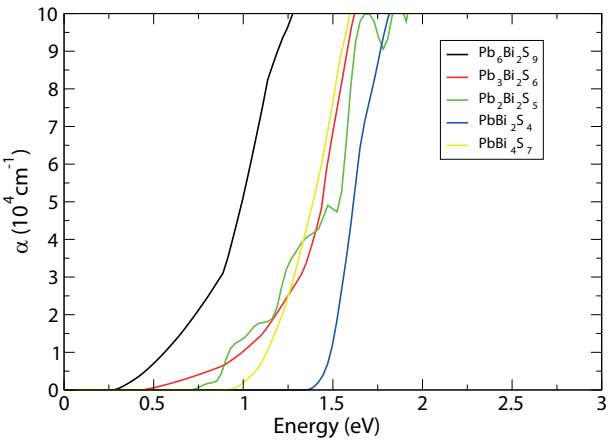

Figure 6.7: HSE06+SOC calculated absorption coefficients of the 5 Pb–Bi–S compounds as a function of energy.

of $10^5\,\mathrm{cm}^{-1}$; comparatively despite their direct band gaps, $Pb_6Bi_2S_9$ and $Pb_3Bi_2S_6$ have relatively shallow absorption, possibly as a result of the higher dispersion of conduction and valence bands leading to a lower overall density of states up to 1.5 eV above the valence band (considering the density of states above) and weaker absorption in that range. Additionally, the high-frequency dielectric constants themselves are given in Table 6.5. As with some of the trends above, again there is no monotonic decrease in dielectric between PbS and Bi_2S_3, with $Pb_6Bi_2S_9$ predicted to have a higher dielectric than both binaries, however in general, the compounds with higher Pb content have a higher dielectric. $PbBi_2S_4$ once again possesses improved properties than would be expected from its position in the series, with a higher dielectric constant than $PbBi_2S_5$. Overall, this should act to aid charge screening, potentially improving defect tolerance and carrier lifetimes. With the calculated optical properties, we can combine these with the information above regarding the band gaps of the system to calculate the SLME for each material in order to quantitatively assess their relative potential for PV; the SLME percentages for a film thickness of 0.2 µm are also included in Table 6.5.

The SLME values primarily reflect the band gaps of the individual materials – although $Pb_6Bi_2S_9$ and $Pb_3Bi_2S_6$ have otherwise promising properties such as low effective masses and high dielectric constants, their narrow band gaps will severely limit the potential V_{oc} of a single junction cell, and so the SLME is low. The phases with greater proportion of Bi, with band gaps closer to the 1.0 eV to 1.5 eV range, possess higher SLMEs which are closer to the 20 % target proposed in the original

Table 6.5: Optical properties of the lead bismuth sulfides: high frequency dielectric constants (ϵ_∞) and Spectroscopically Limited Maximum Efficiency (SLME) at 0.2 µm film thickness, calculated using HSE06+SOC.

Compound	ϵ_∞	SLME/%
PbS	17.20	—
$Pb_6Bi_2S_9$	18.40	7.77
$Pb_3Bi_2S_6$	15.11	10.57
$Pb_2Bi_2S_5$	13.61	19.03
$PbBi_2S_4$	14.65	26.13
$PbBi_4S_7$	14.62	18.46
Bi_2S_3	13.47	21.91

article from Yu and Zunger.[186] However, $Pb_2Bi_2S_5$ and $PbBi_4S_7$ both still lie below the 21.9 % for the binary Bi_2S_3, which is our target to improve upon. $PbBi_2S_4$, on the other hand, has an SLME of 26.1 %, well above the other tenary Pb–Bi–S compounds, Bi_2S_3, and even the 23 % predicted for the champion absorber $CuInSe_2$ for the same film thickness. Additionally, we can calculate the SLME as a function of film thickness, to examine how the efficiency approaches the infinite thickness limit: this is plotted for $PbBi_2S_4$, as well as $Pb_2Bi_2S_5$ and $PbBi_4S_7$ in Figure 6.8.

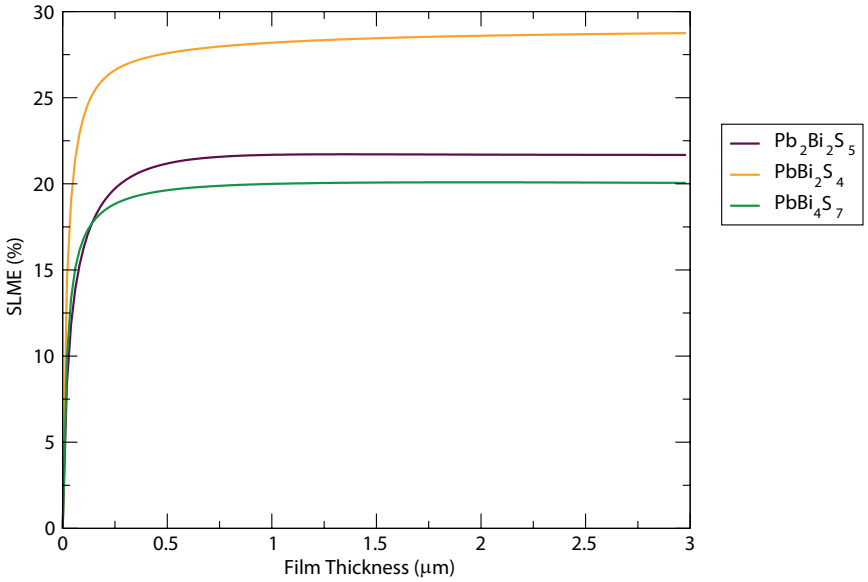

Figure 6.8: Spectroscopically Limited Maximum Efficiency (SLME) for the most efficient lead bismuth sulfides, as a function of thickness, calculated using HSE06+SOC.

While the SLMEs of $Pb_2Bi_2S_5$ and $PbBi_4S_7$ mostly plateau above a thickness of 0.5 µm, $PbBi_2S_4$ still increases with film thickness, reaching 27.5 % at 0.5 µm, and

increasing towards 30 % at micron-thicknesses. While this limit would likely be too large for a 'thin-film' absorber, this does demonstrate the strength of the calculated absorption for $PbBi_2S_4$ and its promise as a PV material.

6.3.4 Towards a functional device: intrinsic defects and alignment

With $PbBi_2S_4$ established as a promising solar absorber candidate material from our screening of the optoelectronic properties of the ternary lead bismuth sulfides, we can now consider in greater detail how it will function within a cell architecture. One of the most crucial aspects to examine are the intrinsic defects, as these will fundamentally influence both whether the material is p or n-type, and thus what buffer layers and alignments will be required, and also the concentrations of potential trap sites or recombination centres for charge carriers, which can severely limit carrier lifetimes and the V_{oc} of a cell.

Before the formation energies of individual defects can be calculated, we must first calculate the chemical potential space that $PbBi_2S_4$ exists within under thermodynamic equilibrium with other competing phases. The limits of this chemical potential space are the most extreme points under which $PbBi_2S_4$ can be formed, and so become the most representative points to evaluate formation energies at in order to summarise the behaviour of the entire formation space. The chemical potential limits for $PbBi_2S_4$, calculated from PBEsol total energies of all competing Pb–Bi–S phases and utilising CPLAP, are plotted in Figure 6.9.

PbS and Bi_2S_3 are the sole limiting phases for $PbBi_2S_4$, giving four chemical potential limits where these intersect with the overall formation space. These four limits are labelled as follows: A ($\mu_{\mathrm{S}} = 0$, $\mu_{\mathrm{Pb}} = -1.0606$, $\mu_{\mathrm{Bi}} = -0.9685$); B ($\mu_{\mathrm{S}} = 0$, $\mu_{\mathrm{Pb}} = -1.0836$, $\mu_{\mathrm{Bi}} = -0.9570$); C ($\mu_{\mathrm{S}} = -0.6457$, $\mu_{\mathrm{Pb}} = -0.4149$, $\mu_{\mathrm{Bi}} = 0$); D ($\mu_{\mathrm{S}} = -0.6380$, $\mu_{\mathrm{Pb}} = -0.4456$, $\mu_{\mathrm{Bi}} = 0$). Given that the chemical potential space is very narrow, there are negligible differences between the two pairs of (A, B) and (C, D), thus for the purposes of the analysis, one of the pair will be treated as the primary thermodynamic extrema – this gives two conditions to consider: sulfur-rich, or most p-type conditions (A, B), and bismuth-rich, the most n-type conditions (C, D). The formation energies of all available vacancies and cation-cation antisites were calculated, with the addition of cation-anion antisites due to prior reports

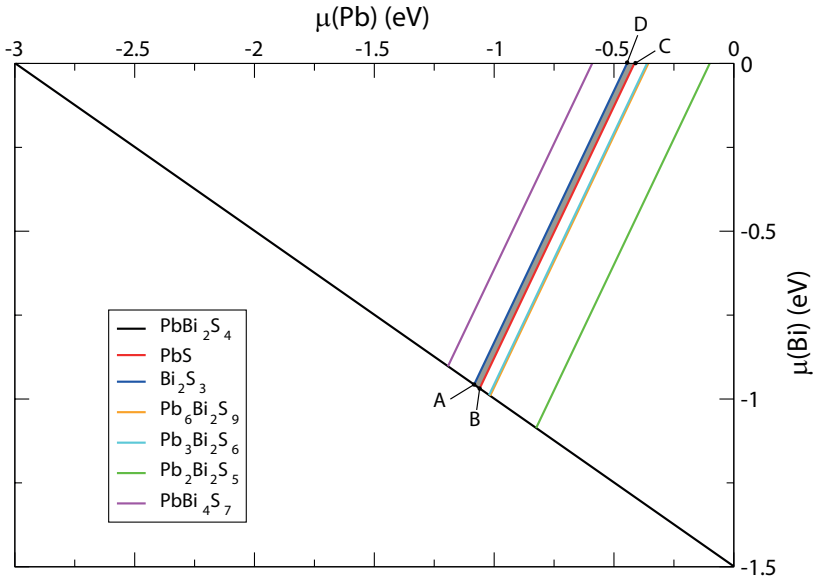

Figure 6.9: Chemical potential space of $PbBi_2S_4$, with the black triangle defining the limit of the formation enthalpy of $PbBi_2S_4$ and μ_S as the dependent variable. The available space is then limited by the formation of competing phases (PbS and Bi_2S_3), with the stable region shaded in grey, and the limits A – D marked. All formation energies were calculated using the PBEsol functional.

demonstrating that in the Bi_2Ch_3 (Ch = S, Se, Te) series, both Bi_{Ch} and Ch_{Bi} can have relatively low formation energies and act as dominant defects, and so could also be present in $PbBi_2S_4$; as the structure is close-packed and all atoms are relatively large, interstitials were not considered as large structural relaxations (and high formation energies) were anticipated. Transition level (TL) diagrams for the chemical potential limits A and C are presented in Figures 6.10 and 6.11 respectively; due to the large number of available sites, and thus potential defects, the figures separate defect types for clarity.

From the TL diagrams, it is clear that the defect physics of $PbBi_2S_4$ is complex. As such, this discussion will focus on the dominating or otherwise significant defects for each limit. In both S-rich and Bi-rich conditions, however, the dominant defects are Pb_{Bi} and Bi_{Pb}, which have formation energies below 1 eV at all Fermi level positions over both thermodynamic conditions, indicating that they will be present in reasonable concentrations in $PbBi_2S_4$, regardless of how it is formed. This is perhaps unsurprising, given the similar sizes and electronic configuration of Pb^{2+} and Bi^{3+}, and the aforementioned observations of Pb/Bi disorder in some samples. As Pb_{Bi} is (primarily) p-type and Bi_{Pb} n-type, for a given starting Fermi level position, if the concentration of one (e.g. Pb_{Bi}) were to be increased through incorporation

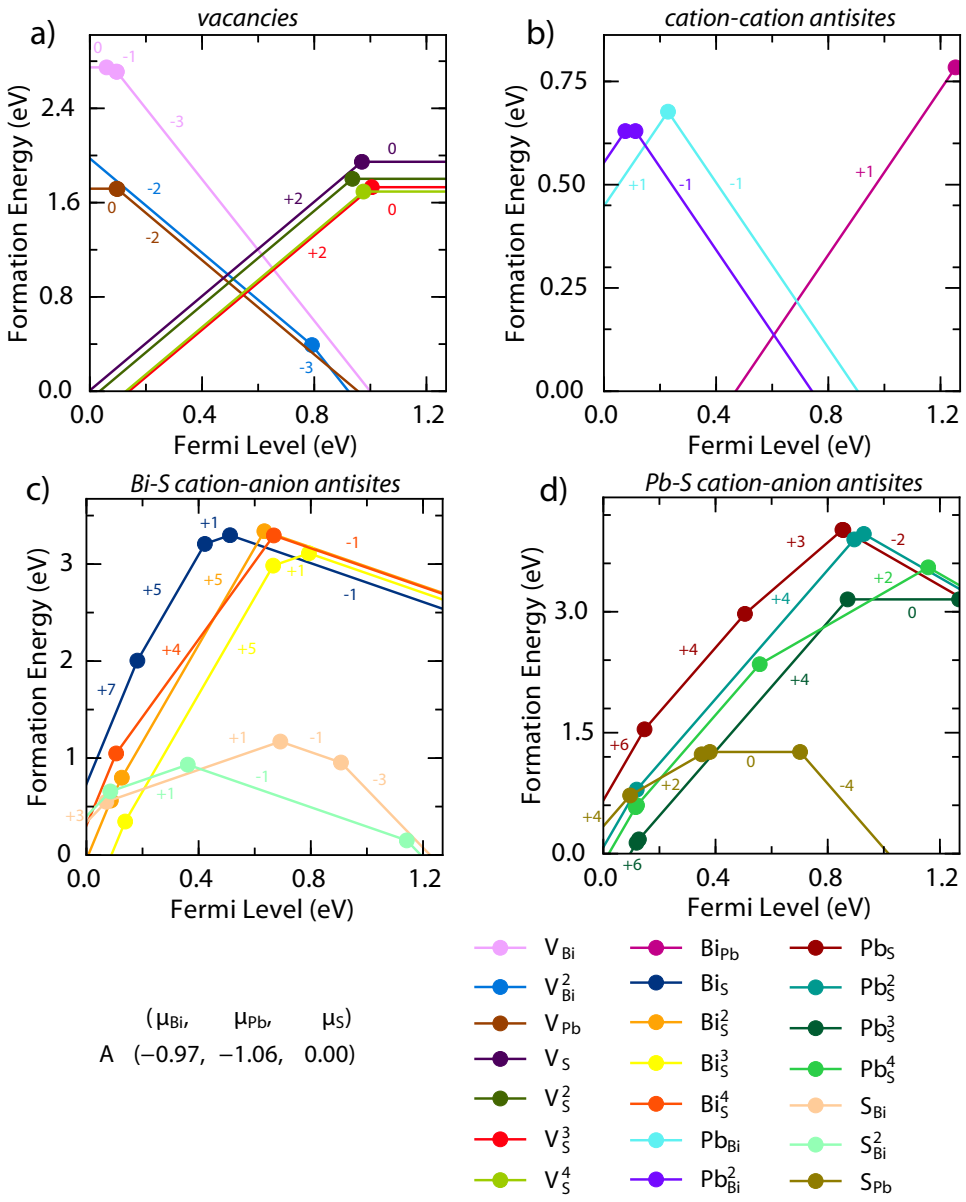

Figure 6.10: Defect transition level diagram of $PbBi_2S_4$, at chemical potential limit A (S-rich conditions), plotting the formation energies of a) Vacancies, b) Cation-cation antisites, c) Bi-S cation-anion antisites and d) Pb-S cation-anion antisites as a function of the Fermi level position above the VBM (0 eV). Superscripts in the defect labels indicate symmetry-inequivalent atomic sites in the $PbBi_2S_4$ unit cell, lines are labelled with charge state (parallel lines represent the same charge state, regardless of defect), and circles represent position of thermodynamic transition levels between charge states.

of excess Pb (or indeed, additional similar-type doping were to be attempted), the Fermi level position will shift towards a band edge – in this example, the VBM. This shift will, however, mean that the formation energy of the other defect (Bi_{Pb}) is reduced, increasing the likelihood of it forming, and this additional formation of

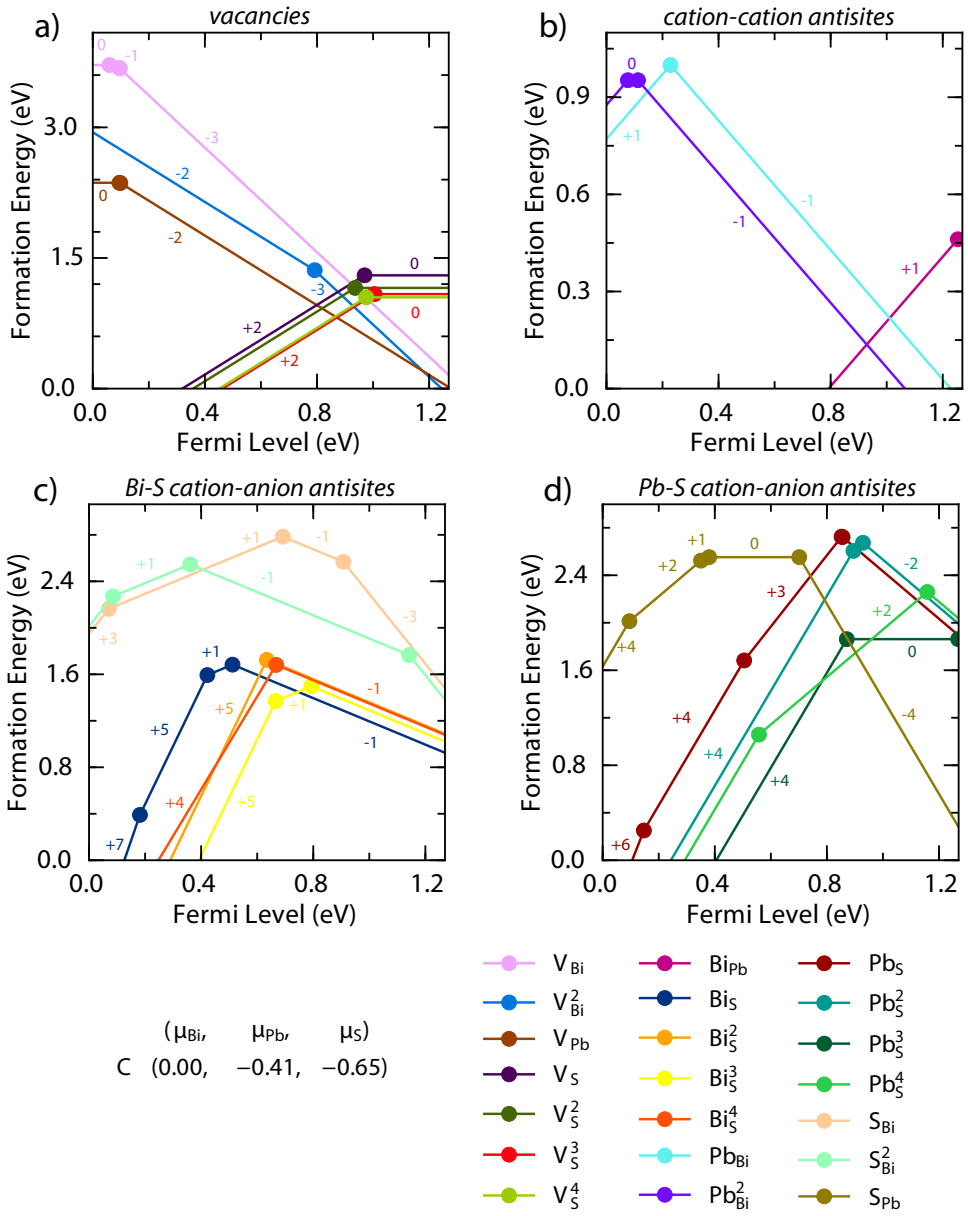

Figure 6.11: Defect transition level diagram of $PbBi_2S_4$, at chemical potential limit C (Bi-rich conditions), plotting the formation energies of a) Vacancies, b) Cation-cation antisites, c) Bi-S cation-anion antisites and d) Pb-S cation-anion antisites as a function of the Fermi level position above the VBM (0 eV). Superscripts in the defect labels indicate symmetry-inequivalent atomic sites in the $PbBi_2S_4$ unit cell, lines are labelled with charge state (parallel lines represent the same charge state, regardless of defect), and circles represent position of thermodynamic transition levels between charge states.

donors acts to shift the Fermi level in the opposite direction, moving the Fermi level back to its original position and compensating for the original change. The practical implication of this equilibrium is that the Fermi level will be pinned around the position in the gap at which the two defects (specifically Pb_{Bi} (-1) and Bi_{Pb} (+1))

intersect due to this compensation, making $PbBi_2S_4$ an intrinsic semiconductor and difficult to dope either p or n-type. Under S-rich conditions, we can predict that this pinning will occur 0.6 eV above the VBM, while in Bi-rich conditions, it will be 0.3 eV below the CBM. We can verify these predictions quantitatively using the self-consistent Fermi level approach developed by Buckeridge and others,[350] which uses all defect formation energies to calculate their relative concentrations and thus the position of the Fermi level. When using this method, the Fermi level positions are predicted to be 0.606 eV above the VBM for S-rich conditions, and 0.302 eV below the CBM for Bi-rich conditions, validating our estimated positions above, and confirming that Pb_{Bi} and Bi_{Pb} are dominant.

Pb_{Bi} and Bi_{Pb} themselves, while dominant defects, should be relatively benign towards charge carriers. Bi_{Pb} is predominantly in the $+1$ charge state, with the $+1/0$ transition level occurring within 0.02 eV of the CBM, allowing the room temperature thermalization of any carriers in the defect state into the conduction band and making it a shallow donor. On both Bi sites, Pb_{Bi} is an amphoteric defect, and on one site it acts as a negative U-defect, with the only charge states predicted to be -1 and $+1$ — this follows from the relative stability and common occurrence of both Pb^{2+} and Pb^{4+} oxidation states. The transition levels occur above the valence band, making it a deep acceptor and ultradeep donor, so could be problematic; the lower formation energy Pb^{1}_{Bi} is shallower than the other site, which bodes well for thermalization into the valence band. The other defects to be considered then vary strongly depending on the chemical potential limits, as these lead to wide variation in formation energies and the Fermi level position to be evaluated.

In the S-rich limit, it is immediately possible to note that, for a Fermi level position of 0.6 eV the Bi_S and Pb_S antisites, over all positions, are too high in formation energy to be present in any appreciable concentration in the material – at room temperature, and even elevated synthesis temperatures, formation energies of >2 eV correspond to defect concentrations $\ll 10^{10}\,cm^{-3}$, orders of magnitude lower than are likely to impact the electronic properties. As a result, the behaviour of these defects will not be considered in this regime. The S_{Pb} and S_{Bi} defects however have formation energies of 1.2 eV and 0.75 eV to 1.0 eV respectively, and are thus likely to be influential. S_{Pb} demonstrates multiple mid-gap transition levels, between $+4/+2$, $+2/+1$, $+1/0$ and $0/-4$ (again, perhaps unsurprising due to the number of

stable oxidation states for sulfur) – as a result, although the neutral defect should be relatively benign, there is strong thermodynamic availability for charge capture and recombination. Similarly, S_{Bi} is amphoteric and has deep transition levels between $+3/+1$, $+1/$-1 and -1/-3, varying in energy dependent on Bi position, and at even lower formation energies than S_{Pb}. In combination, both of these defects are likely to form mid-gap trap states and act as Shockley-Read-Hall recombination centres, likely significantly and detrimentally affecting any cell performance. The vacancies, on the other hand, are less likely to be problematic – with formation energies between 0.8 eV to 1.2 eV, they will be present in non-negligible concentrations, but the $+2$ charge state on all V_S, and the -2 charge state of V_{Pb} will likely compensate each other. While the transition levels for both V_{Pb} and V_{Bi}^{1} are 'deep', they are also well within 0.1 eV of the VBM, meaning thermalization is still definitely a possibility and their impact may be minimal; V_S demonstrates very similar behaviour over all 4 lattice positions, acting as a deep donor.

In the Bi-rich limit, the detrimental anion-on-cation antisites S_{Pb} and S_{Bi} now possess much higher formation energies due to the much lower chemical potential of sulfur: both S_{Bi} have energies $>$2 eV, and while the -4 charge state of S_{Pb} has a steep formation energy trajectory in n-type conditions, at a position of 0.923 eV above the VBM, it still has a formation energy of 1.6 eV and so is also likely to have negligible impact on carrier transport. Conversely, the Bi_S and Pb_S both experience much lower formation energies, particularly where higher charge states such as $+4$ and $+5$ dominate – close to the VB – however, at the point where the Fermi level is pinned, their formation energies remain relatively high – above 1.6 eV for Pb_S and 1.2 eV to 1.5 eV for Bi_S, despite the highly favourable chemical potential. As a result, it appears that in this limit, the limiting and detrimental effect of the multiple deep transition levels presented by cation-anion and anion-cation antisite defects could be minimised. The vacancies are in a very similar situation to the S-rich case, as with the fall in formation energy of V_S, and raising in energy of V_{Pb} and V_{Bi}, are counteracted by the shift in Fermi level position towards the CBM, and so the formation energies are still within the approximate 0.8 eV to 1.2 eV range. As a result, the comments above, and the relative behaviour will hold the same for Bi-rich as S-rich.

In summary, while Bi-rich conditions could reduce the defect concentrations of those anion-cation antisites which could act as problematic trap sites, at all available chem-

ical potentials, $PbBi_2S_4$ is an intrinsic semiconductor, with the Fermi level pinned mid-gap by compensating cation-cation antisites. This has strong implications on the cell architecture that will be needed: instead of a regular $p-n$ junction, a $p-i-n$ architecture can be used instead, sandwiching an intrinsic absorber layer between an n-type buffer layer, or electron transporting material, and a p-type layer, a hole transporting material. As discussed in the Section 1.3.3, this can be very common in sensitized solar cells, with the n-type layer usually an oxide scaffold such as TiO_2 or SnO_2 to allow easy lattice matching with the TCO layer – often the same compound, with higher doping. Considering this, we can predict a solar cell architecture for $PbBi_2S_4$ by calculating its band alignment with the vacuum level, and then matching the band edges to ionization potentials and electron affinities of potential cell partner layers. We calculate the ionization potential of $PbBi_2S_4$ with HSE06+SOC using the vacuum-slab method detailed in the Methodology, finding it to be 6.3 eV, which is notably quite high in comparison with other champion solar absorbers: both CZTS and MAPI possess IPs around 5.7 eV to 5.8 eV, and CdTe is particularly noted to have a high IP at 6.1 eV.[305,306,351] The reasons for this high IP likely come from two sources: firstly, bismuth halides $Cs_3Bi_2I_9$ and BiI_3 have both been recorded to have IPs $>$6 eV,[352,353] and they demonstrate similar high Bi s contribution to the VBM and moderate dispersion, indicating that this could be a feature of Bi compounds in general; secondly, cation coordination has a large effect on the ionization potential, as it affects the Madelung potential around the metal centre, and thus the relative energy levels of the bonding states. This has been noted previously to have influence on the alignment of TiO_2 polymorphs,[312] while in this thesis we have discussed that the low coordination environment of AgCuS can lead to a low IP and so the seven-coordinate environment for both Pb and Bi could result in a high IP.

Using the IP, we can then align the VBM position with that of potential p-type layers, and the CBM position, predicted using the HSE06+SOC band gap, with n-type layers/TCOs, which is plotted in 6.12.

One TCO which has an electron affinity above the 5.1 eV of $PbBi_2S_4$ is In_2O_3 – specifically when doped with Sn (ITO) its IP reaches 5.2 eV,[354,360] which is also one of the most common TCOs in usage.[361] Another highly common n-type scaffolding or transport layer is SnO_2; while its EA is $<$5 eV when undoped,[355] recent work from

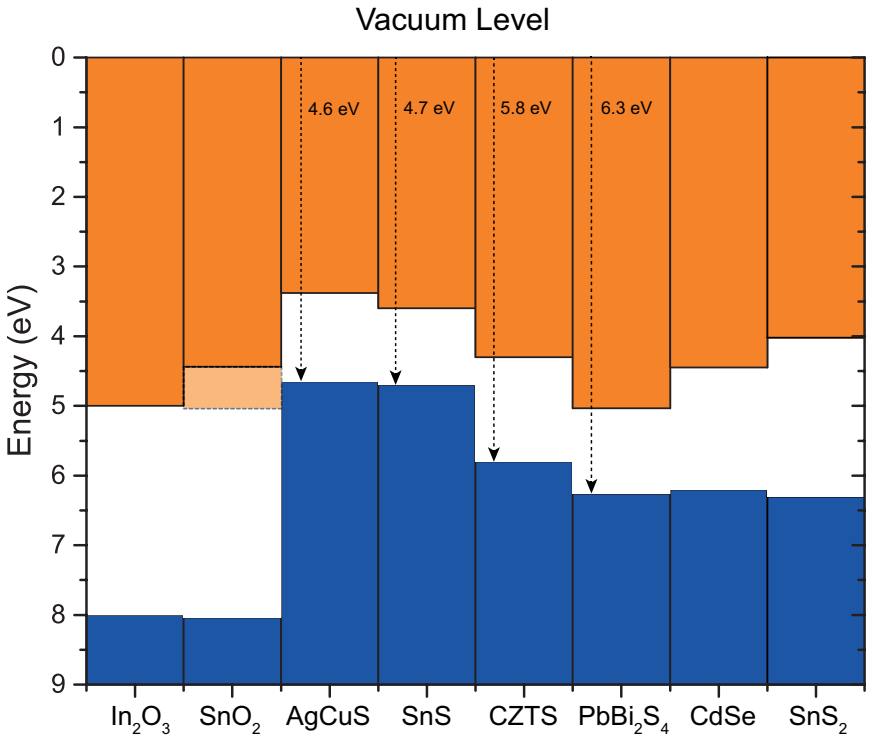

Figure 6.12: HSE06+SOC band alignment of $PbBi_2S_4$ with other solar absorbers, n-type layers/TCOs and p-type dopable semiconductors. The band positions of the other semiconductors are taken from experiment or theoretical calculations in the literature.[305,342,354–358] The conduction band level of SnO_2 is extended to demonstrate how it can be lowered by 0.6 eV by doping with 12 % Pb per formula unit.[359]

within our group has shown that its EA can be effectively increased by up to 0.6 eV through isovalent doping with up to 12 % Pb per formula unit,[359] while retaining transparency, making this another promising candidate to match with. Both also have very deep valence bands, making a substantial potential barrier to minority hole carriers from crossing into the n-type layer (against the expected current flow), which should further act to prevent losses. Finding a suitable p-type layer with minimal band offset is more challenging due to the larger IP of $PbBi_2S_4$, but two other semiconductors with similar ionization potentials that could be doped p-type are bulk SnS_2,[358,362] which with a higher band gap would also provide a minority electron-blocking potential from its CB offset, and nanocrystalline CdSe,[357] which recent reports have suggested could be p-type doped with sufficient concentration of substitutional Ag.[363] Nevertheless, P3HT has recently been used with reasonable success as a back-contact layer for CdTe despite a near 1 eV VB offset, and so there is likely a wide range of possible p-type layers that could be considered.[351]

6.3.5 Conclusions

In this chapter, we have theoretically explored the electronic and optical properties of the previously under-characterised ternary lead bismuth sulfides. We find that in general, trends within the Pb–Bi–S series follow in expectation with the properties of the binary compounds, with the band gaps increasing but becoming more indirect and less dispersive band edges moving from $Pb_6Bi_2S_9$ to $PbBi_4S_7$. $PbBi_2S_4$ appears to stand out as a notable exception to some of these trends, possessing an ideal, near-direct band gap with moderate effective masses, and a high SLME of 26 % for a 200 nm thin film, making it a highly promising candidate for solar absorption within PV devices. To further facilitate study in this area, we calculated the intrinsic defects of $PbBi_2S_4$, predicting it to be an intrinsic semiconductor due to compensation of low-formation energy cation-cation antisite defects. From this we then use band alignment to predict potential partner layers for a working candidate solar cell architecture.

The results included in this chapter were written up as a paper, which was accepted and published in Chemistry of Materials.[364] *Some of the figures in this chapter have been adapted from those included in this paper.*

Chapter 7

Conclusions and Summary

Throughout this thesis, we have discussed the potential for families of materials that demonstrate excellent intrinsic properties on the atomistic scale to become emergent solar absorbers, worthy of future study – however we have also found materials where inherent weaknesses may hold them back. The lead halide perovskites, as explained in the Introduction, provide a case study for how materials with near-optimal electronic and optical properties can become, with only some initial research interest, a major competitor to well-established alternatives, yet that there can still be key challenges that require significant study to try and overcome. Equally, there are numerous other materials that appear to, or are predicted to possess promising properties, however lack of interest, or challenges in development, has led to low performance.[13] This chapter will summarise the key findings of the work enclosed in this thesis, but also attempt to connect these individual studies to the wider search for emergent materials for usage in PV that motivated this study.

In Chapter 4, we examined the caesium silver bismuth halides within the context of lead-free analogues to methylammonium and formamidinium lead iodide. First synthesised in 2016, the double-perovskite Cs_2AgBiX_6 (X = Cl, Br) family initially held promise as a route for removing Pb^{2+}, through equal substitution of Ag^{+} and Bi^{3+}, while retaining the cubic perovskite structure that appeared to allow the exceptional electronic properties of MAPI and related compounds. However, the experimentally-recorded optical band gaps for the caesium silver bismuth halides were large and indirect, and thus demonstrated poor potential efficiencies. Our research into these materials focused on 3 key areas: the electronic properties, and why they differed to the isostructural lead halide perovskites, the thermodynamic stability, and the potential cation disorder between Ag and Bi, due to similar sizes and symmetry sites within the structure.

When comparing to a hypothetical cell with lead substituted back into the $Cs_2AgBiBr_6$ structure, the differences in electronic makeup between these compounds and their lead halide analogues became clear: the combination of s-valence Bi and d-valence Ag leads to a mismatch in symmetry, with the in-phase (Γ point) nearest-neighbour interaction between octahedral units unable to occur, unlike in the equivalent lead-based structure. This has the effect of both reducing the conduction bandwidth, thus widening the gap, and forcing it to be indirect – traits that will occur for any Cu^{+} or Sb^{3+} equivalents; these effects can be reversed, however, if a s-valence cation

such as In^+ or Tl^+ are hypothetically substituted in place of Ag. The absence of a narrower-gap iodide compound is further explained due to a predicted thermodynamic instability towards the experimentally-observed $Cs_3Bi_2I_9$, and equally the instability of the 1+ state for In and Tl leads to those hypothetical substitutions to also be unstable. Furthermore, using a regular solution model, Ag/Bi disorder was predicted to not be complete in room-temperature $Cs_2AgBiBr_6$, however at elevated temperatures it could be relevant, and reduces the band gap significantly. Throughout all 3 key areas, the compounds in the Cs_2AgBiX_6 family demonstrate some intrinsic weaknesses that could hinder or complicate their future application as photovoltaic materials, and thus our findings indicate that, even at this early stage of research, these compounds would be poor candidates for stable, Pb-free replacements to the hybrid lead halide perovskites.

The recent usage of nanoscale Ag_3CuS_2 within a working solar cell motivated our collaborative study of it and AgCuS in Chapter 5, in particular as a potential thin film absorber in the model of other chalcogenide solar absorbers such as CdTe and CZTS. Combining theory with experimental results, we are able to develop a reliable description of the highly-correlated valence band states of AgCuS using hybrid DFT. Both compounds are predicted demonstrate fundamental direct band gaps within the ideal 1.0 eV to 1.5 eV range for high photovoltaic efficiencies, as well as low carrier effective masses. However, further examination reveals significant differences to other thin-film absorbers: in both AgCuS and Ag_3CuS_2, the fundamental direct gap is partially symmetry-forbidden, and while this only increases the effective optical gap of AgCuS by $\sim$0.2 eV, it increases that of Ag_3CuS_2 by over 1 eV, thus severely limiting the predicted SLME, as it is likely to severely impact the EQE and absorption of any device. As such, of the two silver copper sulfides, AgCuS is predicted to be the more promising for solar applications.

Additionally, the slightly unusual cation coordination in AgCuS (in comparison to the regular tetrahedral coordination in both CdTe and CZTS, for example) could have other electronic effects: the dominant contribution from the Cu/S network to the valence band appears to induce anisotropy in the hole effective masses; the lower coordination number in AgCuS could have an effect on the local Madelung potential, giving a much lower ionisation potential in comparison with other established absorbers – and thus we try to align the valence and conduction bands of AgCuS

with potential contacts and n-type layers. Nevertheless, in the context of the search for non-toxic thin film absorbers, AgCuS demonstrates that conforming to known structure types (such as relying on cation mutation of the CdTe structure) is not necessary to produce competitive electronic properties to other absorbers. In all, our study of the silver copper sulfides provides strong evidence that relying on the magnitude of the band gap alone is insufficient for the screening of potential solar absorbers, as optical and structural effects can have significant impact on the inherent behaviour of a material, and that less regular or symmetric structural compositions can still allow for excellent optoelectronic properties.

Finally, Chapter 6 discusses the lead bismuth sulfides, covering our ability to use *ab initio* methods predictively – this family of ternary compounds has had minimal characterisation other than crystal structure determination previously, despite both end-member binaries, PbS and Bi_2S_3, being trialled as solar absorbers. Our calculations find that the electronic structures of the ternary compounds reflect the structural motifs of the binary compounds within the structure, particularly the Pb-S octahedra when present: the Pb-rich members of the series possess narrow, direct band gaps with valence bands dominated by the Pb-S interaction, while the Bi-rich members tend to show wider, indirect band gaps with lower band dispersion, the indirect nature especially occurring when 6-coordinate Pb motif does not occur in the structure at all, and thus high-symmetry orbital interaction is no longer maximal.

Of the 5 Pb–Bi–S compounds studied, $PbBi_2S_4$ emerges as the most promising candidate as an absorber for photovoltaic applications, with a near-direct band gap of 1.2 eV, and a high predicted SLME of 26 $\%$ for a thickness of 200 nm, together with moderate carrier effective masses and dielectric constant. Further *ab initio* prediction of properties was possible through the calculations of the intrinsic point defects of $PbBi_2S_4$: the dominant, low formation energy antisites Pb_{Bi} and Bi_{Pb} will pin the Fermi level within the gap, making the material an intrinsic absorber, there were few other low-energy, deep transition levels, indicating that $PbBi_2S_4$ could be somewhat defect tolerant. This study in particular demonstrates how screening of materials with *ab initio* methods can be used to predict numerous device-relevant properties while requiring minimal prior input – we may start from a crystal structure and end with a specific device architecture to be trialled and verified by experimentalists.

All 3 compound families do provide potential avenues of future study, informed by our results here. The caesium silver bismuth halides, while not appropriate for solar absorbers in photovoltaic devices, could be of use in other applications, such as γ-ray detection, where heavy elements are prized, while still being solution-processable. Additionally, their observed fully cubic structure at room temperature is unusual in comparison to the caesium and methylammonium lead halides, which almost all show distortions or tilting – as such, theoretical exploration of their phonon behaviour and any such structural displacements could be valuable. When discussing the alignment of AgCuS, we relied on its low ionization potential and experimental characterisation to assume p-type behaviour – calculation of defect formation energies in this system could verify this as well as, perhaps more importantly, reveal any potential trap states or recombination centres that could affect its capability as a photovoltaic absorber. In this thesis, we have theoretically characterised bulk $PbBi_2S_4$, although the behaviour of the surface of a material can be at least as important in a device such as a solar cell. As such, future theoretical work could focus on lattice matching with partner layers or the calculation of surface defects such as dislocations and grain boundaries.

Bibliography

[1] Peter, L. M. *Philos. Trans. R. Soc. London, Ser. A* **2011**, *369*, 1840–1856.

[2] Lewis, N. S.; Nocera, D. G. *Proc. Natl. Acad. Sci. U.S.A.* **2006**, *103*, 15729–15735.

[3] Field, C. B. et al. In *Climate Change 2014: Impacts, Adaptation, and Vulnerability. Part A: Global and Sectoral Aspects. Contribution of Working Group II to the Fifth Assessment Report of the Intergovernmental Panel on Climate Change*; Field, C. B. et al. , Eds.; Cambridge University Press: Cambridge, United Kingdom and New York, NY, USA, 2014; pp 35–94.

[4] Haegel, N. M. et al. *Science* **2017**, *356*, 141–143.

[5] Woodhouse, M.; Jones-Albertus, R.; Feldman, D.; Fu, R.; Horowitz, K.; Chung, D.; Jordan, D.; Kurtz, S. *On the Path to SunShot: The Role of Advancements in Solar Photovoltaic Efficiency, Reliability, and Costs*; 2016.

[6] Becquerel, E. *C. R. Acad. Sci.* **1839**, *9*, 145–149.

[7] Adams, W. G.; Day, R. E. *Phil. Trans. Roy. Soc. London* **1877**, *167*, 313–349.

[8] Nelson, J. *The Physics of Solar Cells*; Imperial College Press, 2003.

[9] Shockley, W.; Queisser, H. J. *J. Appl. Phys.* **1961**, *32*, 510–519.

[10] Congreve, D. N.; Lee, J.; Thompson, N. J.; Hontz, E.; Yost, S. R.; Reusswig, P. D.; Bahlke, M. E.; Reineke, S.; Voorhis, T. V.; Baldo, M. A. *Science* **2013**, *340*, 334–337.

[11] Miyata, K.; Kurashige, Y.; Watanabe, K.; Sugimoto, T.; Takahashi, S.; Tanaka, S.; Takeya, J.; Yanai, T.; Matsumoto, Y. *Nat. Chem.* **2017**, *9*, 983–989.

[12] De Wolf, S.; Holovsky, J.; Moon, S.-J.; Löper, P.; Niesen, B.; Ledinsky, M.; Haug, F.-J.; Yum, J.-H.; Ballif, C. *J. Phys. Chem. Lett.* **2014**, *5*, 1035–1039.

[13] Ganose, A. M.; Savory, C. N.; Scanlon, D. O. *Chem. Commun.* **2017**, *53*, 20–44.

[14] Zakutayev, A.; Caskey, C. M.; Fioretti, A. N.; Ginley, D. S.; Vidal, J.; Stevanovic, V.; Tea, E.; Lany, S. *J. Phys. Chem. Lett.* **2014**, *5*, 1117–1125.

[15] Brandt, R. E.; Stevanović, V.; Ginley, D. S.; Buonassisi, T. *MRS Commun.* **2015**, *5*, 265–275.

[16] Walsh, A.; Zunger, A. *Nature Materials* **2017**, *16*, 964–967.

[17] Zhang, S. B.; Wei, S.-H.; Zunger, A.; Katayama-Yoshida, H. *Phys. Rev. B: Condens. Matter* **1998**, *57*, 9642–9656.

[18] Maughan, A. E.; Ganose, A. M.; Bordelon, M. M.; Miller, E. M.; Scanlon, D. O.; Neilson, J. R. *J. Am. Chem. Soc.* **2016**, *138*, 8453–8464.

[19] Walsh, A.; Scanlon, D. O.; Chen, S.; Gong, X. G.; Wei, S.-H. *Angew. Chem. Int. Ed.* **2015**, *54*, 1791–1794.

[20] Brandt, R. E.; Poindexter, J. R.; Gorai, P.; Kurchin, R. C.; Hoye, R. L. Z.; Nienhaus, L.; Wilson, M. W. B.; Polizzotti, J. A.; Sereika, R.; Žaltauskas, R.; Lee, L. C.; MacManus-Driscoll, J. L.; Bawendi, M.; Stevanović, V.; Buonassisi, T. *Chem. Mater.* **2017**, *29*, 4667–4674.

[21] Whittles, T. J.; Veal, T. D.; Savory, C. N.; Welch, A. W.; de Souza Lucas, F. W.; Gibbon, J. T.; Birkett, M.; Potter, R. J.; Scanlon, D. O.; Zakutayev, A.; Dhanak, V. R. *ACS Appl. Mater. Interfaces* **2017**, *9*, 41916–41926.

[22] Du, M.-H.; Singh, D. J. *Phys. Rev. B: Condens. Matter* **2010**, *81*, 144114.

[23] Siemons, W.; McGuire, M. A.; Cooper, V. R.; Biegalski, M. D.; Ivanov, I. N.; Jellison, G. E.; Boatner, L. A.; Sales, B. C.; Christen, H. M. *Adv. Mater.* **2012**, *24*, 3965–3969.

[24] Brivio, F.; Walker, A. B.; Walsh, A. *APL Mater.* **2013**, *1*, 042111.

[25] Steirer, K. X.; Schulz, P.; Teeter, G.; Stevanovic, V.; Yang, M.; Zhu, K.; Berry, J. J. *ACS Energy Lett.* **2016**, *1*, 360–366.

[26] Even, J.; Pedesseau, L.; Jancu, J. M.; Katan, C. *J. Phys. Chem. Lett.* **2013**, *4*, 042111.

[27] Zheng, F.; Tan, L. Z.; Liu, S.; Rappe, A. M. *Nano Lett.* **2015**, *15*, 7794–7800.

[28] Azarhoosh, P.; Frost, J. M.; McKechnie, S.; Walsh, A.; van Schilfgaarde, M. *APL Mater.* **2016**, *4*, 091501.

[29] Mosconi, E.; Etienne, T.; Angelis, F. D. *J. Phys. Chem. Lett.* **2017**, *8*, 2247–2252.

[30] Wenham, S. R.; Green, M. A. *Prog. Photovoltaics Res. Appl.* **1996**, *4*, 3–33.

[31] Yoshikawa, K.; Kawasaki, H.; Yoshida, W.; Irie, T.; Konishi, K.; Nakano, K.; Uto, T.; Adachi, D.; Kanematsu, M.; Uzu, H.; Yamamoto, K. *Nat. Energy* **2017**, *2*, 17032.

[32] Green, M. A.; Hishikawa, Y.; Dunlop, E. D.; Levi, D. H.; Hohl-Ebinger, J.; Ho-Baillie, A. W. *Prog. Photovoltaics Res. Appl.* **2017**, *26*, 3–12.

[33] Nathan, M. I.; Dumke, W. P.; Wrenner, K.; Tiwari, S.; Wright, S. L.; Jenkins, K. A. *Appl. Phys. Lett.* **1988**, *52*, 654–656.

[34] Woodall, J.; Hovel, H. *Appl. Phys. Lett.* **1972**, *21*, 379–381.

[35] Jäger-Waldau, A. *Sol. Energy Mater. Sol. Cells* **2012**, *95*, 373–395.

[36] Kumar, S. G.; Rao, K. S. R. K. *Energy Environ Sci.* **2014**, *7*, 45–102.

[37] Peng, J.; Lu, L.; Yang, H. *Renewable Sustainable Energy Rev.* **2013**, *19*, 255 – 274.

[38] Li, M. et al. *Nat. Photonics* **2016**, *11*, 85–90.

[39] Bush, K. A. et al. *Nat. Energy* **2017**, *2*, 17009.

[40] Li, G.; Zhu, R.; Yang, Y. *Nat. Photonics* **2012**, *6*, 153–161.

[41] Yu, G.; Gao, J.; Hummelen, J. C.; Wudl, F.; Heeger, A. J. *Science* **1995**, *270*, 1789–1791.

[42] Shaheen, S. E.; Brabec, C. J.; Sariciftci, N. S.; Padinger, F.; Fromherz, T.; Hummelen, J. C. *Appl. Phys. Lett.* **2001**, *78*, 841–843.

[43] Janssen, R. A. J.; Nelson, J. *Adv. Mater.* **2012**, *25*, 1847–1858.

[44] Cheng, P.; Li, G.; Zhan, X.; Yang, Y. *Nat. Photonics* **2018**, *12*, 131–142.

[45] Grätzel, M. *Nature* **2001**, *414*, 338–344.

[46] Graetzel, M.; Janssen, R. A. J.; Mitzi, D. B.; Sargent, E. H. *Nature* **2012**, *488*, 304–312.

[47] O'Regan, B.; Grätzel, M. *Nature* **1991**, *353*, 737–740.

[48] Lan, X.; Voznyy, O.; García de Arquer, F. P.; Liu, M.; Xu, J.; Proppe, A. H.; Walters, G.; Fan, F.; Tan, H.; Liu, M.; Yang, Z.; Hoogland, S.; Sargent, E. H. *Nano Lett.* **2016**, *16*, 4630–4634.

[49] Sanehira, E. M.; Marshall, A. R.; Christians, J. A.; Harvey, S. P.; Ciesielski, P. N.; Wheeler, L. M.; Schulz, P.; Lin, L. Y.; Beard, M. C.; Luther, J. M. *Sci. Adv.* **2017**, *3*, eaao4204.

[50] Yang, W. S.; Park, B.-W.; Jung, E. H.; Jeon, N. J.; Kim, Y. C.; Lee, D. U.; Shin, S. S.; Seo, J.; Kim, E. K.; Noh, J. H.; Seok, S. I. *Science* **2017**, *356*, 1376–1379.

[51] Weber, D. *Z. Naturforsch.* **1978**, *33b*, 1443–1445.

[52] Wells, H. L. *Z. Anorg. Chem.* **1893**, *3*, 195–210.

[53] Møller, C. K. *Nature* **1958**, *182*, 1436–1436.

[54] Poglitsch, A.; Weber, D. *J. Chem. Phys.* **1987**, *87*, 6373–6378.

[55] Onoda-Yamamuro, N.; Matsuo, T.; Suga, H. *J. Phys. Chem. Solids* **1990**, *51*, 1383–1395.

[56] Wasylishen, R.; Knop, O.; Macdonald, J. *Solid State Commun.* **1985**, *56*, 581–582.

[57] Kojima, A.; Teshima, K.; Shirai, Y.; Miyasaka, T. *J. Am. Chem. Soc.* **2009**, *131*, 6050–6051.

[58] Im, J.-H.; Lee, C.-R.; Lee, J.-W.; Park, S.-W.; Park, N.-G. *Nanoscale* **2011**, *3*, 4088–4093.

[59] Kim, H.-S.; Lee, C.-R.; Im, J.-H.; Lee, K.-B.; Moehl, T.; Marchioro, A.; Moon, S.-J.; Humphry-Baker, R.; Yum, J.-H.; Moser, J. E.; Grätzel, M.; Park, N.-G. *Sci. Rep.* **2012**, *2*, 591.

[60] Lee, M. M.; Teuscher, J.; Miyasaka, T.; Murakami, T. N.; Snaith, H. J. *Science* **2012**, *338*, 643–647.

[61] Chung, I.; Lee, B.; He, J.; Chang, R. P.; Kanatzidis, M. G. *Nature* **2012**, *485*, 486–489.

[62] Etgar, L.; Gao, P.; Xue, Z.; Peng, Q.; Chandiran, A. K.; Liu, B.; Nazeeruddin, M. K.; Grätzel, M. *J. Am. Chem. Soc.* **2012**, *134*, 17396–17399.

[63] Ball, J. M.; Lee, M. M.; Hey, A.; Snaith, H. J. *Energy Environ. Sci.* **2013**, *6*, 1739–1743.

[64] Liu, M.; Johnston, M. B.; Snaith, H. J. *Nature* **2013**, *501*, 395–398.

[65] Heo, J. H.; Im, S. H.; Noh, J. H.; Mandal, T. N.; Lim, C.-S.; Chang, J. A.; Lee, Y. H.; Kim, H.-j.; Sarkar, A.; K., N.; Gratzel, M.; Seok, S. I. *Nat. Photonics* **2013**, *7*, 486–491.

[66] Burschka, J.; Pellet, N.; Moon, S.-J.; Humphry-Baker, R.; Gao, P.; Nazeeruddin, M. K.; Gratzel, M. *Nature* **2013**, *499*, 316–319.

[67] Tidhar, Y.; Edri, E.; Weissman, H.; Zohar, D.; Hodes, G.; Cahen, D.; Rybtchinski, B.; Kirmayer, S. *J. Am. Chem. Soc.* **2014**, *136*, 13249–13256.

[68] Yantara, N.; Fang, Y.; Chen, S.; Dewi, H. A.; Boix, P. P.; Mhaisalkar, S. G.; Mathews, N. *Chem. Mater.* **2015**, *27*, 2309–2314.

[69] Tripathi, N.; Yanagida, M.; Shirai, Y.; Masuda, T.; Han, L.; Miyano, K. *J. Mater. Chem.A* **2015**, *3*, 12081–12088.

[70] Noh, J. H.; Im, S. H.; Heo, J. H.; Mandal, T. N.; Seok, S. I. *Nano Lett.* **2013**, *13*, 1764–1769.

[71] Jeon, N. J.; Noh, J. H.; Kim, Y. C.; Yang, W. S.; Ryu, S.; Seok, S. I. *Nat. Mater.* **2014**, *13*, 897–903.

[72] Pellet, N.; Gao, P.; Gregori, G.; Yang, T.-Y.; Nazeeruddin, M. K.; Maier, J.; Grätzel, M. *Angew. Chem. Int. Ed.* **2014**, *53*, 3151–3157.

[73] Eperon, G. E.; Stranks, S. D.; Menelaou, C.; Johnston, M. B.; Herz, L. M.; Snaith, H. J. *Energy Environ. Sci.* **2014**, *7*, 982–988.

[74] Kieslich, G.; Sun, S.; Cheetham, T. *Chem. Sci.* **2015**, *6*, 3430–3433.

[75] Travis, W.; Glover, E.; Bronstein, H.; Scanlon, D.; Palgrave, R. *Chem. Sci.* **2016**, *7*, 4548–4556.

[76] Stoumpos, C. C.; Malliakas, C. D.; Kanatzidis, M. G. *Inorg. Chem.* **2013**, *52*, 9019–9038.

[77] Lee, J.-W.; Seol, D.-J.; Cho, A.-N.; Park, N.-G. *Adv. Mater.* **2014**, *26*, 4991–4998.

[78] Jeon, N. J.; Noh, J. H.; Yang, W. S.; Kim, Y. C.; Ryu, S.; Seo, J.; Seok, S. I. *Nature* **2015**, *517*, 476–480.

[79] Yang, W. S.; Noh, J. H.; Jeon, N. J.; Kim, Y. C.; Ryu, S.; Seo, J.; Seok, S. I. *Science* **2015**, *348*, 1234–1237.

[80] Li, Z.; Yang, M.; Park, J.-S.; Wei, S.-H.; Berry, J. J.; Zhu, K. *Chem. Mater.* **2015**, *28*, 284–292.

[81] Lee, J.-W.; Kim, D.-H.; Kim, H.-S.; Seo, S.-W.; Cho, S. M.; Park, N.-G. *Adv. Energy Mater.* **2015**, *5*, 1501310.

[82] Yi, C.; Luo, J.; Meloni, S.; Boziki, A.; Ashari-Astani, N.; Grätzel, C.; Zakeeruddin, S. M.; Röthlisberger, U.; Grätzel, M. *Energy Environ. Sci.* **2016**, *9*, 656–662.

[83] Saliba, M.; Matsui, T.; Seo, J.-Y.; Domanski, K.; Correa-Baena, J.-P.; Nazeeruddin, M. K.; Zakeeruddin, S. M.; Tress, W.; Abate, A.; Hagfeldt, A.; Grätzel, M. *Energy Environ. Sci.* **2016**, *9*, 1989–1997.

[84] McMeekin, D. P.; Sadoughi, G.; Rehman, W.; Eperon, G. E.; Saliba, M.; Hörantner, M. T.; Haghighirad, A.; Sakai, N.; Korte, L.; Rech, B.; Johnston, M. B.; Herz, L. M.; Snaith, H. J. *Science* **2016**, *351*, 151–155.

[85] Eperon, G. E. et al. *Science* **2016**, *354*, 861–865.

[86] Kojima, A.; Teshima, K.; Shirai, Y.; Miyasaka, T. *J. Am. Chem. Soc.* **2009**, *131*, 6050–6051.

[87] Mosconi, E.; Amat, A.; Nazeeruddin, M. K.; Grätzel, M.; Angelis, F. D. *J. Phys. Chem. C* **2013**, *117*, 13902–13913.

[88] Brivio, F.; Butler, K. T.; Walsh, A.; Van Schilfgaarde, M. *Phys. Rev. B: Condens. Matter* **2014**, *89*, 155204.

[89] Walsh, A.; Payne, D. J.; Egdell, R. G.; Watson, G. W. *Chem. Soc. Rev.* **2011**, *40*, 4455–4463.

[90] Even, J.; Pedesseau, L.; Katan, C.; Kepenekian, M.; Lauret, J.-S.; Sapori, D.; Deleporte, E. *J. Phys. Chem. C* **2015**, *119*, 10161–10177.

[91] Amat, A.; Mosconi, E.; Ronca, E.; Quarti, C.; Umari, P.; Nazeeruddin, M. K.; Grätzel, M.; De Angelis, F. *Nano Lett.* **2014**, *14*, 3608–3616.

[92] Hutter, E. M.; Gélvez-Rueda, M. C.; Osherov, A.; Bulović, V.; Grozema, F. C.; Stranks, S. D.; Savenije, T. J. *Nat. Mater.* **2017**, *16*, 115–120.

[93] Herz, L. M. *Annu. Rev. Phys. Chem.* **2016**, *67*, 65–89.

[94] Yamada, Y.; Nakamura, T.; Endo, M.; Wakamiya, A.; Kanemitsu, Y. *J. Am. Chem. Soc.* **2014**, *136*, 11610–11613.

[95] Wehrenfennig, C.; Eperon, G. E.; Johnston, M. B.; Snaith, H. J.; Herz, L. M. *Adv. Mater.* **2014**, *26*, 1584–1589.

[96] Stranks, S. D.; Eperon, G. E.; Grancini, G.; Menelaou, C.; Alcocer, M. J. P.; Leijtens, T.; Herz, L. M.; Petrozza, A.; Snaith, H. J. *Science* **2013**, *342*, 341–344.

[97] Xing, G.; Mathews, N.; Sun, S.; Lim, S. S.; Lam, Y. M.; Grätzel, M.; Mhaisalkar, S.; Sum, T. C. *Science* **2013**, *342*, 344–347.

[98] Wang, Q.; Shao, Y.; Xie, H.; Lyu, L.; Liu, X.; Gao, Y.; Huang, J. *Appl. Phys. Lett.* **2014**, *105*, 163508.

[99] Wehrenfennig, C.; Liu, M.; Snaith, H. J.; Johnston, M. B.; Herz, L. M. *Energy Environ. Sci.* **2014**, *7*, 2269–2275.

[100] Frost, J. M.; Butler, K. T.; Brivio, F.; Hendon, C. H.; van Schilfgaarde, M.; Walsh, A. *Nano Lett.* **2014**, *14*, 2584–90.

[101] Yin, W.-J.; Shi, T.; Yan, Y. *Appl. Phys. Lett.* **2014**, *104*, 063903.

[102] Shi, H.; Du, M.-H. *Phys. Rev. B: Condens. Matter* **2014**, *90*.

[103] Buin, A.; Pietsch, P.; Xu, J.; Voznyy, O.; Ip, A. H.; Comin, R.; Sargent, E. H. *Nano Lett.* **2014**, *14*, 6281–6286.

[104] Meggiolaro, D.; Motti, S. G.; Mosconi, E.; Barker, A. J.; Ball, J.; Perini, C. A. R.; Deschler, F.; Petrozza, A.; Angelis, F. D. *Energy Environ. Sci.* **2018**, *11*, 702–713.

[105] Baena, J. P. C.; Steier, L.; Tress, W.; Saliba, M.; Neutzner, S.; Matsui, T.; Giordano, F.; Jacobsson, T. J.; Kandada, A. R. S.; Zakeeruddin, S. M.; Petrozza, A.; Abate, A.; Nazeeruddin, M. K.; Grätzel, M.; Hagfeldt, A. *Energy Environ. Sci.* **2015**, *8*, 2928–2934.

[106] Jeon, N. J.; Lee, H. G.; Kim, Y. C.; Seo, J.; Noh, J. H.; Lee, J.; Seok, S. I. *J. Am. Chem. Soc.* **2014**, *136*, 7837–7840.

[107] Mei, A.; Li, X.; Liu, L.; Ku, Z.; Liu, T.; Rong, Y.; Xu, M.; Hu, M.; Chen, J.; Yang, Y.; Gratzel, M.; Han, H. *Science* **2014**, *345*, 295–298.

[108] Li, H.; Fu, K.; Hagfeldt, A.; Grätzel, M.; Mhaisalkar, S. G.; Grimsdale, A. C. *Angew. Chem. Int. Ed.* **2014**, *53*, 4085–4088.

[109] Liu, J.; Wu, Y.; Qin, C.; Yang, X.; Yasuda, T.; Islam, A.; Zhang, K.; Peng, W.; Chen, W.; Han, L. *Energy Environ. Sci.* **2014**, *7*, 2963–2967.

[110] Maciejczyk, M.; Ivaturi, A.; Robertson, N. *J. Mater. Chem. A* **2016**, *4*, 4855–4863.

[111] Saliba, M. et al. *Nat. Energy* **2016**, *1*, 15017.

[112] Grätzel, M. *Nat. Mater.* **2014**, *13*, 838–842.

[113] Babayigit, A.; Ethirajan, A.; Muller, M.; Conings, B. *Nat. Mater.* **2016**, *15*, 247–251.

[114] Snaith, H. J.; Abate, A.; Ball, J. M.; Eperon, G. E.; Leijtens, T.; Noel, N. K.; Stranks, S. D.; Wang, J. T.-W.; Wojciechowski, K.; Zhang, W. *J. Phys. Chem. Lett.* **2014**, *5*, 1511–1515.

[115] Kim, H.-S.; Park, N.-G. *J. Phys. Chem. Lett.* **2014**, *5*, 2927–2934.

[116] Wei, J.; Zhao, Y.; Li, H.; Li, G.; Pan, J. *J. Phys. Chem. Lett.* **2014**, *5*, 3937–3945.

[117] Kutes, Y.; Ye, L.; Zhou, Y.; Pang, S.; Huey, B. D.; Padtures, N. P. *J. Phys. Chem. Lett.* **2014**, *5*, 3335–3339.

[118] Beilsten-Edmands, J.; Eperon, G. E.; Johnson, R. D.; Snaith, H. J.; Radaelli, P. G. *Appl. Phys. Lett.* **2015**, *106*, 173502.

[119] Tress, W.; Marinova, N.; Moehl, T.; Zakeeruddin, S. M.; Nazeeruddin, M. K.; Grätzel, M. *Energy Environ Sci.* **2015**, *8*, 995–1004.

[120] Frost, J. M.; Walsh, A. *Acc. Chem. Res.* **2016**, *49*, 528–535.

[121] Azpiroz, J. M.; Mosconi, E.; Bisquert, J.; De Angelis, F. *Energy Environ. Sci.* **2015**, *8*, 2118–2127.

[122] Eames, C.; Frost, J. M.; Barnes, P. R. F.; O'Regan, B. C.; Walsh, A.; Islam, M. S. *Nat. Commun.* **2015**, *6*, 7497.

[123] van Reenen, S.; Kemerink, M.; Snaith, H. J. *J. Phys. Chem. Lett.* **2015**, *6*, 3808–3814.

[124] Bass, K. K.; McAnally, R. E.; Zhou, S.; Djurovich, P. I.; Thompson, M. E.; Melot, B. C. *Chem. Commun.* **2014**, *50*, 15819–15822.

[125] Christians, J. A.; Herrera, P. A. M.; Kamat, P. V. *J. Am. Chem. Soc.* **2015**, *137*, 1530–1538.

[126] Aristidou, N.; Sanchez-Molina, I.; Chotchuangchutchaval, T.; Brown, M.; Martinez, L.; Rath, T.; Haque, S. A. *Angew. Chem. Int. Ed.* **2015**, *54*, 8208–8212.

[127] Bryant, D.; Aristidou, N.; Pont, S.; Sanchez-Molina, I.; Chotchunangatchaval, T.; Wheeler, S.; Durrant, J. R.; Haque, S. A. *Energy Environ. Sci.* **2016**, *9*, 1655–1660.

[128] Conings, B.; Drijkoningen, J.; Gauquelin, N.; Babayigit, A.; D'Haen, J.; D'Olieslaeger, L.; Ethirajan, A.; Verbeeck, J.; Manca, J.; Mosconi, E.; Angelis, F. D.; Boyen, H.-G. *Adv. Energy Mater.* **2015**, *5*, 1500477.

[129] Leijtens, T.; Eperon, G. E.; Pathak, S.; Abate, A.; Lee, M. M.; Snaith, H. J. *Nat. Commun.* **2013**, *4*, 2885.

[130] Li, W.; Zhang, W.; Reenen, S. V.; Sutton, R. J.; Fan, J.; Haghighirad, A. A.; Johnston, M. B.; Wang, L.; Snaith, H. J. *Energy Environ. Sci.* **2016**, *9*, 490–498.

[131] Zhang, Y.-Y.; Chen, S.; Xu, P.; Xiang, H.; Gong, X.-G.; Walsh, A.; Wei, S.-H. *arXiv:1506.01301 [cond-mat.mtrl-sci]* **2015**,

[132] Nagabhushana, G.; Shivaramaiah, R.; Navrotsky, A. *Proc. Natl. Acad. Sci. U.S.A.* **2016**, *113*, 7717–7721.

[133] Ganose, A. M.; Savory, C. N.; Scanlon, D. O. *J. Phys. Chem. Lett.* **2015**, *6*, 4594–4598.

[134] Saliba, M.; Matsui, T.; Domanski, K.; Seo, J.-Y.; Ummadisingu, A.; Zakeeruddin, S. M.; Correa-Baena, J.-P.; Tress, W. R.; Abate, A.; Hagfeldt, A.; Gratzel, M. *Science* **2016**, *354*, 206–209.

[135] Shin, S. S.; Yeom, E. J.; Yang, W. S.; Hur, S.; Kim, M. G.; Im, J.; Seo, J.; Noh, J. H.; Seok, S. I. *Science* **2017**, *356*, 167–171.

[136] Christians, J. A.; Fung, R. C. M.; Kamat, P. V. *J. Am. Chem. Soc.* **2013**, *136*, 758–764.

[137] Bush, K. A.; Bailie, C. D.; Chen, Y.; Bowring, A. R.; Wang, W.; Ma, W.; Leijtens, T.; Moghadam, F.; McGehee, M. D. *Adv. Mater.* **2016**, *28*, 3937–3943.

[138] Vellini, M.; Gambini, M.; Prattella, V. *Energy* **2017**, *138*, 1099–1111.

[139] Needleman, H. *Annu. Rev. Med.* **2004**, *55*, 209–222.

[140] Toscano, C. D.; Guilarte, T. R. *Brain Res. Rev.* **2005**, *49*, 529–554.

[141] Benmessaoud, I. R.; Mahul-Mellier, A.-L.; Horváth, E.; Maco, B.; Spina, M.; Lashuel, H. A.; Forró, L. *Toxicol. Res.* **2016**, *5*, 407–419.

[142] Hailegnaw, B.; Kirmayer, S.; Edri, E.; Hodes, G.; Cahen, D. *J. Phys. Chem. Lett.* **2015**, *6*, 1543–1547.

[143] Babayigit, A.; Thanh, D. D.; Ethirajan, A.; Manca, J.; Muller, M.; Boyen, H.-G.; Conings, B. *Sci. Rep.* **2016**, *6*, 18721.

[144] Noel, N. K.; Stranks, S. D.; Abate, A.; Wehrenfennig, C.; Guarnera, S.; Haghighirad, A.; Sadhanala, A.; Eperon, G. E.; Pathak, S. K.; Johnston, M. B.; Petrozza, A.; Herz, L.; Snaith, H. *Energy Environ. Sci.* **2014**, *7*, 3061–3068.

[145] Zhu, Z.; Chueh, C.-C.; Li, N.; Mao, C.; Jen, A. K.-Y. *Adv. Mater.* **2017**, *30*, 1703800.

[146] Serrano-Lujan, L.; Espinosa, N.; Larsen-Olsen, T. T.; Abad, J.; Urbina, A.; Krebs, F. C. *Adv. Energy Mater.* **2015**, *5*, 1501119.

[147] Hartree, D. R. *Math. Proc. Cambridge Philos. Soc.* **1928**, *24*, 89–110.

[148] Hartree, D. R. *Math. Proc. Cambridge Philos. Soc.* **1928**, *24*, 426–437.

[149] Slater, J. C. *Phys. Rev.* **1929**, *34*, 1293–1322.

[150] Fock, V. *Z. Phys.* **1930**, *62*, 795–805.

[151] Hartree, D. R. *Rep. Prog. Phys.* **1947**, *11*, 113–143.

[152] Thomas, L. H. *Math. Proc. Cambridge Philos. Soc.* **1927**, *23*, 542.

[153] Hohenberg, P. Kohn, W. *Phys. Rev.* **1964**, *136*, 864–871.

[154] Kohn, W.; Sham, L. J. *Phys. Rev.* **1965**, *385*, A1133.

[155] Vosko, S. H.; Wilk, L.; Nusair, M. *Can. J. Phys.* **1980**, *58*, 1200–1211.

[156] Perdew, J. P.; Levy, M. *Phys. Rev. Lett.* **1983**, *51*, 1884–1887.

[157] Perdew, J. P.; Jackson, K. A.; Pederson, M. R.; Singh, D. J.; Fiolhais, C. *Phys. Rev. B: Condens. Matter* **1992**, *46*, 6671–6687.

[158] Ortiz, G. *Phys. Rev. B: Condens. Matter* **1992**, *45*, 11328–11331.

[159] Perdew, J.; Burke, K.; Ernzerhof, M. *Phys. Rev. Lett.* **1996**, *77*, 3865–3868.

[160] Csonka, G. I.; Perdew, J. P.; Ruzsinszky, A.; Philipsen, P. H. T.; Lebègue, S.; Paier, J.; Vydrov, O. A.; Ángyán, J. G. *Phys. Rev. B: Condens. Matter* **2009**, *79*, 155107.

[161] Perdew, J. P.; Ruzsinszky, A.; Csonka, G. I.; Vydrov, O. a.; Scuseria, G. E.; Constantin, L. A.; Zhou, X.; Burke, K. *Phys. Rev. Lett.* **2008**, *100*, 136406.

[162] Dudarev, S. L.; Botton, G. A.; Savrasov, S. Y.; Humphreys, C. J.; Sutton, A. P. *Phys. Rev. B: Condens. Matter* **1998**, *57*, 1505–1509.

[163] Adamo, C.; Barone, V. *J. Chem. Phys.* **1999**, *110*, 6158.

[164] Perdew, J. P.; Ernzerhof, M.; Burke, K. *J. Chem. Phys.* **1996**, *105*, 9982–9985.

[165] Heyd, J.; Scuseria, G. E.; Ernzerhof, M. *J. Chem. Phys.* **2003**, *118*, 8207–8215.

[166] Krukau, A. V.; Vydrov, O. A.; Izmaylov, A. F.; Scuseria, G. E. *J. Chem. Phys.* **2006**, *125*, 224106.

[167] He, J.; Franchini, C. *J. Phys. Condens. Matter* **2017**, *29*, 454004.

[168] Kresse, G.; Hafner, J. *Phys. Rev. B: Condens. Matter* **1993**, *47*, 558–561.

[169] Kresse, G.; Hafner, J. *Phys. Rev. B: Condens. Matter* **1994**, *49*, 14251–14269.

[170] Kresse, G.; Furthmüller, J. *Phys. Rev. B: Condens. Matter* **1996**, *54*, 11169–11186.

[171] Kresse, G.; Furthmüller, J. *Comput. Mater. Sci.* **1996**, *6*, 15–50.

[172] Momma, K.; Izumi, F. *J. Appl. Crystallogr.* **2011**, *44*, 1272–1276.

[173] Ziman, J. *Principles of the Theory of Solids*; Cambridge University Press, 1972.

[174] Bloch, F. *Z. Phys.* **1929**, *52*, 555–600.

[175] Kresse, G. *Physical Review B* **1999**, *59*, 1758–1775.

[176] Blochl, P. *Phys. Rev. B: Condens. Matter* **1994**, *50*, 17953–17979.

[177] Pulay, P. *Chem. Phys. Lett.* **1980**, *73*, 393–398.

[178] Pulay, P. *Mol. Phys.* **1969**, *17*, 197–204.

[179] Bradley, C. J.; Cracknell, A. P. *Mathematical Theory of Symmetry in Solids*; Oxford University Press, 1972.

[180] Wei, S.-H.; Zunger, A. *Appl. Phys. Lett.* **1998**, *72*, 2011–2013.

[181] Walsh, A.; Butler, K. T. *Acc. Chem. Res.* **2014**, *47*, 364–372.

[182] Butler, K. T.; Hendon, C. H.; Walsh, A. *J. Am. Chem. Soc.* **2014**, *136*, 2703–2706.

[183] Sham, L. J.; Rice, T. M. *Phys. Rev.* **1966**, *144*, 708–714.

[184] Gajdoš, M.; Hummer, K.; Kresse, G.; Furthmüller, J.; Bechstedt, F. *Phys. Rev. B: Condens. Matter* **2006**, *73*, 045112.

[185] Birkett, M.; Savory, C. N.; Fioretti, A. N.; Thompson, P.; Muryn, C. A.; Weerakkody, A. D.; Mitrovic, I. Z.; Hall, S.; Treharne, R.; Dhanak, V. R.; Scanlon, D. O.; Zakutayev, A.; Veal, T. D. *Phys. Rev. B: Condens. Matter* **2017**, *95*, 115201.

[186] Yu, L.; Zunger, A. *Phys. Rev. Lett.* **2012**, *108*, 068701.

[187] Yu, L.; Kokenyesi, R. S.; Keszler, D. A.; Zunger, A. *Adv. Energy Mater.* **2013**, *3*, 43–48.

[188] Blank, B.; Kirchartz, T.; Lany, S.; Rau, U. *Phys. Rev. Appl* **2017**, *8*, 024032.

[189] Mott, N. F.; Littleton, M. J. *Trans. Faraday Soc.* **1938**, *34*, 485.

[190] Zhang, S.; Northrup, J. *Phys. Rev. Lett.* **1991**, *67*, 2339–2342.

[191] van de Walle, C. G.; Laks, D. B.; Neumark, G. F.; Pantelides, S. T. *Phys. Rev. B: Condens. Matter* **1993**, *47*, 9425–9434.

[192] Persson, C.; Zhao, Y.-J.; Lany, S.; Zunger, A. *Phys. Rev. B: Condens. Matter* **2005**, *72*, 035211.

[193] Freysoldt, C.; Grabowski, B.; Hickel, T.; Neugebauer, J.; Kresse, G.; Janotti, A.; Van de Walle, C. G. *Rev. Mod. Phys.* **2014**, *86*, 253–305.

[194] Buckeridge, J.; Scanlon, D. O.; Walsh, A.; Catlow, C. R. A. *Comput. Phys. Commun.* **2014**, *185*, 330–338.

[195] Lany, S.; Zunger, A. *Phys. Rev. B: Condens. Matter* **2008**, *78*, 235104.

[196] Komsa, H.-P.; Rantala, T. T.; Pasquarello, A. *Phys. Rev. B: Condens. Matter* **2012**, *86*.

[197] Makov, G.; Payne, M. C. *Phys. Rev. B: Condens. Matter* **1995**, *51*, 4014–4022.

[198] Lany, S.; Zunger, A. *Modell. Simul. Mater. Sci. Eng.* **2009**, *17*, 084002.

[199] Murphy, S. T.; Hine, N. D. M. *Phys. Rev. B: Condens. Matter* **2013**, *87*, 094111.

[200] Beal, R. E.; Slotcavage, D. J.; Leijtens, T.; Bowring, A. R.; Belisle, R. A.; Nguyen, W. H.; Burkhard, G. F.; Hoke, E. T.; McGehee, M. D. *J. Phys. Chem. Lett.* **2016**, *7*, 746–751.

[201] Chen, Y.; Li, B.; Huang, W.; Gao, D.; Liang, Z. *Chem. Commun.* **2015**, *51*, 11997–11999.

[202] Jiang, Q.; Rebollar, D.; Gong, J.; Piacentino, E. L.; Zheng, C.; Xu, T. *Angew. Chem. Int. Ed.* **2015**, *54*, 7617–7620.

[203] Halder, A.; Chulliyil, R.; Subbiah, A. S.; Khan, T.; Chattoraj, S.; Chowdhury, A.; Sarkar, S. K. *J. Phys. Chem. Lett.* **2015**, *6*, 3483–3489.

[204] Ke, W. et al. *Adv. Mater.* **2016**, *28*, 5214–5221.

[205] Chiang, Y.-H.; Li, M.-H.; Cheng, H.-M.; Shen, P.-S.; Chen, P. *ACS Appl. Mater. Interfaces* **2017**, *9*, 2403–2409.

[206] Ganose, A. M.; Savory, C. N.; Scanlon, D. O. *J. Mater. Chem. A* **2017**, *5*, 7845–7853.

[207] Smith, I. C.; Hoke, E. T.; Solis-Ibarra, D.; McGehee, M. D.; Karunadasa, H. I. *Angew. Chem. Int. Ed.* **2014**, *53*, 11232–11235.

[208] Cao, D. H.; Stoumpos, C. C.; Farha, O. K.; Hupp, J. T.; Kanatzidis, M. G. *J. Am. Chem. Soc.* **2015**, *137*, 7843–7850.

[209] Quan, L. N.; Yuan, M.; Comin, R.; Voznyy, O.; Beauregard, E. M.; Hoogland, S.; Buin, A.; Kirmani, A. R.; Zhao, K.; Amassian, A.; Kim, D. H.; Sargent, E. H. *J. Am. Chem. Soc.* **2016**, *138*, 2649–2655.

[210] Lin, Y.; Bai, Y.; Fang, Y.; Wang, Q.; Deng, Y.; Huang, J. *ACS Energy Lett.* **2017**, *2*, 1571–1572.

[211] Rodríguez-Romero, J.; Hames, B. C.; Mora-Seró, I.; Barea, E. M. *ACS Energy Lett.* **2017**, *2*, 1969–1970.

[212] Juarez-Perez, E. J.; Sanchez, R. S.; Badia, L.; Garcia-Belmonte, G.; Kang, Y. S.; Mora-Sero, I.; Bisquert, J. *J. Phys. Chem. Lett.* **2014**, *5*, 2390–2394.

[213] Deng, Y.; Xiao, Z.; Huang, J. *Adv. Energy Mater.* **2015**, *5*, 1500721.

[214] Saidaminov, M. I.; Mohammed, O. F.; Bakr, O. M. *ACS Energy Lett.* **2017**, *2*, 889–896.

[215] Grancini, G.; Roldán-Carmona, C.; Zimmermann, I.; Mosconi, E.; Lee, X.; Martineau, D.; Narbey, S.; Oswald, F.; Angelis, F. D.; Graetzel, M.; Nazeeruddin, M. K. *Nat. Commun.* **2017**, *8*, 15684.

[216] Slavney, A. H.; Hu, T.; Lindenberg, A. M.; Karunadasa, H. I. *J. Am. Chem. Soc.* **2016**, *138*, 2138–2141.

[217] McClure, E. T.; Ball, M. R.; Windl, W.; Woodward, P. M. *Chem. Mater.* **2016**, *28*, 1348–1354.

[218] Volonakis, G.; Filip, M. R.; Haghighirad, A. A.; Sakai, N.; Wenger, B.; Snaith, H. J.; Giustino, F. *J. Phys. Chem. Lett.* **2016**, *7*, 1254–1259.

[219] Filip, M. R.; Hillman, S.; Haghighirad, A. A.; Snaith, H. J.; Giustino, F. *J. Phys. Chem. Lett.* **2016**, *7*, 2579–2585.

[220] Wei, F.; Deng, Z.; Sun, S.; Xie, F.; Kieslich, G.; Evans, D. M.; Carpenter, M. A.; Bristowe, P. D.; Cheetham, A. K. *Mater. Horiz.* **2016**, *3*, 328–332.

[221] Morrs, L. R.; Robinson, W. R. *Acta. Crystallogr., Sect. B: Struct. Sci.* **1972**, *28*, 653–654.

[222] Prokert, F.; Aleksandrov, K. *Phys. Status Solidi B* **1984**, *124*, 503–513.

[223] Pelle, F.; Blanzat, B.; Chevalier, B. *Solid State Commun.* **1984**, *49*, 1089–1093.

[224] Smit, W.; Dirksen, G.; Stufkens, D. *J. Phys. Chem. Solids* **1990**, *52*, 189–196.

[225] Deng, Z.; Wei, F.; Sun, S.; Kieslich, G.; Cheetham, A. K.; Bristowe, P. D. *J. Mater. Chem. A* **2016**, *4*, 12025–12029.

[226] Xiao, Z.; Meng, W.; Wang, J.; Yan, Y. *ChemSusChem* **2016**, *9*, 2628–2633.

[227] Du, M.-H. *J. Phys. Chem. Lett.* **2015**, *6*, 1461–1466.

[228] Xiao, Z.; Meng, W.; Saparov, B.; Duan, H.-S.; Wang, C.; Feng, C.; Liao, W.-Q.; Ke, W.; Zhao, D.; Wang, J.; Mitzi, D. B.; Yan, Y. *J. Phys. Chem. Lett.* **2016**, *7*, 1213–1218.

[229] Hautier, G.; Fischer, C.; Ehrlacher, V.; Jain, A.; Ceder, G. *Inorganic Chemistry* **2011**, *50*, 656–663.

[230] Lufaso, M. W.; Woodward, P. M. *Acta. Crystallogr., Sect. B: Struct. Sci.* **2001**, *57*, 725–738.

[231] Xiao, Z.; Meng, W.; Wang, J.; Mitzi, D. B.; Yan, Y. *Mater. Horiz.* **2017**, *4*, 206–216.

[232] Weller, M. T.; Weber, O. J.; Henry, P. F.; Pumpo, M. D.; Hansen, T. C. *Chem. Commun.* **2015**, *51*, 4180–4183.

[233] Frost, J. M.; Butler, K. T.; Walsh, A. *APL Mater.* **2014**, *2*, 081506.

[234] Etienne, T.; Mosconi, E.; Angelis, F. D. *J. Phys. Chem. Lett.* **2016**, *7*, 1638–1645.

[235] Xiao, Z.; Du, K.-Z.; Meng, W.; Wang, J.; Mitzi, D. B.; Yan, Y. *J. Am. Chem. Soc.* **2017**, *139*, 6054–6057.

[236] Volonakis, G.; Haghighirad, A. A.; Snaith, H. J.; Giustino, F. *J. Phys. Chem. Lett.* **2017**, *8*, 3917–3924.

[237] Shannon, R. D. *Acta Crystallogr., Sect. A: Found Crystallogr.* **1976**, *32*, 751–767.

[238] Lufaso, M. W.; Woodward, P. M.; Goldberger, J. *J. Solid State Chem.* **2004**, *177*, 1651–1659.

[239] Karen, P.; Moodenbaugh, A.; Goldberger, J.; Santhosh, P.; Woodward, P. *J. Solid State Chem.* **2006**, *179*, 2120–2125.

[240] Feldberg, N.; Aldous, J. D.; Linhart, W. M.; Phillips, L. J.; Durose, K.; Stampe, P. A.; Kennedy, R. J.; Scanlon, D. O.; Vardar, G.; Field, R. L.; Jen, T. Y.; Goldman, R. S.; Veal, T. D.; Durbin, S. M. *Appl. Phys. Lett.* **2013**, *103*, 042109.

[241] Veal, T. D.; Feldberg, N.; Quackenbush, N. F.; Linhart, W. M.; Scanlon, D. O.; Piper, L. F. J.; Durbin, S. M. *Adv. Energy Mater.* **2015**, *5*, 1501462, 1501462.

[242] Scanlon, D. O.; Walsh, A. *Appl. Phys. Lett.* **2012**, *100*, 251911.

[243] Chen, S.; Walsh, A.; Yang, J.-H.; Gong, X. G.; Sun, L.; Yang, P.-X.; Chu, J.-H.; Wei, S.-H. *Phys. Rev. B: Condens. Matter* **2011**, *83*, 125201.

[244] Siebentritt, S. *Thin Solid Films* **2013**, *535*, 1–4.

[245] Bourdais, S.; Choné, C.; Delatouche, B.; Jacob, A.; Larramona, G.; Moisan, C.; Lafond, A.; Donatini, F.; Rey, G.; Siebentritt, S.; Walsh, A.; Dennler, G. *Adv. Energy Mater.* **2016**, 1502276.

[246] Zunger, A.; Wei, S.-H.; Ferreira, L. G.; Bernard, J. E. *Phys. Rev. Lett.* **1990**, *65*, 353–356.

[247] Wei, S.-H.; Ferreira, L. G.; Bernard, J. E.; Zunger, A. *Phys. Rev. B* **1990**, *42*, 9622–9649.

[248] Hass, K. C.; Davis, L. C.; Zunger, A. *Physical Review B* **1990**, *42*, 3757–3760.

[249] Shin, D.; Arróyave, R.; Liu, Z.-K.; de Walle, A. V. *Physical Review B* **2006**, *74*, 024204.

[250] Volonakis, G.; Haghighirad, A. A.; Milot, R. L.; Sio, W. H.; Filip, M. R.; Wenger, B.; Johnston, M. B.; Herz, L. M.; Snaith, H. J.; Giustino, F. *J. Phys. Chem. Lett.* **2017**, *8*, 772–778.

[251] Zhou, J.; Xia, Z.; Molokeev, M. S.; Zhang, X.; Peng, D.; Liu, Q. *J. Mater. Chem. A* **2017**, *5*, 15031–15037.

[252] Savory, C. N.; Walsh, A.; Scanlon, D. O. *ACS Energy Lett.* **2016**, *1*, 949–955.

[253] Tiwari, A. N.; Krejci, M.; Haug, F.-J.; Zogg, H. *Prog. Photovoltaics Res. Appl.* **1999**, *7*, 393–397.

[254] Romeo, A.; Khrypunov, G.; Kurdesau, F.; Arnold, M.; Bätzner, D.; Zogg, H.; Tiwari, A. *Sol. Energy Mater. Sol. Cells* **2006**, *90*, 3407–3415.

[255] Godt, J.; Scheidig, F.; Grosse-Siestrup, C.; Esche, V.; Brandenburg, P.; Reich, A.; Groneberg, D. A. *J. Occup. Med. Toxicol.* **2006**, *1*, 22.

[256] Fee, D. B. *Clinical Neurotoxicology*; Elsevier, 2009; pp 273–276.

[257] Major, J. D.; Treharne, R. E.; Phillips, L. J.; Durose, K. *Nature* **2014**, *511*, 334–337.

[258] Gaultois, M. W.; Sparks, T. D.; Borg, C. K. H.; Seshadri, R.; Bonificio, W. D.; Clarke, D. R. *Chem. Mater.* **2013**, *25*, 2911–2920.

[259] Zweibel, K. *Science* **2010**, *328*, 699–701.

[260] Jong, U.-G.; Yu, C.-J.; Ri, G.-C.; McMahon, A.; Harrison, N.; Barnes, P. R. F.; Walsh, A. *J. Mater. Chem. A* **2018**, *6*, 1067–1074.

[261] Kumar, M.; Persson, C. *J. Renewable Sustainable Energy* **2013**, *5*, 031616.

[262] Banu, S.; Ahn, S. J.; Ahn, S. K.; Yoon, K.; Cho, A. *Sol. Energy Mater. Sol. Cells* **2016**, *151*, 14 – 23.

[263] Yakushev, M.; Maiello, P.; Raadik, T.; Shaw, M.; Edwards, P.; Krustok, J.; Mudryi, A.; Forbes, I.; Martin, R. *Thin Solid Films* **2014**, *562*, 195–199.

[264] Sfaelou, S.; Raptis, D.; Dracopoulos, V.; Lianos, P. *RSC Adv.* **2015**, *5*, 95813–95816.

[265] Hahn, N. T.; Self, J. L.; Mullins, C. B. *J. Phys. Chem. Lett.* **2012**, *3*, 1571–1576.

[266] Ganose, A. M.; Butler, K. T.; Walsh, A.; Scanlon, D. O. *J. Mater. Chem. A* **2016**, *4*, 2060–2068.

[267] Ganose, A. M.; Cuff, M.; Butler, K. T.; Walsh, A.; Scanlon, D. O. *Chem. Mater,* **2016**, *28*, 1980–1984.

[268] Todorov, T. K.; Reuter, K. B.; Mitzi, D. B. *Adv. Mater.* **2010**, *22*, E156–E159.

[269] Chen, S.; Gong, X. G.; Walsh, A.; Wei, S. H. *Appl. Phys. Lett.* **2009**, *94*, 041903.

[270] Wang, W.; Winkler, M. T.; Gunawan, O.; Gokmen, T.; Todorov, T. K.; Zhu, Y.; Mitzi, D. B. *Adv. Energy Mater.* **2014**, *4*, 1301465.

[271] Kumar, M.; Dubey, A.; Adhikari, N.; Venkatesan, S.; Qiao, Q. *Energy Environ. Sci.* **2015**, *8*, 3134–3159.

[272] Wallace, S. K.; Mitzi, D. B.; Walsh, A. *ACS Energy Lett.* **2017**, *2*, 776–779.

[273] Lee, Y. S.; Gershon, T.; Gunawan, O.; Todorov, T. K.; Gokmen, T.; Virgus, Y.; Guha, S. *Adv. Energy Mater.* **2015**, *5*, 1401372.

[274] Yan, C.; Sun, K.; Huang, J.; Johnston, S.; Liu, F.; Veettil, B. P.; Sun, K.; Pu, A.; Zhou, F.; Stride, J. A.; Green, M. A.; Hao, X. *ACS Energy Lett.* **2017**, *2*, 930–936.

[275] Liu, Z.; Han, J.; Guo, K.; Zhang, X.; Hong, T. *Chem. Commun.* **2015**, *51*, 2597–2600.

[276] Lei, Y.; Yang, X.; Gu, L.; Jia, H.; Ge, S.; Xiao, P.; Fan, X.; Zheng, Z. *J. Power Sources* **2015**, *280*, 313–319.

[277] Kadrgulov, R. F.; Yakshibaev, R. A.; Khasanov, M. A. *Ionics* **2001**, *7*, 156–160.

[278] Baker, C. L.; Lincoln, F. J.; Johnson, A. W. S. *Acta Crystallogr., Sect. B: Struct. Sci* **1991**, *47*, 891–899.

[279] Trots, D. M.; Senyshyn, A.; Mikhailova, D. A.; Knapp, M.; Baehtz, C.; Hoelzel, M.; Fuess, H. *J. Phys. Condens. Matter* **2007**, *19*, 136204.

[280] Guin, S. N.; Pan, J.; Bhowmik, A.; Sanyal, D.; Waghmare, U. V.; Biswas, K. *J. Am. Chem. Soc.* **2014**, *136*, 12712–12720.

[281] Guin, S. N.; Sanyal, D.; Biswas, K. *Chem. Sci.* **2016**, *7*, 534–543.

[282] Fox, B. S.; Beyer, M. K.; Bondybey, V. E. *J. Am. Chem. Soc.* **2002**, *124*, 13613–13623.

[283] Bowmaker, G. A.; Kennedy, B. J.; Reid, J. C. *Inorg. Chem.* **1998**, *37*, 3968–3974.

[284] Orgel, L. E. *J. Chem. Soc. (Resumed)* **1958**, *0*, 4186–4190.

[285] Baker, C.; Lincoln, F.; Johnson, A. *Aust. J. Chem.* **1992**, *45*, 1441–1449.

[286] Trots, D. M.; Senyshyn, A.; Mikhailova, D. A.; Vad, T.; Fuess, H. *J. Phys. Condens. Matter* **2008**, *20*, 455204.

[287] Scanlon, D. O.; Walsh, A.; Morgan, B. J.; Watson, G. W.; Payne, D. J.; Egdell, R. G. *Phys. Rev. B: Condens. Matter* **2009**, *79*, 035101.

[288] Allen, J. P.; Scanlon, D. O.; Watson, G. W. *Phys. Rev. B: Condens. Matter* **2011**, *84*, 115141.

[289] Santamaria-Perez, D.; Morales-Garcia, A.; Martinez-Garcia, D.; Garcia-Domene, B.; Mühle, C.; Jansen, M. *Inorg. Chem.* **2013**, *52*, 355–361.

[290] Janesko, B. G.; Henderson, T. M.; Scuseria, G. E. *Phys. Chem. Chem. Phys.* **2009**, *11*, 443–454.

[291] Temple, D. J.; Kehoe, A. B.; Allen, J. P.; Watson, G. W.; Scanlon, D. O. *J. Phys. Chem. C* **2012**, *2*, 7334–7340.

[292] Tokuhara, Y.; Tezuka, K.; Shan, Y. J.; Imoto, H. *J. Ceram. Soc. Jpn.* **2009**, *117*, 359–362.

[293] Chowdari, B.; Mok, K.; Xie, J.; Gopalakrishnan, R. *J. Non-Cryst. Solids* **1993**, *160*, 73 – 81.

[294] Gebhardt, J.; McCarron, J.; Richardson, P.; Buckley, A. *Hydrometallurgy* **1986**, *17*, 27 – 38.

[295] Perry, D. L.; Taylor, J. A. *J. Mater. Sci. Lett.* **1986**, *5*, 384–386.

[296] Yeh, J.; Lindau, I. *At. Data Nucl. Data Tables* **1985**, *32*, 1 – 155.

[297] Jackson, A. J.; Ganose, A. M.; Regoutz, A.; Egdell, R. G.; Scanlon, D. O. *Journal of Open Source Software* **2018**, *3*, 773.

[298] Hautier, G.; Miglio, A.; Waroquiers, D.; Rignanese, G.-M.; Gonze, X. *Chem. Mater.* **2014**, *26*, 5547–5458.

[299] Persson, C. *J. Appl. Phys.* **2010**, *107*, 053710.

[300] Liu, H.-R.; Chen, S.; Zhai, Y.-T.; Xiang, H. J.; Gong, X. G.; Wei, S.-H. *J. Appl. Phys.* **2012**, *112*, 093717.

[301] Giorgi, G.; Fujisawa, J.-I.; Segawa, H.; Yamashita, K. *J. Phys. Chem. Lett.* **2013**, *4*, 4213–4216.

[302] Tanaka, T.; Nagatomo, T.; Kawasaki, D.; Nishio, M.; Guo, Q.; Wakahara, A.; Yoshida, A.; Ogawa, H. *J. Phys. Chem. Solids* **2005**, *66*, 1978 – 1981.

[303] Liu, F.; Li, Y.; Zhang, K.; Wang, B.; Yan, C.; Lai, Y.; Zhang, Z.; Li, J.; Liu, Y. *Sol. Energy Mater. Sol. Cells* **2010**, *94*, 2431 – 2434.

[304] Tai, K. F.; Gunawan, O.; Kuwahara, M.; Chen, S.; Mhaisalkar, S. G.; Huan, C. H. A.; Mitzi, D. B. *Adv. Energy Mater.* **2016**, *6*, 1501609.

[305] Burton, L. A.; Walsh, A. *Appl. Phys. Lett.* **2013**, *102*, 132111.

[306] Butler, K. T.; Frost, J. M.; Walsh, A. *Mater. Horiz.* **2015**, *2*, 228–231.

[307] Walsh, A.; Chen, S.; Wei, S.-H.; Gong, X.-G. *Adv. Energy Mater.* **2012**, *2*, 400–409.

[308] Swank, R. K. *Phys. Rev.* **1967**, *153*, 844–849.

[309] Teeter, G. *J. Appl. Phys.* **2007**, *102*, 034504.

[310] Davis, R. J.; Lloyd, M. T.; Ferreira, S. R.; Bruzek, M. J.; Watkins, S. E.; Lindell, L.; Sehati, P.; Fahlman, M.; Anthony, J. E.; Hsu, J. W. P. *J. Mater. Chem.* **2011**, *21*, 1721–1729.

[311] Scanlon, D. O.; Dunnill, C. W.; Buckeridge, J.; Shevlin, S. A.; Logsdail, A. J.; Woodley, S. M.; Catlow, C. R. A.; Powell, M. J.; Palgrave, R. G.; Parkin, I. P.; Watson, G. W.; Keal, T. W.; Sherwood, P.; Walsh, A.; Sokol, A. A. *Nat. Mater.* **2013**, *12*, 798–801.

[312] Buckeridge, J.; Butler, K. T.; Catlow, C. R. A.; Logsdail, A. J.; Scanlon, D. O.; Shevlin, S. A.; Woodley, S. M.; Sokol, A. A.; Walsh, A. *Chem. Mater.* **2015**, *27*, 3844–3851.

[313] Savory, C. N.; Palgrave, R. G.; Bronstein, H.; Scanlon, D. O. *Sci. Rep.* **2016**, *6*, 20626.

[314] Noda, Y.; Masumoto, K.; Ohba, S.; Saito, Y.; Toriumi, K.; Iwata, Y.; Shibuya, I. *Acta Crystallogr., Sect. C: Cryst. Struct. Commun* **1987**, *43*, 1443–1445.

[315] Strehlow, W. H.; Cook, E. L. *J. Phys. Chem. Ref. Data* **1973**, *2*, 163–200.

[316] Harman, T. C.; Taylor, P. J.; Walsh, M. P.; LaForge, B. E. *Science* **2002**, *297*, 2229–2232.

[317] Girard, S. N.; He, J.; Zhou, X.; Shoemaker, D.; Jaworski, C. M.; Uher, C.; Dravid, V. P.; Heremans, J. P.; Kanatzidis, M. G. *J. Am. Chem. Soc.* **2011**, *133*, 16588–16597.

[318] Pei, Y.; Shi, X.; LaLonde, A.; Wang, H.; Chen, L.; Snyder, G. J. *Nature* **2011**, *473*, 66–69.

[319] Biswas, K.; He, J.; Blum, I. D.; Wu, C.-I.; Hogan, T. P.; Seidman, D. N.; Dravid, V. P.; Kanatzidis, M. G. *Nature* **2012**, *489*, 414–418.

[320] McDonald, S. A.; Konstantatos, G.; Zhang, S.; Cyr, P. W.; Klem, E. J. D.; Levina, L.; Sargent, E. H. *Nat. Mater.* **2005**, *4*, 138–142.

[321] Hines, M.; Scholes, G. *Adv. Mater.* **2003**, *15*, 1844–1849.

[322] Stavrinadis, A.; Pradhan, S.; Papagiorgis, P.; Itskos, G.; Konstantatos, G. *ACS Energy Lett.* **2017**, *2*, 739–744.

[323] Bhattacharya, R. N.; Pramanik, P. *J. Electrochem. Soc.* **1982**, *129*, 332–335.

[324] Lundegaard, L.; Makovicky, E.; Boffa-Ballaran, T.; Balic-Zunic, T. *Phys. Chem. Miner.* **2005**, *32*, 578–584.

[325] Moreno-García, H.; Nair, M. T. S.; Nair, P. K. *Thin Solid Films* **2011**, *519*, 2287–2295.

[326] ten Haaf, S.; Sträter, H.; Brüggemann, R.; Bauer, G. H.; Felser, C.; Jakob, G. *Thin Solid Films* **2013**, *535*, 394–397.

[327] Esparza, D.; Zarazúa, I.; López-Luke, T.; Carriles, R.; Torres-Castro, A.; la Rosa, E. D. *Electrochim. Acta* **2015**, *180*, 486–492.

[328] Whittaker-Brooks, L.; Gao, J.; Hailey, A. K.; Thomas, C. R.; Yao, N.; Loo, Y.-L. *J. Mater. Chem. C* **2015**, *3*, 2686–2692.

[329] Rath, A. K.; Bernechea, M.; Martinez, L.; Konstantatos, G. *Adv. Mater.* **2011**, *23*, 3712–3717.

[330] Craig, J. R. *Miner. Deposita* **1967**, *1*, 278–306.

[331] Takéuchi, Y.; Takagi, J. *Proc. Jpn. Acad.* **1974**, *50*, 76–79.

[332] Takagi, J.; Takéuchi, Y. *Acta Crystallogr., Sect. B: Struct. Sci* **1972**, *28*, 649–651.

[333] Weitz, G.; Hellner, E. *Z. Kristallogr.* **1960**, *113*, 385–402.

[334] Iitaka, Y.; Nowacki, W. *Acta Crystallogr.* **1962**, *15*, 691–698.

[335] Takéuchi, Y.; Takagi, J.; Yamanaka, T. *Proc. Jpn. Acad.* **1974**, *50*, 317–321.

[336] Ohta, M.; Chung, D. Y.; Kunii, M.; Kanatzidis, M. G. *J. Mater. Chem. A* **2014**, *2*, 20048–20058.

[337] Malika, B.; Noureddine, B.; Mourad, M.; Abdelkader, O.; Attouya, B.; Hind, T.-D. *Results Phys.* **2013**, *3*, 30–37.

[338] Allgaier, R. S.; Scanlon, W. W. *Phys. Rev.* **1958**, *111*, 1029–1037.

[339] Grau-Crespo, R.; Hamad, S.; Catlow, C. R. A.; de Leeuw, N. H. *J. Phys. Condens. Matter* **2007**, *19*, 256201.

[340] Pervukhina, N. V.; Borisov, S. V.; Magarill, S. A.; Kuratieva, N. V.; Mozgova, N. N.; Chaplygin, I. V. *J. Struct. Chem.* **2012**, *53*, 588–592.

[341] Berlepsch, P.; Armbruster, T.; Makovicky, E.; Hejny, C.; Topa, D.; Graeser, S. *Can. Mineral.* **2001**, *39*, 1653–1663.

[342] Savory, C. N.; Ganose, A. M.; Travis, W.; Atri, R. S.; Palgrave, R. G.; Scanlon, D. O. *J. Mater. Chem. A* **2016**, *4*, 12648–12657.

[343] Kehoe, A. B.; Temple, D. J.; Watson, G. W.; Scanlon, D. O. *Phys. Chem. Chem. Phys.* **2013**, *15*, 15477–15484.

[344] Katan, C.; Pedesseau, L.; Kepenekian, M.; Rolland, A.; Even, J. *J. Mater. Chem. A* **2015**, *3*, 9232–9240.

[345] Svane, A.; Christensen, N. E.; Cardona, M.; Chantis, A. N.; van Schilfgaarde, M.; Kotani, T. *Phys. Rev. B: Condens. Matter* **2010**, *81*, 245120.

[346] Filip, M. R.; Patrick, C. E.; Giustino, F. *Phys. Rev. B: Condens. Matter* **2013**, *87*, 205125.

[347] Gildart, L.; Kline, J.; Mattox, D. *J. Phys. Chem. Solids* **1961**, *18*, 286–289.

[348] Liao, H.-C.; Wu, M.-C.; Jao, M.-H.; Chuang, C.-M.; Chen, Y.-F.; Su, W.-F. *CrystEngComm* **2012**, *14*, 3645–3652.

[349] Williamson, B. A. D.; Buckeridge, J.; Brown, J.; Ansbro, S.; Palgrave, R. G.; Scanlon, D. O. *Chem. Mater.* **2017**, *29*, 2402–2413.

[350] Buckeridge, J.; Jevdokimovs, D.; Catlow, C. R. A.; Sokol, A. A. *Phys. Rev. B: Condens. Matter* **2016**, *94*, 180101.

[351] Major, J.; Phillips, L.; Turkestani, M. A.; Bowen, L.; Whittles, T.; Dhanak, V.; Durose, K. *Sol. Energy Mater. Sol. Cells* **2017**, *172*, 1–10.

[352] Lehner, A. J.; Fabini, D. H.; Evans, H. A.; Hébert, C.-A.; Smock, S. R.; Hu, J.; Wang, H.; Zwanziger, J. W.; Chabinyc, M. L.; Seshadri, R. *Chem. Mater.* **2015**, *27*, 7137–7148.

[353] Lehner, A. J.; Wang, H.; Fabini, D. H.; Liman, C. D.; Hébert, C.-A.; Perry, E. E.; Wang, M.; Bazan, G. C.; Chabinyc, M. L.; Seshadri, R. *Appl. Phys. Lett.* **2015**, *107*, 131109.

[354] Höffling, B.; Schleife, A.; Rödl, C.; Bechstedt, F. *Phys. Rev. B: Condens. Matter* **2012**, *85*, 035305.

[355] Scanlon, D. O.; Watson, G. W. *J. Mater. Chem.* **2012**, *22*, 25236–25245.

[356] Walsh, A.; Chen, S.; Wei, S. H.; Gong, X. G. *Adv. Energy Mater.* **2012**, *2*, 400–409.

[357] Munro, A. M.; Zacher, B.; Graham, A.; Armstrong, N. R. *ACS Appl. Mater. Interfaces* **2010**, *2*, 863–869.

[358] Williams, R. H.; Murray, R. B.; Govan, D. W.; Thomas, J. M.; Evans, E. L. *J. Phys. C: Solid State Phys.* **1973**, *6*, 3631.

[359] Ganose, A. M.; Scanlon, D. O. *J. Mater. Chem. C* **2016**, *4*, 1467–1475.

[360] Gassenbauer, Y.; Klein, A. *J. Phys. Chem. B* **2006**, *110*, 4793–4801.

[361] Liu, H.; Avrutin, V.; Izyumskaya, N.; Özgür, U.; Morkoç, H. *Superlattices and Microstructures* **2010**, *48*, 458–484.

[362] Burton, L. A.; Whittles, T. J.; Hesp, D.; Linhart, W. M.; Skelton, J. M.; Hou, B.; Webster, R. F.; O'Dowd, G.; Reece, C.; Cherns, D.; Fermin, D. J.; Veal, T. D.; Dhanak, V. R.; Walsh, A. *J. Mater. Chem. A* **2016**, *4*, 1312–1318.

[363] Sahu, A.; Kang, M. S.; Kompch, A.; Notthoff, C.; Wills, A. W.; Deng, D.; Winterer, M.; Frisbie, C. D.; Norris, D. J. *Nano Lett.* **2012**, *12*, 2587–2594.

[364] Savory, C. N.; Ganose, A. M.; Scanlon, D. O. *Chem. Mater.* **2017**, *29*, 5156–5167.

Appendix A

Appendix

A.1 Brillouin Zones

Notation for high symmetry $\mathbf{k}$-points in all Brillouin zones taken from Bradley and Cracknell.[179]

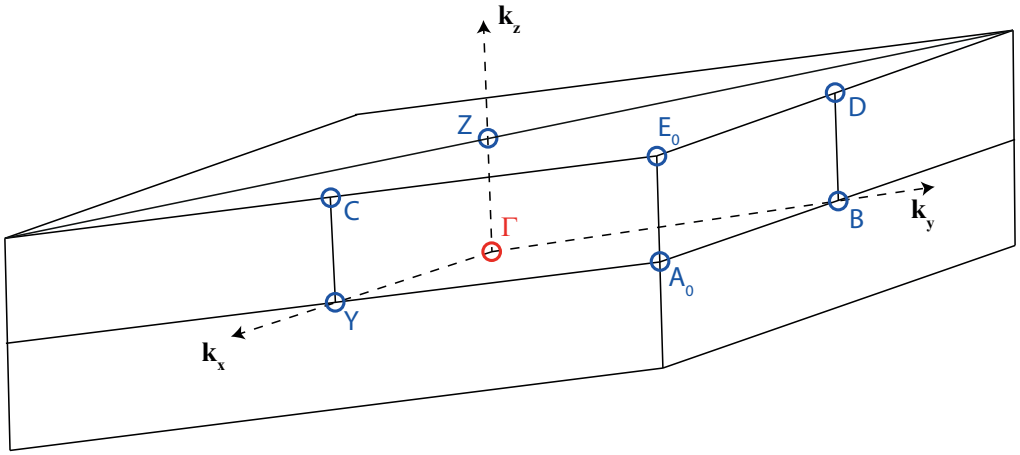

Figure A.1: Brillouin zone of cells with a primitive monoclinic Bravais lattice, with high-symmetry points labelled: $\Gamma = (0,0,0)$; $B = (-\frac{1}{2},0,0)$; $Y = (0,\frac{1}{2},0)$; $D = (-\frac{1}{2},0,\frac{1}{2})$; $C = (0,\frac{1}{2},\frac{1}{2})$; $A_0 = (\frac{1}{2},\frac{1}{2},0)$; $E_0 = (\frac{1}{2},\frac{1}{2},\frac{1}{2})$

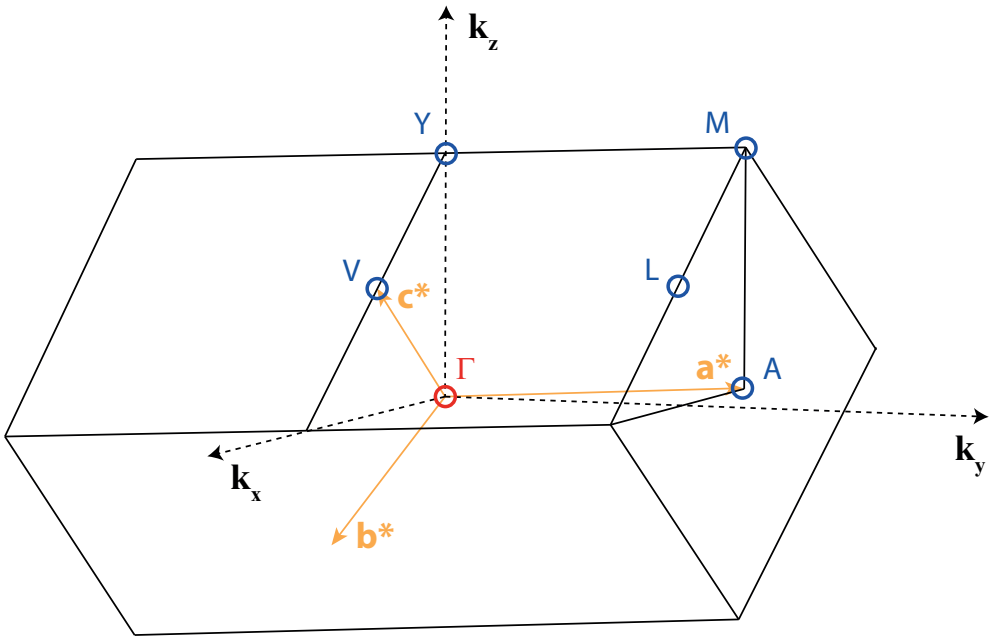

Figure A.2: Brillouin zone of cells with a C-centred monoclinic Bravais lattice, with high-symmetry points labelled: Γ = (0,0,0); A = $(-\frac{1}{2},0,0)$; V = $(0,0,\frac{1}{2})$; Z = $(0,-\frac{1}{2},\frac{1}{2})$; L = $(-\frac{1}{2},0,\frac{1}{2})$; M = $(-\frac{1}{2},-\frac{1}{2},\frac{1}{2})$. Orange axes mark the reciprocal vectors ($\mathbf{a}^*$, $\mathbf{b}^*$, $\mathbf{c}^*$) of the calculated *primitive* cell with respect to the reciprocal vectors of the conventional cell ($\mathbf{k}_x$, $\mathbf{k}_y$, $\mathbf{k}_z$)

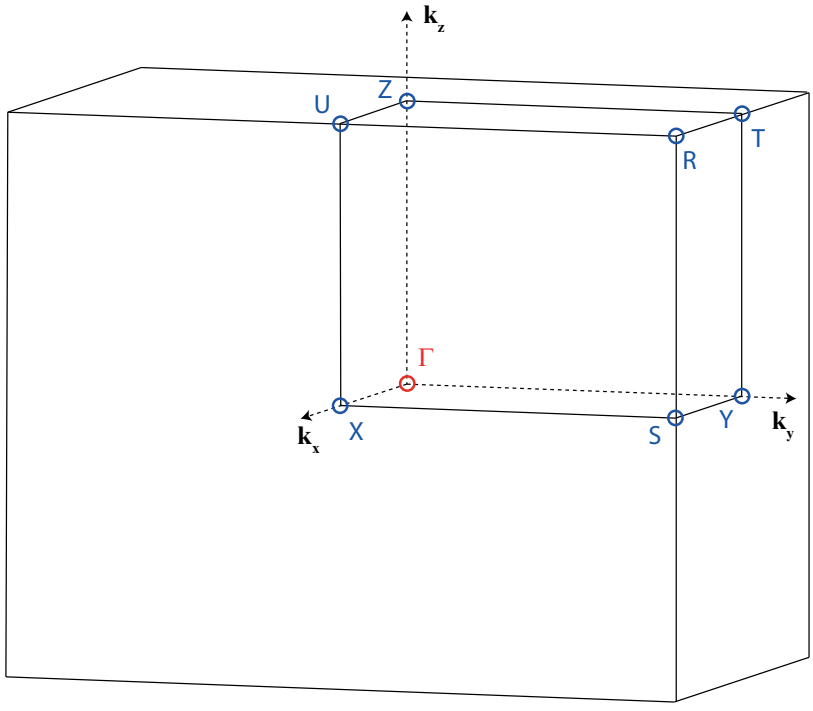

Figure A.3: Brillouin zone of cells with a primitive orthorhombic Bravais lattice, with high-symmetry points labelled: Γ = (0,0,0); Y = $(-\frac{1}{2},0,0)$; X = $(0,\frac{1}{2},0)$; Z = $(0,0,\frac{1}{2})$; U = $(0,\frac{1}{2},\frac{1}{2})$; S = $(-\frac{1}{2},\frac{1}{2},0)$; S = $(-\frac{1}{2},0,\frac{1}{2})$; R = $(-\frac{1}{2},\frac{1}{2},\frac{1}{2})$

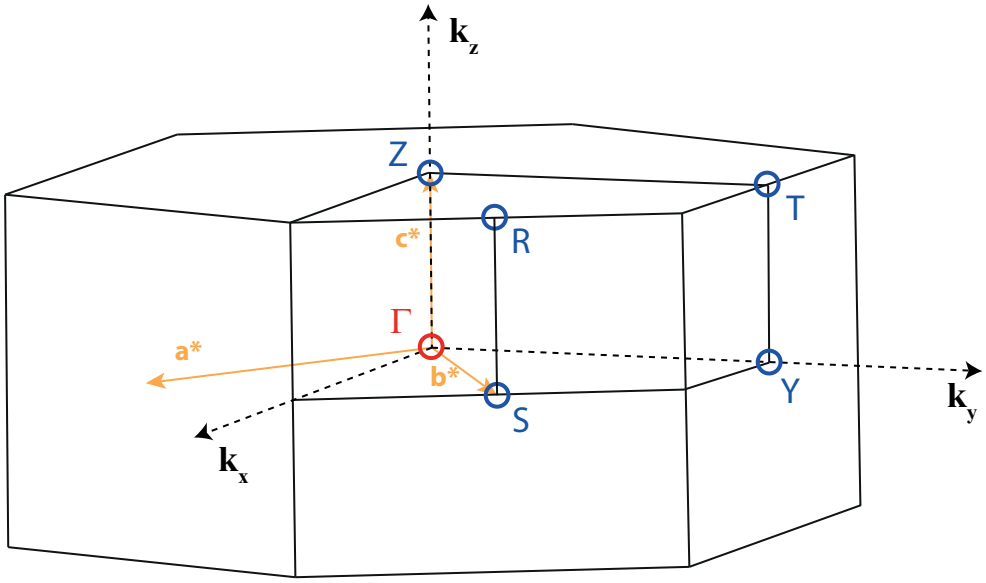

Figure A.4: Brillouin zone of cells with a C-centred orthorhombic Bravais lattice, with high-symmetry points labelled: Γ = (0,0,0); Y = $(-\frac{1}{2},\frac{1}{2},0)$; Z = $(0,0,\frac{1}{2})$; T = $(\frac{1}{2},\frac{1}{2},\frac{1}{2})$; R = $(0,\frac{1}{2},\frac{1}{2})$. Orange axes mark the reciprocal vectors ($\mathbf{a}^*$, $\mathbf{b}^*$, $\mathbf{c}^*$) of the calculated *primitive* cell with respect to the reciprocal vectors of the conventional cell ($\mathbf{k}_x$, $\mathbf{k}_y$, $\mathbf{k}_z$)

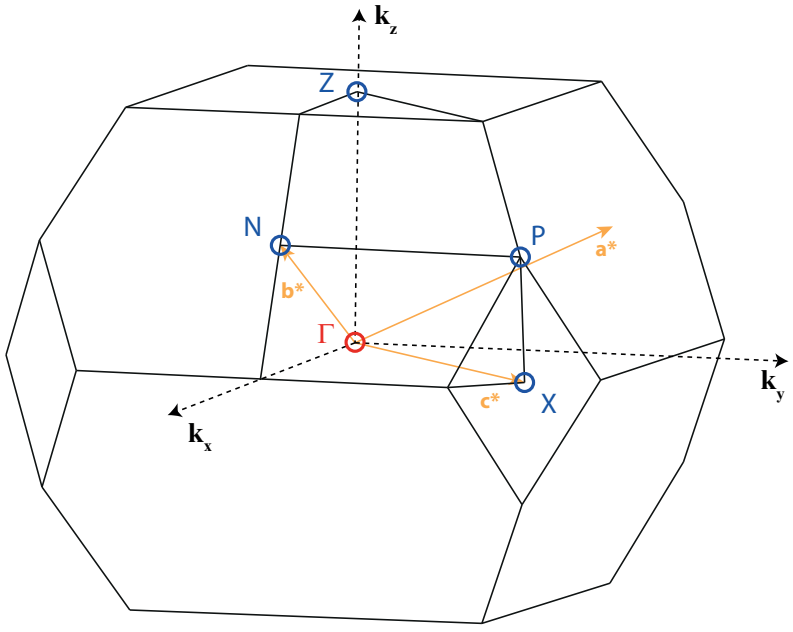

Figure A.5: Brillouin zone of cells with a body-centred tetragonal Bravais lattice, with high-symmetry points labelled: Γ = (0,0,0); N = $(0,\frac{1}{2},0)$; X = $(0,0,\frac{1}{2})$; Z = $(-\frac{1}{2},\frac{1}{2},\frac{1}{2})$; P = $(\frac{1}{4},\frac{1}{4},\frac{1}{4})$. Orange axes mark the reciprocal vectors ($\mathbf{a}^*$, $\mathbf{b}^*$, $\mathbf{c}^*$) of the calculated *primitive* cell with respect to the reciprocal vectors of the conventional cell ($\mathbf{k}_x$, $\mathbf{k}_y$, $\mathbf{k}_z$)

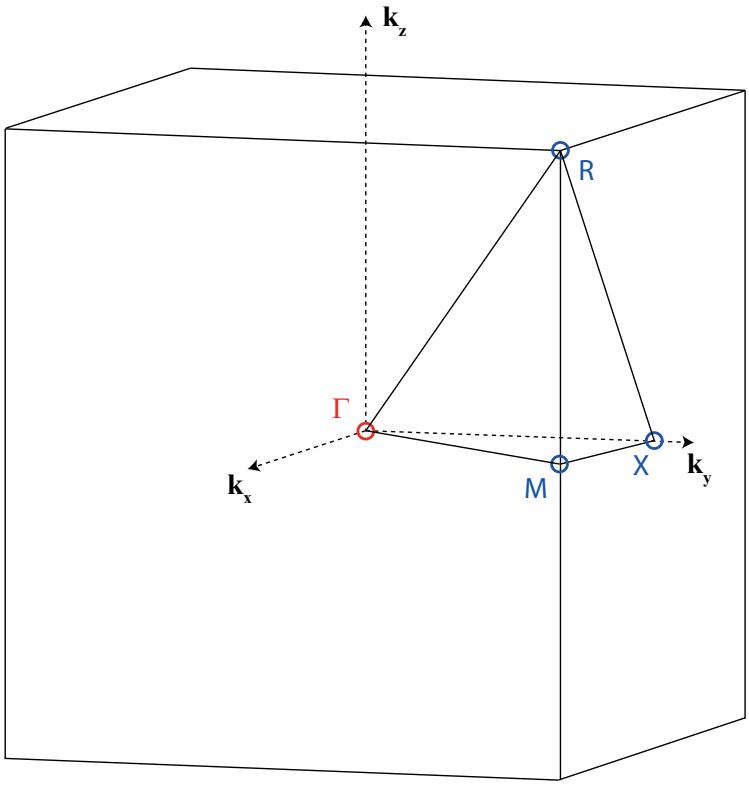

Figure A.6: Brillouin zone of cells with a primitive cubic Bravais lattice, with high-symmetry points labelled: Γ = (0,0,0); X = (0,$\frac{1}{2}$,0); M = ($\frac{1}{2}$,$\frac{1}{2}$,0); Z = ($\frac{1}{2}$,$\frac{1}{2}$,$\frac{1}{2}$)

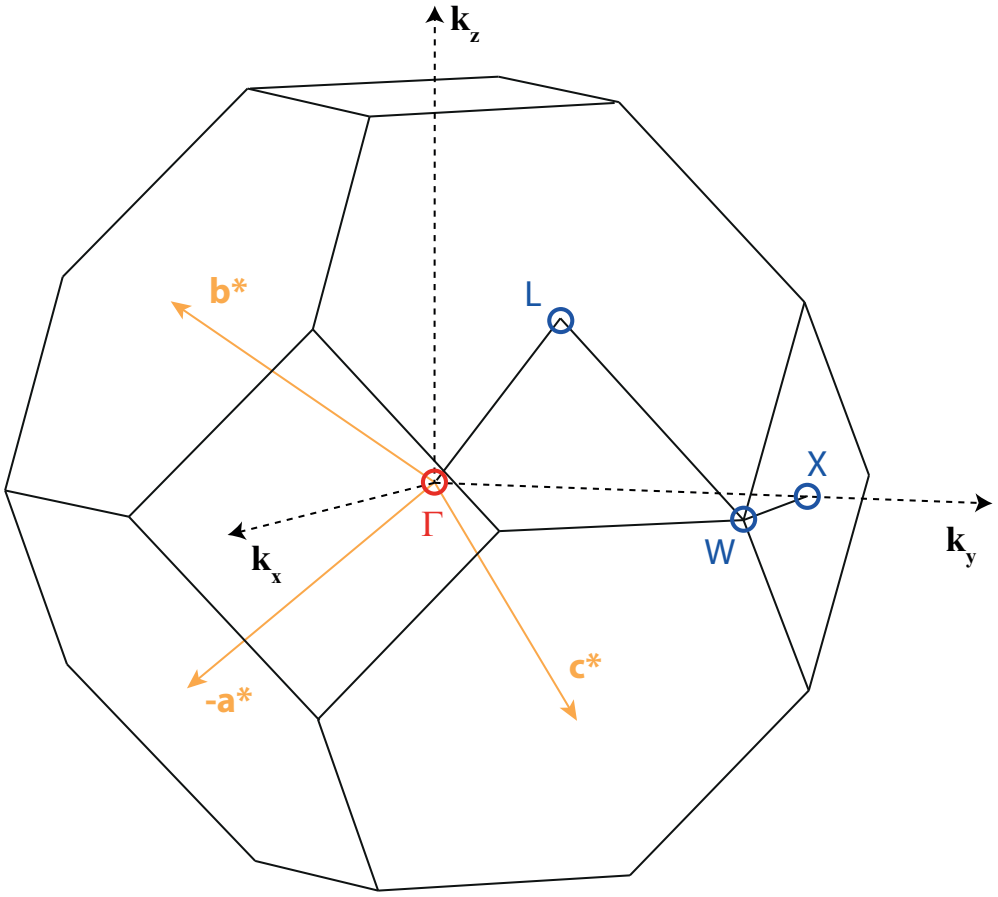

Figure A.7: Brillouin zone of cells with a face-centred cubic Bravais lattice, with high-symmetry points labelled: $\Gamma = (0,0,0)$; $\mathrm{X} = (\frac{1}{2},0,\frac{1}{2})$; $\mathrm{L} = (\frac{1}{2},\frac{1}{2},\frac{1}{2})$; $\mathrm{W} = (\frac{1}{2},\frac{1}{4},\frac{3}{4})$. Orange axes mark the reciprocal vectors ($\mathbf{a}^*$, $\mathbf{b}^*$, $\mathbf{c}^*$) of the calculated *primitive* cell with respect to the reciprocal vectors of the conventional cell ($\mathbf{k}_x$, $\mathbf{k}_y$, $\mathbf{k}_z$)

A.2 Experimental methods regarding AgCuS and Ag_3CuS_2

AgCuS was synthesised using the hydrothermal method of Tokuhara *et al.*:[292] non-stoichiometric quantities of Ag (1.4314 g, 0.0133 mol), Cu (1.0306 g, 0.0162 mol), and S (0.4727 g, 0.0147 mol) were ground in an agate pestle and mortar (forming a molar ratio of 0.9:1.1:1.0). 0.5 g of this mixture was transferred with 15 ml distilled water to a Teflon-lined steel autoclave which was then heated at 180 °C for 10 h, before being cooled slowly to room temperature. AgCuS was isolated via filtration, washed with distilled water and dried.

Ag_3CuS_2 was synthesised via high-temperature synthesis from the elements: non-stoichiometric quantities of Ag (1.6039 g, 0.0143 mol), Cu (0.3000 g, 0.0047 mol), and S (0.3027 g, 0.0094 mol) were ground in an agate pestle and mortar (forming a molar ratio of 3.05:1.00:2.00) and transferred with 15 ml distilled water to a 1 cm diameter quartz tube. The filled tube was evacuated and flame-sealed, then heated at 5 °C min^{-1} from room temperature to 500 °C with a dwell time of 10 h, before being cooled slowly to room temperature. Ag_3CuS_2 was obtained in good yield without further purification.

Powder X-ray diffraction was collected on a Stoe StadiP diffractometer, using samples in 0.5 mm capillaries; data was collected over a 5° to 60° range of 2θ in steps of 0.5° and a collection time of 20 s for each step, with a Cu Kα1 (λ = 1.540 56 Å) radiation source. Optical diffuse-reflectance data for the determination of optical band gap was recorded at room temperature using a Lambda 950 spectrophotometer equipped with an integrating sphere. Data was collected between 300 nm to 2000 nm in steps of 1 nm. The Kubelka-Munk method is used to relate the measured reflectance function to the wavelength and determine the optical gap of each material. X-ray photoemission spectroscopy (XPS) measurements were recorded using a Thermo Scientific Al-Kα spectrometer.

Electrical measurements were performed on an AgCuS pellet using 4-point contacts in a van der Pauw geometry on an Ecopia hall Measurement System (HMS-3000) at room temperature to obtain the Hall coefficient, resistivity and charge carrier concentration and mobility. 13 mm diameter pellets of AgCuS and Ag_3CuS_2 were pressed at 5 bar pressure, resulting in thicknesses of 1.04 mm and 1.24 mm respectively. The resistance of the Ag_3CuS_2 pellet was too high for Hall effect measurement, so four point probe measurements were performed to obtain the sheet resistance.